

BIPED GAIT GENERATION FOR HUMANOID  
DYNAMIC WALKING

By  
NG BUCK SIN

SUBMITTED IN PARTIAL FULFILLMENT OF THE  
REQUIREMENTS FOR THE DEGREE OF  
DOCTOR OF PHILOSOPHY  
AT  
DEPARTMENT OF ELECTRICAL AND COMPUTER ENGINEERING,  
NATIONAL UNIVERSITY OF SINGAPORE  
4 ENGINEERING DRIVE 3, SINGAPORE 117576  
MAY 2013

# Table of Contents

<b>Table of Contents</b>	<b>ii</b>
<b>List of Tables</b>	<b>viii</b>
<b>List of Figures</b>	<b>x</b>
<b>Declaration</b>	<b>xviii</b>
<b>Acknowledgements</b>	<b>xix</b>
<b>Abstract</b>	<b>xx</b>
<b>1 Introduction</b>	<b>1</b>
1.1 Biped Locomotion . . . . .	2
1.1.1 Biped Model . . . . .	2
1.1.2 Stability Criterion . . . . .	5
1.1.3 Locomotion Mechanism . . . . .	12
1.1.4 Biped Gait Generation . . . . .	16
1.1.5 Compliant Control . . . . .	20

1.1.6	Walking Control . . . . .	21
1.2	Research Consideration . . . . .	23
1.3	Thesis Aim . . . . .	24
1.4	Thesis Contributions . . . . .	24
1.5	Thesis Organization . . . . .	26
<b>2</b>	<b>Humanoid Robot Platform</b>	<b>29</b>
2.1	Robo-Erectus Junior . . . . .	30
2.2	Hardware Design . . . . .	31
2.2.1	Mechanical Structure . . . . .	31
2.2.2	Electrical System . . . . .	35
2.3	Locomotion Control . . . . .	38
2.3.1	Walk Gait Engine . . . . .	38
2.3.2	Inverse Kinematics . . . . .	39
2.3.3	Actuator Control . . . . .	45
2.3.4	Force Sensor . . . . .	46
2.3.5	Rate Gyroscope . . . . .	47
2.3.6	Inertia Measurement Unit . . . . .	50
2.3.7	Position Feedback . . . . .	53
<b>3</b>	<b>Generation of Lateral Walk-Oscillation using Sinusoidal Pat- tern</b>	<b>56</b>
3.1	Lateral Motion Using Sinusoidal Reference Pattern . . . . .	59
3.1.1	Biped Model . . . . .	59

3.1.2	Sinusoidal Foot Trajectories . . . . .	60
3.1.3	Zero Moment Point (ZMP) Trajectory . . . . .	62
3.1.4	Generating Stable Lateral Motion . . . . .	64
3.2	Offline Gait Generation of Lateral Walk-Oscillation . . . . .	65
3.2.1	Foot Lifting and Landing Motion . . . . .	66
3.2.2	Support Phases For Oscillation Cycle . . . . .	68
3.2.3	Foot Placement Trajectories . . . . .	70
3.3	Simulations . . . . .	73
3.3.1	Simulation Model and ZMP Computation . . . . .	75
3.3.2	Lateral Walk Oscillations . . . . .	77
3.3.3	Influence of Walking Environment Disturbance . . . . .	83
3.4	Experiments . . . . .	86
3.4.1	Center of Pressure (CoP) Measurement for Experimental Result Validation . . . . .	88
3.4.2	Implementation of Lateral Walk-Oscillation . . . . .	91
3.5	Conclusion . . . . .	92
<b>4</b>	<b>Sustainable Lateral Walk-Oscillation</b>	<b>95</b>
4.1	Lateral Shift Amplitude Controller . . . . .	99
4.1.1	Adjustment of Shift Amplitude . . . . .	99
4.1.2	Peak Amplitude Measurement Window . . . . .	100
4.2	Real-Time Zero Moment Point Compensator . . . . .	101
4.2.1	Stability Zone for Compensation . . . . .	102

4.2.2	Compensator Design . . . . .	103
4.3	Online Phase Generator . . . . .	108
4.3.1	Phase Detector . . . . .	108
4.3.2	Foot Placement Trajectories . . . . .	109
4.4	Simulations . . . . .	111
4.4.1	Shift Amplitude Correction . . . . .	112
4.4.2	Zero Moment Point (ZMP) Compensation . . . . .	113
4.4.3	Phase Detection for Transitions . . . . .	114
4.4.4	Walking Environment Disturbances Rejection . . . . .	117
4.4.5	Reaction to Impulsive Disturbances . . . . .	117
4.5	Experiments . . . . .	119
4.5.1	Online Generation of Walk-Oscillations . . . . .	120
4.5.2	Walking Environment Disturbances . . . . .	120
4.5.3	Impulsive Disturbances . . . . .	122
4.6	Conclusion . . . . .	124
<b>5</b>	<b>OmniDirectional Walking</b>	<b>126</b>
5.1	Real-Time Foot Placement Generation . . . . .	129
5.1.1	Frontal Plane Movement . . . . .	132
5.1.2	Transverse Plane Movement . . . . .	133
5.1.3	Sagittal Plane Movement . . . . .	134
5.2	Walk-Stepper Controller . . . . .	140
5.2.1	Step Acceleration Control . . . . .	140

5.2.2	Concept of 'Master' Foot . . . . .	141
5.3	Motion Steering Controller . . . . .	142
5.3.1	Motion Steering . . . . .	143
5.3.2	Step Displacement Estimation . . . . .	144
5.3.3	Velocity Compensation . . . . .	147
5.4	Simulations . . . . .	148
5.4.1	Frontal, Sagittal and Transverse Plane Movements .	148
5.4.2	OmniDirectional Walk . . . . .	152
5.5	Experiments . . . . .	154
5.5.1	Plane Movements . . . . .	155
5.5.2	OmniDirectional Walk . . . . .	156
5.5.3	Motion Steering . . . . .	158
5.6	Conclusion . . . . .	161
<b>6</b>	<b>Compliant Control</b>	<b>162</b>
6.1	Compliant Knee Joints . . . . .	164
6.1.1	Compliant Motion using Torque Control . . . . .	164
6.1.2	Stiffness and Damping Coefficients . . . . .	165
6.1.3	Translating to Actuator Control Parameter . . . . .	166
6.2	Foot Landing Impact Reduction . . . . .	168
6.2.1	Foot and Ground Contact Model . . . . .	168
6.2.2	Virtual Spring-Damper System . . . . .	170
6.2.3	Stiffness Control using Angular Tilt Measurement . .	171

6.3	Estimation of Center of Pressure using Accelerometers and Compliant Joints . . . . .	175
6.3.1	Vertical Ground Reaction Force Estimation using Compliant Joints . . . . .	176
6.3.2	Computation of Center of Pressure (CoP) using Accelerometers . . . . .	179
6.4	Energy Saving using Under-Actuation . . . . .	181
6.4.1	Under-Actuation of Ankle Roll Joint . . . . .	182
6.4.2	Phase Tracking and Modified Oscillation Cycle . . . . .	184
6.4.3	Energy-Saving Measurement . . . . .	185
6.5	Conclusion . . . . .	187
<b>7</b>	<b>Conclusion</b>	<b>189</b>
7.1	Implemented Work . . . . .	189
7.2	Summing Up . . . . .	190
7.3	Future Direction . . . . .	194
<b>8</b>	<b>Author's Publications</b>	<b>195</b>
	<b>Bibliography</b>	<b>196</b>

# List of Tables

2.1	Physical specifications of the Robo-Erectus Junior . . . . .	31
2.2	List of degrees of freedom for robot . . . . .	32
2.3	Specifications of the sensors . . . . .	36
2.4	Specifications of the actuator. . . . .	36
2.5	Specifications of the processors . . . . .	37
2.6	General description of blocks in locomotion control . . . . .	38
2.7	Dimensions and masses of biped model . . . . .	40
2.8	Denavit - Hartenberg parameters . . . . .	54
3.1	Dimensions and masses of 2D model . . . . .	76
3.2	Parameters for simulation . . . . .	78
3.3	Sinusoidal trajectories applied for lateral motion . . . . .	78
3.4	Average measured peak ZMP amplitudes . . . . .	79
3.5	Parameters for walk-oscillation simulation . . . . .	81



4.1	Parameters for walk-oscillations simulation . . . . .	112
4.2	Time instances for foot lift and landing . . . . .	115
4.3	Parameters for walk-oscillations experiment . . . . .	120
4.4	Average time instances on different walking surface . . . . .	122
5.1	Six stages of motion execution . . . . .	130
5.2	Parameters for omnidirectional walk simulation . . . . .	148
5.3	Parameters for omnidirectional walk experiment . . . . .	155
5.4	Velocities and accelerations for omnidirectional walk . . . . .	155
5.5	Velocities and accelerations for omnidirectional walk with motion steering . . . . .	161
6.1	Characteristic of the freed actuator surface . . . . .	184
6.2	Average voltage drop measured for 20 trials . . . . .	186

# List of Figures

1.1	Anatomical position and reference frame . . . . .	2
1.2	Linear inverted pendulum model . . . . .	4
1.3	Foot support polygon . . . . .	5
1.4	Center of Pressure (CoP) . . . . .	6
1.5	Zero Moment Point (ZMP) . . . . .	8
1.6	Relationship of ZMP and COP . . . . .	9
1.7	Foot-Rotation Indicator . . . . .	10
1.8	Centroidal Moment Pivot . . . . .	11
1.9	CMP versus ZMP/COP . . . . .	12
1.10	Leg structure for biped locomotion . . . . .	13
1.11	Mechanism subjected to angle errors in joints . . . . .	14
1.12	Cornell University passive-dynamic bipedal robot [1] . . . . .	16
1.13	Honda ASIMO [2] . . . . .	17
1.14	Matsuoka neural oscillator . . . . .	19

1.15 Omnidirectional walking . . . . .	22
1.16 Decoupling of dynamic walking . . . . .	28
2.1 Singapore Polytechnic Robo-Erectus Junior Bv-MkIII . . . . .	30
2.2 Mechanical assembly of humanoid robot . . . . .	32
2.3 Degree-of-freedoms configuration of robot . . . . .	33
2.4 Parallel double crank mechanism . . . . .	34
2.5 Parallel double crank mechanism leg structure . . . . .	34
2.6 Electrical system architecture . . . . .	35
2.7 Locomotion control system architecture . . . . .	37
2.8 Mass distribution of biped model . . . . .	40
2.9 Angular quantities of the biped model . . . . .	41
2.10 Leg swing motion in sagittal plane . . . . .	42
2.11 Decoupling of leg motion . . . . .	43
2.12 Reference points for inverse kinematics . . . . .	44
2.13 Inverse kinematic parameters . . . . .	44
2.14 Mechanical installation of force sensors . . . . .	47
2.15 Position of force sensors . . . . .	48
2.16 Force sensor: Resistance-to-voltage circuit . . . . .	48
2.17 Fixed-point DC blocker with ‘fraction-saving’ . . . . .	49

2.18 Inertia measurement unit . . . . .	50
2.19 Kalman filter algorithm [3] . . . . .	51
2.20 Link coordinate frame using D-H convention . . . . .	55
3.1 Decoupling of dynamic walk motions . . . . .	57
3.2 Phases of walking in frontal plane . . . . .	58
3.3 Linear inverted pendulum model . . . . .	60
3.4 Foot placement in the frontal plane . . . . .	61
3.5 Lateral shifting of CoM . . . . .	62
3.6 ZMP and CoM trajectories of lateral motion . . . . .	63
3.7 Lateral motion support polygon . . . . .	64
3.8 ZMP and CoM trajectories of stable lateral motion . . . . .	66
3.9 Position for foot lift . . . . .	67
3.10 Single and double support phases . . . . .	70
3.11 ZMP trajectory of walk-oscillations . . . . .	71
3.12 Foot placement trajectories generated offline for lateral walk- oscillation . . . . .	74
3.13 3D model of the humanoid . . . . .	75
3.14 2D model of the humanoid in the frontal plane . . . . .	76
3.15 3D humanoid model in stable lateral motion . . . . .	79

3.16 ZMP trajectories of lateral motion . . . . .	80
3.17 3D humanoid model in stable walk-oscillation . . . . .	82
3.18 ZMP trajectory of 4 walk-oscillation cycles . . . . .	83
3.19 Disturbance effect of 3° floor inclination . . . . .	84
3.20 ZMP trajectory with 3° floor inclination . . . . .	85
3.21 Contact dynamics of the foot and ground . . . . .	85
3.22 ZMP trajectories with different contact dynamics . . . . .	87
3.23 Reading of the force sensors . . . . .	88
3.24 Center of Pressure (CoP) measurement . . . . .	89
3.25 Snapshots of REJr in stable lateral motion . . . . .	90
3.26 ZMP measurement of lateral motion . . . . .	93
3.27 Snapshots of REJr in stable walk-oscillation . . . . .	94
3.28 ZMP measurement of lateral walk-oscillations . . . . .	94
4.1 Online lateral walk-oscillation gait generation . . . . .	98
4.2 ZMP trajectories during $k^{th}$ oscillation cycle . . . . .	100
4.3 Measurement window for shift amplitude controller . . . . .	101
4.4 Stability zone . . . . .	103
4.5 Stability zone measurement experiment . . . . .	104
4.6 CoP measurement in single support phase . . . . .	105

4.7	Inverted pendulum representation in single support phase .	106
4.8	ZMP trajectory during phase transition . . . . .	109
4.9	Simulation block diagram . . . . .	111
4.10	ZMP trajectories with lateral shift amplitude controller . . .	113
4.11	ZMP trajectories with compensator and lateral shift amplitude controller. . . . .	114
4.12	Trajectories of gaits generated with disturbances . . . . .	116
4.13	Impulse disturbance generation . . . . .	118
4.14	Simulations of impulse disturbance . . . . .	118
4.15	ZMP trajectories with 4 N disturbance force . . . . .	119
4.16	ZMP trajectories of online and offline walk-oscillations generated . . . . .	121
4.17	Different walking surfaces . . . . .	122
4.18	Walk-oscillations on different walking surfaces . . . . .	123
4.19	Normalized amount of lateral Shift compensation . . . . .	124
4.20	Impulse disturbance generation experiment . . . . .	125
4.21	Experiment of impulse disturbance . . . . .	125
5.1	Omnidirectional gait generation . . . . .	128
5.2	Foot placement trajectories and joint angles for omnidirectional walk movements . . . . .	131

5.3	Walk-oscillation - Dynamic walking . . . . .	136
5.4	Frontal plane movement . . . . .	137
5.5	Transverse plane movement . . . . .	137
5.6	Sagittal plane movement . . . . .	138
5.7	Foot placement trajectories for frontal plane movement . . .	139
5.8	Joint trajectories for transverse plane movement . . . . .	139
5.9	Foot placement trajectories for sagittal plane movement . .	139
5.10	Omnidirectional walking . . . . .	141
5.11	Trapezoidal profile used for step acceleration control . . . .	142
5.12	Foot placement of transverse plane movement . . . . .	143
5.13	Concept of 'master' foot . . . . .	144
5.14	Foot slip problem . . . . .	145
5.15	Compensation techniques for foot slip . . . . .	146
5.16	Step displacement estimation . . . . .	146
5.17	Foot trajectories for frontal plane movement . . . . .	149
5.18	Real-time foot placement trajectories generated for frontal plane movement . . . . .	149
5.19	Angular change during transverse plane movement . . . . .	150
5.20	Real-time hip yaw joints trajectories generated for trans- verse plane movement . . . . .	150

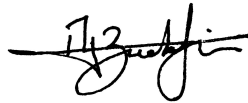
5.21	Foot trajectories for sagittal plane movement . . . . .	151
5.22	Real-time foot placement trajectories generated for sagittal plane movement . . . . .	151
5.23	Foot trajectories for omnidirectional walk . . . . .	152
5.24	CoM and foot trajectories for omnidirectional walk . . . . .	153
5.25	Real-time foot placement trajectories generated for omnidi- rectional walk . . . . .	153
5.26	Walking movements . . . . .	156
5.27	Omnidirectional walking . . . . .	157
5.28	Color markers mounted on the humanoid head . . . . .	158
5.29	Humanoid set on a circular path . . . . .	159
5.30	Captured movement of humanoid set on a circular path . . .	160
6.1	Spring-damper compliant knee joint . . . . .	165
6.2	Servo control parameter $k_{stretch1} > k_{stretch2}$ [4] . . . . .	166
6.3	Compliant knee reacting to a force from the top . . . . .	168
6.4	Spring-damper contact model . . . . .	169
6.5	Virtual spring-damper system . . . . .	170
6.6	Foot landing impact experiment . . . . .	170
6.7	Stiffness versus ground reaction force . . . . .	172



6.8	Angular tilt in the frontal plane with and without compliant knee joints . . . . .	173
6.9	Snapshot of unequal hip height phenomena . . . . .	174
6.10	Resultant tilt due to unequal depression in compliant knees	175
6.11	Stiffness control . . . . .	176
6.12	Angular tilt in the frontal plane with compliant knee joints and stiffness control . . . . .	176
6.13	Stiffness control system . . . . .	177
6.14	Compliant knee joint with load . . . . .	178
6.15	Force projection and ground reaction force vector . . . . .	179
6.16	Force measured by force sensor and compliant knee joint . .	180
6.17	Centroidal Moment Pivot (CMP) . . . . .	182
6.18	Center of Pressure (CoP) computed using accelerometer and compliant joint . . . . .	183
6.19	Under-actuation for energy saving . . . . .	184
6.20	Falling of the lifted foot's hip . . . . .	185
6.21	Roll joints of the ankle and hip . . . . .	186
6.22	Under-actuated phase . . . . .	187

# Declaration

I hereby declare that the thesis is my original work and it has been written by me in its entirety. I have duly acknowledged all the sources of information which have been used in the thesis. This thesis has also not been submitted for any degree in any university previously.



---

NG BUCK SIN

May 15, 2013

# Acknowledgements

My foremost thank goes to my supervisor Dr. Prahlad Vadakkepat. I thank him for his support and encouragement throughout the course of the research, and for his insights and advices that helped to shape my research skills. His valuable feedback contributed greatly to the progress of the research. Special thanks to Dr Zhou Changjiu, centre director of Singapore Polytechnic *Advanced Robotics Intelligent and Control Centre* for agreeing to the development and use of Robo-Erectus Junior humanoid robot as part of the research carried out.

I would like to thank A/Prof. Loh Ai Poh and Dr. Tang Kok Zeuk for their kind help and suggestions during the course of the research. Many thanks goes to Mr. Dip Goswami, Mr. Daniel Hong, Mr. Jim Tan and Mr. Yong See Wei for their support and encouragement. Special thanks to the laboratory officer Mr. Tan Chee Siong for his support and friendly behaviour. I would like to express my appreciation to my colleagues in Singapore Polytechnic, Dr Carlos Acosta and Mr Jhohan Ng for various constructive discussions and suggests in helping the completion of this research.

I would like to thank my wife and family for their support, understanding and encouragement. Without them, I would not possibly have achieved whatever I have.

# Abstract

Gait generation of the humanoid robot for bipedal locomotion is a complex and difficult problem. The high dimensional state space and inherently hard-to-stabilize dynamics of the humanoid pose challenges in creating robust bipedal walking. Physical constraints and limitations in the implementation further aggravate the stability control of bipedal systems. In this dissertation, gait generation of the humanoid robot for fast dynamical walking is proposed and realized through ① generation of sustainable lateral walk-oscillation, ② omnidirectional walking and ③ compliant control. The approaches have low computational complexity, are simple and do not require the detailed dynamical model of the robot.

Lateral walk-oscillations comprise of the single and double support phase gaits. An offline gait generation approach based on the Zero Point Moment (ZMP) criterion, sinusoidal reference pattern and linear inverted pendulum model (LIPM) used to generate lateral walk-oscillation on a flat terrain without incurring high complexity and computational cost.

The lateral walk-oscillation gaits are improved by using an online gait generation approach that utilizes offline reference gait with online ZMP compensation. A two stage compensator and a phase generator is proposed and implemented to create lateral walk-oscillations with dynamic single and double support phase time periods. The approach is able to produce sustainable walk-oscillations subjected to walking environment disturbances.

Omnidirectional walking is parametrized by a walk stepper controller using a devised 'master' foot concept and super-position of the foot placement trajectory. The walking movements in the frontal, sagittal and transverse planes are generated in real-time and imposed with the lateral walk-oscillation gaits to produce sustainable omnidirectional walking. A motion steering controller based on rate-gyroscope feedback is introduced to enhance the directional control of the biped walk in the presence of foot slip.

Compliant control is applied to the knee joints for foot landing impact reduction and ground reaction force measurement without explicit sensing. A stiffness controller is implemented to facilitate stiffness adjustment without ill-effects. A method for the estimation of the Centre of Pressure (CoP) based on compliant knee joints and accelerometer readings is proposed. An energy-saving scheme is conceived and realized through motion compliance by the under-actuation of the ankle joints. The proposed work is implemented on a physical humanoid robot, Robo-Erectus Junior, and demonstrated in the RoboCup competition.

# Chapter 1

## Introduction

For the past decade, research on humanoid robots is one of the exciting topics that had drawn a lot of attention in the field of robotics. One of the key driving forces behind this research is the suitability of biped humanoid within the human environment. Humanoid robots, often with many degrees of freedom, are non-linear complex dynamic system which is difficult to control from the biped locomotion perspective. To overcome the challenge, many successful research studies have developed various techniques and solutions.

Despite the numerous research studies, the current biped locomotion technology is yet to attain the level of human-like capabilities. Humanoid robots at present are yet to take a major role in terms of real applications. There is still a lot to achieve for biped locomotion in terms of the stability, effectiveness, dexterity, flexibility and adaptability.

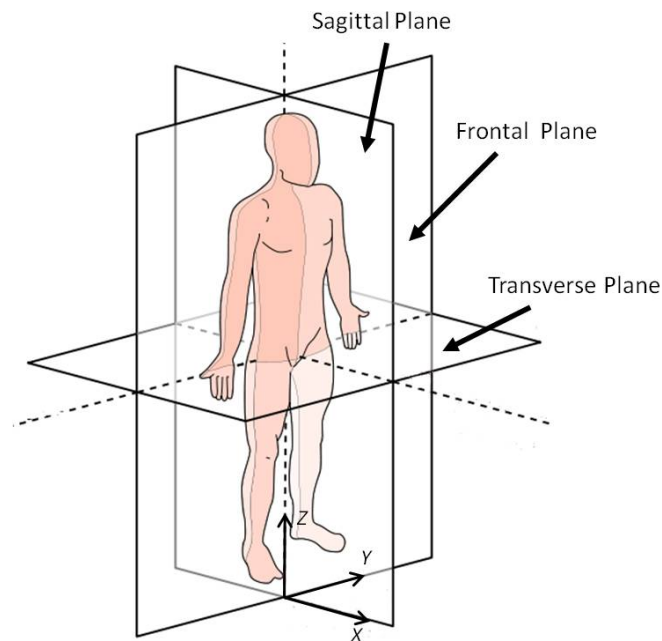


Figure 1.1: Anatomical position and reference frame

## 1.1 Biped Locomotion

Biped locomotion pertains to robot motion achieved using two legs; walking, hopping, running and shuffling are different forms of biped locomotion. Biped locomotion in this thesis pertains to bipedal walking. Bipedal walking is defined as the displacement of the robot in the transverse plane (Fig. 1.1). The transverse plane is defined as the plane parallel to the  $xy$ -plane of the reference frame, the plane parallel to the  $yz$ -plane is the frontal plane and the plane parallel to the  $xz$ -plane is the sagittal plane.

### 1.1.1 Biped Model

In biped locomotion research, gait generation approach can be roughly classified into two groups. The first group utilizes the dynamical model of

the robot whereas the other group uses a simplified dynamical model.

The dynamics of a  $n$  degree-of-freedom (DOFs) biped robot can be expressed by its motion equation [5] as:

$$\begin{bmatrix} h_{11} & h_{12} & h_{13} \\ h_{21} & h_{22} & h_{23} \\ h_{31} & h_{32} & h_{33} \end{bmatrix} \begin{pmatrix} \dot{v}_B \\ \dot{w}_B \\ \ddot{\theta} \end{pmatrix} + \begin{pmatrix} b_1 \\ b_2 \\ b_3 \end{pmatrix} + \begin{pmatrix} u\varepsilon_1 \\ u\varepsilon_2 \\ u\varepsilon_3 \end{pmatrix} = \begin{pmatrix} 0 \\ 0 \\ \tau \end{pmatrix}, \quad (1.1)$$

where  $h$  is the  $3 \times 3$  robot inertia matrix;  $h_{11}$ ,  $h_{12}$ ,  $h_{21}$  and  $h_{22}$  are  $3 \times 3$  submatrices,  $h_{13}$  and  $h_{23}$  are  $3 \times n$  submatrices,  $h_{31}$  and  $h_{32}$  are  $n \times 3$  submatrices, and,  $h_{33}$  is a  $n \times n$  submatrix.  $v_B$  and  $w_B$  are the  $3 \times 1$  submatrices of linear and angular velocities of the body respectively,  $\theta$  is a  $n \times 1$  joints displacement vector submatrix.  $b$  is the bias vector matrix;  $b_1$  and  $b_2$  are  $3 \times 1$  submatrices, and,  $b_3$  is a  $n \times 1$  submatrix.  $u\varepsilon_1$  and  $u\varepsilon_2$  are respectively the net force and net torque effect of the reaction forces on the body ( $3 \times 1$  submatrices), and  $u\varepsilon_3$  represents the effect of the reaction forces on the joints ( $n \times 1$  submatrix).  $\tau$  is the  $n \times 1$  generalized joint vector submatrix." Using the motion equations, necessary control laws can be applied to produce bipedal locomotion for the robot [6, 7]. However, the humanoid with many degree-of-freedom (DOFs) have highly complex nonlinear dynamics which make computation costly and difficult in practice using 1.1. Rather, computation of the matrices is often calculated using Newton-Euler dynamics formulation or Lagrangian dynamics formulation (1.2) [8–10]. The Lagrangian equations of the dynamics of a humanoid with  $n$  actuated leg joints can be expressed as:

$$M(\theta)\ddot{\theta} + C(\theta, \dot{\theta}) + K(\theta) = \tau, \quad (1.2)$$

where  $M$  is the  $n \times n$  inertial matrix,  $C$  is the  $n \times 1$  vector including the Coriolis and centrifugal terms,  $K$  is the  $n \times 1$  gravity vector,  $\tau$  is the vector for actuator torques and  $\theta$  is the joint angle vector.



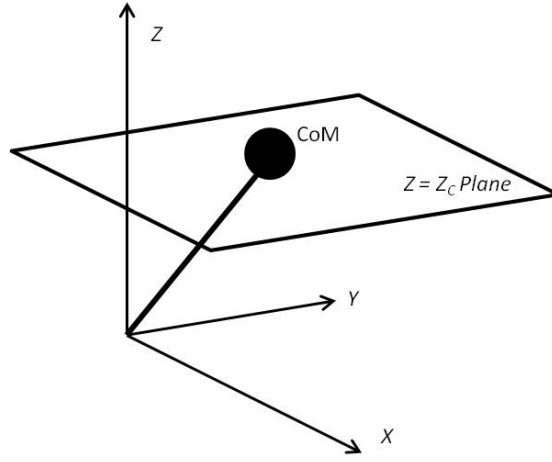


Figure 1.2: Linear inverted pendulum model

Simplified dynamical model is often utilized by researchers due to the complex nature of the bipedal locomotion. The simplified dynamical model is represented by concentrate masses in which it simplifies and maintains effective representation of the robot's dynamics. Computation in simplified dynamical model uses information such as the location and angular position of the concentrate masses. One of the simplified dynamical models used extensively is the Linear Inverted Pendulum Model (LIPM) [11] (Fig. 1.2). The LIPM consists of an inverted pendulum where a lump mass representing the robot's center of mass (CoM) is connected to a massless link. By constraining the movement of the CoM to the  $z_c$  plane (Fig. 1.2), the dynamics of the robot is decoupled into the frontal and sagittal plane. Motion equations of the decoupled dynamics are expressed as (1.3). Many biped research based on LIPM for reference generation have shown success [12–17].

$$\begin{aligned}\ddot{c}_x &= \frac{g}{z_c}c_x + \frac{1}{mz_c}\tau_x, \\ \ddot{c}_y &= \frac{g}{z_c}c_y - \frac{1}{mz_c}\tau_y,\end{aligned}$$

(1.3)

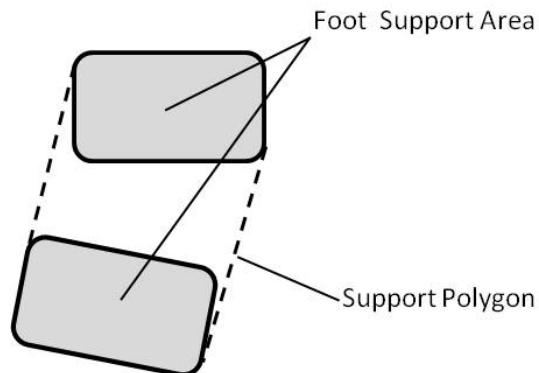


Figure 1.3: Foot support polygon

where  $c_x, c_y, c_z$  are the Cartesian coordinates of the CoM,  $m$  is mass of the robot,  $z_c$  is height of the plane in which the COM is constrained,  $g$  is the acceleration due to gravity,  $\tau_x$  and  $\tau_p$  are the pitch and roll control torque respectively.

### 1.1.2 Stability Criterion

Stability is the most critical component in bipedal locomotion. Stability in bipedal locomotion is defined as the degree of ability to sustain walking. To address stability, researchers have devised stability criterion such as Zero Moment Point (ZMP), Foot-Rotational Indicator (FRI) and Centroidal Moment Pivot (CMP). Stability criterion is commonly described from the viewpoint of the stability indicators, often denoted by a point on the ground, with respect to the foot support polygon; i.e. stability indicator lies within or outside the foot support polygon. The foot support polygon is defined as the convex hull encompassed by the supporting contact points or foot support area of the robot's feet with the ground (Fig. 1.3).

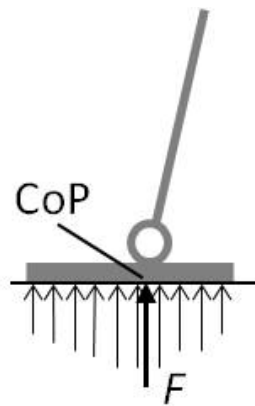


Figure 1.4: Center of Pressure (CoP)

The notion of postural stability in bipedal locomotion is defined as the ability to sustain bipedal walking while keeping the body upright. Postural stability of bipeds can broadly be defined as static, dynamic or orbital. In static stability, a biped robot in motion can be stopped at any instance and the robot posture remains stable. In a statically stable walking gait, the CoM lies within the support polygon throughout the motion. In dynamic stability, a robot in motion can only sustain stability if the motion continues and completes, any stoppages in between might result in postural instability. In a dynamically stable walking gait, the CoM lies outside the support polygon for certain durations, however the robot does not overturn as the dynamics of the robot remains in equilibrium. Orbital stability is a unique case of dynamic stability where the robot is posturally unstable periodically but does not result in instability. Dynamics of the robot is not in equilibrium in certain instances however does not result in overturning of the robot

In bipedal system, the vertical forces (field of pressure forces normal to the foot sole) act on the supporting contact points between the foot

and the ground. When a single resultant force equivalent to the field of pressure forces is exerted at a point where the resultant moment is zero, the exerted point is known as the Center of Pressure (CoP) (Fig. 1.4). The CoP is expressed as:

$$P_{CoP} = \frac{\sum_i q_i \cdot F_{ni}}{\sum_i F_{ni}}, \quad (1.4)$$

where  $P_{CoP}$  is the center of pressure,  $q_i$  is the vector to the point in which the force  $F_{ni}$  (normal to the foot sole) acts.

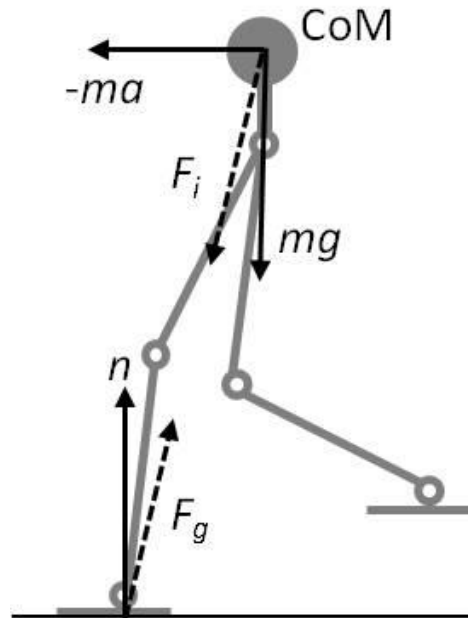
The CoP is not defined outside the support polygon. The CoP is not a direct indicator of stability as regardless of gait stability, the CoP exists as long as contact points between foot and ground are maintained. However, it is noted that the CoP coincide with the Zero Moment Point (ZMP) when the gait is statically and dynamically stable [18, 19].

Zero Moment Point (ZMP) criterion is one of the most widely applied and used approach in humanoid robot research for biped locomotion [2, 17, 19–33]. The Zero Moment Point is defined as the point on the ground at which the net moment generated by the inertia and gravity forces has no component along the horizontal axes [22]. Stability is asserted whenever the ZMP is within the foot support polygon. The ZMP equation is as:

$$P_{ZMP} = \frac{n \times M^{gi}}{F^{gi} \cdot n}, \quad (1.5)$$

where  $P_{ZMP}$  is the Cartesian coordinate of ZMP,  $n$  is the unit normal vector directed outwards from the support surface,  $M^{gi}$  is the moment about the origin in which the position of ZMP is with respect to the reference frame and  $F^{gi}$  is the resultant of gravity plus inertia forces (Fig.1.5).

The ZMP in its nature does not exist outside the support polygon. By

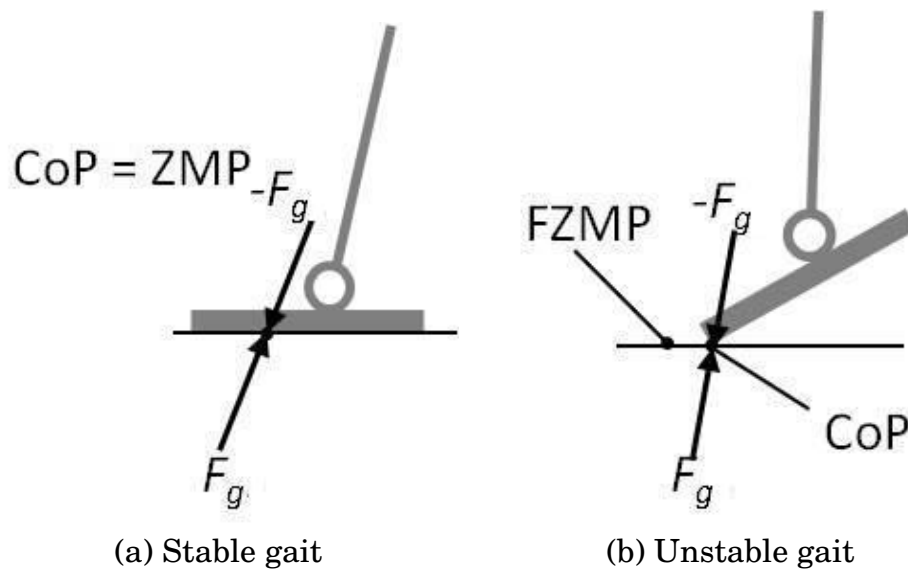


$F_g$  is the ground reaction force,  $F_i$  is the inertia force,  $a$  is the horizontal acceleration of the CoM,  $g$  is acceleration due to gravity,  $m$  is the mass

Figure 1.5: Zero Moment Point (ZMP)

definition, if the ZMP falls outside the support polygon, no ground reaction force can act upon. In reality, this is not possible as ground reaction forces exist and these forces cannot exit the support polygon. To address the concept of stability outside the support polygon, the concept of Fictitious ZMP (FZMP) [22] or Foot Rotation Indicator (FRI) Point [18] is used. When ZMP fall outside the support polygon, the point is deemed as FZMP and the robot is unstable. The distance of the point outside the support polygon from the support polygon is a measure of the amount of perturbation moment that acts on the foot at that instance.

ZMP coincide with CoP when the gait is statically and dynamically stable [18, 19]. However, it is noted that CoP is not ZMP; CoP relates to the ground reaction force-moment whereas ZMP relates to inertia and gravity

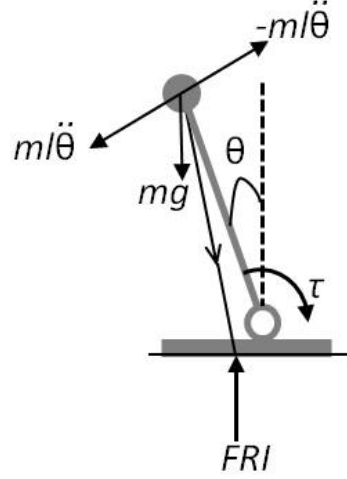


(a) Stable gait (b) Unstable gait  
 $F_g$  is the ground reaction force. The CoP coincide with the ZMP when the gait is dynamically balanced.

Figure 1.6: Relationship of ZMP and COP

force-moment. CoP always exist within the support polygon regardless of stability whereas ZMP exist only in the support polygon when the gait is stable. Fig. 1.6 highlights the difference in ZMP and CoP in the case of stable and unstable gaits.

The Foot-Rotation Indicator (FRI) or known as Fictitious ZMP (FZMP), is an indication of postural instability measured as the point on the foot / ground where the net ground forces would have to act to keep the foot stationary [18]. Fig. 1.7 shows the foot in static equilibrium where  $\tau$  is given by  $ml^2\ddot{\theta} - mgl \cos \theta$ . Unlike the ZMP, the FRI is defined as the resultant moment of force / torque impressed on the foot normal to the surface in which the FRI point can fall within or outside the foot support polygon. The FRI is a measure of the severity of unbalanced torque acting on the foot causing the foot to rotate. The further the FRI point is from the boundaries of the foot support polygon, the greater the amount of foot-rotation possible and hence unstable. As by [18], expression of the FRI is



$l$  is the length of the link,  $\tau$  is the torque acting upon the ankle,  $\ddot{\theta}$  is the angular acceleration about the ankle,  $g$  is the acceleration due to gravity,  $m$  is the mass

Figure 1.7: Foot-Rotation Indicator

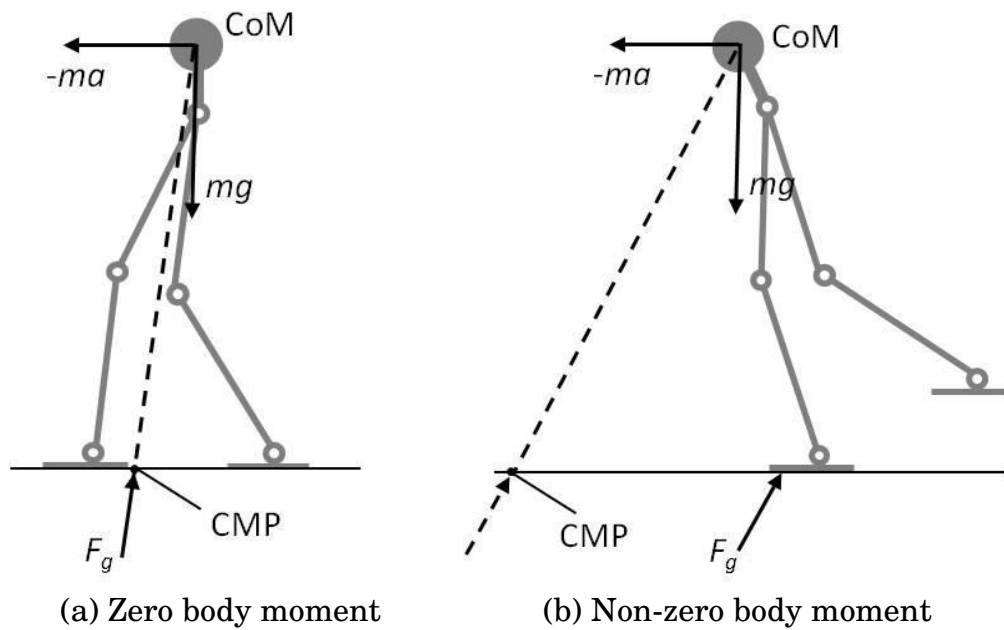
given by:

$$P_{FRI_x} = \frac{m_1 G_{1y} g + \sum_{i=2}^N m_i G_{iy} (a_{iz} + g) - \sum_{i=2}^N m_i G_{iz} a_{iy} + \sum_{i=2}^N \dot{H}_{G_{ix}}}{m_1 g + \sum_{i=2}^N m_i (a_{iz} + g)},$$

$$P_{FRI_y} = \frac{m_1 G_{1x} g + \sum_{i=2}^N m_i G_{ix} (a_{iz} + g) - \sum_{i=2}^N m_i G_{iz} a_{ix} - \sum_{i=2}^N \dot{H}_{G_{iy}}}{m_1 g + \sum_{i=2}^N m_i (a_{iz} + g)},$$
(1.6)

where  $(P_{FRI_x}, P_{FRI_y})$  is the Cartesian coordinate of the FRI point,  $N$  is the total number of segments in the robot (not including the foot),  $m_i$  is the mass,  $a_i$  is the linear acceleration and  $H_{G_i}$  is the angular momentum about the  $G_i$  for the segment  $i$ .

Centroidal Moment Pivot (CMP) is defined as a point where a line parallel to the ground reaction force passes through the CoM intersects with



(a) Zero body moment                      (b) Non-zero body moment  
 $F_g$  is the ground reaction force,  $a$  is the horizontal acceleration of the CoM,  
 $g$  is acceleration due to gravity,  $m$  is the mass of the CoM

Figure 1.8: Centroidal Moment Pivot

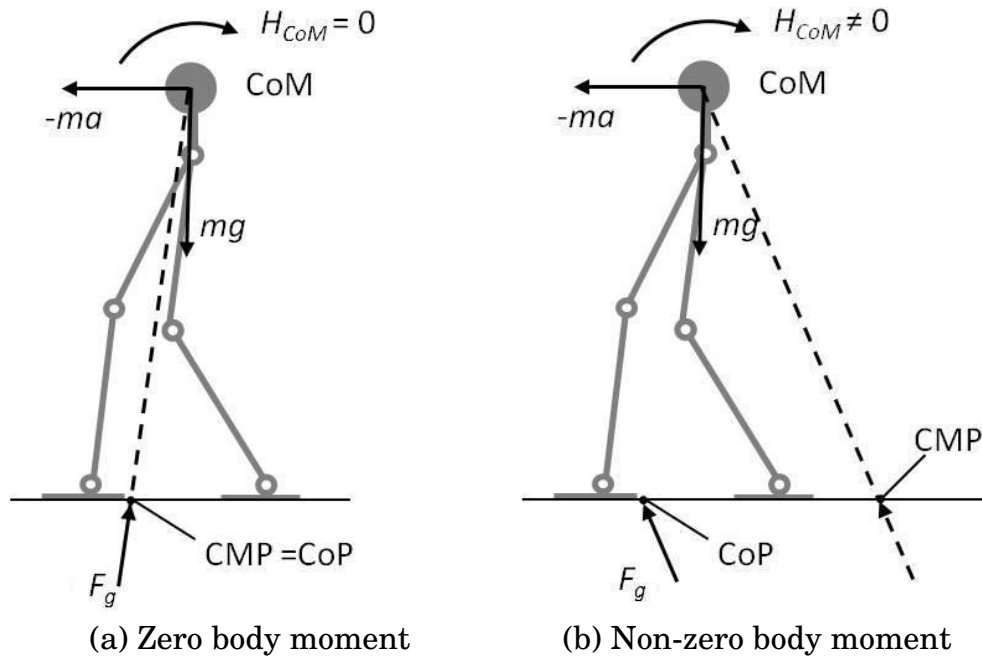
the ground [34–38] (Fig. 1.8). Mathematically, CMP can be expressed as:

$$\begin{aligned}
 P_{CMP_x} &= CoM_x - \frac{F_{gx}}{F_{gz}} CoM_z, \\
 P_{CMP_y} &= CoM_y - \frac{F_{gy}}{F_{gz}} CoM_z,
 \end{aligned}
 \tag{1.7}$$

where  $(P_{CMP_x}, P_{CMP_y})$  is the Cartesian coordinate of the CMP,  $CoM$  is the Cartesian Coordinate of the center of mass and  $F_g$  is the ground reaction force.

The CMP is the point that the ground reaction force would have to act to keep the horizontal component of the body angular constant [35]. The angular momentum of the body about the CoM is zero when the projection of the ground reaction force acting at the CoP intersects and passes through the CoM (Fig. 1.9(a)). At that instance, the body is at orbital equilibrium





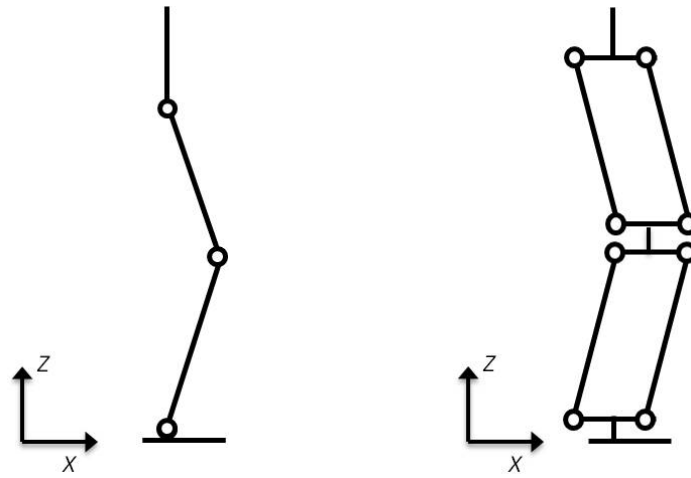
$F_g$  is the ground reaction force,  $a$  is the horizontal acceleration of the CoM,  $g$  is acceleration due to gravity,  $m$  is the mass of the CoM.  $H_{CoM}$  is the body angular momentum

Figure 1.9: CMP versus ZMP/COP

and the CoP coincides with the CMP. When significant angular momentum acts upon the body ( Fig. 1.9(b)), the CMP does not coincide with CoP. The distance in which the CMP is away from the CoP is the measurement of orbital instability. The CMP can lie within and outside the support polygon and is applicable to both single and multiple support phases.

### 1.1.3 Locomotion Mechanism

The locomotion mechanism plays an important role as it relates to the kinematics and dynamics of the bipedal system. In biped and humanoid robots, the conventional leg structure comprises of the hip, thigh, knee, shrank, ankle and foot. For the humanoid robot, bilateral bending of the



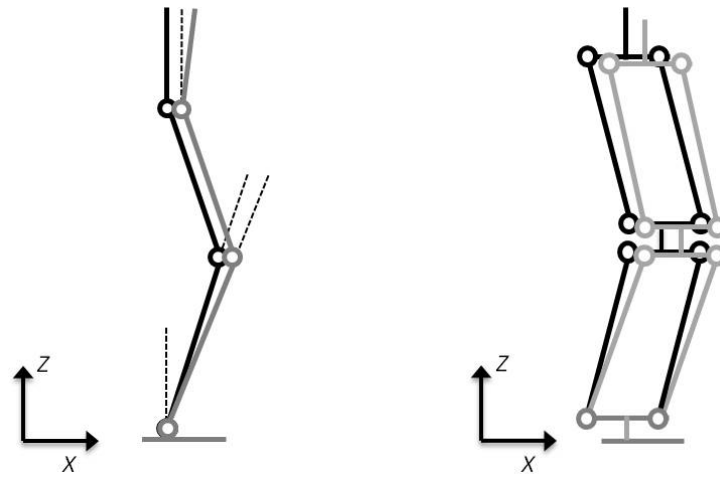
(a) Serial mechanism (a) Parallel double crank mechanism

Figure 1.10: Leg structure for biped locomotion

knee is not permitted; knee-bend is pointing towards the front, similar to what the human does.

In recent years, one of the notable changes made in the mechanical design of humanoid robots is the employment of parallel double crank mechanism leg structure (Fig. 1.10) to enhance locomotion. One drawback of the conventional serial mechanism leg structure is the issue of angular cumulative errors caused by joint actuators. Accumulation of angle errors from the pitch hip, ankle and knee joints constitute to a change in the incline of the body torso in the sagittal plane (Fig.1.11(a)). Stability control of the robot is dependent on the dynamics whereas the dynamics is influenced by the incline of the body torso. The sagittal and frontal dynamics of the robot are inter-coupled and changes in the sagittal dynamics will significantly influence the overall dynamics of the robot. Deviation of the body incline in the sagittal plane will affect the overall dynamics and thereafter the stability of the robot.

The parallel double crank mechanism addresses the issue raised in the



(a) Serial mechanism (a) Parallel double crank mechanism

*Black skeleton: Original standing posture with no angle error; Gray skeleton: standing posture of the robot with angle errors introduced to the joints.*

Figure 1.11: Mechanism subjected to angle errors in joints

serial mechanism. Closed-kinematic mechanism constraints the links in the crank mechanism such that regardless of the knee angle, the torso remain upright (Fig. 1.11(b)). In addition, the mechanism overcomes the problem of singularity which occurs when extending the knees. Singularity creates control issues as it leads to extremely large values of the joint velocities and accelerations. Actuators are not able to handle such extreme values of velocities and accelerations. Parallel double crank mechanism also reduces the degree-of-freedom required for flat terrain walking, in which the actuation of the crank can facilitate both leg lift and swing. In addition, a key advantage of the parallel double crank mechanism as highlighted by [39] and [40] is that the mechanism consumes less energy in comparison to the serial mechanism leg structure.

In biped locomotion, excitation of the joints in the leg can be divided into three categories; ① active, ② passive and ③ hybrid.

Active joints are actuator-driven and necessary control law is needed to govern the actuation. A fully *actuated robot* is one that adopts active joints for all actuations. The naturalness of the motion produced by active joints are dependent on the inherent properties, control paradigms and type of the actuators used.

Passive joints have no excitation means on its own. Motion of passive joints is (a) resultant due to coupling effects introduced by active joints, (b) driven solely based on natural dynamics of the systems or (c) based on material properties such as elasticity. Bipedes that only uses passive joints in the legs for locomotion are deemed as *passive walker* [41]. The use of passive joints for bipedal locomotion often requires specific mechanical design in the leg.

Hybrid joints are specifically design mechanisms that utilize both active and passive joint excitations. The notation of hybrid joint is to capitalize on the naturalness of motion produced by and the energy efficiency of the passive excitation while at the same time maintaining control using active excitation. Hybrid joints are also used in the context of compliance control for purposes such as reducing impact and instantaneous dynamical compensation in motion control. The series elastic actuator by [42] by-far is one of the most notable hybrid joint developed. The actuator comprises of an elastic element coupled in series with the output of the actuator for compliance control.

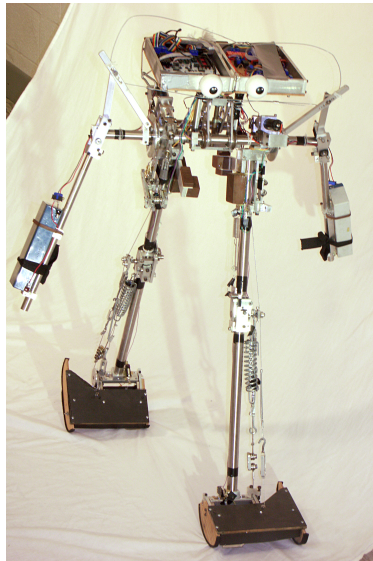


Figure 1.12: Cornell University passive-dynamic bipedal robot [1]

#### 1.1.4 Biped Gait Generation

Gait generators for biped locomotion can be divided into three types; ① dynamics-based, ② trajectory-based, and ③ Central Pattern Generator (CPG).

Dynamics-based gait generators are based on the use of passive-dynamics in biped such as the passive walker (Fig. 1.12). The passive-dynamic approach capitalizes on the natural dynamics of the system by means of excitation using the inertia of mass and gravity [1, 43–45]. This method is energy efficient and produces more natural walking motions. However, bipeds based on passive-dynamics often require some form of impulse excitation and a medium for sustaining motion. The approach is confined and task exploitation is limited with most of the passive biped research mainly focusing on locomotion.



Figure 1.13: Honda ASIMO [2]

One of the most commonly used method of gait generation in humanoid research is the trajectory-based approach. In this approach, joint reference trajectories are generated and tracked. Joint reference trajectories can be generated using three approaches: ① “anthropomorphic gaits”, ② mathematical models and ③ design of experiments.

In the anthropomorphic approach, the recorded joint trajectories of a natural human walking gait is applied to a dimensionally similar robot [46–49]. The recorded joint trajectories are normalized, generalized and translated to fit the kinematic constraints of the humanoid robot.

The next approach, which is commonly used, is based on well-defined mathematical models and computations in which stability criterion such as the ZMP, CMP or FRI are used to formulate the joint trajectories to produce stable walking motion [18, 20, 38, 50]. The most famous example of the second approach using trajectory based gait generator is the Honda

ASIMO robot (Fig. 1.13) [2] which uses ZMP to produce stable and robust bipedal walk.

The design of experiments approach uses intuition in which joint trajectories are determined through a series of experimentations and manual adjustment of open-loop parameters. Repeated trial and error testing of the gaits are conducted to determine if the motions produced are stable. Although the approach is viable, the approach is confined with little research value and lacks good supporting guidelines for the approach to be generalized.

Trajectory-based generators have proved to be effective, robust and versatile in generating biped locomotion. Trajectory-based generators are often energy inefficient due to the need of precision control of the joint angles to conform to the reference trajectories for stability. Walking motion is also deemed as less natural due to the limitation of actuators. However, in several research works [17, 33, 51–55], it was highlighted that trajectory based generators can produce natural motion. In earlier researches [51–54], energy optimization approaches are used to produce natural motion through minimizing the energy usage. Specific constraints on control effort and optimization of movement trajectories to minimize the input energy consumed are applied as solutions. Recent researches [17, 33, 55] have shown that walking trajectories similar to that of the human in terms of ZMP can lead to more natural walking that is energy efficient.

The Central Pattern Generators (CPG) is a biological inspired paradigm. The CPG-based approach uses neural oscillators such as McCulloch-Pitts,

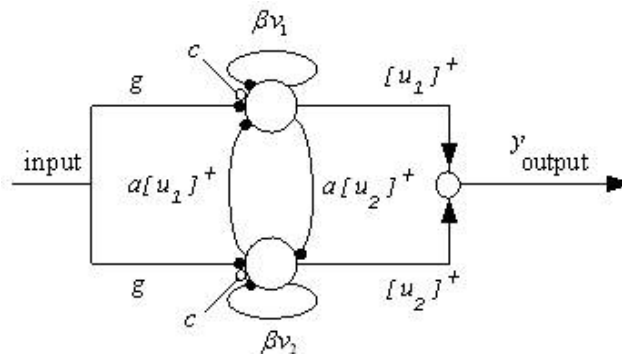


Figure 1.14: Matsuoka neural oscillator

Leaky integrator and Matsuoka Neural Oscillators [56] (Fig. 1.14). Neural oscillators, which are non-linear, are used to produce rhythmic patterns that couples with body dynamics to produce locomotive motions. The approach has been successfully implemented to produce biped locomotion in humanoids [57–62]. The design of the interconnections and feedback connection of the neural oscillators is often difficult and manual tuning of open parameters is required to achieve the desired behaviour.

Gait generation can take place offline and online. Offline gait generation is the play-back of pre-computed / pre-recorded gaits, in which the joint trajectories are pre-planned, during biped locomotion. Offline gait generation has the key advantage of being highly computational efficient as no computation is necessary however often at the expense of huge data storage space of the trajectories. Offline gait generation is highly suitable for environment with minimum disturbance. Research using offline gait generation mainly focuses on the study of gait generation methodology and algorithm [63–65], and optimization of locomotion in terms of stability [66–68] or energy [69, 70].



Biped robots experienced disturbances during locomotion. Walking gaits generated offline are often not sufficiently robust against these disturbances. There is a need to generate walking gaits online; walking motion that can continuously adapt. One of the most commonly used approach for online gait generation for bipedal locomotion is the ZMP trajectory based tracking and modification of reference walking gaits [28–31, 71–74]. In this approach, the walking gaits are generated offline and modified online. The ZMP trajectory is tracked during walking and motion compensation, such as alteration of joint trajectories or modification of gaits, is used to keep the ZMP within the support polygon in the presence of environment disturbances. Real-time gait pattern generation is another approach of online gait generation [12, 27, 75–77]. In this approach, gaits are generated solely based on the current dynamics using system feedback without pre-determined walking gaits. Real-time gait pattern generation is robust and is able to cope and response immediately to unforeseen disturbances or perturbations. However, huge amount of computations are often required for real-time gait pattern generation.

### **1.1.5 Compliant Control**

Compliant control in biped locomotion can be mechanical based or motion control based. Mechanical based compliance is realized using compliant mechanism that can conform to surfaces whereas motion control based compliance is realized through the act of conforming through controlled motion.

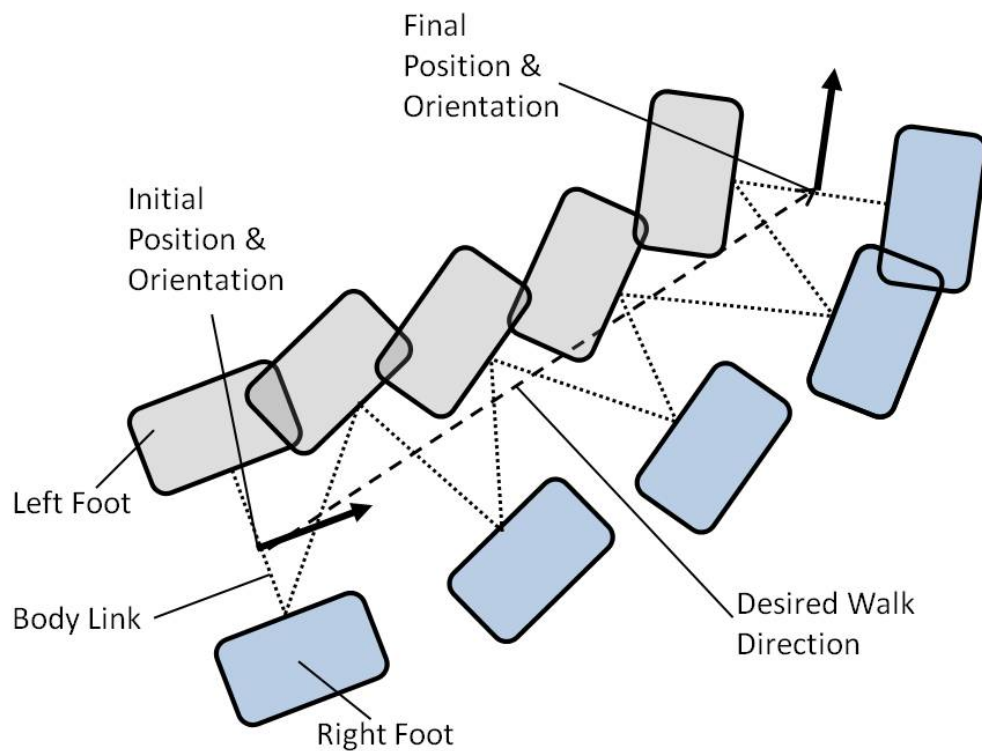
Mechanical based compliance is the use of compliant mechanism with

the necessary controls to achieve compliance control. Examples of compliant mechanisms include compliant joints [78], flexible links [79], and compliant actuators [80,81]. The use of compliant mechanism can introduce under-actuation and uncontrollability which requires complex and nonlinear control for handling the dynamics. Using mechanical compliance has several advantages. Compliant mechanism have lower inertial forces which result in better energy efficiency, is able to reduce impact and hence greater shock tolerance, and can be used for compensation of instantaneous dynamics due to latency in communication between the controller and the actuators.

Motion control based compliance achieve compliance using specific control of motion similar to that of motion produced by compliant mechanism. Actuating joints are modelled as compliant joints during computation with force / torque feedback to determine the necessary control for conformance. The notation of motion control based compliance is to have the benefits of mechanical based compliance while avoiding under-actuation and uncontrollability. A number of bipedal locomotion research based on motion control compliance have shown success in producing robust biped locomotion that is capable of handling dynamic walking conditions [82–85] and uneven terrain walking [86–88].

### **1.1.6 Walking Control**

One of the key research areas in bipedal locomotion is walking control for dexterous manoeuvring. Dexterous manoeuvring refers to the ability of the robot to move in any direction during walk. [89] and [12] are early



*Desired foot placement as robot move from the initial to final position and orientation along the desired direction of movement; Fine dotted line denote the physical link between the left and the right foot.*

Figure 1.15: Omnidirectional walking

successful implementation of dexterous manoeuvring on humanoid robots however the walking speed of the robots are relatively slow in comparison to present day. With the emergence of new technologies over the past decade, robots today are able to walk much faster. However, increased walking speed leads to increased difficulty in walking control in which the dexterous manoeuvrability remains as a key challenge in bipedal locomotion research.

Omnidirectional locomotion relates to the ability to move in any direction irrespective of the facing of the bipedal robot. In recent years, omnidirectional walking has increased attention for bipedal locomotion. Several approaches to omnidirectional walking have been proposed [90–95] for biped robot. Omnidirectional walking in biped refers to the ability of the robot to execute arbitrary foot placement to achieve the desired motion (Fig. 1.15). Omnidirectional walking pertains to creating walking gait trajectories that allow the robot to walk forward, sideways and turn at the same instance. The ability to produce smooth transitions of the trajectories and stability are the key research focus.

One of the fundamental problems in the implementation of biped walking is the foot motion slip. Foot motion slip occurs when the driving forces exceed the traction forces between the foot and ground, resulting in the rotation of the whole robot. Severity of motion slip increase with fast walking motion. To overcome the problem, two approaches are used. The first approach performs compensation or reduced motion slip through motion control means [96–100]. In the second approach, compensation is achieved through the use of sensory feedback such as visual information [101–103] or gyroscopic feedback [104].

## **1.2 Research Consideration**

The methodology of formulation taken in the proposed research is to include theoretical analysis, simulation, physical implementation and experimentations. A robot is built in the process to facilitate the implementation of the research work. Key considerations on the limitation of

the physical hardware are taken in the formulation to ensure that the research outcome is tangible and implementable.

### 1.3 Thesis Aim

The proposed research aims to formulate an approach that provides a means of *simple* and effective dynamic walking gait generation for *actuated robots*. The proposed approach is simple in its ability to determine the required parameters and controls for dynamic walking without having the need to derive the detailed dynamic model of the system. The approach is effective with respect to its the ability to generate fast dynamical and omnidirectional walking. In addition, it is desirable to make the approach implementable and generalizable on the physical humanoid robots without expensive and sophisticated computation and sensors. The naturalness of the robot walk is not considered in this work.

### 1.4 Thesis Contributions

The thesis elaborates on a simple and practical approach for gait generation for biped dynamic walking without expensive and complex computations, and, costly sensors. Contributions of the thesis are:

1. Shown and proven the viability of using simplified biped model (LIPM) and simple sinusoidal functions to generate stable walk-oscillations in a physical humanoid. (Chapter 3)
2. Designed a two stage ZMP compensation system using lateral shift

amplitude correction and real-time compensation that utilizes and manipulates a single parameter in the lateral motion to achieve ZMP compensation. Existing literature on ZMP compensation reports the requirement of manipulation of prescribed ZMP through modification of different joints, trajectories or walking parameters. (Chapter 4)

3. Devised a phase generator that dynamically modifies the single and double support phase timings to assert stability for enhancing the compensation system. Such an approach eliminates the need for ZMP prediction often required in ZMP compensation. (Chapter 4)
4. Decoupling of dynamic walking (Fig. 1.16) into independent movements to simplify and parametrize the dynamics and control, which allows the formulation of simple and computationally inexpensive solutions. Foot placement trajectories are superimposed together to address the complex topic of biped gait generation. Viability of the approach is successfully verified and demonstrated in simulation and experiments. (Chapters 3,4 and 5)
5. Unlike the existing literature work on compliant control with physical implementation, compliant joints in this work are realized by simple manipulation of the position control system in commercial servo without the need of additional hardware and mechanism, or extensive control algorithms. (Chapter 6)
6. A novel approach of using compliant joints for measuring ground reaction forces without explicit sensing devices is proposed and demonstrated. The approach, to the best of the author's knowledge, extends beyond the conventional work done on the use of complaint

joints in humanoid robots. (Chapter 6)

## 1.5 Thesis Organization

The thesis is organized as follows. Following the introduction, the physical humanoid robot utilized in the implementation of the research is presented in Chapter 2. The robot named Robo-Erectus Junior (REJr) is a 22 DOFs humanoid robot. The hardware design and locomotion control of REJr is introduced. The hardware design provides an overview of the mechanical structure and electrical system architecture of the robot. The locomotion control highlights the various systems used for the generation of dynamical walking gaits.

In Chapter 3, biped walking gait generation in the frontal plane is presented. An offline approach of generating lateral walk-oscillations using sinusoidal foot trajectories is described. The generation of single and double support phases for stable biped dynamical walking based on the ZMP criterion is presented. The viability of the approach is verified through theoretical modelling, simulation and implementation on the physical humanoid.

A gait generation approach to produce sustaining lateral walk-oscillation online is described and presented in Chapter 4. The approach is realized using gait patterns generated offline with online compensation control. ZMP based tracking and compensation techniques are used to keep the ZMP to the reference. Simulation and experimental results of the approach to produce sustainable lateral walk-oscillations are presented.

Chapter 5 presents the real-time gait generation of the omnidirectional humanoid walking. Sustain lateral walk-oscillations are superimposed with walking movements to produce omnidirectional walking. Regulation of the step size produces sustainable dynamic walk. Sensory feedback is employed to enhance the directional walking control of the humanoid. Simulation and implementation works on the chapter are highlighted and discussed.

In Chapter 6, the use of compliant joints in the humanoid is presented. Compliant joint are realized using motion based compliance installed in the knee of the humanoid robot. The compliant joints are utilized for foot landing impact reduction and ground reaction force sensing without explicit sensing devices. A energy-saving scheme is proposed using under-actuations of the ankle joints. Experimentation work done on the compliant control are presented.

Chapter 7 concludes the thesis with discussion on the implemented work based on the research conducted, and the direction of future work.



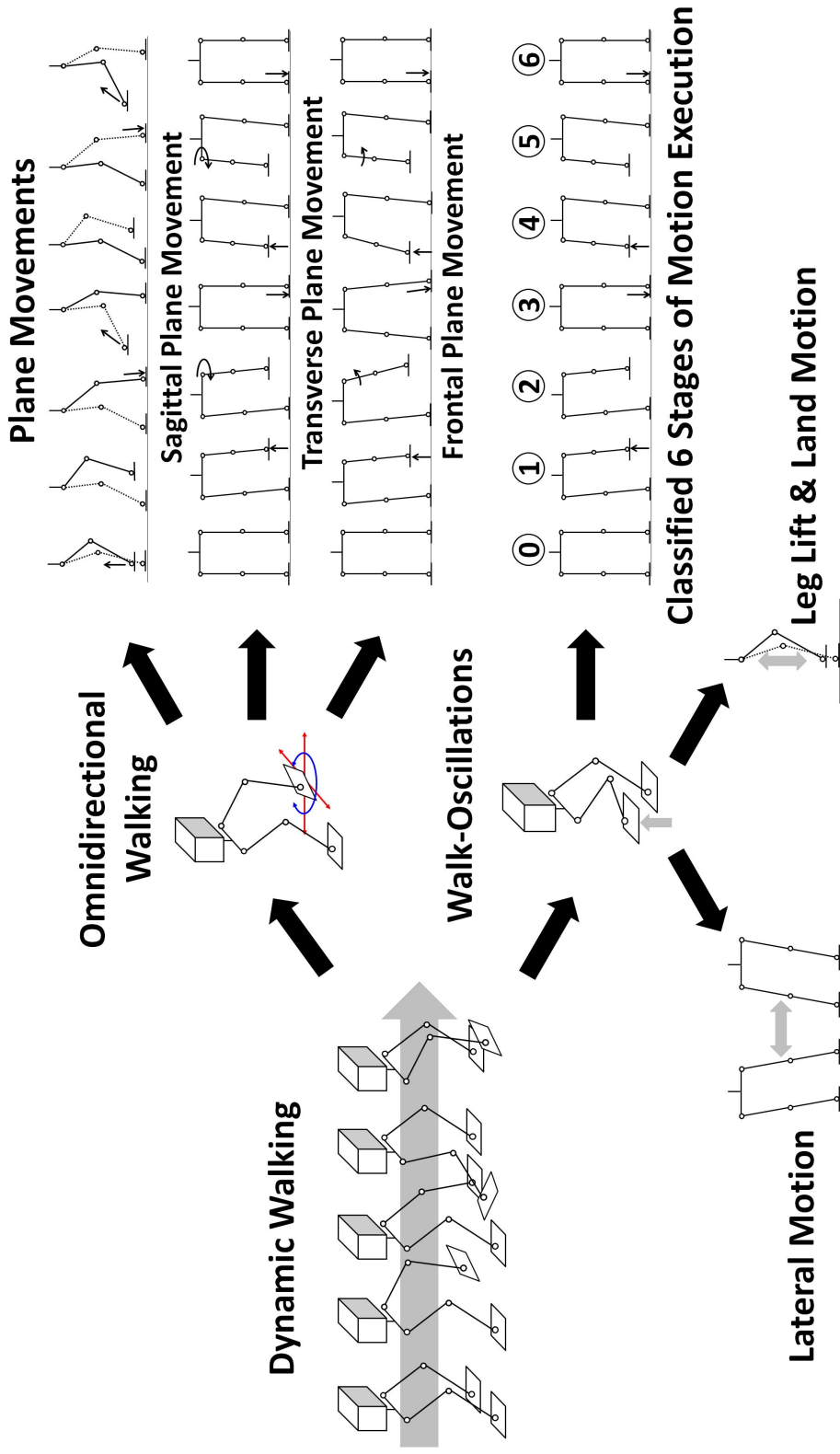


Figure 1.16: Decoupling of dynamic walking

## **Chapter 2**

# **Humanoid Robot Platform**

Development of humanoid robots have manifested worldwide over the years with a variety of them being built for various robotic research and application. In the early years, much of the focus was on bipedal robots (robot having only the legs). When HONDA unveiled its humanoid robot ASIMO [2] at 130 centimetres in 2000, followed by SONY's QRIO [105] at 60 centimetres in 2001, the humanoid research started to intensify worldwide. In the subsequent years, universities, educational institutes and companies began developing their own humanoids. Particularly of interest and popular are humanoid robots of heights between 30 to 60 centimetres. Economic cost, safety and size of power to weight ratio in electrical actuators are the factor which made the 30 - 60 cm range popular. Humanoids of this size are deemed as less intimidating and has hence become a popular choice of for entertainment and service robotics. Other driving factors include robotic competitions held annually such as the FIRA [106] and RoboCup [107] competitions in which humanoid robots of this size compete.



Figure 2.1: Singapore Polytechnic Robo-Erectus Junior Bv-MkIII

## 2.1 Robo-Erectus Junior

The Robo-Erectus Junior (REJr<sup>1</sup>) [108, 109] robot (Fig. 2.1) is designed and developed for various robotic research studies such as locomotion, artificial intelligence, image processing, multi-agent autonomous system and human robot interaction. REJr is built in full compliance to the RoboCup Humanoid KidSize League 2010, 2011 and 2012 Competition

---

<sup>1</sup>REJr is developed in the *Advanced Robotics and Intelligent Control Centre (ARICC)* of *Singapore Polytechnic (SP)* as part of the author's employment in SP.

Table 2.1: Physical specifications of the Robo-Erectus Junior

Weight	Dimensions		
	Height	Width	Depth
3.8kg	560mm	240mm	120mm

rules and participated in RoboCup 2010 and 2011. REJr is a fully *actuated robot* with all the joints actuated by digital robotic servo. The dimensions of REJr are decided in accordance to the competition rules in which the lengths of the legs, body, arms, head and size of the foot are in proportional to the human body. . Robot motions and degree-of-freedoms are kinematically constrained to that of human executable. No active sensors (emitting sensors) are utilized. Only passive sensors such as camera and forces, torque and temperature sensors are utilized. REJr is capable of many feats for autonomous soccer playing such as kicking, recovery and omnidirectional walking and. Table 2.1 shows the general specification of REJr.

## 2.2 Hardware Design

In this section, the hardware design of the robot is presented. The mechanical structure and electrical system pertaining to biped locomotion are introduced.

### 2.2.1 Mechanical Structure

The mechanical structure of the humanoid robot is designed using Autodesk Inventor. Fig. 2.2 shows the mechanical skeleton assembly of the humanoid robot REJr. The humanoid robot is designed and constructed

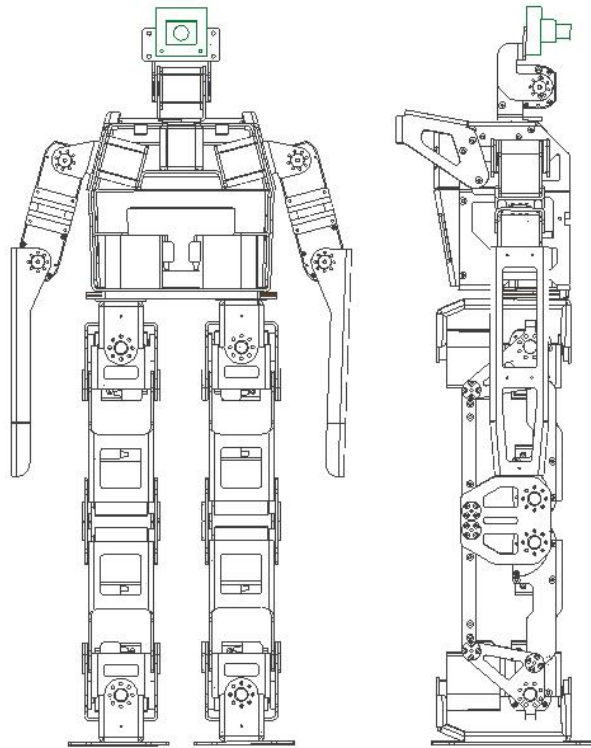


Figure 2.2: Mechanical assembly of humanoid robot

using aluminium alloy which is light-weight, and able to provide adequate structural strength.

The humanoid robot consist of 22 degree-of-freedom (Fig. 2.3); 14 degree-of-freedom in the legs, 6 degree-of-freedom for the hands and 2 degree-of-freedom in the head. Table 2.2 depicts the degree-of-freedom axes in

Table 2.2: List of degrees of freedom for robot

Body Part	Roll	Pitch	Yaw
Head		✓	✓
Shoulder	✓	✓	
Elbow		✓	
Hip	✓	✓	✓
Knee		✓	
Ankle	✓	✓	

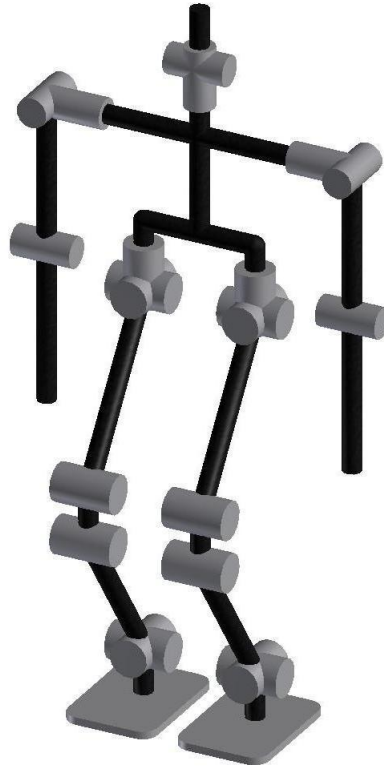


Figure 2.3: Degree-of-freedom configuration of robot

each joint of the robot. The pitch, roll and yaw joints in the hip are orthogonal and intersect at a single point in the hip. Both the shoulder and ankle joints have orthogonal pitch and roll joints. The robot adopts a parallel double crank mechanism in the leg structure with double actuation in the knee increasing the degree-of-freedom to 14.

The parallel double crank mechanism leg structure is formed by two crank mechanisms linked together at the knee (Fig. 2.4). Each crank mechanism consists of four linkages coupled using four angular joints to form a closed kinematic loop. The mechanism constrains the linkages mechanically in parallel creating a parallelogram, in which the angular motion of the crank joints determines the bending of the legs. Each crank mechanism can be driven with single or multiple synchronized actuators

coupled to the angular joints. The parallel double crank mechanism in REJr is realized using servo actuators coupled to the angular joints in the knee (Fig. 2.5).

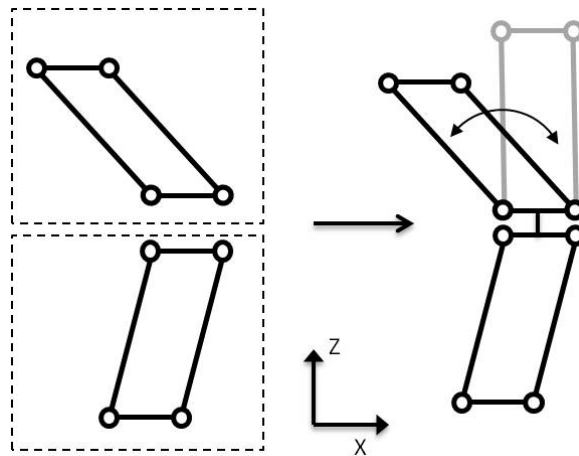


Figure 2.4: Parallel double crank mechanism

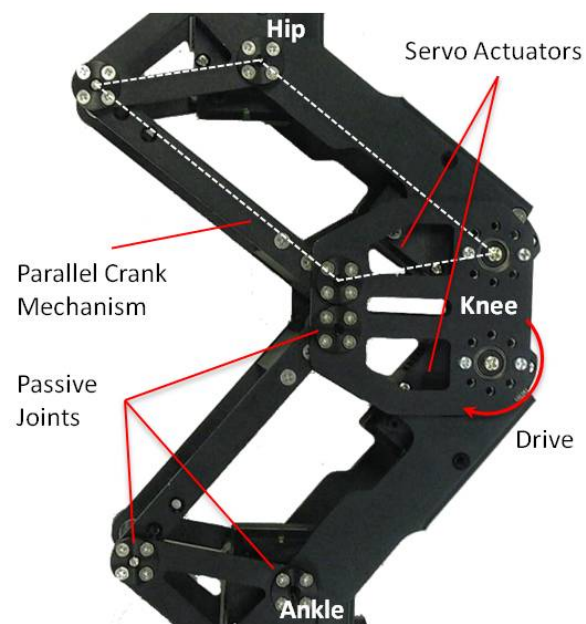


Figure 2.5: Parallel double crank mechanism leg structure

## 2.2.2 Electrical System

Fig. 2.6 shows the electrical system architecture of the robot. The robot system is driven by two processors, a high level host processor and a low level micro processor, connected to various peripherals. The robot's task and peripherals are sub-divided and handled by the two processors independently.

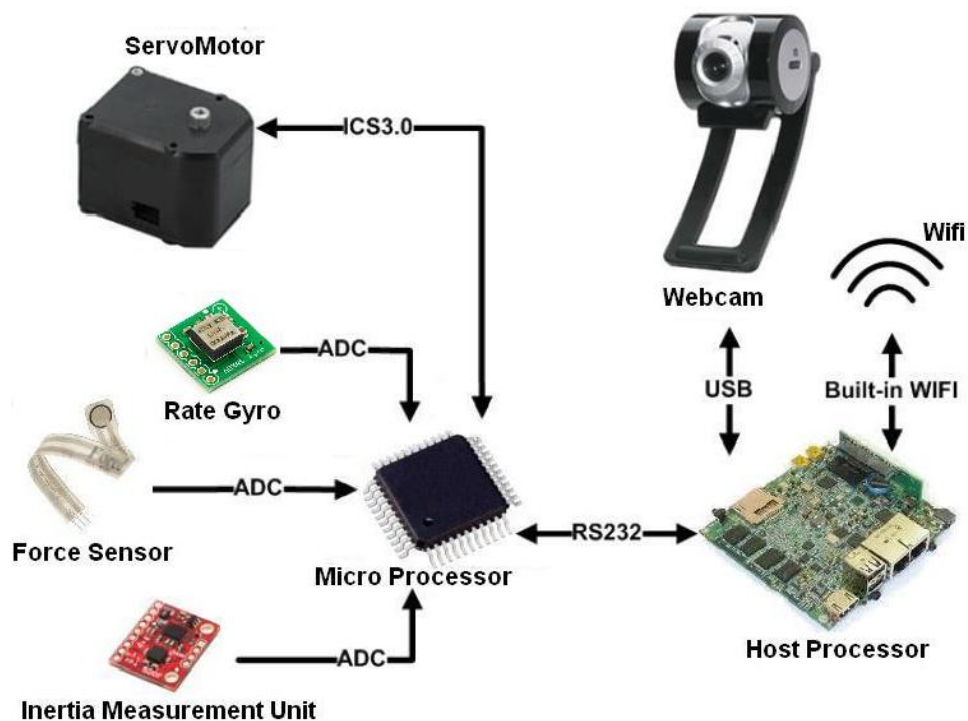


Figure 2.6: Electrical system architecture

Five types of sensors are mounted on the robot; camera, inertia measurement unit (IMU), force sensor, rate gyroscope and absolute rotary encoder. Table 2.3 shows the specifications of the sensors employed. The camera is mounted in the robot head to provide monocular vision. The IMU and rate gyroscope are mounted in the body to measure the linear acceleration, angular tilt and rotation. Force sensors are mounted in the feet to for ground reaction forces sensing. The actuators in each joints



are embedded with an absolute rotary encoder for measurement of joints angle.

Table 2.3: Specifications of the sensors

Sensor	Details
Camera	Resolution:640x480, Frame rate:30fps
Rotary Encoder	Type:Absolute, Resolution:0.03375°
Force Sensor	Range:0-25lb (110N)
Gyroscope	Full scale range:±500°/sec , Sensitivity:2.0mV/°/sec
Accelerometer	Full scale range:±3g
Rate Gyroscope	Full scale range:±300°/sec , Sensitivity:3.3mV/°/sec

The robot is actuated by digital servos coupled to each of the leg joints. Two power rated servos are employed; the upper body uses lesser power, lighter and smaller servos in compared to the lower body. The servos are connected using the daisy chain configuration and controlled using half-duplex serial communication. Four communication lines are used to control the arms (left, right) and legs (left, right). The servos are commanded at a frequency of 50Hz. Specifications of the servo are presented in Table 2.4.

Table 2.5 shows the specification of the two processors. The high level host processor processes and coordinates behavioural aspects of the robot. Vision sensor and communication module are connected to the host processor. Complex or computationally demanding tasks such as image processing, cognition, game strategy and behavioural control are handled by the host processor.

Table 2.4: Specifications of the actuator.

Actuator	Torque	Speed
Upper Body	40.8 kg.cm @ 10.8v	0.19 sec / 60 deg @ 10.8v
Lower Body	67.0 kg.cm @ 11.1v	0.22 sec / 60 deg @ 11.1v

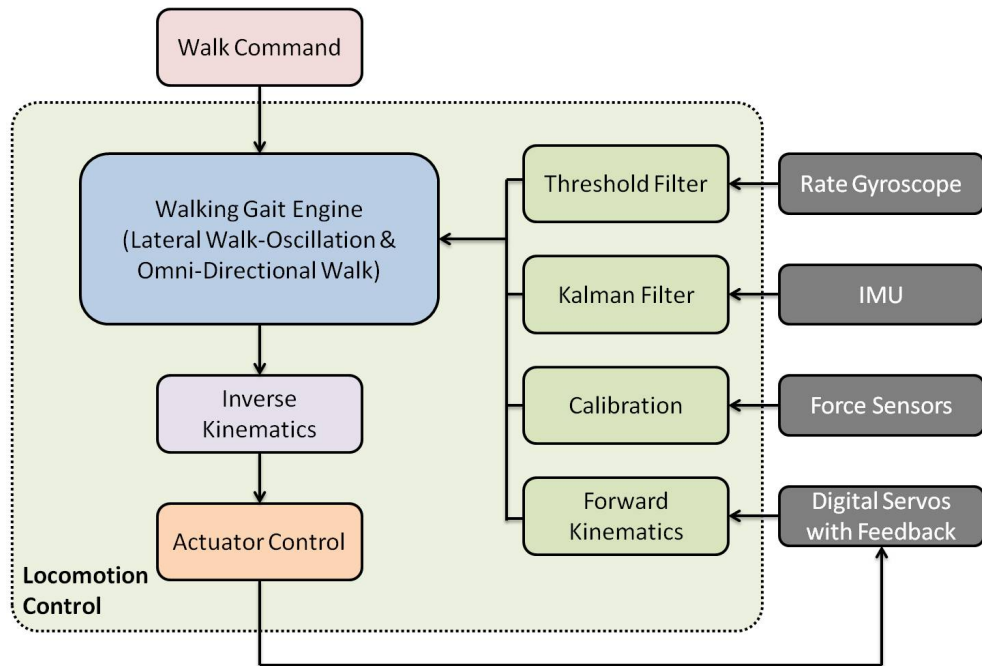


Figure 2.7: Locomotion control system architecture

The low level micro processor handles tasks that require real-time execution and handling. Sensors and actuators for biped locomotion are connected to the micro processor. The micro processor handles tasks such as gait generation, motion control, user inputs and sensory feedbacks. The two processors communicate via serial communication using customized protocols.

Table 2.5: Specifications of the processors

-	High Level Host Processor	Low Level Micro-Processor
Processor	Intel Atom	dsPIC
Speed	2000Mhz	80Mhz

## 2.3 Locomotion Control

The locomotion control system architecture of the robot is divided into several modules (Fig. 2.7). The general description of each block is presented in Table 2.6. The input to the locomotion control system is the *Walk Command* which comprises of the stride speed with reference to robot body frame on the transverse plane. The *Walk Command* is send to the *Walk Gait Engine*. The *Walk Gait Engine* generates the reference coordinates of the foot placement in the Cartesian space. Computation of the foot placement reference coordinates in the *Walk Gait Engine* are based on processed data read in from the respective sensors. The joints angles of the biped are computed from the foot placement coordinates using *Inverse Kinematics*. The joints angles are subsequently send to control the actuators accordingly in *Actuator Control*. Details of the computation and implementation of the modules are discussed and presented in the following sections.

### 2.3.1 Walk Gait Engine

The *Walk Gait Engine* generates the reference coordinates for the placement of each foot based on the input data from the *Walk Command* and

Table 2.6: General description of blocks in locomotion control

Blocks	Description
Walk Command	Frontal, sagittal and angular speed command.
Walk Gait Engine	Gait generation module for walking.
Inverse Kinematic	Translate gait reference to joints reference.
Actuator Control	Position, speed and stretch control of actuators.
Sensory Feedback	Reading of information from sensors.

sensory feedback data. The module consist of two key components, *Sustainable Lateral Walk-Oscillation* and *OmniDirectional Walk*, to generate gait references for stable dynamic walking; *Sustainable Lateral Walk-Oscillation* pertains to the online generation of the gaits in the frontal plane using sinusoidal references while *OmniDirectional Walk* pertains to the determination of the foot placement to create sustainable and stable omnidirectional walking. Details of *Sustainable Lateral Walk-Oscillation* is presented and discussed in Chapters 4 and 6 and *OmniDirectional Walk* in Chapter 5.

### 2.3.2 Inverse Kinematics

A simplified biped model (Fig. 2.8) is adopted for representation of the humanoid robot. The biped model allows the simplification of the robot's kinematics and dynamics to reduce computational complexity and cost. The biped is modelled using concentrated masses with massless links (Fig. 2.8). The upper body including the head and arms is represented by a single concentrated mass. The other concentrated masses are assumed to be at the positions of the actuators. This assumption is reasonable as the robot structure is made of light-weight aluminium material which contributed less significantly to the overall mass. Table 2.7 shows the parameters of the biped model;  $f_1$  and  $f_2$  are the dimensions of the foot plate,  $w_1$  is the width of the hip,  $d_1$  and  $d_2$  are the shank and thigh length,  $d_3$  is the distance of the concentrated mass representing the upper body from the ground.

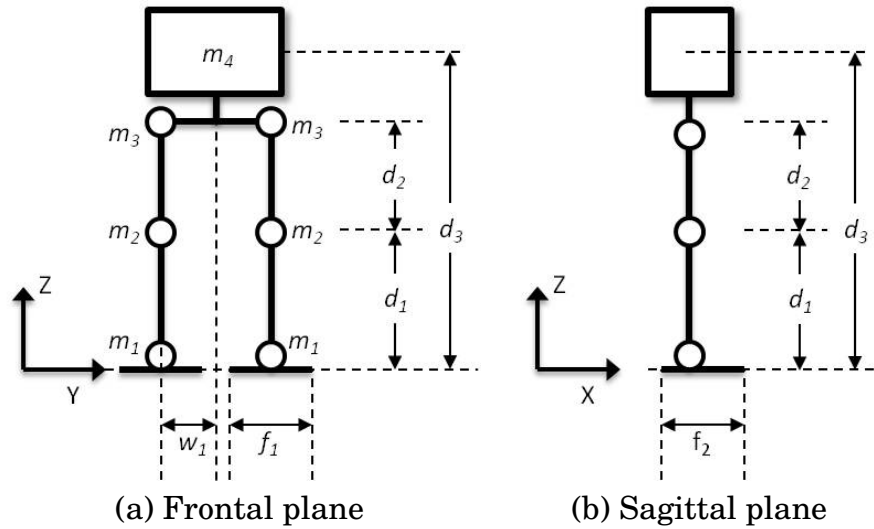


Figure 2.8: Mass distribution of biped model

Table 2.7: Dimensions and masses of biped model

Parameter	Value
$m_1$ (kg)	0.248
$m_2$ (Kg)	0.258
$m_3$ (kg)	0.381
$m_4$ (kg)	2.154
$d_1$ (m)	0.127
$d_2$ (m)	0.127
$d_3$ (m)	0.375
$w_1$ (m)	0.045
$f_1$ (m)	0.075
$f_2$ (m)	0.120

The biped model has 14 degrees-of-freedom in the legs which are independently actuated. A 14 x 1 vector of angular quantities is used to express the leg configuration of the robot model,  $[\theta_1, \theta_2, \theta_3, \dots, \theta_{14}]^T$  (Fig. 2.9). The inverse kinematics of the robot is obtained by finding solutions to the 14 x 1 vector of angular quantities.

The adoption of the parallel double crank mechanism in the leg structure resulted in redundancy in the sagittal plane where multiple leg configurations or inverse kinematic solutions exist. The leg swing in the

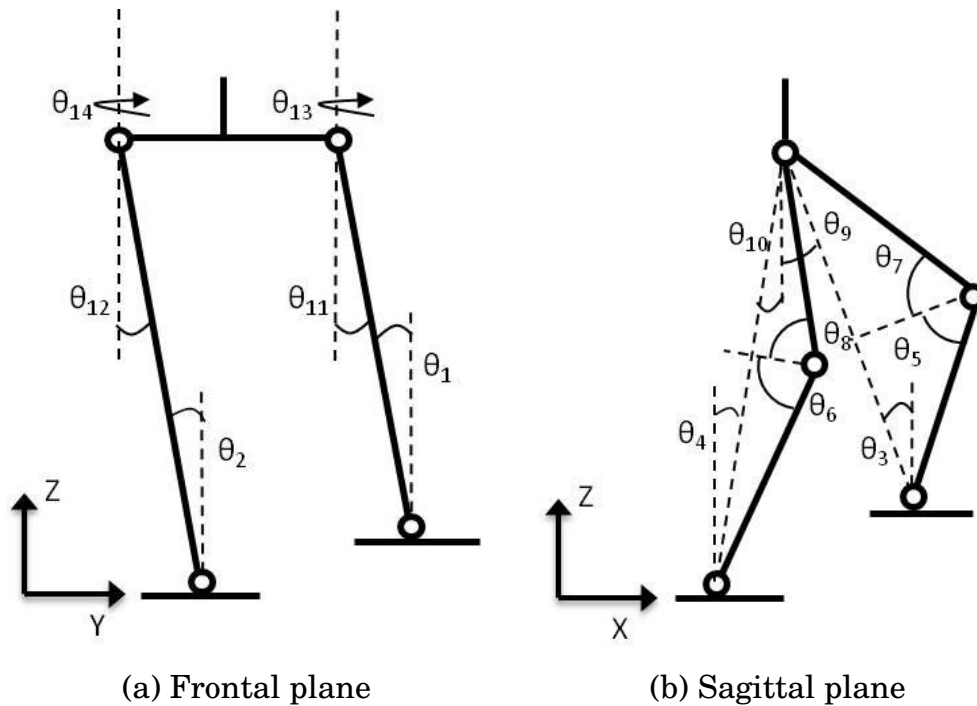


Figure 2.9: Angular quantities of the biped model

sagittal plane for a particular foot placement in Cartesian space ( $X$ ,  $Y$ ,  $Z$ ) can be achieved by actuating various combinations of the joints (Fig. 2.10). To reduce the complexity in the computation and implementation, constraints are placed on the forward kinematic to decouple the leg motion such that a unique solution for the inverse kinematics is achievable.

The leg motion is decoupled into the leg-lift and leg-swing motions (Fig. 2.11). In the leg lift, the parallel double crank mechanism is used to achieve the necessary bending of the knee. The thigh and shank are constrained to form the necessary knee angle ( $\theta_5, \theta_7$ ) with no displacement of the ankle joint from the hip joint in the sagittal plane (Fig. 2.11(a)). The actuation of the pitch joint, angle ( $\theta_9$ ) formed between the vertical denoted from the hip to the ankle joint in the sagittal plane and the  $Z$  axis, determines the leg swing angle (Fig. 2.11(b)).

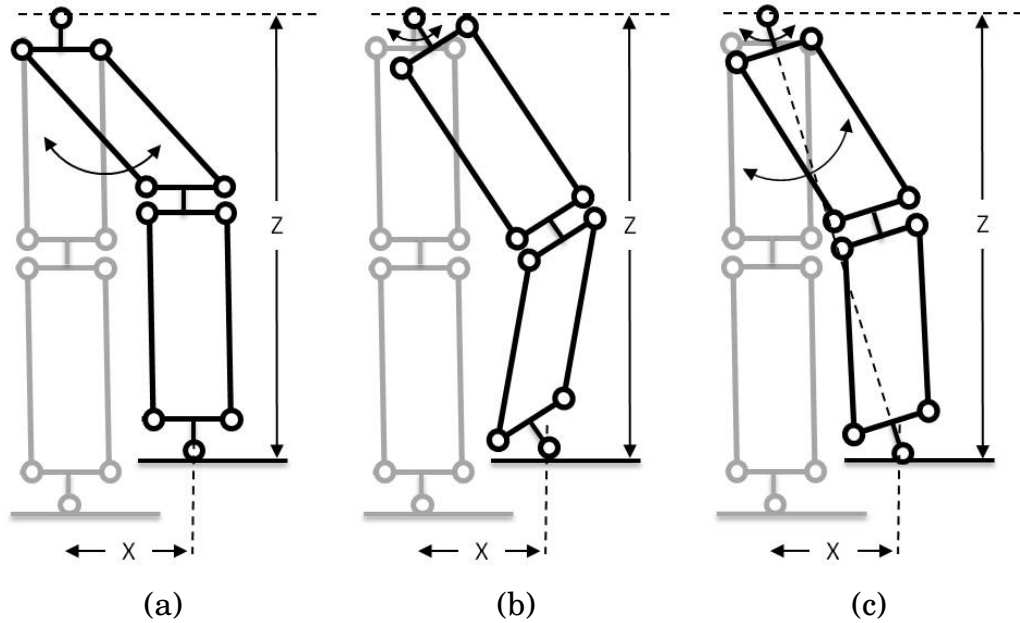


Figure 2.10: Leg swing motion in sagittal plane

The concentrated masses in the legs of the biped are denoted by reference points in the Cartesian space (Fig. 2.12);  $P_1$  and  $P_2$  are the ankle joints,  $P_3$  and  $P_4$  are the knee joints, and,  $P_5$  and  $P_6$  are the hip joints. The inverse kinematic parameters of the legs are defined in term of the reference points as:

$$X_l = P_{1x} - P_{5x}$$

$$X_r = P_{2x} - P_{6x}$$

$$Y_l = -P_{5y}$$

$$Y_r = -P_{6y}$$

$$Z_l = P_{1z} - P_{5z}$$

$$Z_r = P_{2z} - P_{6z}$$

(2.1)

The inverse kinematic parameters of the legs are defined as the displacements of the ankle joint from the hip joint in the sagittal, frontal

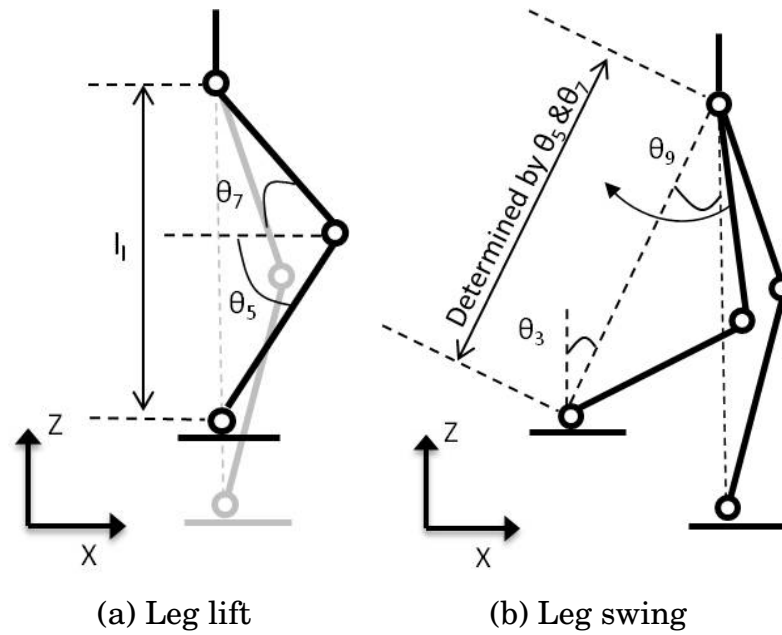


Figure 2.11: Decoupling of leg motion

and transverse planes for each leg (Fig. 2.13). Displacements along the sagittal plane is defined as  $X_l$  and  $X_r$ , along the frontal plane, as  $Y_l$  and  $Y_r$ , and along the transverse plane as  $Z_l$  and  $Z_r$ . In addition, six kinematic parameters of interest (Fig. 2.13) are defined as follows:

$$\begin{aligned}
 l_l &= \sqrt{X_l^2 + Y_l^2 + Z_l^2} \\
 l_r &= \sqrt{X_r^2 + Y_r^2 + Z_r^2} \\
 \theta_{p3} &= \cos^{-1} \left[ \frac{d_1^2 + d_2^2 - l_l^2}{2d_1d_2} \right] \\
 \theta_{p4} &= \cos^{-1} \left[ \frac{d_1^2 + d_2^2 - l_r^2}{2d_1d_2} \right] \\
 \theta_{p1} &= \sin^{-1} \left[ \frac{d_2 \sin(\theta_{p3})}{l_l} \right] \\
 \theta_{p2} &= \sin^{-1} \left[ \frac{d_2 \sin(\theta_{p4})}{l_r} \right]
 \end{aligned}$$

(2.2)



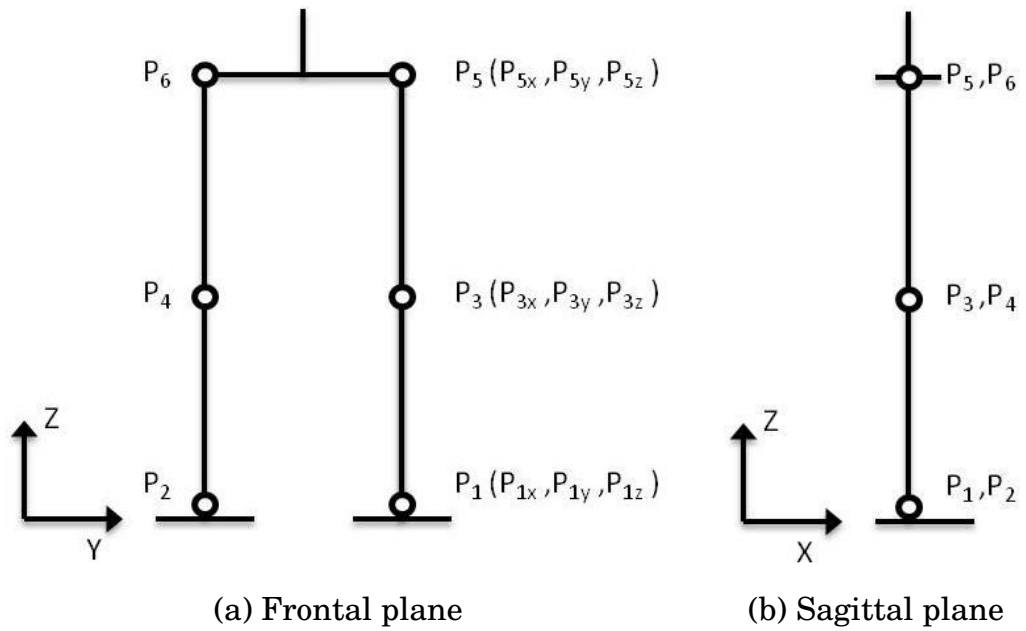


Figure 2.12: Reference points for inverse kinematics

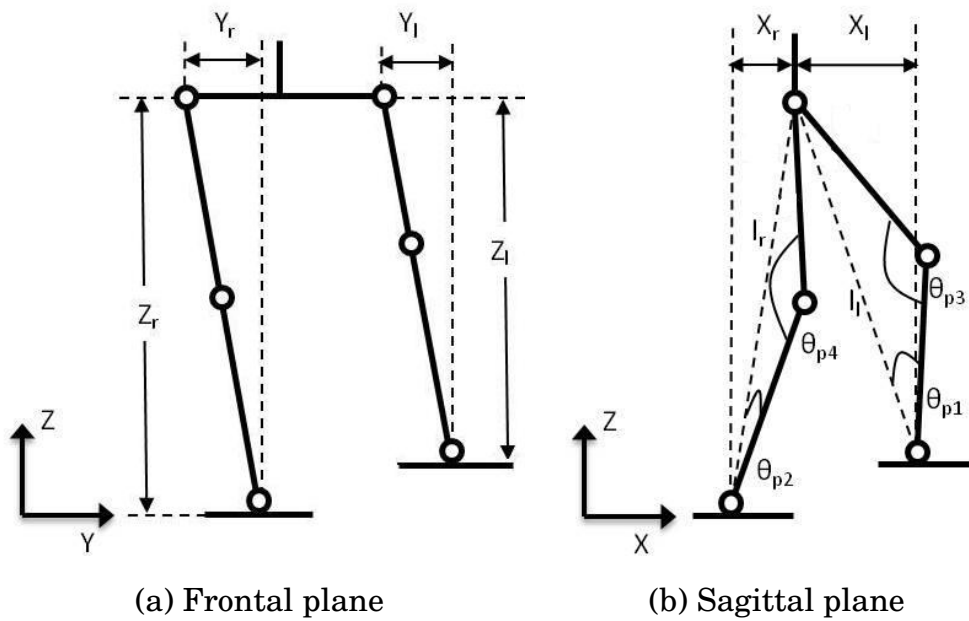


Figure 2.13: Inverse kinematic parameters

For straight walking using motion decoupling, a unique solution to the inverse kinematics of the robot is computed. The 14 x 1 vector of angular quantities expressed in terms of the inverse kinematic parameters are presented in (2.3).

$$\begin{aligned}
\theta_1 &= \tan^{-1}\left(\frac{Y_l}{Z_l}\right) \\
\theta_2 &= \tan^{-1}\left(\frac{Y_r}{Z_r}\right) \\
\theta_{11} &= -\theta_1 \\
\theta_{12} &= -\theta_2 \\
\theta_5 &= \pi/2 - \theta_{p1} \\
\theta_6 &= \pi/2 - \theta_{p2} \\
\theta_7 &= \theta_{p3} - \theta_5 \\
\theta_8 &= \theta_{p4} - \theta_6 \\
\theta_3 &= \tan^{-1}\left(\frac{X_l}{Z_l}\right) \\
\theta_4 &= \tan^{-1}\left(\frac{X_r}{Z_r}\right) \\
\theta_9 &= -\theta_3 \\
\theta_{10} &= -\theta_4 \\
\theta_{13} &= 0 \\
\theta_{14} &= 0
\end{aligned}
\tag{2.3}$$

### 2.3.3 Actuator Control

The actuators utilized are commercial digital servos which can be configured for position or speed control. Position control is utilized in this work. The joint angles computed from the inverse kinematics are translated into

position commands and sent to the servos (2.4). The servos has a number of control parameters which are configured to determine the servos' performance and response. These control parameters can be configured on-the-fly to modify the servo response. These control parameters include the controller closed-loop gains, acceleration profile and actuating direction. Operating limits such as the maximum permissible current drawn, the permissible actuating angle and maximum temperature allowed are also configurable for the safety and protection.

$$sc_i = \frac{\theta_i}{\theta_{max}} sc_{max}, \quad (2.4)$$

where  $sc_i$  is the digital value sent to the  $i$  servos for position control and  $\theta_i$  is the joint angles at joint  $i$ .  $\theta_{max}$  and  $sc_{max}$  are the maximum operating angle of the servos in degrees and digital value respectively.

### 2.3.4 Force Sensor

Force sensitive resistors (FSR)s or commonly referred as force sensors are mounted on the foot of the robot for contact and force sensing. FSRs are relatively low cost and easy to use sensors. With appropriate number of FSRs and proper mechanical mounting, good measurement of ground reaction forces can be measured which is useful for postural stability control.

A total of 8 FSR are mounted in the robot with 4 FSR on each foot (Fig. 2.14). The FSRs are mounted at the foot corners (Fig. 2.15). Each FSR is mounted with a puck on the sensing area to ensure that the sensor captures the maximum percentage of the applied force even if the contact surface is larger than the sensing area diameter. In addition, the puck

reduces the high pressure resulted by point force. A sole plate is mounted to the pucks to amplify the force sensing area to the entire foot.

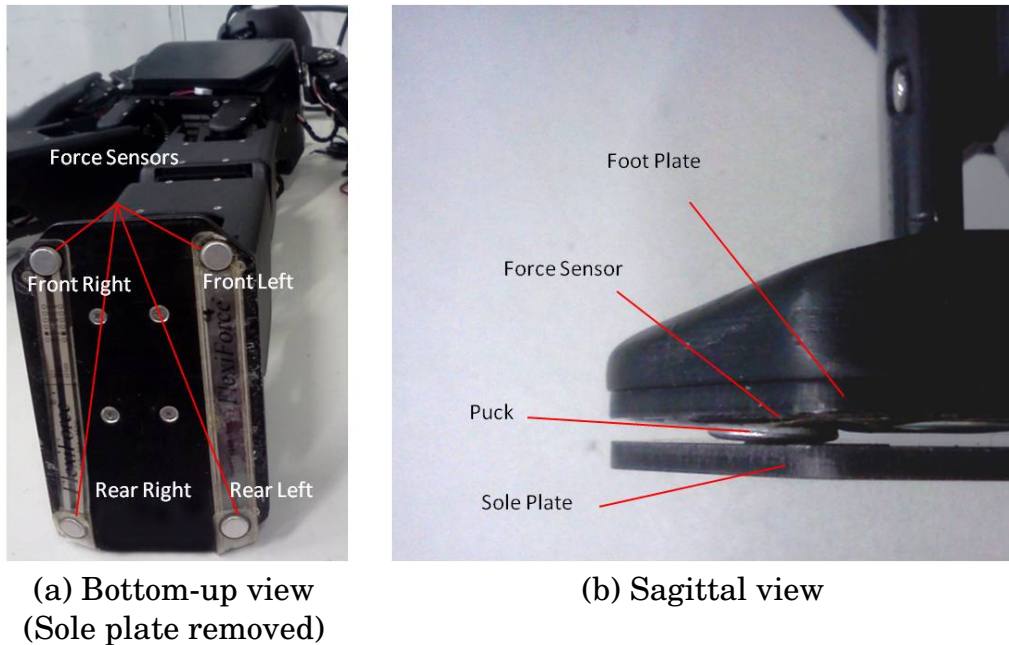


Figure 2.14: Mechanical installation of force sensors

A simple circuit (Fig. 2.16) converts the resistance into a voltage which is read using an analog-to-digital converter (ADC). Resolution of the force sensed is dependent on the accuracy of the FSR and the resolution of the ADC of the micro processor. (2.5) converts the sensed resistance to voltage.

$$V_{ADC} = \frac{R_1}{R_1 + R_{sense}} V_{DD} \quad (2.5)$$

where  $V_{ADC}$  is the voltage read by the ADC and  $R_{sense}$  is the resistance of the FSR.

### 2.3.5 Rate Gyroscope

A rate gyroscope is mounted in the robot body to measure the angular rotation in the transverse plane. The rate gyroscope provides information

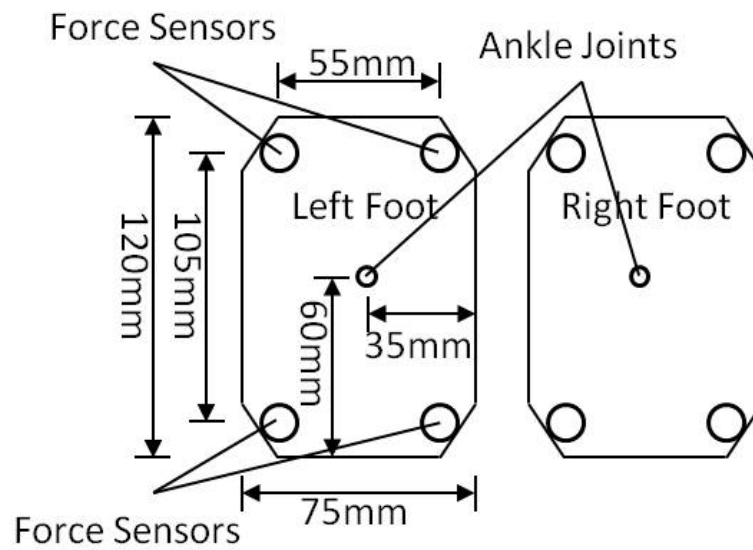


Figure 2.15: Position of force sensors

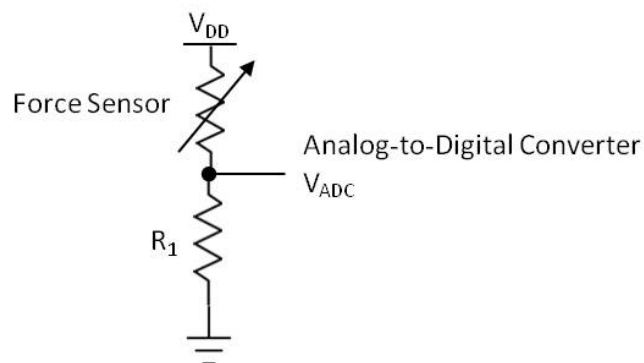
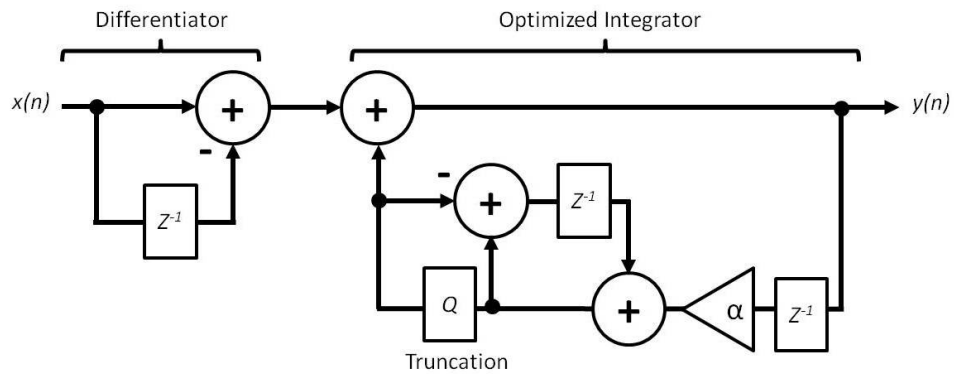


Figure 2.16: Force sensor: Resistance-to-voltage circuit

in relation to the orientation of the robot. A 10-bit ADC in the micro-processor reads the analog signal from the gyroscope and converts the signal to the angular rate. A direct-current (DC) filter is implemented to remove the bias from the analog signal and a threshold filter to eliminate the accumulation of angular error.

The analog signal output from the rate gyroscope has a DC bias to indicate null or zero angular rate. A digital DC filter, fixed-point DC blocker with ‘fraction-saving’ [110], is implemented to remove the bias. The DC



$\alpha$  is the location of the pole that correlates the trade-off between the time-domain transient response and bandwidth

Figure 2.17: Fixed-point DC blocker with ‘fraction-saving’

filter comprises of a differentiator and an optimized integrator (Fig. 2.17). The location of the pole determines the frequencies that are attenuated. For DC filtering, the location of the pole ( $\alpha$ ) is often chosen close to unity to filter out very low frequencies. The DC filter is also implemented in the the inertia measurement unit (IMU) for removing the bias in the gyroscope and accelerometer readings.

Orientation of the robot is given by the integration of the angular velocity from the rate gyroscope. Small fluctuations in the reading constitute to the accumulation of errors resulting in an orientation drift even if the robot is stationary. To address the problem, a simple threshold filter is implemented such that the variations in readings that are less than a noise sensitivity threshold are discarded. Loss of information due to threshold filter is insignificant as the minimum turning velocity of the robot is relatively large. The voltage reading of the angular rate from the gyro is calibrated against the amount of angular velocity to compensate for the

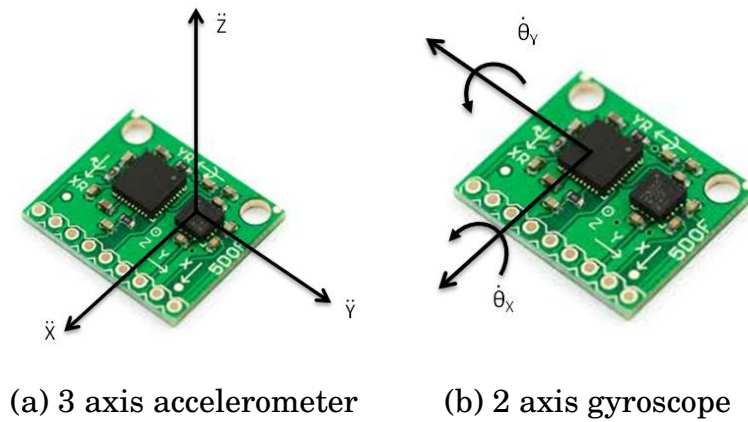


Figure 2.18: Inertia measurement unit

lost information. The threshold filter is expressed as follows:

$$y(n) = \begin{cases} 0, & \text{for } x(n) < V_{threshold} \\ x(n), & \text{otherwise} \end{cases} \quad (2.6)$$

### 2.3.6 Inertia Measurement Unit

The inertia measurement unit (IMU) consists of a 3 axis accelerometer and a 2 axis gyroscope. Fig. 2.18 shows the axes of the accelerometer and gyroscope. The IMU is mounted in the body to measure the angular tilt and the linear acceleration of the robot. Angular tilt is defined as the angular rotation of the body in the frontal and sagittal planes whereas the linear acceleration is related to the displacement of the body in the transverse plane. A 10-bit ADC in the micro processor reads the analog signal from the IMU. A Kalman filter [111] via a 4<sup>th</sup> Order Runge-Kutta [112] is implemented on the IMU to eliminate the ill effects such as drifting and vibrations on the gyroscopes and accelerometers. A correction calculation is implemented to obtain the estimate of the linear acceleration from the biased readings in the accelerometers in the presence of angular tilting.

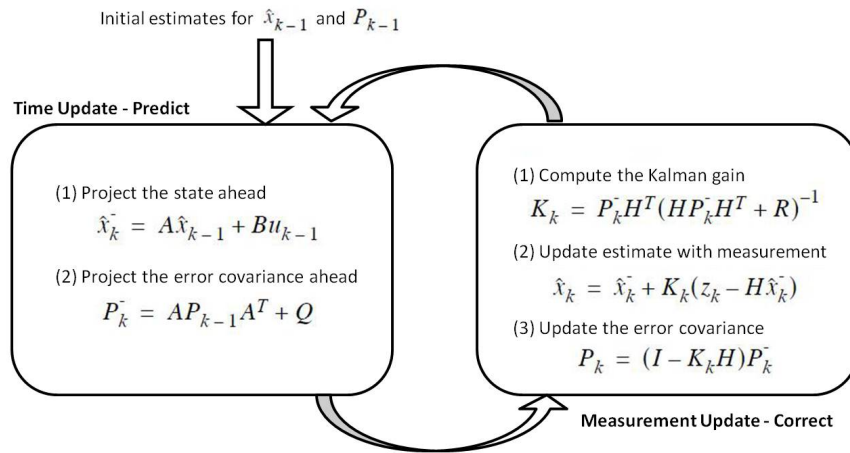


Figure 2.19: Kalman filter algorithm [3]

The Runge-Kutta 4<sup>th</sup> Order is a simple, computational inexpensive and fast integral algorithm to removes jitters via an average weighted system. It helps to smooth out the voltage output readings of the accelerometer and gyroscope in the IMU. The Runge-Kutta 4<sup>th</sup> Order is given as:

$$\theta_k = \theta_{k-1} + \frac{1}{6}(\dot{\theta}_k + 2\dot{\theta}_{k-1} + 2\dot{\theta}_{k-2} + \dot{\theta}_{k-3}), \quad (2.7)$$

where  $\theta_k$  is the angular tilt given by the integration of the gyroscope raw output data ( $\dot{\theta}_k, \dot{\theta}_{k-1}, \dot{\theta}_{k-2}, \dot{\theta}_{k-3}$ ).

The Kalman Filter is an iterative filter that combines the knowledge of statistical nature of the system error with a knowledge of system dynamics to provide an estimation of the system states. State-space equations of Kalman filter given by:

$$x_k = Ax_{k-1} + Bu_{k-1} + w_{k-1},$$

$$z_k = Hx_k + v_k,$$

$$w_k \sim N(0, Q),$$

$$v_k \sim N(0, R),$$

(2.8)



where  $x_k$  is the angular tilt and bias to be estimated,  $u_k$  is the input measurement from the gyroscope,  $z_k$  is the input from the accelerometer,  $w_k$  is the process noise with covariance  $Q$  which relates to the amount of noise in the gyroscope readings, and  $v_k$  is the measurement noise with covariance  $R$  which relates to the amount of noise expected from the accelerometers. The Kalman filter algorithm is presented in Fig. 2.19.

The state-space equations of the IMU is formulated as (2.9) and (2.10) for the sagittal and frontal tilt angles respectively.

$$\begin{bmatrix} \hat{\theta}_{Y_{Kalman}} \\ \alpha \end{bmatrix}_k = \begin{bmatrix} 1 & dt \\ 0 & 1 \end{bmatrix} \begin{bmatrix} \hat{\theta}_{Y_{Kalman}} \\ \alpha \end{bmatrix}_{k-1} + \begin{bmatrix} dt \\ 0 \end{bmatrix} \dot{\theta}_{Y_{Gyro}k-1}, \quad (2.9)$$

$$\begin{bmatrix} \hat{\theta}_{X_{Kalman}} \\ \beta \end{bmatrix}_k = \begin{bmatrix} 1 & dt \\ 0 & 1 \end{bmatrix} \begin{bmatrix} \hat{\theta}_{X_{Kalman}} \\ \beta \end{bmatrix}_{k-1} + \begin{bmatrix} dt \\ 0 \end{bmatrix} \dot{\theta}_{X_{Gyro}k-1}, \quad (2.10)$$

where  $\hat{\theta}_{X_{Kalman}}$  and  $\hat{\theta}_{Y_{Kalman}}$  are the estimated angular tilts of the robot;  $\dot{\theta}_{X_{Gyro}}$  and  $\dot{\theta}_{Y_{Gyro}}$  are the angular velocities from the gyroscope;  $\alpha$  and  $\beta$  are the biases that automatically update to correct the drifting.

The input from the accelerometer are denoted as:

$$\begin{aligned} z_{k(sagittal)} &= \text{atan2}(\ddot{X}_{Accel}/g, \ddot{Z}_{Accel}/g), \\ z_{k(frontal)} &= \text{atan2}(\ddot{Y}_{Accel}/g, \ddot{Z}_{Accel}/g), \end{aligned} \quad (2.11)$$

where  $\ddot{X}_{Accel}$ ,  $\ddot{Y}_{Accel}$  and  $\ddot{Z}_{Accel}$  are the acceleration values from the accelerometer; and,  $g$  is gravity.

Based on the estimated angular tilt from the Kalman filter, a bias correction calculation as (2.12) is used to obtain the estimated linear acceleration. Correction is performed on the readings obtained by the accelerometer in presence of the angular tilting.

$$\begin{aligned}
A &= \tan(\hat{\theta}_{X_{Kalman}}), \\
B &= \tan(\hat{\theta}_{Y_{Kalman}}), \\
\ddot{Z}_{Offset} &= g\sqrt{\frac{1}{A^2 + B^2 + 1}}, \\
\ddot{X}_{Accel} &= \ddot{X} - B\ddot{Z}_{Offset}, \\
\ddot{Y}_{Accel} &= \ddot{Y} - A\ddot{Z}_{Offset}, \\
\ddot{Z}_{Accel} &= \ddot{Z} - \ddot{Z}_{Offset}, \\
\begin{bmatrix} \hat{\ddot{X}}_{Robot} \\ \hat{\ddot{Y}}_{Robot} \\ \hat{\ddot{Z}}_{Robot} \end{bmatrix} &= R_y(\hat{\theta}_{X_{Kalman}})R_x(\hat{\theta}_{Y_{Kalman}}) \begin{bmatrix} \ddot{X}_{Accel} \\ \ddot{Y}_{Accel} \\ \ddot{Z}_{Accel} \end{bmatrix},
\end{aligned} \tag{2.12}$$

where  $\ddot{Z}_{Offset}$  is the acceleration offset due to any angular tilting of the robot;  $\ddot{X}_{Accel}$ ,  $\ddot{Y}_{Accel}$  and  $\ddot{Z}_{Accel}$  are the estimated linear accelerations with respect to the IMU's acceleration frame (Fig. 2.18(a));  $\hat{\ddot{X}}_{Robot}$ ,  $\hat{\ddot{Y}}_{Robot}$  and  $\hat{\ddot{Z}}_{Robot}$  are the estimated linear accelerations with respect to robot frame;  $R_x$  and  $R_y$  denote the rotation matrices of the robot frame and IMU frame; and,  $g$  is gravity.

### 2.3.7 Position Feedback

The digital servos provide position feedback in which a simple mathematical conversion converts the digital feedback value to the joint angle as (2.13). The position of the foot with respect to the origin at the hip is

Table 2.8: Denavit - Hartenberg parameters

Joint	$\alpha_i$	$d_i$	$a_i$	$\theta_i$
1	0°	0	$a_1$	90°
2	90°	0	0	$\theta_2$
3	-90°	0	0	$\theta_3$
4	0°	0	$a_4$	$\theta_4$
5	0°	0	$a_5$	$\theta_5$
6	0°	0	$a_6$	$\theta_6$
7	90°	0	0	$\theta_7$
8	0°	0	$a_8$	0°

computed using the forward kinematics.

$$\theta_i = \frac{\theta_{servo}}{fb_{max} - fb_{min}} fb_i \quad (2.13)$$

where  $\theta_i$  is the joint angle at joint  $i$ ,  $\theta_{servo}$  is the maximum permissible operating angle of the servo,  $fb_{max}$  and  $fb_{min}$  are the digital values fed back by the servo when servo positions are at the minimum and maximum operating angles respectively, and,  $fb_i$  is the digital value fed back by the servo at joint  $i$ . The forward kinematic of the foot position is calculated using the Denavit - Hartenberg (D-H) [113] parameters. Fig. 2.20 shows the coordinate frames assigned to the respective links in the leg using the D-H convention. Table 2.8 shows the D-H parameters. The transformation matrix is given by:

$$H_i^{i-1} = \begin{bmatrix} \cos(\theta_i) & -\cos(\alpha_i) \sin(\theta_i) & \sin(\alpha_i) \sin(\theta_i) & a_i \cos(\theta_i) \\ \sin(\theta_i) & \cos(\alpha_i) \cos(\theta_i) & -\sin(\alpha_i) \cos(\theta_i) & a_i \sin(\theta_i) \\ 0 & \sin(\alpha_i) & \cos(\alpha_i) & d_i \\ 0 & 0 & 0 & 1 \end{bmatrix} \quad (2.14)$$

Substituting the D-H parameters, the continuous homogeneous transformation ( $H_1^0, H_2^1, \dots, H_F^8$ ) can be obtained. The transformation matrices are used to compute the foot coordinate to the origin as:

$$H_F^0 = H_1^0 H_2^1 H_3^2 H_4^3 H_5^4 H_6^5 H_7^6 H_8^7 H_F^8 \quad (2.15)$$

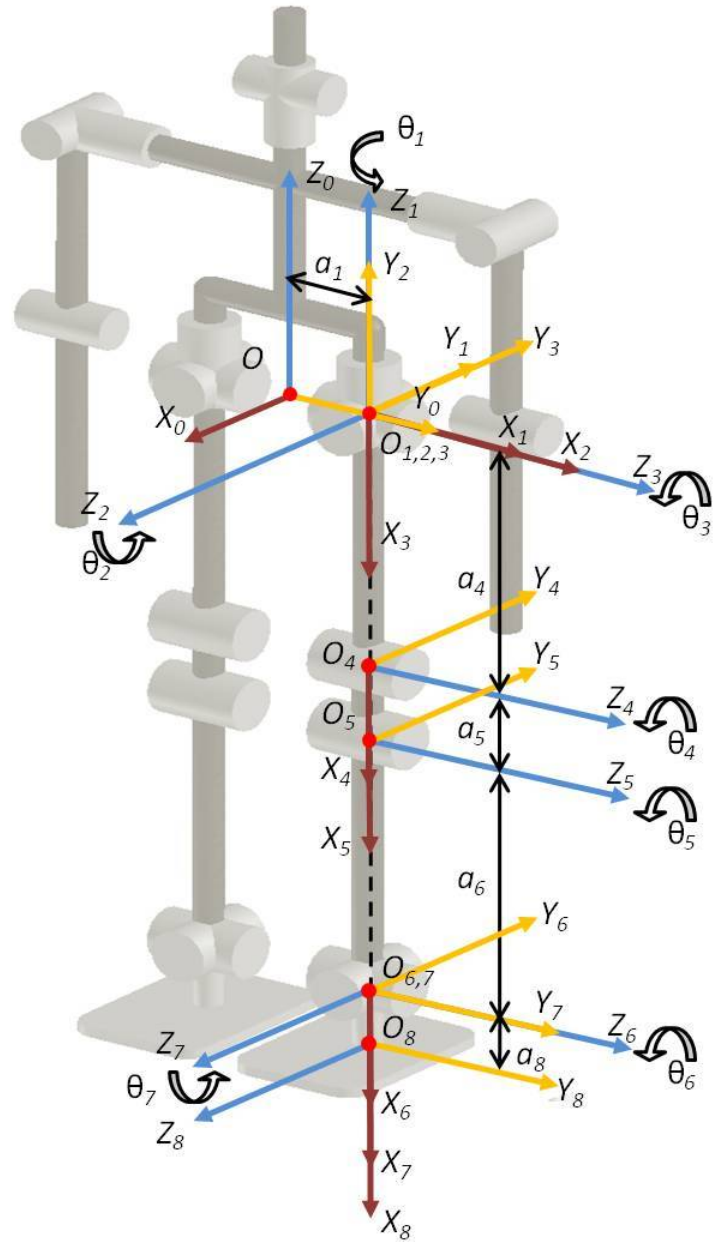


Figure 2.20: Link coordinate frame using D-H convention

## **Chapter 3**

# **Generation of Lateral Walk-Oscillation using Sinusoidal Pattern**

The ZMP criterion is the most established and widely used approach for gait generation in bipedal walking. Using the ZMP criterion, various trajectory based gait generation approaches over the years have shown success in producing gaits that are suitable for dynamical walking in humanoid robots. Notable successful examples of humanoids using ZMP based biped walking include Honda Asimo Robot [2], Sony Qrio [114] and Kaist (KHR-3) HUBO [30].

The use of sinusoidal pattern for gait generation of bipedal walking has proven to be successful [29, 90, 115, 116]. In most of the researches using sinusoidal pattern, sine and cosine functions are used as the basic walking trajectories. One of the most common use of the sinusoid is to generate the lateral shifting in dynamical walking. Sinusoidal functions are simple which are ideal for online gait generation where computation time and complexity are key considerations. The motions produced by sinusoidal

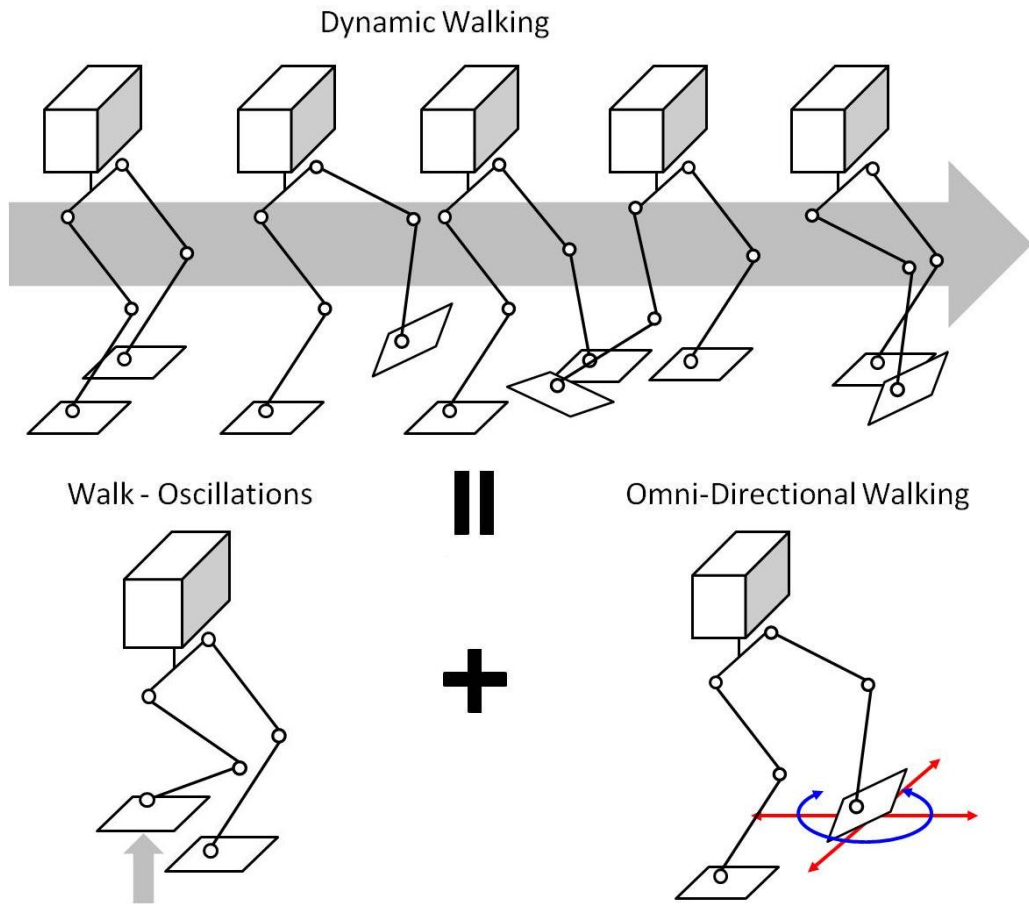


Figure 3.1: Decoupling of dynamic walk motions

functions are also smooth. The use of sinusoidal functions for online gait generation are successfully demonstrated [90] and [116]. Modulation of sinusoidal patterns by coupled oscillator for biped walking is proposed in [115] and [77]. The modulated sinusoidal trajectories enabled the generation of walking gaits.

In this research, the motion of biped dynamic walking on flat terrain is decoupled into two components, ① lateral walk-oscillations and ② omni-directional walking (Fig. 3.1). Lateral walk-oscillation is the generation of the single support phase (Fig. 3.2(a)) and the double support phase (Fig. 3.2(b)) using oscillatory movement. The movement involves the shifting

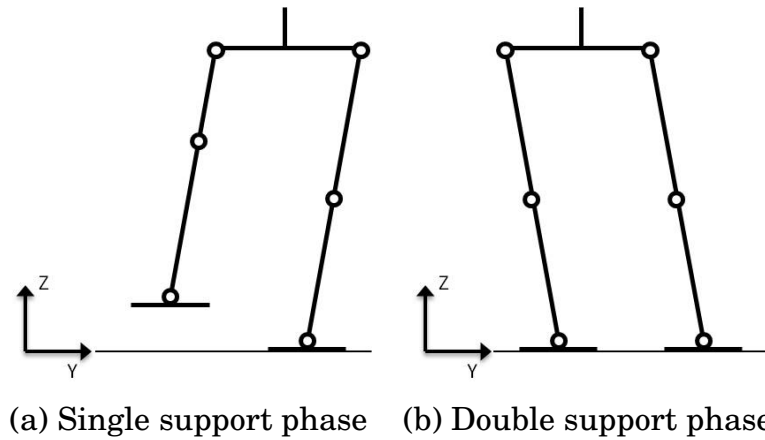


Figure 3.2: Phases of walking in frontal plane

of the body in a periodical manner for alternate stable lifting of the foot. The lifted foot is therefore arbitrary placed to locomote the humanoid in the desired walking direction.

In this chapter, an approach using sinusoidal trajectories and the ZMP criterion for offline gait generation of lateral walk-oscillation are discussed and implemented. Sinusoidal trajectories are applied to the foot placement to produce stable lateral motion. Based on the ZMP trajectory for stable lateral motion, the single and double support phases are produced to generate the walk-oscillations gaits. Limitations of the offline gait generation approach is highlighted by examining the influence of the walking environment on the locomotion stability. The gait generation approach is verified in simulation and implemented on the humanoid robot 'REJr'.

The gait generation of lateral motion using sinusoidal reference pattern is discussed in section 3.1. In section 3.2, the offline gait generation approach of lateral walk-oscillation is presented. Section 3.3 and section 3.4 present the simulation and experiment results. Section 3.5 concludes the chapter.

## **3.1 Lateral Motion Using Sinusoidal Reference Pattern**

Lateral walk-oscillation is the generation of the single and double support phases that are suited for dynamic walking. Lateral walk-oscillation is realized through two phases:

1. Generate stable lateral motion - The oscillation of the humanoid body in the frontal plane in a stable manner suitable for facilitating walk-oscillation.
2. Create single and double support phases - The leg is lifted and landed at appropriate instances without compromising on the stability of the lateral motion.

The sinusoidal reference pattern is used for the generation of lateral motion. Sinusoidal functions provide smooth motion trajectories, and, are relatively simple, computationally inexpensive and easy to implement for biped gait generation as highlighted in several research works [29,90,115,116].

### **3.1.1 Biped Model**

The Linear Inverted Pendulum Model (LIPM) [11] (Fig. 3.3) is adopted in this research. The LIPM decouples the motions of the humanoid into the



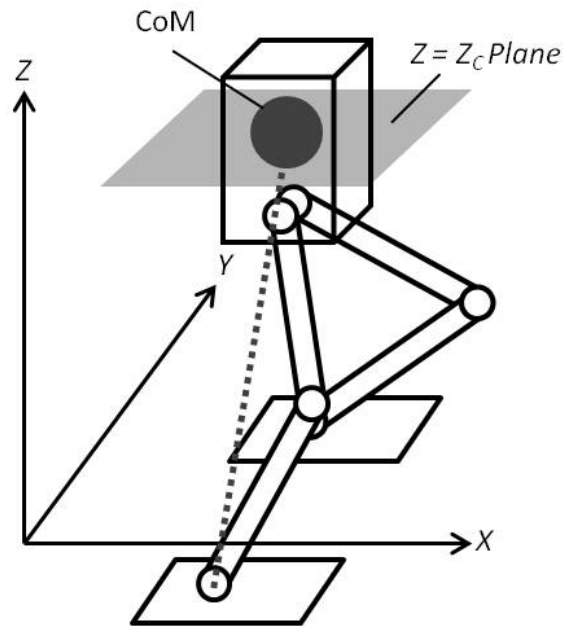


Figure 3.3: Linear inverted pendulum model

frontal and sagittal planes (3.1).

$$\begin{aligned}\ddot{x}_{CoM} &= \frac{g}{z_c}x_{CoM} + \frac{1}{mz_c}\tau_x, \\ \ddot{y}_{CoM} &= \frac{g}{z_c}y_{CoM} - \frac{1}{mz_c}\tau_y,\end{aligned}\tag{3.1}$$

where  $x_{CoM}$ ,  $y_{CoM}$  and  $z_{CoM}$  are the Cartesian coordinates of the CoM,  $m$  is mass of the humanoid,  $z_c$  is height of the plane in which the CoM is constrained,  $g$  is the acceleration due to gravity,  $\tau_x$  and  $\tau_p$  are the pitch and roll control torque respectively.

### 3.1.2 Sinusoidal Foot Trajectories

Lateral motion involves the shifting of the CoM in the frontal plane. The shifting of the CoM is realized by applying sinusoidal trajectories to the

lateral motion of the foot (Fig. 3.4). The desired foot placement trajectories are expressed as:

$$\begin{aligned}
 X_r^{walk-osc}(t) &= X_l^{walk-osc}(t) = 0, \\
 Y_r^{walk-osc}(t) &= Y_l^{walk-osc}(t) = A \sin(\omega t), \\
 Z_r^{walk-osc}(t) &= \sqrt{d^2 - (Y_r^{walk-osc}(t))^2}, \\
 Z_l^{walk-osc}(t) &= \sqrt{d^2 - (Y_l^{walk-osc}(t))^2},
 \end{aligned}
 \tag{3.2}$$

where  $d$  is the height of the hip from the ground in standing posture and  $A$  is the maximum amount of lateral shift in the foot.  $\omega$  is the oscillating frequency where one oscillation period ( $T = \frac{2\pi}{\omega}$ ) is defined as a phase cycle of lateral shifting from the centre to left, to the right, and back to the centre.

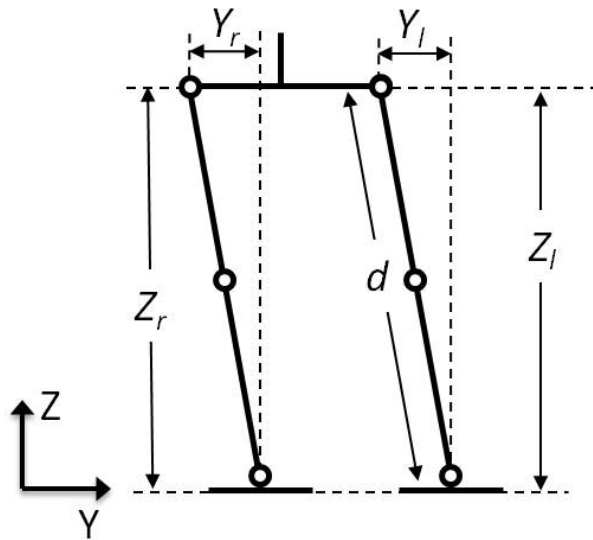


Figure 3.4: Foot placement in the frontal plane

The sinusoidal trajectories (3.2) are applied to the humanoid in the standing posture. Assuming that necessary torque are applied to the joints to achieved the desired foot trajectories, the CoM shifts left and

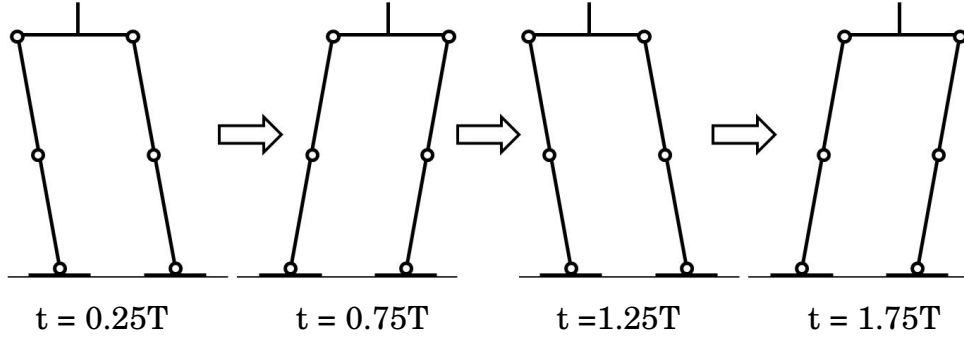


Figure 3.5: Lateral shifting of CoM

right periodically, creating lateral motion (Fig. 3.5). The motions of the foot is in relative movement to the CoM and hence the lateral shift of the CoM ( $y_{CoM}$ ) in the frontal plane is given by (3.3).

$$y_{CoM}(t) = A \sin(\omega t), \quad (3.3)$$

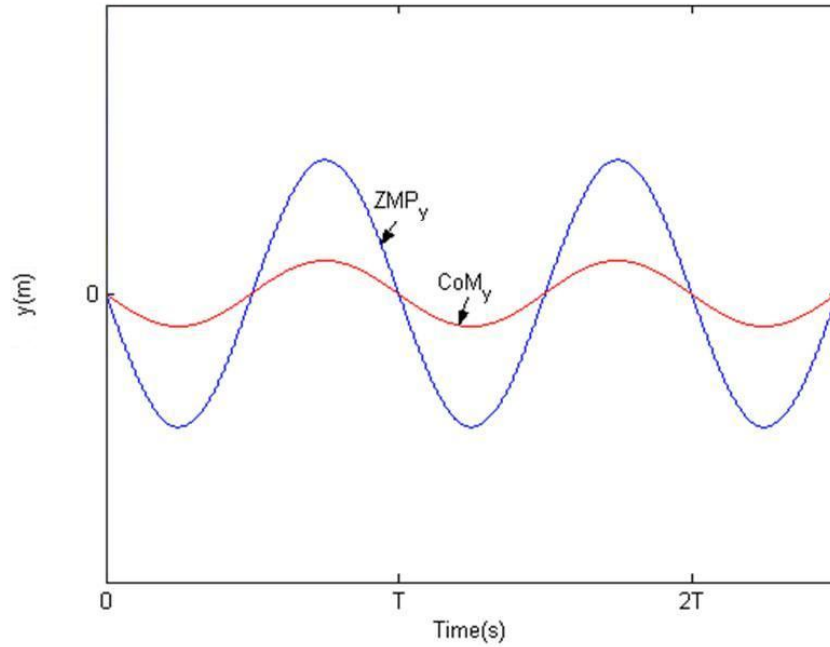
where the amount of lateral shift of the inverted pendulum in the LIPM is equivalent to the lateral shift exerted by the foot.

### 3.1.3 Zero Moment Point (ZMP) Trajectory

The stability of the lateral motion is determined using the ZMP criterion. The assumption is that the foot does not slip or rotate during lateral motion as the ZMP criterion does not address the stability when foot rotation or slippage occurs [22]. Based on the LIPM (3.1), the ZMP of the robot is decoupled [117] and expressed as:

$$\begin{aligned} \ddot{x}_{ZMP}(t) &= x_{CoM}(t) - \frac{z_c}{g} \ddot{x}_{CoM}(t), \\ \ddot{y}_{ZMP}(t) &= y_{CoM}(t) - \frac{z_c}{g} \ddot{y}_{CoM}(t), \end{aligned} \quad (3.4)$$

where  $(x_{ZMP}, y_{ZMP})$  is the ZMP and  $(x_{CoM}, y_{CoM}, z_{CoM})$  is the location of the CoM in the Cartesian coordinate respectively.  $m$  is mass of the humanoid,



*The ZMP trajectory produced by sinusoidal foot trajectories is in phase with the CoM trajectory.*

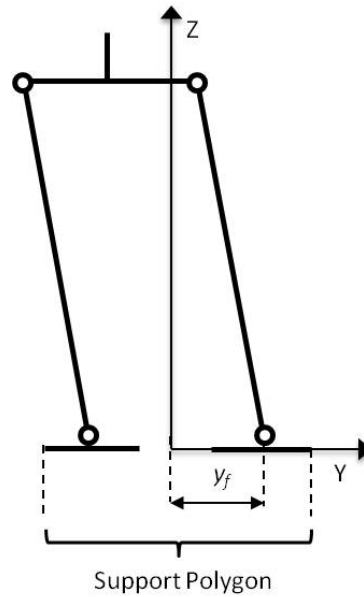
Figure 3.6: ZMP and CoM trajectories of lateral motion

and  $g$  is the acceleration due to gravity. The ZMP in the frontal plane is computed as:

$$\begin{aligned}
 y_{CoM}(t) &= A \sin(\omega t), \\
 \ddot{y}_{CoM}(t) &= -A\omega^2 \sin(\omega t), \\
 y_{ZMP}(t) &= A \sin(\omega t) + \frac{z_c}{g} A\omega^2 \sin(\omega t), \\
 &= A\left(1 + \frac{\omega^2 z_c}{g}\right) \sin(\omega t), \\
 &= A\left(1 + \frac{\omega^2}{\omega_n^2}\right) \sin(\omega t),
 \end{aligned}$$

(3.5)

where  $z_c$  is the height of the LIPM in which the CoM is constricted,  $\omega_n$  is the natural oscillating frequency of the LIPM given by  $\omega_n = \sqrt{\frac{g}{z_c}}$ .



$y_f$  is the distance from the ankle to the center between the feet assuming that the feet are equidistant from the CoM.

Figure 3.7: Lateral motion support polygon

The resulted ZMP trajectory in the frontal plane is a stable sinusoid (Fig. 3.6). The peak amplitude of the ZMP sinusoid occurs when the CoM is shifted to the extreme left or right. The CoM is at the extremes when  $t = 0.25T$  and  $t = 0.75T$  in one oscillation period. The peak amplitude of the ZMP ( $|y_{ZMP(peak)}|$ ) is computed as:

$$\begin{aligned}
 |\sin(\omega t)| &= 1, \\
 |y_{ZMP(peak)}| &= \left| A \left( 1 + \frac{\omega^2}{\omega_n^2} \right) \right|.
 \end{aligned}
 \tag{3.6}$$

### 3.1.4 Generating Stable Lateral Motion

The lateral motion is stable if the ZMP remains in the support polygon (Fig. 3.7). The ZMP trajectory is a stable sinusoid in which the peak

ZMP amplitude determines the stability; if the peak ZMP goes beyond the support polygon, the motion is unstable. For optimal stability during single support phases, a logical choice of the peak ZMP amplitude would be the middle of the foot support area ( $y_f$ ) (Fig. 3.7). Assuming that an appropriate oscillating frequency is selected, the amount of lateral shift ( $A$ ) required to achieve the desired peak ZMP amplitude is computed as (3.7). Fig. 3.8 shows the ZMP and CoM trajectories of the stable lateral motion generated with the peak ZMP amplitude equal to  $y_f$ .

$$\begin{aligned} |y_{ZMP(peak)}| &= \left| A \left( 1 + \frac{\omega^2}{\omega_n^2} \right) \right|, \\ y_f &= A \left( 1 + \frac{\omega^2}{\omega_n^2} \right), \\ A &= \frac{y_f}{1 + \frac{\omega^2}{\omega_n^2}}, \end{aligned} \tag{3.7}$$

where  $y_f$  is the distance from the ankle to the center between the foot assuming that the feet are equidistant from the CoM.

## 3.2 Offline Gait Generation of Lateral Walk-Oscillation

The lateral motion is in the double support phase and the intention is to determine the appropriate time period for alternate foot to be off the ground periodically to create the single support phases. Stable single and double support phases are realized when the foot is lifted and landed without causing instability. Offline lateral walk-oscillation gaits are generated with the computation of the foot placement trajectories based on stable single and double support phases.

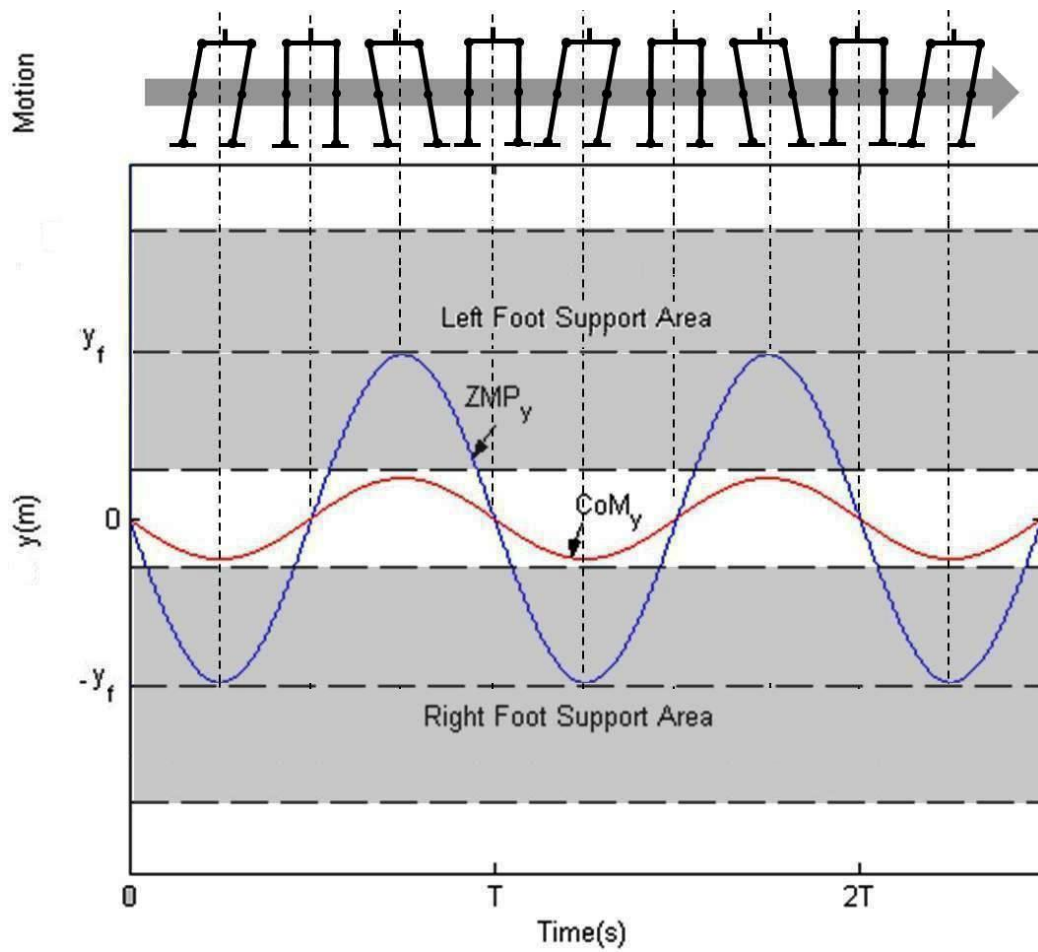
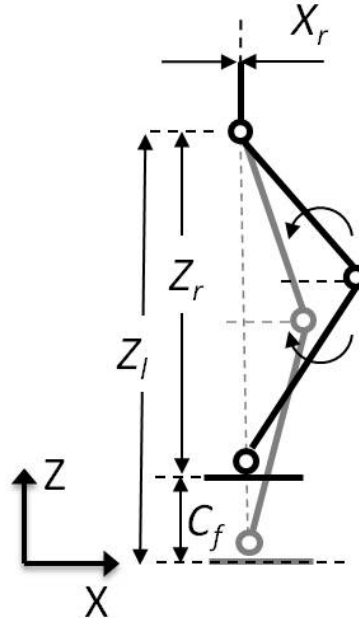


Figure 3.8: ZMP and CoM trajectories of stable lateral motion

### 3.2.1 Foot Lifting and Landing Motion

For the humanoid to transit from the double to single support phase and vice versa, foot lifting and landing are required respectively. The position



*The amount of foot clearance must be sufficient to ensure that the toe and heel do not strike against the ground during leg swinging. The foot clearance is determined experimentally.*

Figure 3.9: Position for foot lift

of the foot when lifted is given by:

$$\begin{aligned}
 X_f &= 0, \\
 Y_f &= \left(1 - \frac{C_f}{z_c}\right)y_{CoM}, \\
 Z_f &= z_c - C_f,
 \end{aligned}
 \tag{3.8}$$

where  $C_f$  is the amount of foot clearance required and  $(X_f, Y_f, Z_f)$  is the foot placement position. Cubic polynomial trajectory (3.9) is applied to interpolate the motion of the foot lift. The cubic polynomial trajectory provides smooth interpolation of the motion allowing control over the initial and final joints states (position and velocity) [118]. Linear acceleration profile of cubic polynomial trajectories allow ease of computation of the



dynamical forces generated for control.

$$\begin{aligned}
a_o &= Z_o, \\
a_1 &= \frac{3}{t_f^2}(Z_f - Z_o), \\
a_2 &= \frac{-2}{t_f^3}(Z_f - Z_o), \\
Z_f(t) &= a_o + a_1(t - t_s)^2 + a_2(t - t_s)^3, \\
Y_f(t) &= \frac{Z_f(t)}{Z_c}y_{CoM}, \\
X_f(t) &= 0,
\end{aligned}
\tag{3.9}$$

where  $t_s$  is starting time of the motion and  $t_f$  the time period of the motion.  $Z_o$  is the initial foot position given by (3.2) and  $Z_f$  is the final foot position given by (3.8).  $(X_l^{walk-osc}, Y_l^{walk-osc}, Z_l^{walk-osc})$  is equated to  $(X_f, Y_f, Z_f)$  when the left foot is lifted and  $(X_r^{walk-osc}, Y_r^{walk-osc}, Z_r^{walk-osc})$  is equated to  $(X_f, Y_f, Z_f)$  when the right foot is lifted.

For the foot landing, the same motion trajectory (3.9) for the foot lift is applied with the initial foot position given by (3.8) and the final foot position given by (3.2). The knee joints are actuated for the foot lift and landing in accordance to the decoupling of motion discussed in Chapter 2.

### 3.2.2 Support Phases For Oscillation Cycle

Considering that the notation of the walk-oscillations is to facilitate fast dynamical walking, the time period for the single support phases in each oscillation cycle is desired to be as long as possible for maximum stride. Without compromising on the stability, the oscillation cycle is divided as

(3.10) for lateral walk-oscillation (Fig.3.10).

$$SupportPhase = \begin{cases} Double, & \text{for } -y_f + y_r \leq y_{ZMP} \leq y_f - y_r \\ Single, & \text{for } -y_f - y_l < y_{ZMP} < -y_f + y_r \\ & \text{or } y_f - y_r < y_{ZMP} < y_f + y_l \\ Unstable, & \text{for otherwise} \end{cases}, \quad (3.10)$$

where  $y_r$  and  $y_l$  are the distances of the respective left and right foot edges from the ankle in the frontal plane.  $y_f$  is the distance from the ankle to the center between the foot assuming that the foot are equidistant from the CoM.  $y_{ZMP}$  is the distance of the ZMP from the CoM.

To determine the time instances for the single support phase, the distance of the inner edge of the foot is equated to the ZMP trajectories as follows:

$$\begin{aligned} y_f - y_r &= A\left(1 + \frac{\omega^2}{\omega_n^2}\right) \sin(\omega t) \text{ for } 0 \leq t < 0.5T, \\ -y_f + y_r &= A\left(1 + \frac{\omega^2}{\omega_n^2}\right) \sin(\omega t) \text{ for } 0.5T \leq t < T, \end{aligned} \quad (3.11)$$

Solutions of (3.11) provided the single support phase time instances,

$$t = T_d, 0.5T - T_d, 0.5T + T_d, T - T_d, \quad (3.12)$$

where  $T_d = \frac{\sin^{-1}\left(\frac{y_f - y_r}{A\left(1 + \frac{\omega^2}{\omega_n^2}\right)}\right)}{\omega}$ . The time period of the double and single support phases respectively are:

$$\begin{aligned} T_{double} &= 2T_d, \\ T_{single} &= 0.5T - T_d, \end{aligned} \quad (3.13)$$

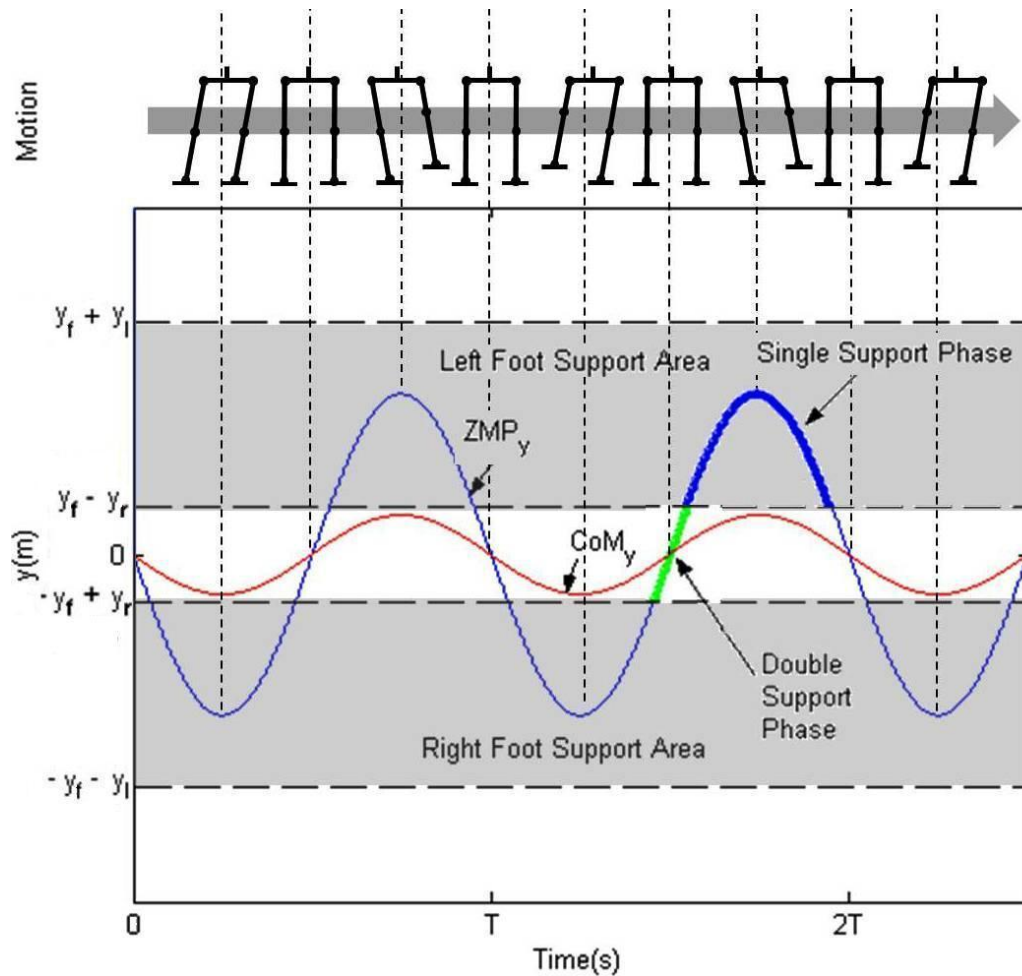


Figure 3.10: Single and double support phases

The time period of the support phases are used for the computation of the foot placement trajectories.

### 3.2.3 Foot Placement Trajectories

The offline generation of lateral walk-oscillation is formulated by computing the foot placement trajectories based on time instances of the single and double support phase (3.12). Assuming that the total time for foot lifting and landing is much less than the time period of the single support phase, the execution of the foot lift and landing in one oscillation cycle is

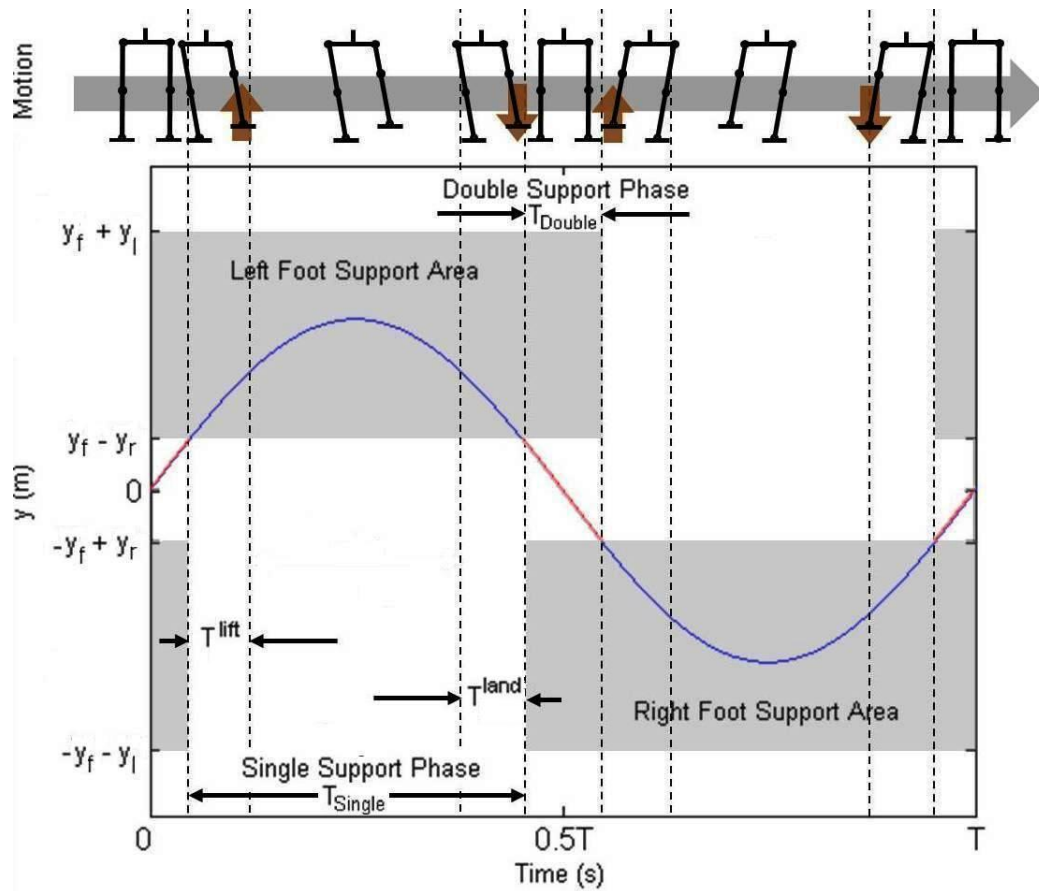


Figure 3.11: ZMP trajectory of walk-oscillations

given by:

$$T_r^{lift} = 0.5T + T_{double/2},$$

$$T_l^{lift} = T_{double/2},$$

$$T_r^{land} = T - T_{double/2} - t_f,$$

$$T_l^{land} = 0.5T - T_{double/2} - t_f,$$

(3.14)

where  $t_f$  is the time period of the foot lifting / landing motion and  $T$  is the period of one oscillation cycle. Foot placement trajectories for the lateral

walk-oscillations are as follows:

$$\begin{aligned}
y_{CoM} &= A \sin(\omega t), \\
X(t) &= 0, \\
X_l(t) &= 0, \\
Y_r(t) &= \begin{cases} (1 - \frac{C_f}{z_c})y_{CoM}, & \text{for } T_r^{lift} + t_f \leq t \leq T_r^{land} \\ \frac{Z_r(t)}{Z_c}y_{CoM}, & \text{for } T_r^{lift} < t < (T_r^{lift} + t_f) \\ & \text{and } T_r^{land} < t < (T_r^{land} + t_f) \\ y_{CoM}(t), & \text{otherwise} \end{cases} \\
Y_l(t) &= \begin{cases} (1 - \frac{C_f}{z_c})y_{CoM}, & \text{for } (T_l^{lift} + t_f) \leq t \leq T_l^{land} \\ \frac{Z_l(t)}{Z_c}y_{CoM}, & \text{for } T_l^{lift} < t < (T_l^{lift} + t_f) \\ & \text{and } T_l^{land} < t < (T_l^{land} + t_f) \\ y_{CoM}(t), & \text{otherwise} \end{cases} \\
Z_r(t) &= \begin{cases} z_c - C_f, & \text{for } T_r^{lift} + t_f \leq t \leq T_r^{land} \\ a_o + a_1(t - t_s)^2 + a_2(t - t_s)^3, & \text{for } T_r^{lift} < t < (T_r^{lift} + t_f) \\ & \text{and } T_r^{land} < t < (T_r^{land} + t_f) \\ \sqrt{d^2 - (Y_r(t))^2}, & \text{otherwise} \end{cases} \\
Z_l(t) &= \begin{cases} z_c - C_f, & \text{for } (T_l^{lift} + t_f) \leq t \leq T_l^{land} \\ a_o + a_1(t - t_s)^2 + a_2(t - t_s)^3, & \text{and } T_l^{land} < t < (T_l^{land} + t_f) \\ \sqrt{d^2 - (Y_r(t))^2}, & \text{otherwise} \\ \sqrt{d^2 - (Y_l(t))^2}, & \text{otherwise} \end{cases} \\
\text{Cubic Poly.} &= \begin{cases} a_o = Z_o, \\ a_1 = \frac{3}{t_f^2}(Z_f - Z_o), \\ a_2 = \frac{-2}{t_f^3}(Z_f - Z_o), \end{cases}
\end{aligned}
\tag{3.15}$$

where with respect to 1 oscillation cycle,

$d$  is the height of the hips from the ground in the standing posture,

$C_f$  is the amount of foot clearance required for the lifted foot,

$z_c$  is the height of the CoM,

$t_s$  is the starting time of the foot lift or landing motion,

$t_f$  is the time period of the foot lift or landing motion,

$Z_o$  is the initial foot position before foot lift or landing, and,

$Z_f$  is the final foot position for foot lift or landing.

Fig. 3.11 shows the graphical representation of the execution of the lateral walk-oscillation. Fig. 3.12 shows the foot placement trajectories for 4 oscillation cycles computed where lateral walk-oscillations are initiated after an oscillation cycle of lateral motion.

### 3.3 Simulations

The proposed gait generation approach is simulated in the MATLAB / Simulink and Autodesk Inventor Dynamic Simulation environment. A 3-Dimensional (3D) model of the physical humanoid REJr is simulated in the Autodesk Inventor Dynamic Simulation. The trajectories from the 3D model simulations are translated into a 2D biped model for the computation of the ZMP. The ZMP computations are based on an approximation-based approach proposed by [119]. The 2D model and computation of the ZMP are done in MATLAB / Simulink.

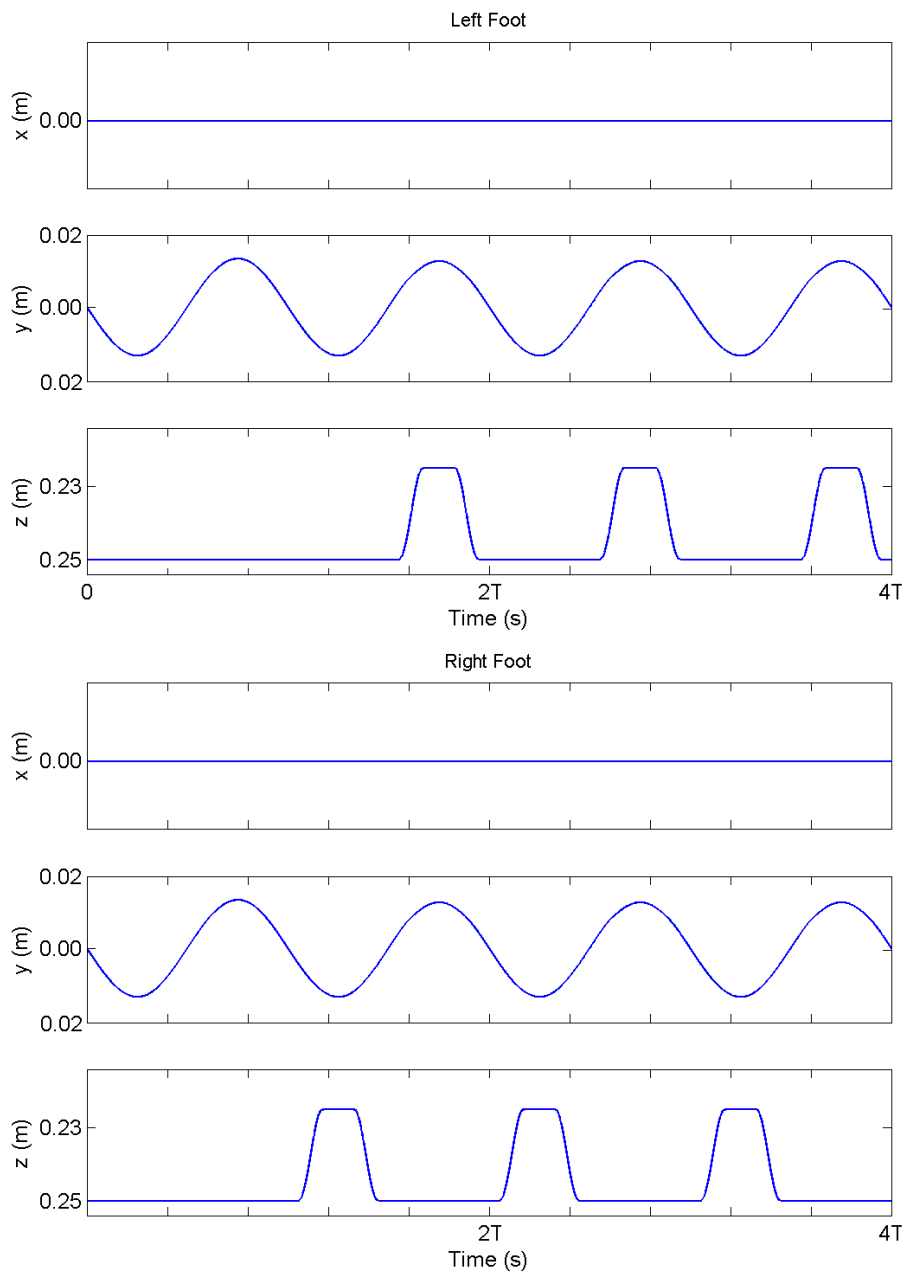


Figure 3.12: Foot placement trajectories generated offline for lateral walk-oscillation

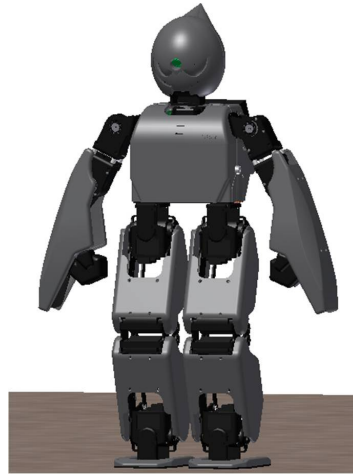


Figure 3.13: 3D model of the humanoid

### 3.3.1 Simulation Model and ZMP Computation

The 3D model of the humanoid robot (Fig. 3.13) is based on the mechanical design model (Chapter 2.2.1). Each component in the humanoid, including the mechanical parts, electrical components and aesthetic covers, are modelled to make the model as realistic as possible. The dimension, weight and material of each component model are constructed in accordance to the physical humanoid system.

The Autodesk Inventor Dynamic Simulation provided a realistic model for simulation. However, the computation of the ZMP of the 3D model is very complex and computationally expensive. To overcome the issues, a simplified 2D biped model (Fig. 3.14) is used for the computation of the ZMP. The 2D model uses concentrated masses to model the humanoid in the frontal plane. The trajectories from the 3D model simulations are applied to the 2D model. These trajectories are acquired by tracing the respective representative 3D component's model of the concentrated masses in the 2D model. The upper body of the humanoid including the head and



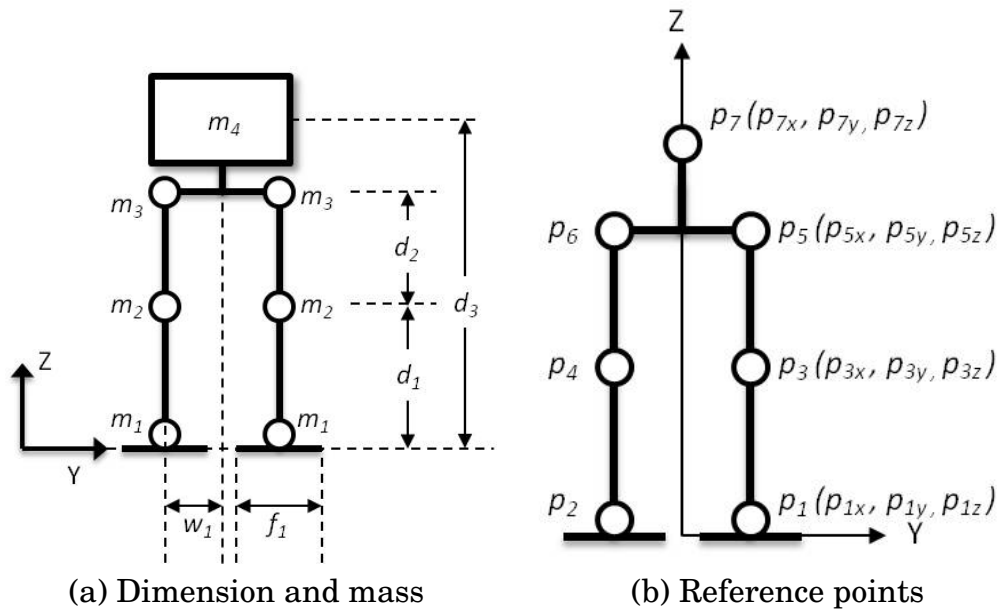


Figure 3.14: 2D model of the humanoid in the frontal plane

arms are represented by a single rigid body as there is no upper body motion. Table 3.1 shows the mass distribution of the 2D model.

Table 3.1: Dimensions and masses of 2D model

Parameter	Value
$m_1$ (kg)	0.248
$m_2$ (kg)	0.258
$m_3$ (kg)	0.381
$m_4$ (kg)	2.154
$d_1$ (m)	0.127
$d_2$ (m)	0.127
$d_3$ (m)	0.375
$w_1$ (m)	0.045
$f_1$ (m)	0.075

The computation of the ZMP is based on an approximation-based approach which does not require system dynamics [119]. Based on the 2D

model (Fig. 3.14), the CoM is defined as:

$$\begin{aligned} x_{CoM} &= \frac{\sum_i m_i p_{ix}}{\sum_i m_i}, \\ y_{CoM} &= \frac{\sum_i m_i p_{iy}}{\sum_i m_i}, \\ z_{CoM} &= \frac{\sum_i m_i p_{iz}}{\sum_i m_i}, \end{aligned} \quad (3.16)$$

where  $p_i$  is the reference point in the Cartesian coordinate,  $m_i$  is the concentrated mass at the reference point  $p_i$ . The ZMP expressed in terms of the CoM is given by (3.17) [18]:

$$\begin{aligned} x_{ZMP} &= x_{CoM} + \frac{\sum_i m_i p_{ix} \ddot{p}_{iz} - \sum_i m_i p_{iz} \ddot{p}_{ix}}{g \sum_i m_i} + \frac{\sum_i M_{iy}}{g \sum_i m_i}, \\ y_{ZMP} &= y_{CoM} + \frac{\sum_i m_i p_{iy} \ddot{p}_{iz} - \sum_i m_i p_{iz} \ddot{p}_{iy}}{g \sum_i m_i} + \frac{\sum_i M_{ix}}{g \sum_i m_i}, \end{aligned} \quad (3.17)$$

where  $M_{ix}$  and  $M_{iy}$  are the moments of the links about the  $x$  and  $y$  axes. The 2D biped model is represented by a massless link which implies that the inertia tensor of the links are zero and therefore the moments ( $M_{ix}$ ,  $M_{iy}$ ) are zero [10]. ZMP is computed as:

$$\begin{aligned} x_{ZMP} &= x_{CoM} + \frac{\sum_i m_i p_{ix} \ddot{p}_{iz} - \sum_i m_i p_{iz} \ddot{p}_{ix}}{g \sum_i m_i}, \\ y_{ZMP} &= y_{CoM} + \frac{\sum_i m_i p_{iy} \ddot{p}_{iz} - \sum_i m_i p_{iz} \ddot{p}_{iy}}{g \sum_i m_i}. \end{aligned} \quad (3.18)$$

### 3.3.2 Lateral Walk Oscillations

Simulations of the lateral walk oscillations are conducted on the 3D model using the offline gait generation approach. Pre-determined joint trajectories computed are applied to generate stable lateral motion followed by

Table 3.2: Parameters for simulation

Parameter	Value
LIPM CoM Mass, $m$ (kg)	3.8
LIPM CoM Height, $z_c$ (m)	0.25
Ankle Distance Apart (m)	0.090
Foot Width (Inner) (m)	0.035
Foot Width (Outer) (m)	0.040
Ground Contact Stiffness (N/mm)	$2 \times 10^3$
Ground Contact Damping (N s/mm)	$2 \times 10^2$
Number of Oscillation Cycles	30

Table 3.3: Sinusoidal trajectories applied for lateral motion

Sinusoidal Trajectory	A	B	C
Oscillating Frequency, $f$ (Hz)	1.0	2.0	4.0
Oscillating Frequency, $\omega$ (rad/s)	6.283	12.566	25.133
CoM Lateral Shift Amplitude, $A$ (rad)	0.0249	0.0100	0.0029
Reference Peak ZMP Amplitude, $p_{y(peak)}$ (m)	0.0501	0.0502	0.0496
Single Support Period, $T_{single}$ (s)	0.4358	0.2182	0.1088
Double Support Period, $T_{double}$ (s)	0.0642	0.0318	0.0162

walk-oscillations. Table 3.2 shows the parameters used for the simulation.

A desired peak ZMP amplitude is selected as a reference to generate stable lateral motion. Based on the mechanical specifications of the humanoid, the reference peak ZMP amplitude is selected as 0.050 m which is near to the middle of the foot support area. Three different sets of oscillating frequency are used for lateral motion simulation. The respective amount of lateral shift for each oscillating frequency is computed using (3.7) and are presented in Table 3.3.

The simulations of the 3D model produced stable lateral motion for all the trajectory sets (Fig. 3.15). The ZMP trajectories of the respective sinusoidal sets are presented in Fig. 3.16. From the trajectories, it is

Table 3.4: Average measured peak ZMP amplitudes

Sinusoidal Trajectory	A	B	C
Avg. Peak ZMP Amp. (m)	0.0442	0.0437	0.0458
Avg. Deviation of Peak ZMP Amp. (m)	0.0059	0.0063	0.0038
Avg. Peak ZMP Amp. of Left Foot (m)	0.0416	0.0422	0.0447
Avg. Peak ZMP Amp. of Right Foot (m)	0.0468	0.0451	0.0469

seen that the use of the sinusoidal reference pattern can result in stable lateral motion. The results also show the suitability of using the LIPM for ZMP computation to address the dynamic stability of a humanoid without incurring expensive computations.

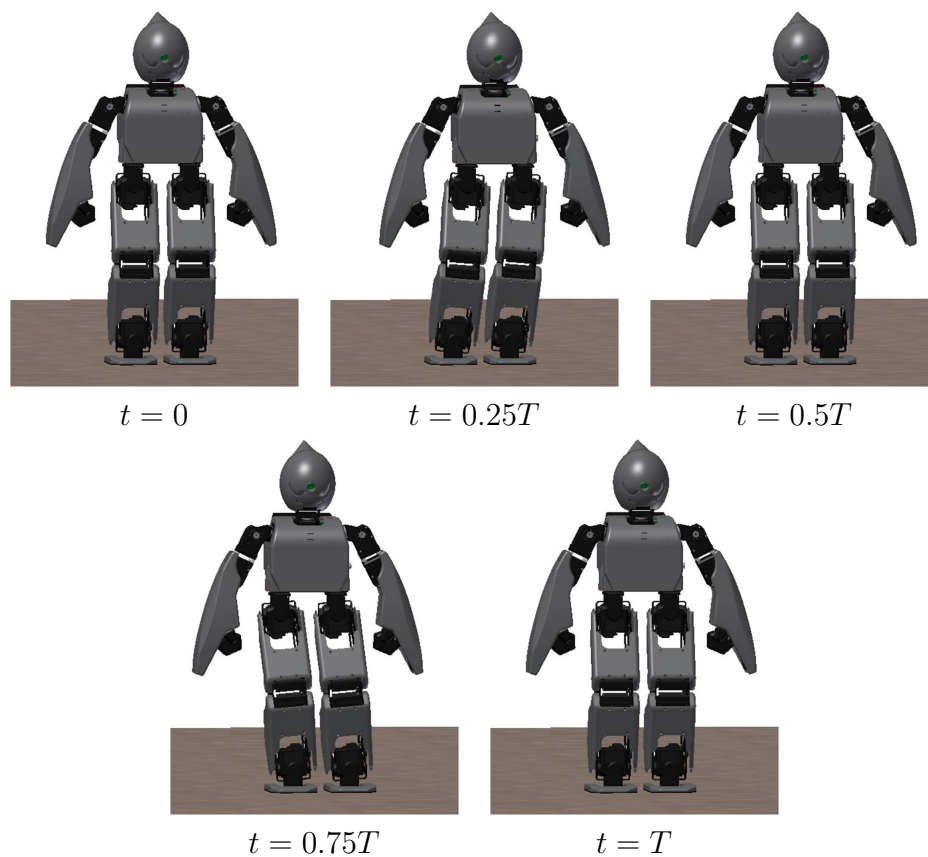
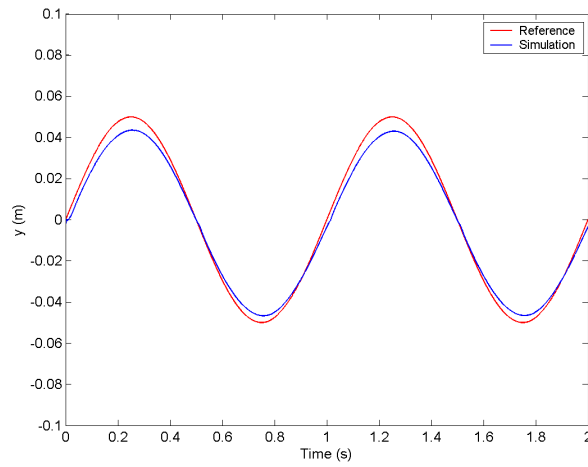
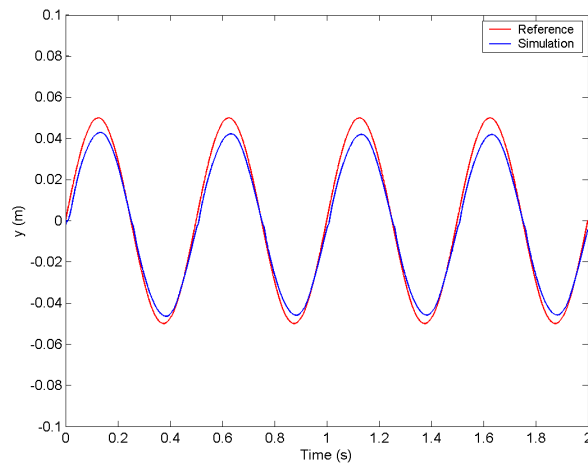


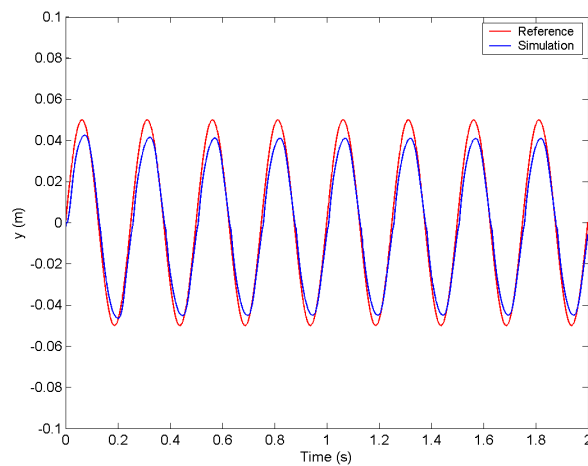
Figure 3.15: 3D humanoid model in stable lateral motion



Sinusoidal trajectory A:  $\omega = 6.283$  rad/s and  $A = 0.0965$  rad



Sinusoidal trajectory B:  $\omega = 12.566$  rad/s and  $A = 0.0382$  rad



Sinusoidal trajectory C:  $\omega = 25.133$  rad/s and  $A = 0.0112$  rad

Figure 3.16: ZMP trajectories of lateral motion

Table 3.5: Parameters for walk-oscillation simulation

Parameter	Value
Number of Oscillation Cycles	30
Oscillating Frequency, $f$ (Hz)	2.0
Oscillating Frequency, $\omega$ (rad/s)	12.566
CoM Lateral Shift Amplitude, $A$ (rad)	0.0100
Reference Peak ZMP Amplitude, $ p_{y(peak)} $ (m)	0.0502
Foot Clearance (m)	0.015
Time Period for Foot Lift and Landing Motion (s)	0.06
Foot Lift Instances Within 1 Cycle (s)	0.0159 , 0.2659
Foot Land Instances Within 1 Cycle (s)	0.2341 , 0.4841

Table 3.4 shows the average measured peak ZMP amplitudes and deviations from the simulations for 30 oscillation cycles. The average measured peak ZMP amplitudes are slightly lower than that of the reference. The deviations of the ZMP did not result in unstable lateral motions but are undesired as it compromises on generating optimal stability during single support phase. These deviations are likely to be attributed by modelling discrepancies as the computation of the applied trajectories are based on the LIPM which is a simplified dynamical model. The peak ZMP amplitudes of the left and right foot are not equal which indicates that the humanoid is not laterally balanced; the right is deemed to be heavier due to the higher ZMP amplitudes. The centre of gravity of the humanoid computed using the mechanical software indeed indicates that the robot is heavier on the right (CoM is 0.005 m shifted to the right).

The walk-oscillations are simulated based on the offline foot placement trajectories computed (Fig. 3.12). The foot lift and landing are executed based on the actuation of the knee joints with a foot clearance of 0.015 m. Table 3.5 shows the parameters used for the simulation of the walk-oscillations. Walk-oscillation is initiated after 1 oscillation cycle of lateral

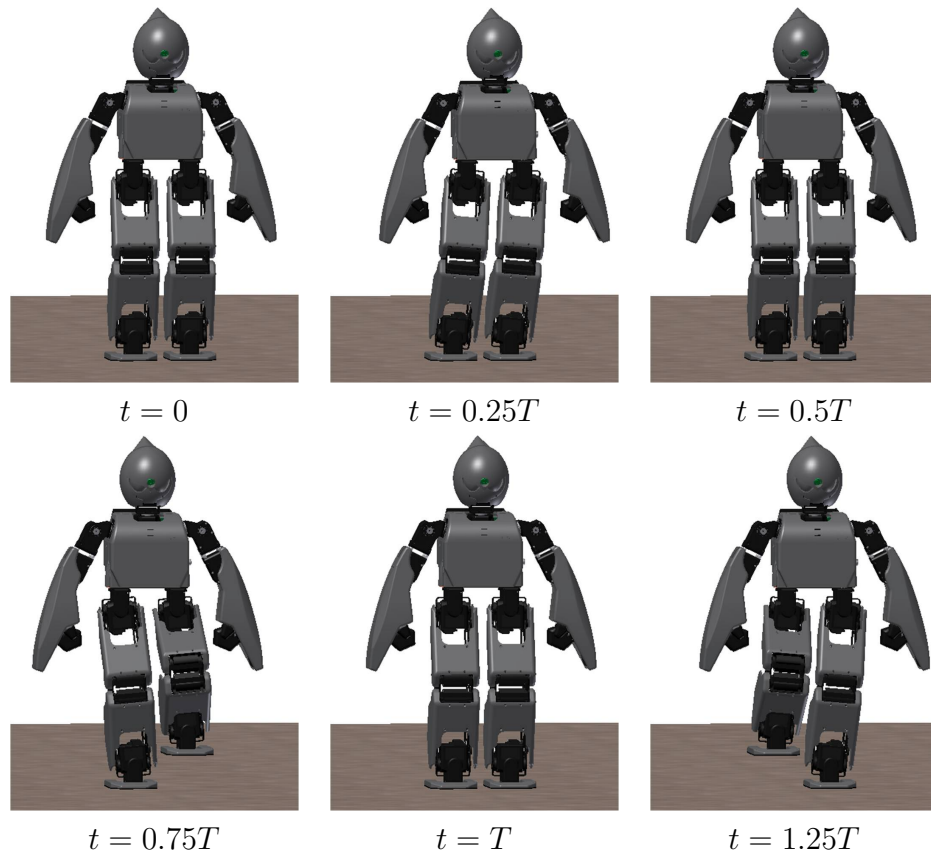
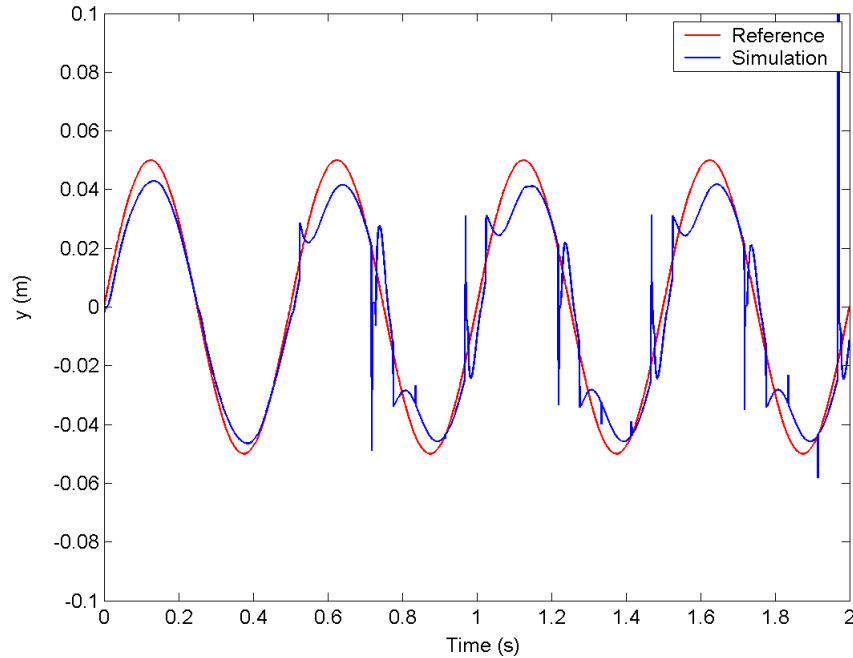


Figure 3.17: 3D humanoid model in stable walk-oscillation

motion.

Stable walk-oscillations are produced using the offline gait generation approach on the 3D model simulation (Fig. 3.17). The single support phase is successfully generated with the necessary foot lift and landing. The ZMP trajectory of the stable walk-oscillations produced is presented in Fig. 3.18. The ZMP trajectory of the walk-oscillation is similar to that generated by lateral motion. Spikes in ZMP calculations are observed at the foot lift and landing instances. These spikes are attributed by the resultant dynamical contact forces between the foot and walking surface.



*The systematic spikes in the trajectory are attributed to the contact dynamics between the foot and ground during lifting (small spikes) and landing of foot (larger spikes).*

Figure 3.18: ZMP trajectory of 4 walk-oscillation cycles

### 3.3.3 Influence of Walking Environment Disturbance

Disturbances can be attributed by the walking environment even flat terrain. In this simulation work, the limitations of the offline gait generation approach is studied by understanding the effects of disturbances that can be attributed by a typical flat terrain.

Typical flat surfaces suffer from local inclination of  $\pm 1 \sim 2$  degrees. The inclination of the walking surface can result in instability. Walk-oscillation simulations are conducted and repeated with incremental steps



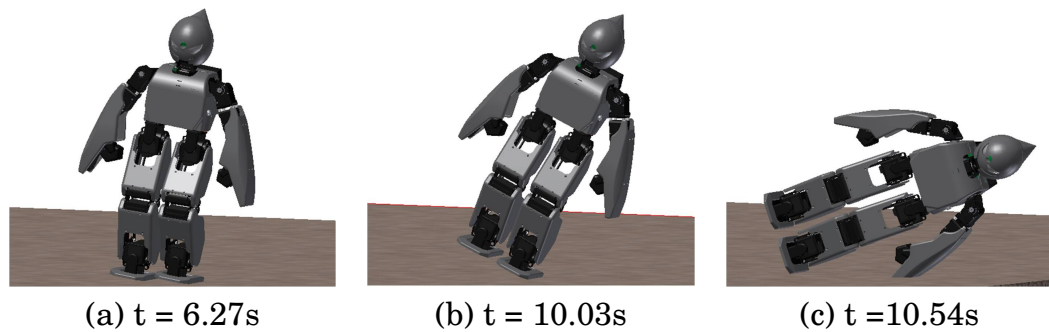
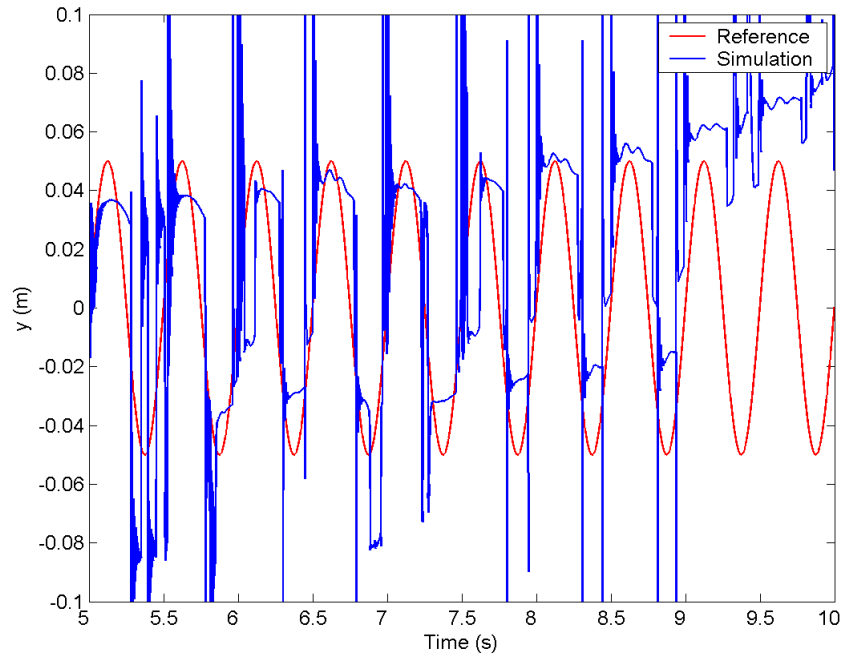


Figure 3.19: Disturbance effect of  $3^\circ$  floor inclination

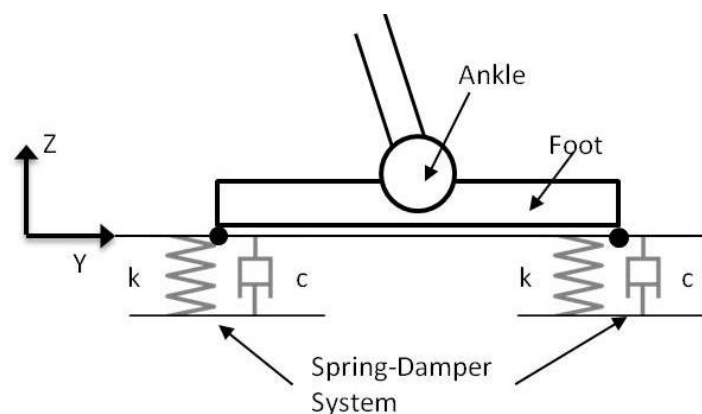
of 1 degree floor inclination in the frontal plane until the humanoid exhibits instability and falls over.

The simulation results show that the humanoid is able to sustain walk-oscillations for floor inclination of up to 3 degrees. Although the humanoid exhibited increasing instability behaviour for each simulation as the floor inclination increases, the humanoid did not overturn. When floor inclination of  $3^\circ$  is applied, the humanoid fell over after 10.5 seconds. Fig. 3.20 shows the ZMP trajectory of the walk-oscillations on a floor inclination of  $3^\circ$  before falling. The large oscillations in the ZMP trajectory shows the instability exhibited by the humanoid on the inclined surface. The simulations shows that the offline approach is only able to produce stable walk-oscillations on floor inclination of less than  $3^\circ$ .



*The ZMP fall outside the support polygon during walk-oscillations when subjected to floor inclination resulting in unstable gait.*

Figure 3.20: ZMP trajectory with 3° floor inclination



*$k$  and  $c$  are the stiffness and damping coefficient of the spring-damper system model of the contact dynamics between the floor and the foot.*

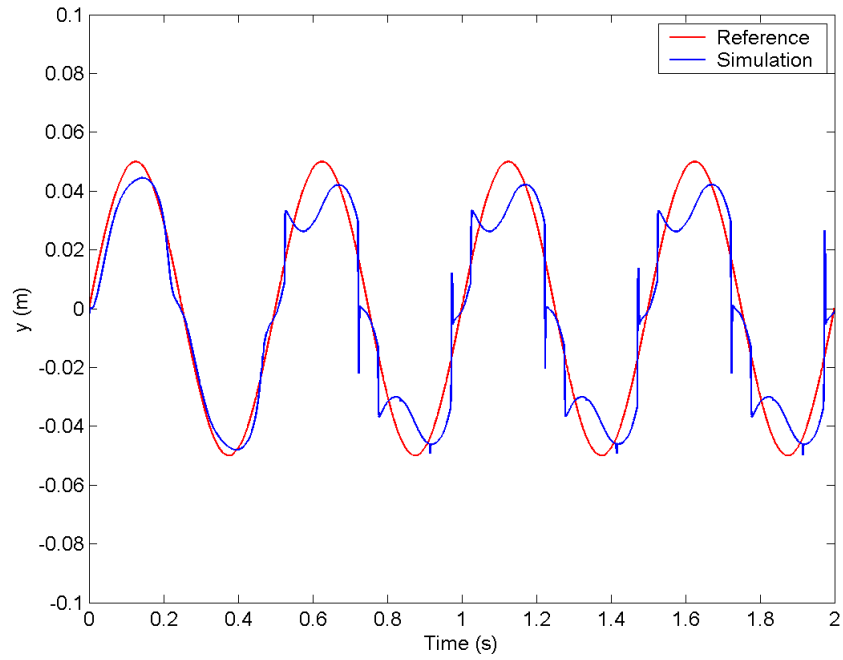
Figure 3.21: Contact dynamics of the foot and ground

The contact dynamics, often described and modelled as mass spring-damper system (Fig. 3.21), has an influence on the dynamics of the humanoid. In the case of biped locomotion, contact dynamics are attributed by the surface contact between the foot and ground. The surface material properties of the foot and ground determine the contact dynamics exhibited. In this simulation, the effects of stiffness and damping are studied.

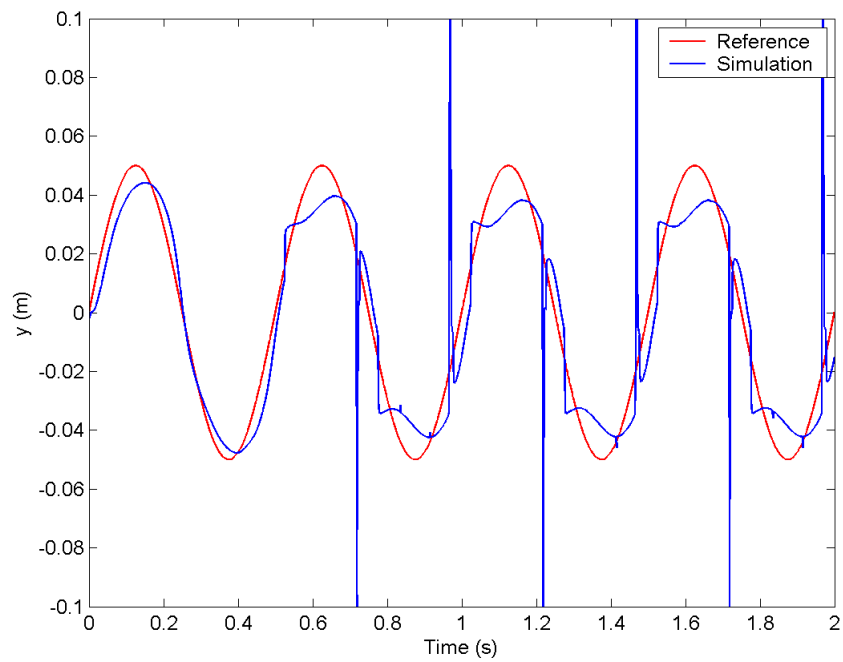
Various walking surface contact dynamics are applied for the simulations of the walk-oscillations. Results show that the contact dynamics can affect the ZMP trajectory in one way or another, and in some cases even cause instability. Fig. 3.22 shows the results in which ZMP fluctuations are introduced due to different contact dynamic stiffness and damping coefficients. Control paradigms incorporating contact dynamics can be utilized for improved control. The stiffness and damping coefficients of walking surface are often hard to obtain or estimate, and there must be pre-information on the walking surface. As such, the offline approach is only able to generate stable walk-oscillations on certain walking surfaces. Surface material of the foot sole in contact with the walking surface must also be considered.

### **3.4 Experiments**

The offline gait generation of walk-oscillations is applied on the REJr humanoid robot on a carpeted flat terrain with measured inclination of approximately less than  $2^\circ$ . Force sensors mounted in the humanoid foot are used to measure the ZMP. The walk-oscillation parameters applied to REJr are the same as in the simulation (Table 3.5).



(a) Stiffness =  $2 \times 10^5$  N/mm  
Damping =  $2 \times 10^2$  N s/mm



(b) Stiffness =  $2 \times 10^3$  N/mm  
Damping =  $2 \times 10$  N s/mm

Figure 3.22: ZMP trajectories with different contact dynamics

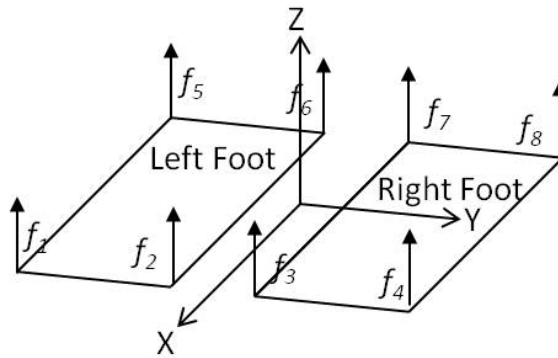


Figure 3.23: Reading of the force sensors

### 3.4.1 Center of Pressure (CoP) Measurement for Experimental Result Validation

The humanoid has force sensors mounted in the foot (Chapter 2.3.4). The force sensors are used for sensing ground reaction forces to measure the Center of Pressure (CoP) (Fig. 3.23). Without loss of generality, the CoP measurement is based on the following assumptions:

1. The motion only occurs in the frontal plane, motions in the frontal and sagittal plane are weakly coupled [120] hence the motions in the two planes are considered separated.
2. The position of the foot is stationary and the foot does not slip.
3. The ankle is located at the foot with zero height.
4. The feet of the humanoid are laterally symmetrical.
5. The contact between the foot and the ground is flat.

Measurement of the CoP is divided into the single support phase (Fig. 3.24(a)) and the double support phase (Fig. 3.24(b)).

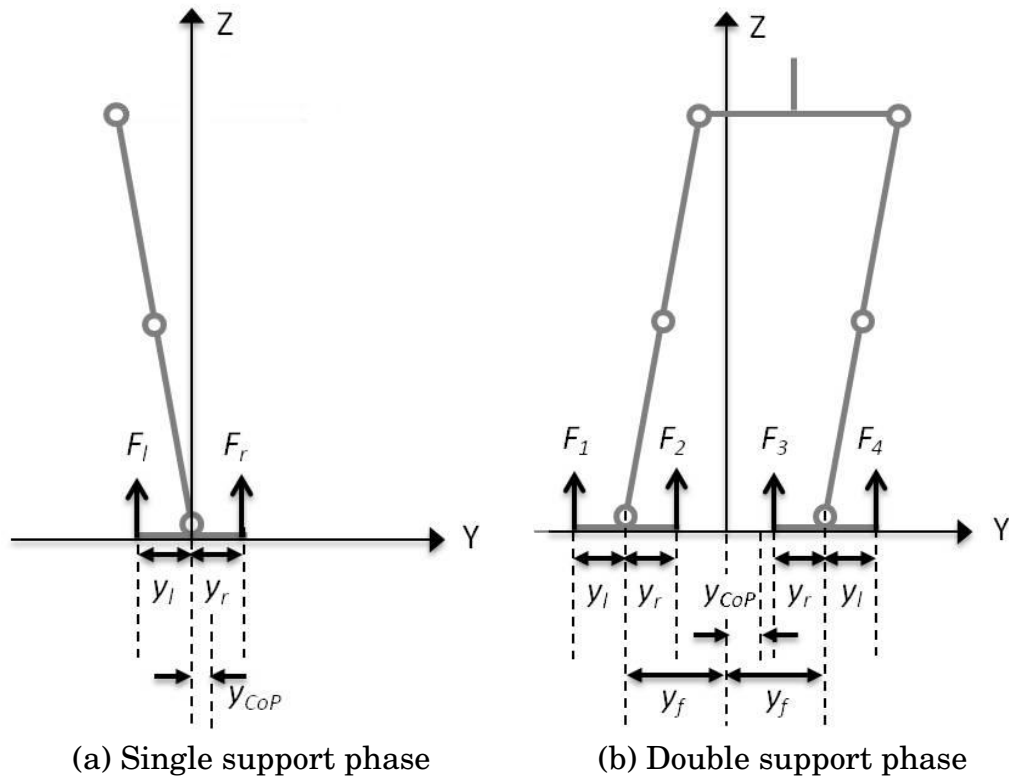


Figure 3.24: Center of Pressure (CoP) measurement

The CoP is the point where the ground reaction forces are assumed to act only at the single point. The resultant moment generated by the ground reaction forces about the CoP is zero. By equating the moment generated by the ground reaction forces ( $F_l$  and  $F_r$ ) to be at equilibrium, the CoP in the single support phase can be computed as:

$$y_{CoP} = \frac{F_l y_l - F_r y_r}{F_l + F_r}, \quad (3.19)$$

where  $F_l$  and  $F_r$  are the measured vertical ground reaction forces;  $F_l = f_1 + f_5$  and  $F_r = f_2 + f_6$  when the left foot is in contact with the ground;  $F_l = f_4 + f_8$  and  $F_r = f_3 + f_7$  when the right foot is in contact with the ground.  $y_r$  and  $y_l$  are the distance of the respective left and right ground reaction forces from the ankle in the frontal plane.  $y_{CoP}$  is the distance of the CoP from the ankle.

For the double support phase, at equilibrium the moments generated by the ground reaction forces ( $F_1$ ,  $F_2$ ,  $F_3$  and  $F_4$ ) are equated to compute the CoP as:

$$\begin{aligned}
 F_{total} &= F_1 + F_2 + F_3 + F_4, \\
 y_{CoP} &= -\frac{F_1}{F_{total}}(y_f + y_l) - \frac{F_2}{F_{total}}(y_f - y_r) \\
 &\quad + \frac{F_3}{F_{total}}(y_f - y_r) + \frac{F_4}{F_{total}}(y_f + y_l),
 \end{aligned}
 \tag{3.20}$$

where  $F_1 = f_1 + f_5$ ,  $F_2 = f_2 + f_6$ ,  $F_3 = f_3 + f_7$  and  $F_4 = f_4 + f_8$  are the vertical ground reaction forces,  $y_r$  and  $y_l$  are the distances of the respective left and right ground reaction forces from the ankle in the frontal plane.  $y_f$  is the distance from the ankle to the center between the foot assuming the foot are equidistant from the CoM.  $y_{CoP}$  is the distance of the CoP from the CoM. The CoP coincides with the ZMP when the gait is statically and dynamically stable [18, 19, 35]. The CoP measured is used to infer the ZMP for experimentation ( $y_{ZMP} \equiv y_{CoP}$ ).

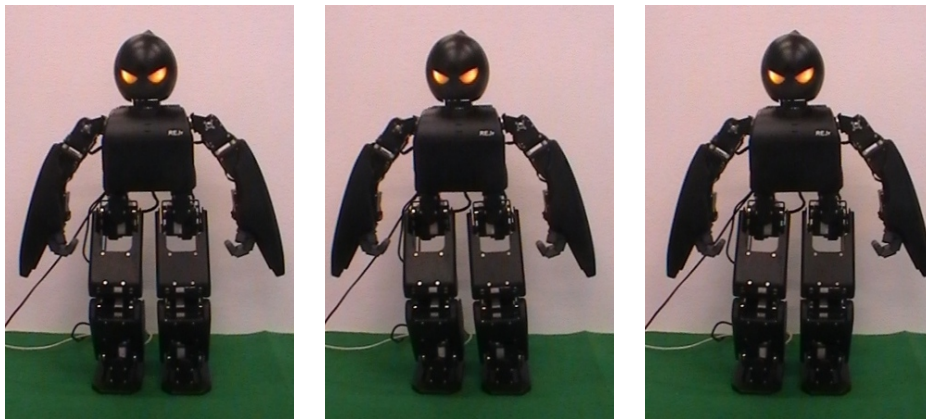


Figure 3.25: Snapshots of REJr in stable lateral motion

### 3.4.2 Implementation of Lateral Walk-Oscillation

An initial experiment to generate lateral motion is conducted to manually tune the amount of lateral shift ( $A$ ) required to achieve the desired ZMP peak amplitude (Fig. 3.25). The amount of lateral shift before the trajectory tuning is 0.0100 m and after manual tuning is 0.0117 m. Fig. 3.26 shows the measured ZMP trajectories before and after tuning. The tuned ZMP trajectory is applied to the humanoid for generating the walk-oscillations.

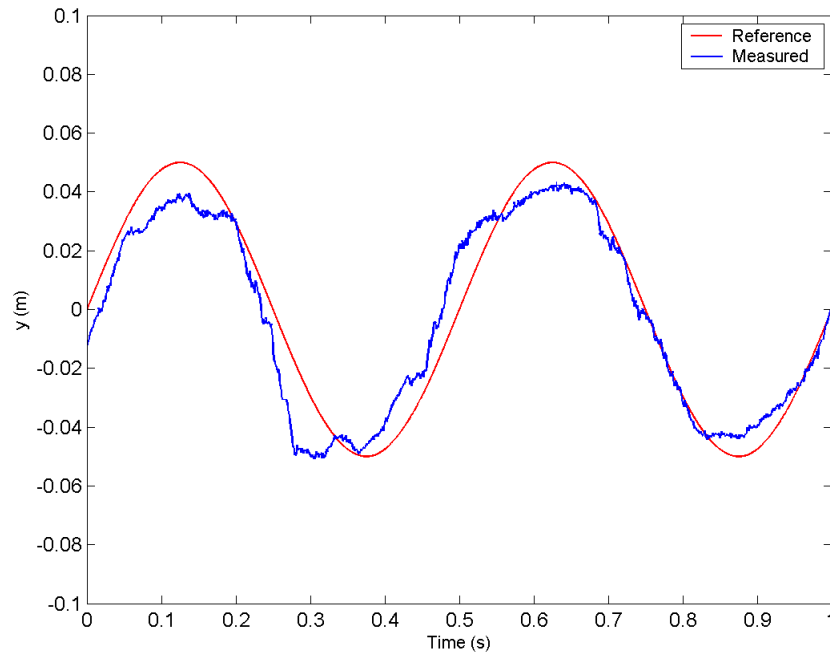
Based on the tuned lateral motion, the humanoid REJr executes foot lift and landing on pre-determined time instances to produce walk-oscillations. Experimental result shows that the humanoid is able to oscillate in a stable manner with single and double support phases (Fig. 3.27). Recorded measurement of the ZMP during stable walk-oscillations are shown in Fig. 3.27. In comparison to the ZMP trajectory produced during lateral motion, higher magnitude of ZMP fluctuations are observed in the single support phases generated. The ZMP generally deviates from the reference trajectory but remains within the support polygon most of the time. Instances of the ZMP falling outside the support polygon are observed but did not result in instability. A likely explanation is that the nature of the oscillating gait tend to tilt inwards during unstable instances. and hence the tendency to sustain the oscillations. The average peak amplitudes of the ZMP measured is slightly higher in the right foot indicating that the humanoid is heavier on the right. This coincides with the simulation results as the humanoid hardware is unbalanced. The experiment shows that the use of sinusoidal trajectories to produce stable



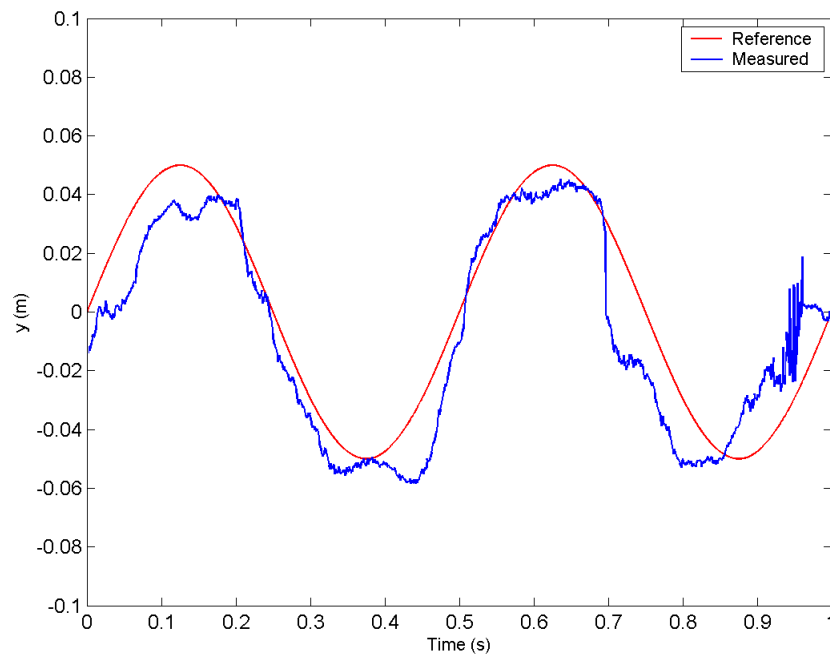
walk-oscillations offline in practice is a viable approach.

### **3.5 Conclusion**

An offline gait generation approach for lateral walk-oscillation using sinusoidal pattern is discussed and implemented in both simulation and hardware. The approach is computationally inexpensive and simple. Using the LIPM, the amount of required lateral shift to generate the desired ZMP trajectory is estimated. The approach is successfully tested and implemented on the humanoid robot, REJr to produce stable lateral walk-oscillations on a carpeted surface. The offline approach is sensitive to disturbances and can only produce stable lateral walk-oscillation under certain walking environment. Work to improve the robustness of the walk-oscillations is presented in the following chapter.



(a) Before tuning,  $A = 0.0100m$



(b) After manual tuning,  $A = 0.0107m$

*Manual adjustment of the amount of lateral shift,  $A$ , to balance the ZMP amplitude due to unsymmetrical mass distribution of the humanoid robot.*

Figure 3.26: ZMP measurement of lateral motion

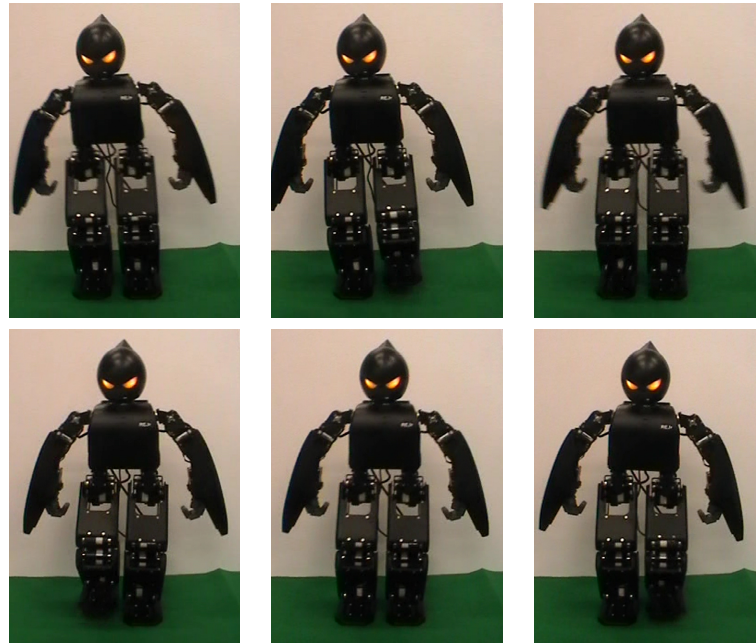
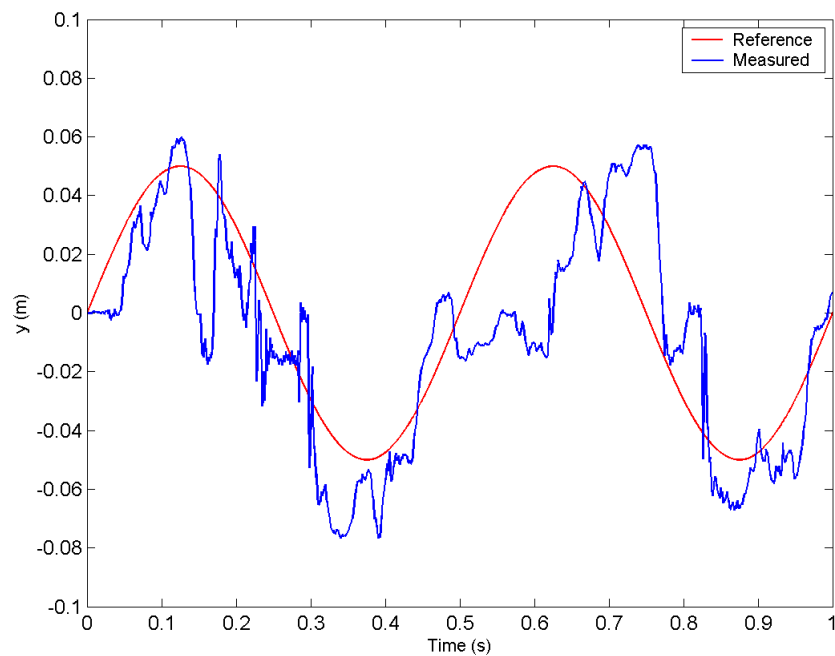


Figure 3.27: Snapshots of REJr in stable walk-oscillation



*ZMP fluctuates and deviates from reference but remains within the support polygon most of the time. Instances of ZMP falling outside the support polygon did not result in instability.*

Figure 3.28: ZMP measurement of lateral walk-oscillations

## **Chapter 4**

# **Sustainable Lateral Walk-Oscillation**

The offline approach of gait generation is viable to produce stable dynamic walking. However, the approach is highly sensitive to walking conditions where the humanoid can be destabilized easily. To overcome the stability issues and to have robust gaits, researchers have utilized online gait generation approaches. These approaches are roughly classified into offline gait generation with online feedback compensation [28–31, 71–74], and online gait generation with online feedback control [12, 27, 75–77]. In offline gait generation with online feedback compensation approach, walking gaits are designed offline with online stabilization control. Reference trajectories used for the joints are constantly modified online through feedback compensation techniques. In online gait generation with online feedback control, also known as real-time gait generation, simpler dynamical models are often used to reduce computation time and complexity. The approach generates the gaits based on the current system dynamics using sensory feedback.

One of most popular methods for online feedback compensation is using ZMP compensation. Joint torques and trajectories are modified in real-time to keep the ZMP within the support polygon in response to disturbances. ZMP compensation is realized by ① manipulation of the prescribed ZMP [2, 15, 23, 27], ② whole-body-motion control [7, 26] and ③ specific joints control [73, 75, 121]. In the manipulation of the ZMP, the prescribed ZMP is modified by changing the walking parameters such as speed and step length. Whole-body-motion control compensation requires precise control of the joint motion of the robot. The ZMP compensation using specific joints control makes modifications to particular joint trajectories only to keep the ZMP within the support polygon.

The gait generation method described in the Chapter 3 showed the suitability of sinusoidal reference trajectories for producing offline stable lateral walk-oscillations. The offline gait generation approach is viable but to a limited extent. Uncertainties and disturbances inherently present in physical system can easily destabilize the humanoid resulting in unsustainable walk-oscillations even on flat walking surface.

A gait generation approach to produce sustaining lateral walk-oscillation online is presented in this chapter. The approach adopts the offline gait generation with online feedback compensation method. The offline gait generation is based on the use of sinusoidal trajectories highlighted in Chapter 3 . Feedback compensation is achieved based on ZMP tracking and compensation techniques to improve the robustness of the walk-oscillations. The gait generation approach is realized by a lateral shift amplitude controller, a real-time ZMP compensator and a simple online phase detector (Fig. 4.1). The lateral shift amplitude controller and ZMP

compensator form a two stage compensation system. The lateral shift amplitude controller minimizes the error in the ZMP peak amplitude after every oscillation cycle whereas the ZMP compensator minimizes the ZMP deviations within the oscillation cycle. The phase generator executes the foot lift and landing based on the measured ZMP. Simulation and experiments are conducted to verify the approach.

The lateral shift amplitude controller is described in Section 4.1. Section 4.2 presents the real-time ZMP compensator design whereas section 4.3 highlights the functions of the online phase generator. In section 4.4, simulation results of the online approach are presented and discussed. Section 4.5 is the implementation of the gait generation approach on the humanoid REJr. Section 4.6 concludes the chapter.

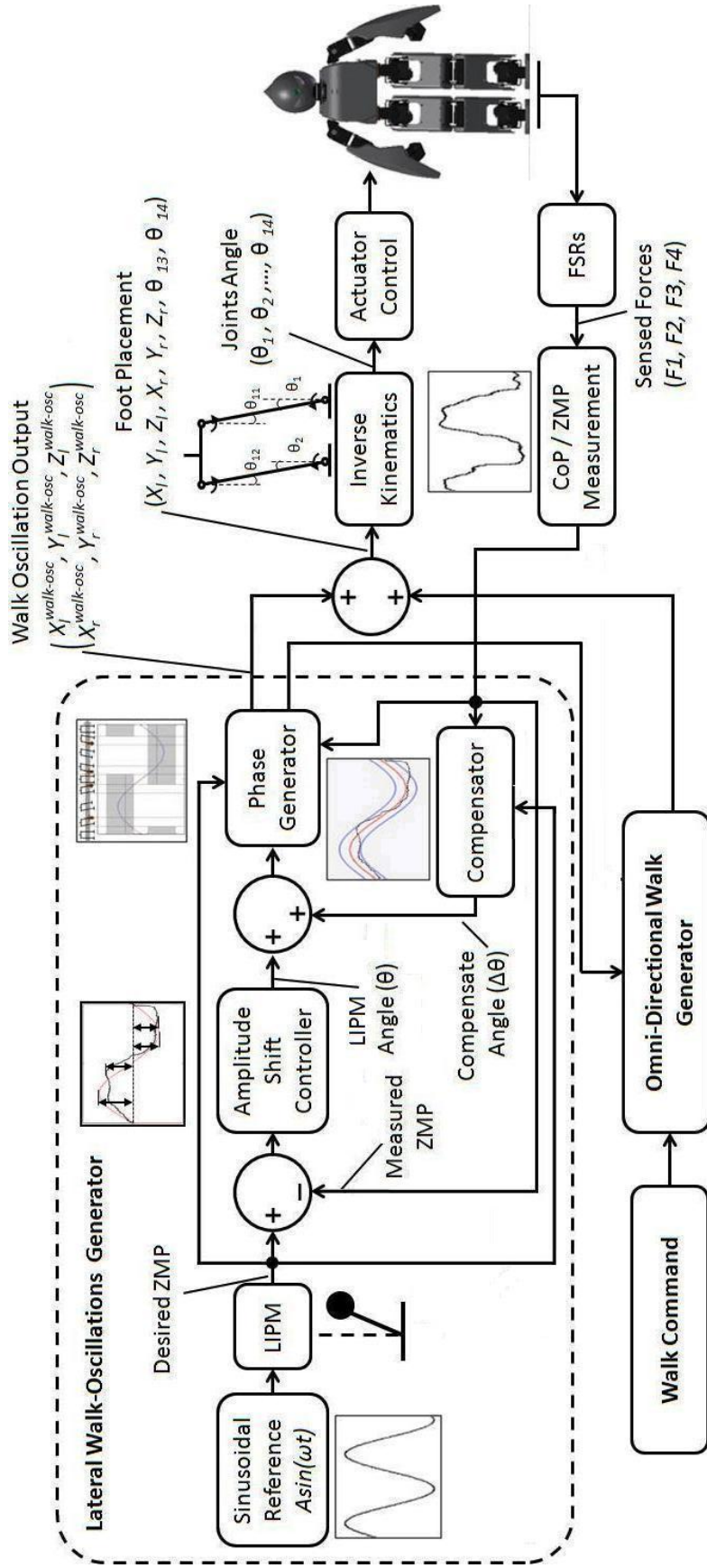


Figure 4.1: Online lateral walk-oscillation gait generation

## 4.1 Lateral Shift Amplitude Controller

A lateral shift amplitude controller is implemented by formulating the amount of lateral shift as a control problem. The lateral shift amplitude controller measures the difference in the peak ZMP amplitudes between successive oscillation cycle. The error in peak ZMP measurement is used to correct the amount of lateral shift.

### 4.1.1 Adjustment of Shift Amplitude

A Proportional-Integrator (PI) controller is implemented to adjust the amplitude of the sinusoidal trajectories during walk-oscillations. The lateral shift control is divided into the left and right foot and defined as:

$$\begin{aligned}
 e_{ZMP(left)}(k) &= y_{ZMP(left)}^{desired(peak)}(k) - y_{ZMP(left)}^{measured(peak)}(k), \\
 e_{ZMP(right)}(k) &= y_{ZMP(right)}^{desired(peak)}(k) - y_{ZMP(right)}^{measured(peak)}(k), \\
 A_{left}(k+1) &= A + k_p e_{ZMP(left)}(k) + k_i \int e_{ZMP(left)}(k) dk, \\
 A_{right}(k+1) &= A + k_p e_{ZMP(right)}(k) + k_i \int e_{ZMP(right)}(k) dk, \\
 \hat{y}_{CoM}(t) &= \begin{cases} A_{left}(k+1) \sin(\omega t), & \text{for } 0 \leq t < 0.5T \\ A_{right}(k+1) \sin(\omega t), & \text{for } 0.5T \leq t < T \end{cases}
 \end{aligned} \tag{4.1}$$

where  $e_{ZMP(left)}(k)$  and  $e_{ZMP(right)}(k)$  are the error for the left and right foot respectively between the peak ZMP amplitudes of the desired and measured during  $k^{th}$  oscillation cycle (Fig. 4.2).  $A$  is the computed reference lateral shift.  $A_{left}(k+1)$  and  $A_{right}(k+1)$  are the lateral shift for the following oscillation cycle.  $k_p$  and  $k_i$  are the proportional and integral gains for the controller.  $\hat{y}_{CoM}$  is the amount of lateral CoM shift.



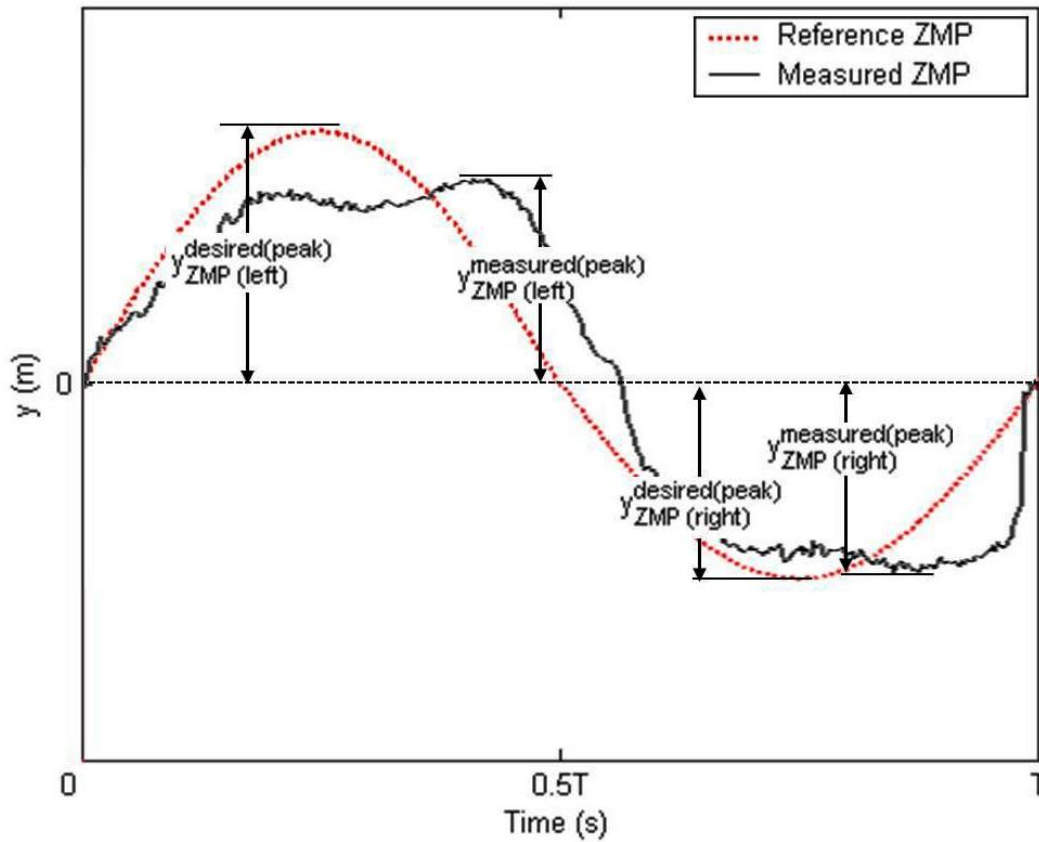
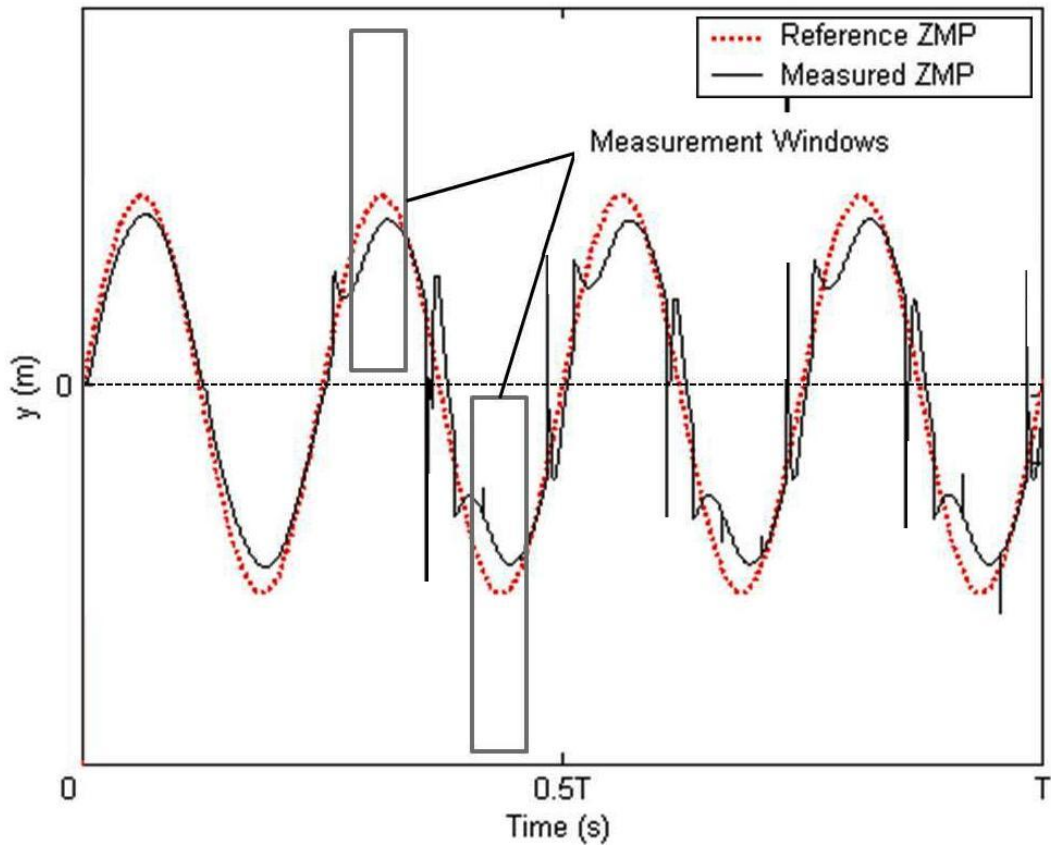


Figure 4.2: ZMP trajectories during  $k^{th}$  oscillation cycle

### 4.1.2 Peak Amplitude Measurement Window

Impulsive large deviations of the ZMP can occur during foot landing due to contact dynamics. As such, there is a tendency for the controller to register the deviations as the maximum ZMP peak of the walk cycle resulting in erroneous corrections for the following cycle. To overcome, a measurement window for the lateral shift controller is implemented to ensure that the ZMP peak measured during landing are not registered (Fig. 4.3).



*The measurement window starts after the foot lift and stops before the foot landing.*

Figure 4.3: Measurement window for shift amplitude controller

## 4.2 Real-Time Zero Moment Point Compensator

A real-time ZMP compensator is implemented based on the compensation technique proposed in [73]. The compensator functions by keeping the measured ZMP within the desired trajectory. The compensator is designed based on the following assumptions:

1. The motion only occurs in the frontal plane.

2. The position of the foot is stationary and the foot does not slip.
3. The ankle is located at the foot with zero height.
4. The foot of the humanoid are laterally symmetrical.
5. The contact between the foot and the ground is flat.
6. The effects of the Coriolis and centrifugal forces are neglected. The velocities of the compensating link does not change, the compensation torque only causes changes in acceleration of the link.
7. The ZMP fluctuation varies gradually and the actuators provide sufficient torque for compensation.

The compensator system determines the ZMP error between the desired and measured. Angular compensations are generated and used to change the CoM trajectory.

#### **4.2.1 Stability Zone for Compensation**

The readings from the force sensors are noisy in nature which leads to the fluctuations of the measured ZMP. A stability zone is demarcated along the desired ZMP trajectory to handle the fluctuations. The stability zone is defined by a threshold such that when the deviation of the measured ZMP from the desired is less than the threshold, it is assumed that there are no disturbances acting on humanoid (Fig. 4.4). The threshold is determined based on the approach proposed in [122]. Using the offline approach, the ZMP readings of stable walk-oscillations are recorded. Readings of ZMP are plotted to determine the maximum amount of ZMP deviations from reference (Fig. 4.5). The stability threshold is determined

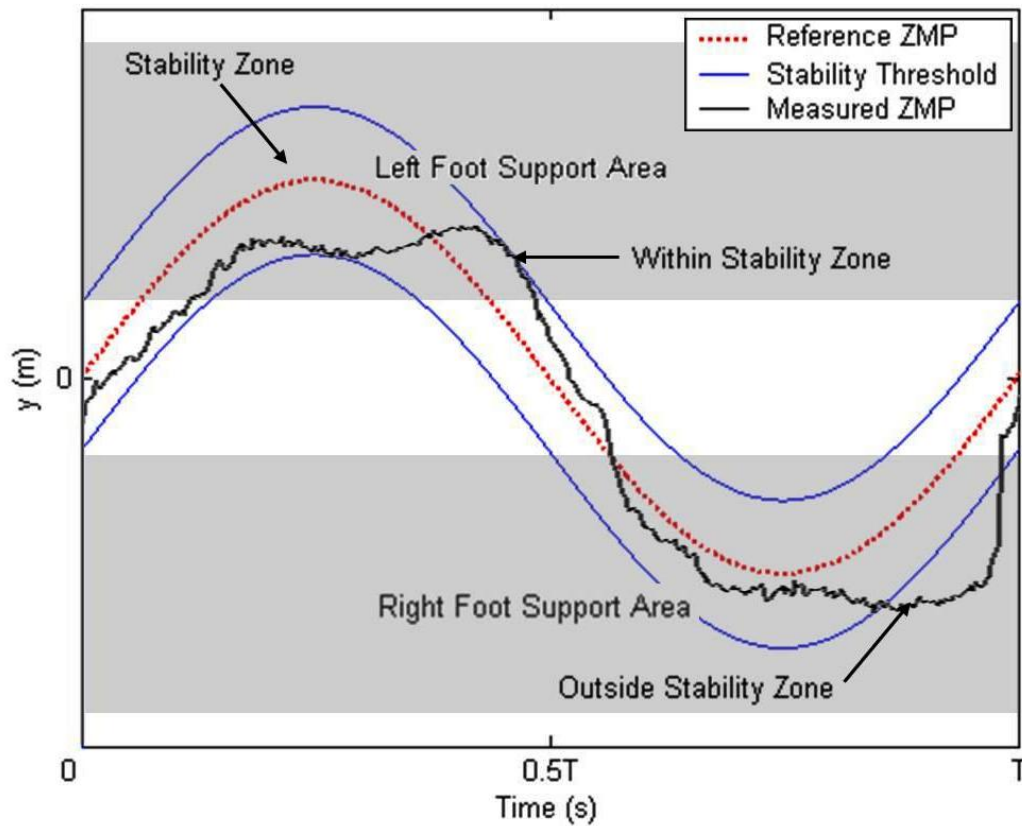


Figure 4.4: Stability zone

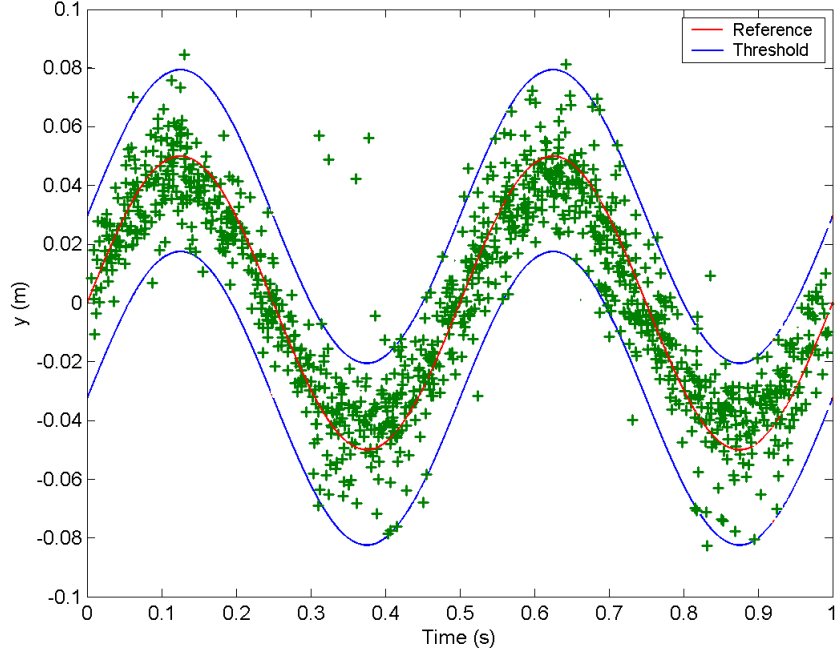
from the maximum deviation.

## 4.2.2 Compensator Design

The moment about the ZMP at a particular time instance without disturbances in the single support phase is given by:

$$y_{CoP} = \frac{F_l y_l - F_r y_r}{F_l + F_r}, \quad (4.2)$$

where  $F_l$  and  $F_r$  are the measured vertical ground reaction forces (Fig. 4.6).  $y_r$  and  $y_l$  are the distances of the respective left and right ground reaction forces from the ankle in the frontal plane.  $y_{CoP}$  is the distance of the CoP from the ankle.



*ZMPs measured during stable lateral walk-oscillations are plotted to determine the threshold of the stability zone.*

Figure 4.5: Stability zone measurement experiment

Consider that the humanoid is subjected to disturbances after a time interval, the moment about the measured ZMP is given by:

$$\begin{aligned}
 M_{zmp}(t + \Delta t) = & - (F_l + \Delta F_l)(y_l - y_{ZMP}) \\
 & - (F_r + \Delta F_r)(y_r + y_{ZMP})
 \end{aligned} \tag{4.3}$$

where  $\Delta F_l$  and  $\Delta F_r$  are the changing force sensor measurement after  $\Delta t$  time interval. The ZMP is deviated by:

$$\Delta y_{ZMP} = \frac{M_{zmp}(t + \Delta t)}{F_l + \Delta F_l + F_r + \Delta F_r}. \tag{4.4}$$

The compensator only acts when:

$$|y_{ZMP} + \Delta y_{ZMP} - y_{ZMP}^{desired}| > y_{ZMP}^{threshold}, \tag{4.5}$$

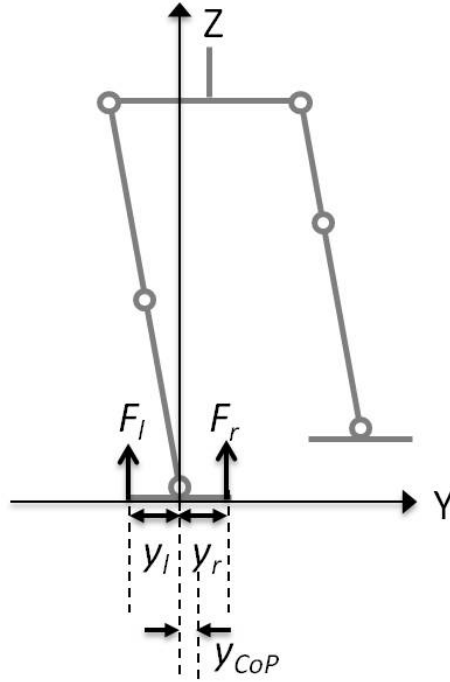
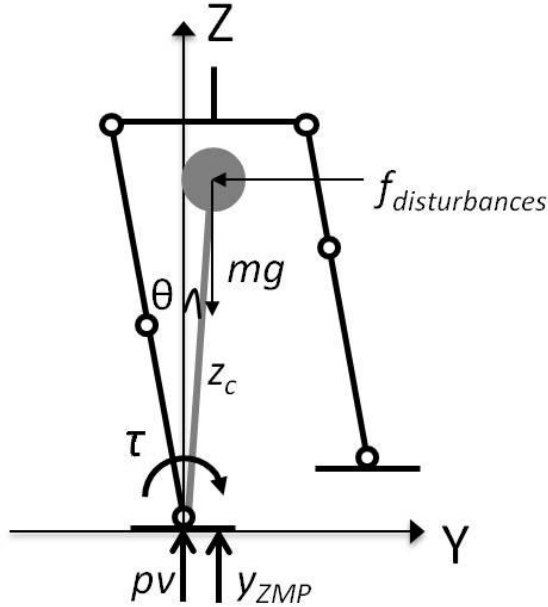


Figure 4.6: CoP measurement in single support phase

where  $y_{ZMP}^{threshold}$  is the stability threshold and  $y_{ZMP}^{desired}$  is the desired ZMP trajectory.

The humanoid in the single support phase is represented by an inverted pendulum (Fig. 4.7). The representation is equivalent to a two-link planar manipulator with joints at  $pv$  and  $y_{ZMP}$ . The length of the links are  $z_c$  and  $y_{ZMP}$ , assuming that the ankle is located at the foot with zero height. Using the Lagrangian formulation, the dynamics of the humanoid about the joints  $pv$  and  $y_{ZMP}$  subjected to disturbances are as:

$$\begin{aligned} \tau &= J\ddot{\theta} + mgz_c \sin(\theta) + f_{disturbances} z_c \cos(\theta), \\ M_{zmp}(t + \Delta t) &= (J - mz_c y_{ZMP} \sin(\theta))\ddot{\theta} + mgz_c \cos(\theta) + mgy_{ZMP}, \end{aligned} \tag{4.6}$$



$\theta$  is the angle of the link mass from the upright position,  $m$  is the mass,  $z_c$  is the length of the link,  $\tau$  is the torque acting on the system at the ankle, and,  $g$  is acceleration due to gravity.  $f_{disturbances}$  is the disturbance acting on the link mass.

Figure 4.7: Inverted pendulum representation in single support phase

where  $J$  is the moment of inertia about the point  $pv$  in the  $x$ -axis direction;  $J = mz_c^2$ , where  $m$  is the mass of the CoM. Assuming that the compensation torque is applied so that the moment about  $y_{ZMP}$  is zero. The dynamics of the humanoid with the compensation torque is given by:

$$\begin{aligned}\tau + \Delta\tau &= J(\ddot{\theta} + \Delta\ddot{\theta}) + mgz_c \sin(\theta) + f_{disturbances}z_c \cos(\theta), \\ 0 &= (J - mz_c y_{ZMP} \sin(\theta))(\ddot{\theta} + \Delta\ddot{\theta}) + mgz_c \cos(\theta) + mgy_{ZMP}.\end{aligned}\tag{4.7}$$

From (4.6) and (4.7),

$$\begin{aligned}
J &= m z_c^2, \\
\eta &= \frac{J}{(\Delta t)^2}, \\
\Delta \tau &= J \Delta \ddot{\theta} = J \frac{\Delta \theta}{(\Delta t)^2} = \eta \Delta \theta, \\
0 &= M_{zmp}(t + \Delta t) + (J - m z_c y_{ZMP} \sin(\theta)) \Delta \ddot{\theta}, \\
M_{zmp}(t + \Delta t) &= - (J - m z_c y_{ZMP} \sin(\theta)) \frac{\Delta \tau}{J}, \\
\Delta \tau &= - \frac{M_{zmp}(t + \Delta t)}{1 - \frac{m z_c y_{ZMP} \sin(\theta)}{J}}, \\
&= - \frac{M_{zmp}(t + \Delta t)}{1 - \frac{y_{ZMP}}{z_c} \sin(\theta)}, \\
\Delta \theta &= \frac{\Delta \tau}{\eta}, \\
&= - \frac{M_{zmp}(t + \Delta t)}{\eta (1 - \frac{y_{ZMP}}{z_c} \sin(\theta))},
\end{aligned} \tag{4.8}$$

where  $\Delta \theta$  is the amount of angular change needed for compensation.  $M_{zmp}(t + \Delta t)$  is measurable using (4.3). The angular change ( $\Delta \theta$ ) is applied to modify the lateral shift of the CoM as:

$$y_{CoM}^{compensated} = z_c \tan(\tan^{-1}(\frac{\hat{y}_{CoM}}{z_c} + \Delta \theta)), \tag{4.9}$$

where  $y_{CoM}^{compensated}$  is the compensated CoM,  $\hat{y}_{CoM}$  is computed from (4.1) and  $z_c$  is the height of the CoM. The compensation applied is limited by the torque-rating of the physical actuators. Without loss of generality, the compensator design is also applicable to the double support phases during walk-oscillations.



## 4.3 Online Phase Generator

The online phase generator produces the single and double support phases dynamically. The phase generator produces walk-oscillations by tracking the measured ZMP during lateral motion and executing the foot lift and landing accordingly. Time instances of the support phases, foot lift and landing are also generated.

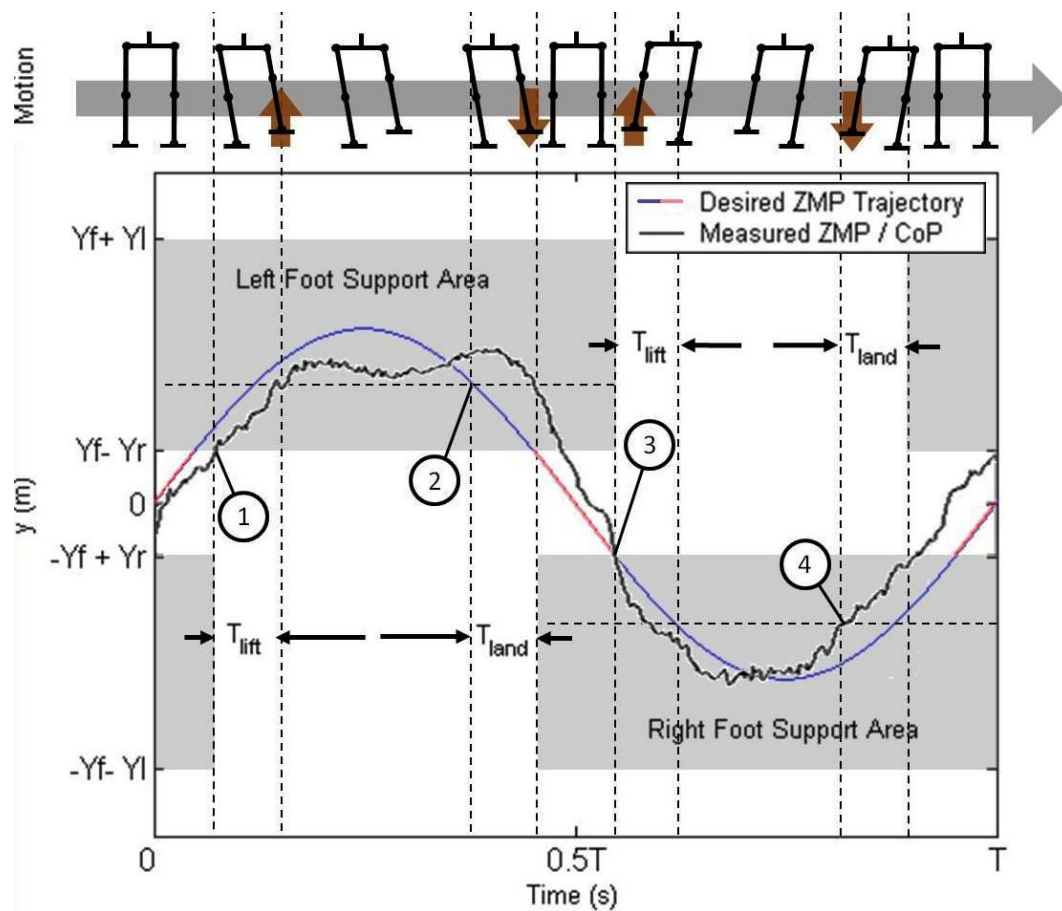
### 4.3.1 Phase Detector

The operations of the phase detector are as follows:

1. The phase detector executes the foot lift only when the desired and measured ZMP have move into the foot support area during lateral motion.
2. The phase detector executes the foot landing whenever the desired or measured ZMPs cross the minimum stability bound ( $y_{land}$ ) for foot landing during single support phase. The bound is computed as:

$$y_{land} = A\left(1 + \frac{\omega^2}{\omega_n^2}\right) \sin(\omega(0.5T - T_{land})). \quad (4.10)$$

The implementation of the phase detector implies that the oscillating period of the walk-oscillation is the same but the single and double support phase time periods are dynamic depending on the measured ZMP (Fig. 4.8).



- ① Executes foot lift motion after measured ZMP enter foot support area.
- ② Executes foot landing motion when desired ZMP crosses  $y_{land}$ .
- ③ Executes foot lift motion after desired ZMP enter foot support area.
- ④ Executes foot landing motion when measured ZMP crosses  $y_{land}$ .

Figure 4.8: ZMP trajectory during phase transition

### 4.3.2 Foot Placement Trajectories

The compensated CoM is applied to compute the foot placement trajectories for generation of walk-oscillations. The foot placement of each foot is

given as follows:

$$X_r^{walk-osc}(t) = 0,$$

$$X_l^{walk-osc}(t) = 0,$$

$$Y_r^{walk-osc}(t) = \begin{cases} \left(1 - \frac{C_f}{z_c}\right) y_{CoM}^{compensated}, & \text{if foot is lifted} \\ \frac{Z_r(t)}{Z_c} y_{CoM}^{compensated}, & \text{if foot is lifting / landing} \\ y_{CoM}^{compensated}(t), & \text{otherwise} \end{cases}$$

$$Y_l^{walk-osc}(t) = \begin{cases} \left(1 - \frac{C_f}{z_c}\right) y_{CoM}^{compensated}, & \text{if foot is lifted} \\ \frac{Z_l(t)}{Z_c} y_{CoM}^{compensated}, & \text{if foot is lifting / landing} \\ y_{CoM}^{compensated}(t), & \text{otherwise} \end{cases}$$

$$Z_r^{walk-osc}(t) = \begin{cases} z_c - C_f, & \text{if the foot is lifted} \\ a_o + a_1(t - t_s)^2 + a_2(t - t_s)^3, & \text{if foot is lifting / landing} \\ \sqrt{d^2 - (Y_r^{walk-osc}(t))^2}, & \text{otherwise} \end{cases}$$

$$Z_l^{walk-osc}(t) = \begin{cases} z_c - C_f, & \text{if the foot is lifted} \\ a_o + a_1(t - t_s)^2 + a_2(t - t_s)^3, & \text{if foot is lifting / landing} \\ \sqrt{d^2 - (Y_l^{walk-osc}(t))^2}, & \text{otherwise} \end{cases}$$

$$\text{Cubic Poly.} = \begin{cases} a_o = Z_o, \\ a_1 = \frac{3}{t_f^2}(Z_f - Z_o), \\ a_2 = \frac{-2}{t_f^3}(Z_f - Z_o), \end{cases}$$

where with respect to 1 oscillation cycle,

$d$  is the height of the hips from the ground in the standing posture,

$C_f$  is the amount of foot clearance required for the lifted foot,

$z_c$  is the height of the CoM,

$t_s$  is the starting time of the foot lift or landing motion,

$t_f$  is the time period of the foot lift or landing motion,

$Z_o$  is the initial foot position before foot lift or landing, and,

$Z_f$  is the final foot position for foot lift or landing.

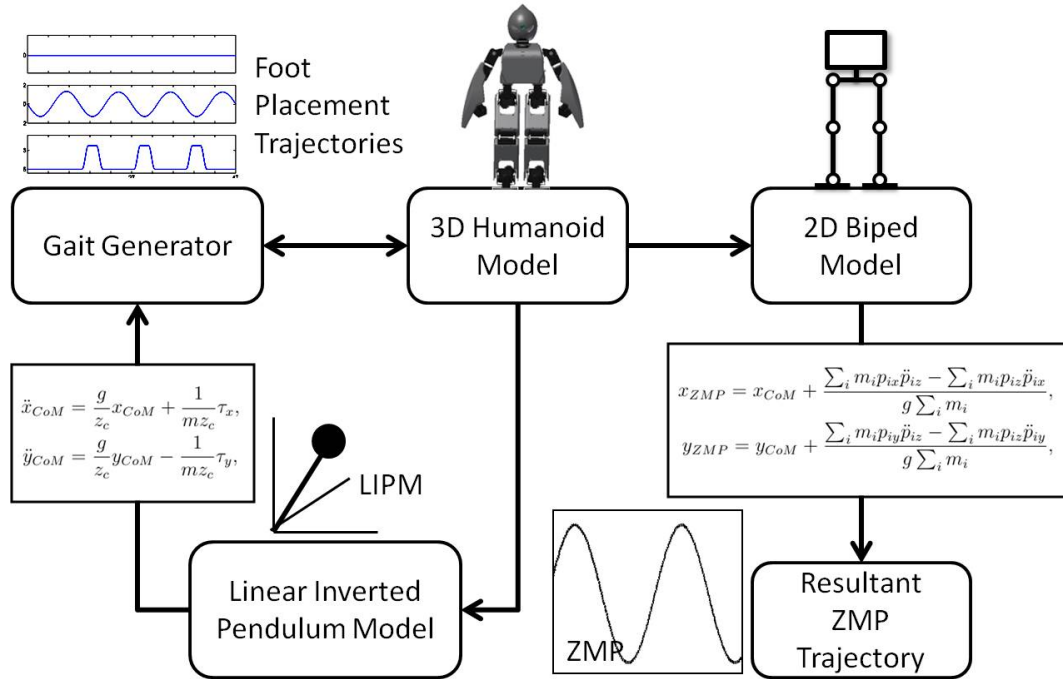


Figure 4.9: Simulation block diagram

## 4.4 Simulations

The proposed gait generation approach is simulated in the MATLAB / Simulink and Autodesk Inventor Dynamic Simulation environments. On-line gait generation requires the measurement of the ZMP for online feedback compensation. For reduced computation and ease of implementation, an estimated ZMP measurement approach is adopted using the LIPM (Fig. 4.9). The ZMP is computed by equating the center of gravity (CoG) of the 3D model to the COM of the LIPM for feedback control simulation. Computation of the resultant ZMP is realized by the translation to a 2D model which provides more accurate results. Table 4.1 shows the parameter applied for the simulation of the offline and online gait generation of lateral walk-oscillations. Walk-oscillation is initiated after the first oscillation cycle of lateral motion.

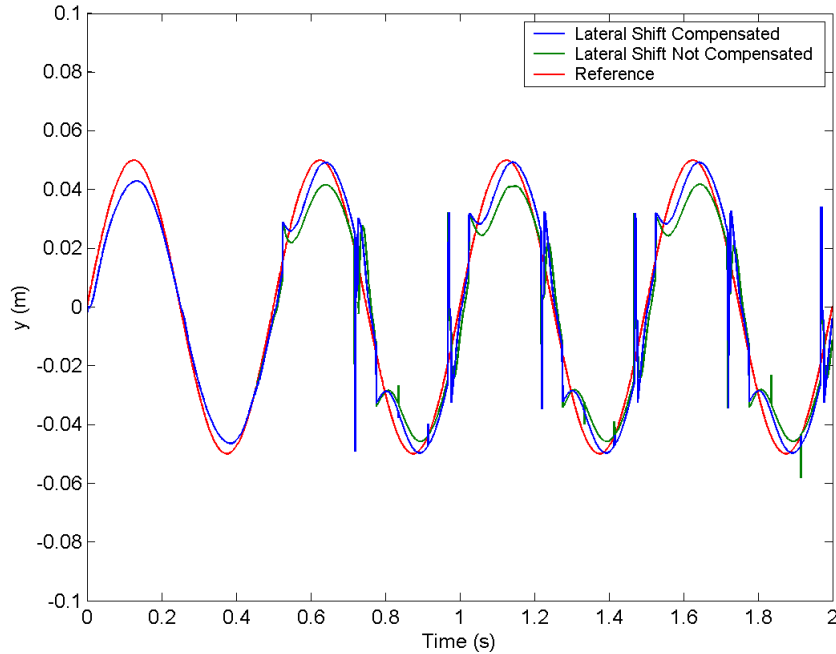
Table 4.1: Parameters for walk-oscillations simulation

Parameter	Value
Number of Oscillation Cycles	30
Oscillating Frequency, $f$ (Hz)	2.0
Oscillating Frequency, $\omega$ (rad/s)	12.566
CoM Lateral Shift Amplitude, $A$ (rad)	0.0100
Desired Peak ZMP Amplitude, $ p_{y(peak)} $ (m)	0.0502
Foot Clearance (m)	0.015
Time Period for Foot Lift Motion (s)	0.06
Time Period for Foot Landing Motion (s)	0.06
Foot Lift Instances Within 1 Cycle (s)	0.0159 , 0.2659
Foot Land Instances Within 1 Cycle (s)	0.2341 , 0.4841
Ground Contact Stiffness (N/mm)	$2 \times 10^3$
Ground Contact Damping (N s/mm)	$2 \times 10^2$

#### 4.4.1 Shift Amplitude Correction

The shift amplitude controller is simulated with a proportional and integral gains of 0.2 and 0.005 respectively. Fig. 4.10 shows the ZMP trajectory of the walk-oscillations with the lateral shift amplitude controller.

The first oscillation cycle shows the original ZMP peak without compensation. After the initial cycle of lateral motion, it can be seen that the peak ZMP amplitude deviations are minimized with the controller. The unequal left and right peak ZMP amplitudes caused by unbalanced hardware is also addressed. Fluctuations in the ZMP within the oscillation cycles are not compensated and hence the ZMP deviations attributed by the contact dynamics (spikes in Fig. 4.10) during foot lifting and landing are not reduced. The average amount of the peak CoM lateral shift ( $A$ ) to the left is 0.0178 m and to the right is 0.0110 m for 30 oscillation cycles. The lateral shift to the left is more to balance the unequal ZMP peaks in the left and right feet.



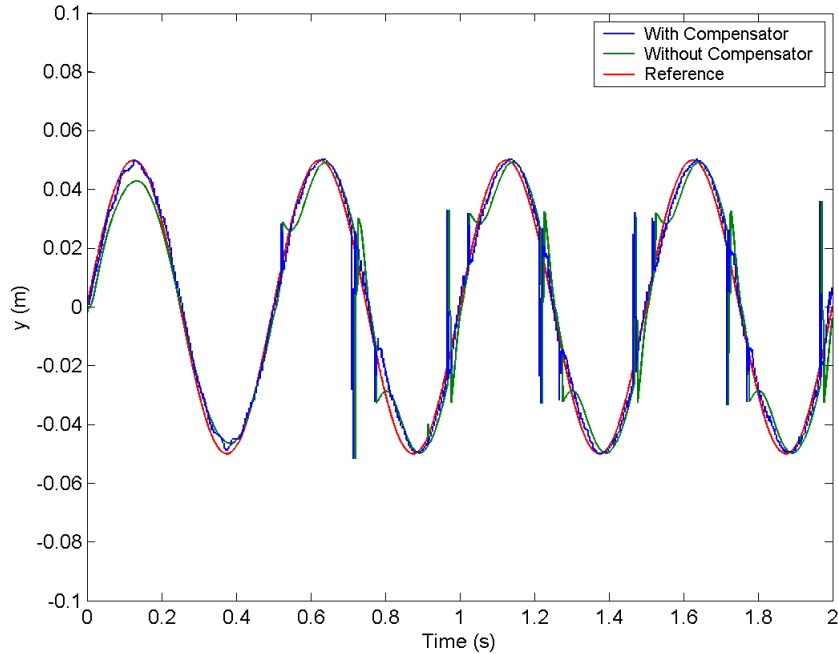
*With lateral shift amplitude controller: ZMP amplitude is balanced.  
 Without lateral shift amplitude controller: ZMP amplitude unbalanced.  
 The systematic spikes are attributed to the contact dynamics between the foot and ground as highlighted in Chapter 3.*

Figure 4.10: ZMP trajectories with lateral shift amplitude controller

#### 4.4.2 Zero Moment Point (ZMP) Compensation

Walk-oscillations are simulated using the ZMP compensator with a 0.005 m threshold for the stability zone. Fig. 4.11 shows the ZMP trajectory of the walk-oscillations with the compensator.

In the first oscillation cycle, the ZMP deviations are compensated by the compensator as the lateral shift amplitude correction only takes place from successive oscillation cycles after the first. ZMP ripples are observed near the peak due to the compensator stability zone. A minimum amount



*With addition of the compensator, ZMP deviations in the first oscillation is compensated. Spike readings due to foot lifting and landing are reduced.*

Figure 4.11: ZMP trajectories with compensator and lateral shift amplitude controller.

of deviation needs to be present before compensation can act. ZMP deviations due to foot lift and landing are reduced but not the initial impulse deviations as the compensator reacts only after a deviation is detected. The results show that the compensator can effectively minimize ZMP deviations.

### 4.4.3 Phase Detection for Transitions

The phase generator is implemented using a foot landing stability bound ( $y_{land}$ ) of 0.0095. For comparison studies, three approaches to obtain the time instances of the foot lifting and landing are studied:

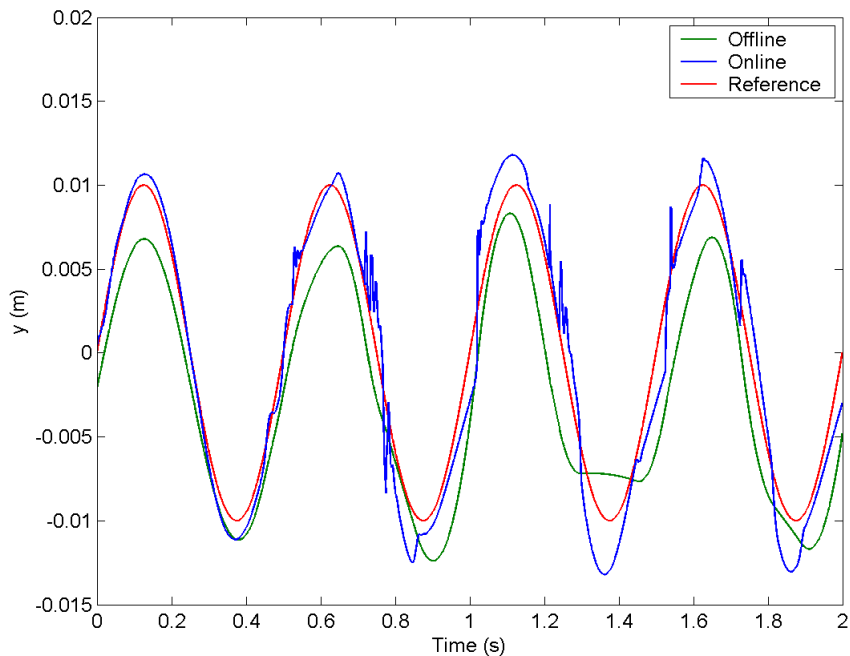
Table 4.2: Time instances for foot lift and landing

Approach	Offline Gait Generation	Phase Generator w/o Compensation	Phase Generator w/ Compensation
Left Foot Lift	0.0159s	0.0249s	0.0162s
Left Foot Land	0.2341s	0.2332s	0.2348s
Right Foot Lift	0.2659s	0.2697s	0.2669s
Right Foot Land	0.4841s	0.4894s	0.4835s

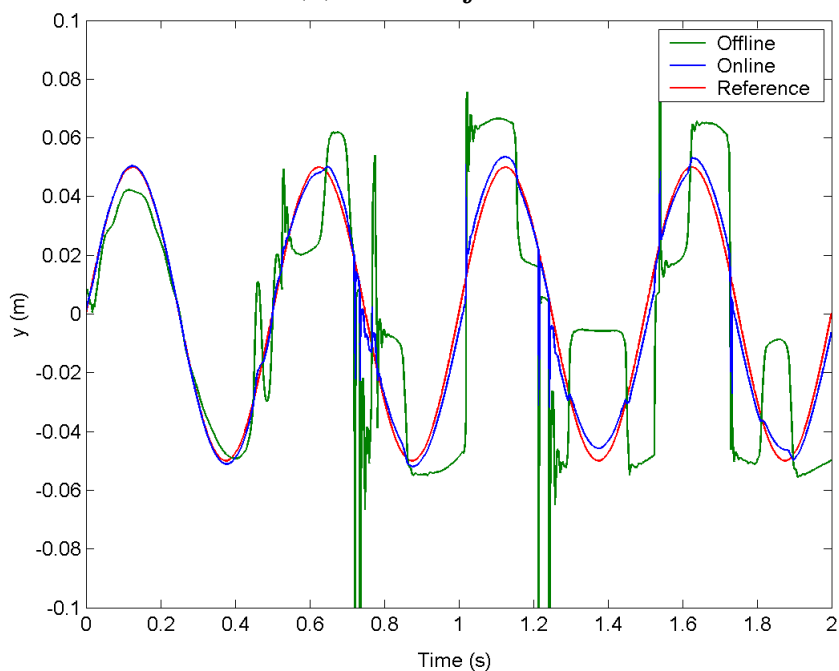
1. Offline gait generation - The time instances in which the ZMP leaves and enters the foot support area are computed using LIPM.
2. Simulated walk-oscillation using phase generator without compensation - Walk-oscillations are simulated using the phase generator for the foot lift and landing but without the lateral shift controller and ZMP compensator.
3. Simulated walk-oscillation using phase generator with compensation - Walk-oscillations are simulated based on the proposed gait generation approach.

Table 4.2 shows the tabulation of the time instances for foot lifting and landing within a simulated walk-oscillation, with an oscillating period of 0.5 s, for the three approaches. The phase generator ensure that stability is asserted before the phase transitions. Without compensation, the foot lift and landing are based on the uncompensated ZMP which results in differences of the foot lift and landing time instances. The compensated ZMP follows the desired trajectory closely resulting in time instances of the foot lift and landing to be closer to those computed offline using the LIPM.





(a) CoM trajectories



(b) ZMP trajectories

*The online gait generation approach has better disturbance rejection as there is less deviations of the ZMP trajectory from the reference.*

Figure 4.12: Trajectories of gaits generated with disturbances

#### 4.4.4 Walking Environment Disturbances Rejection

The online generation of walk-oscillations is simulated with walking environment disturbances applied. A  $3^\circ$  floor inclination is applied in the frontal plane of the humanoid with a stiffness and damping setting of  $2 \times 10^5$  N/mm and  $2 \times 10^2$  N s/mm for the ground.

Fig. 4.12 shows the CoM and ZMP trajectories generated with disturbances applied. It can be seen that the deviations of the ZMP in the online approach are reduced and the trajectory conforms better to the reference ZMP. The amount of lateral shifting applied for the compensation are highlighted by the fluctuating changes in the CoM trajectory. The simulations shows that with the online gait generation approach, the humanoid is able to reject disturbances due to the environment better in comparison to the offline approach.

#### 4.4.5 Reaction to Impulsive Disturbances

To determine the robustness of the walk-oscillation with the online approach, a free swinging pendulum is used to generate an impulsive disturbance on the humanoid during lateral walk-oscillations (Fig. 4.13) in the frontal plane. Simulations of walk-oscillation are conducted and repeated with increasing magnitude of the impulse disturbance force until the humanoid falls over. Both offline and online gait generation approach are simulated (Fig. 4.14) to study the robustness of the algorithms and not as a measure of the balancing and recovery capabilities of the humanoid.

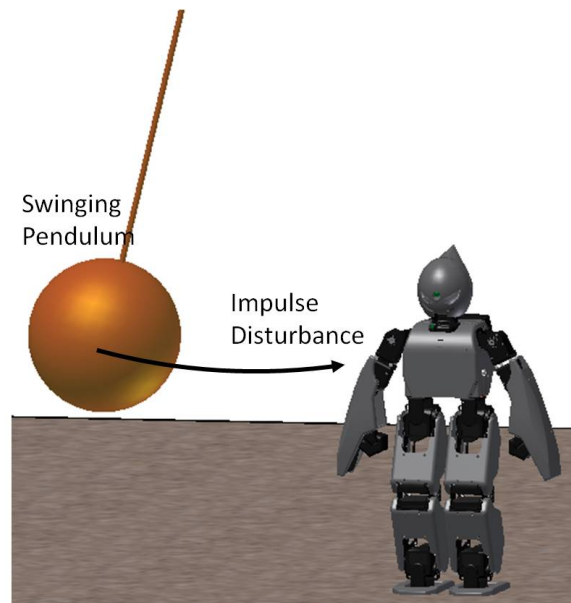


Figure 4.13: Impulse disturbance generation

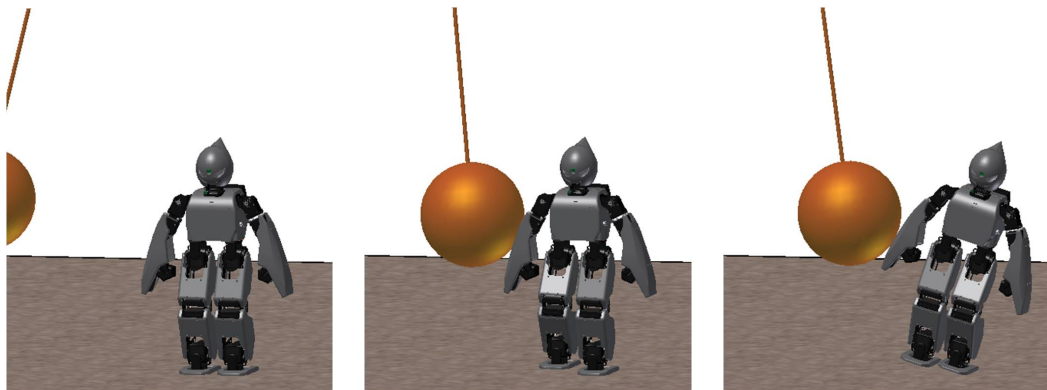
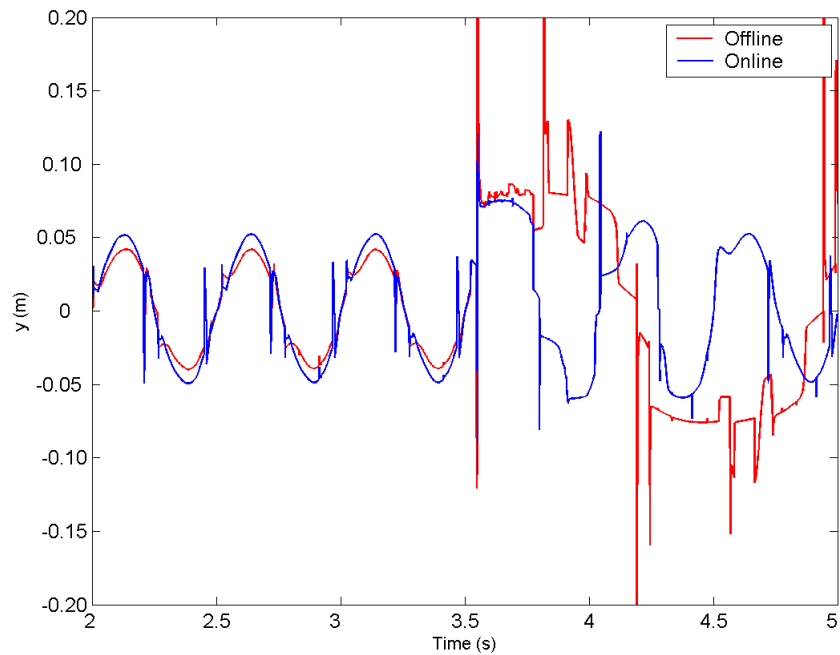


Figure 4.14: Simulations of impulse disturbance

The simulation results show that the humanoid with the offline and online approaches is able to sustain oscillation with a maximum force disturbance of 5 N and 8.5 N respectively. Fig. 4.15 shows the ZMP trajectories of the offline and online approaches when a force disturbance of 4 N is injected at 3.511 s. It can be seen that the online approach damps the ZMP trajectory back to stable oscillations whereas the offline approach exhibited prolonged effects of instability. The simulation results show that with the online approach the walk-oscillations is improved.



*Online gait generation approach is able to recover back into stable oscillation whereas offline gait generation approach exhibited prolonged effects of instability.*

Figure 4.15: ZMP trajectories with 4 N disturbance force

## 4.5 Experiments

The online gait generation of walk-oscillations is implemented to the REJr humanoid robot. The gait generation approach is implemented in the low level micro processor of the robot which operates at 80MHz. Force sensors mounted in the humanoid foot are used to measure the ZMP at a sampling rate of 200Hz. The joint actuators are commanded at a frequency of 50Hz. The walk-oscillation parameters applied are shown in Table 4.3.

Table 4.3: Parameters for walk-oscillations experiment

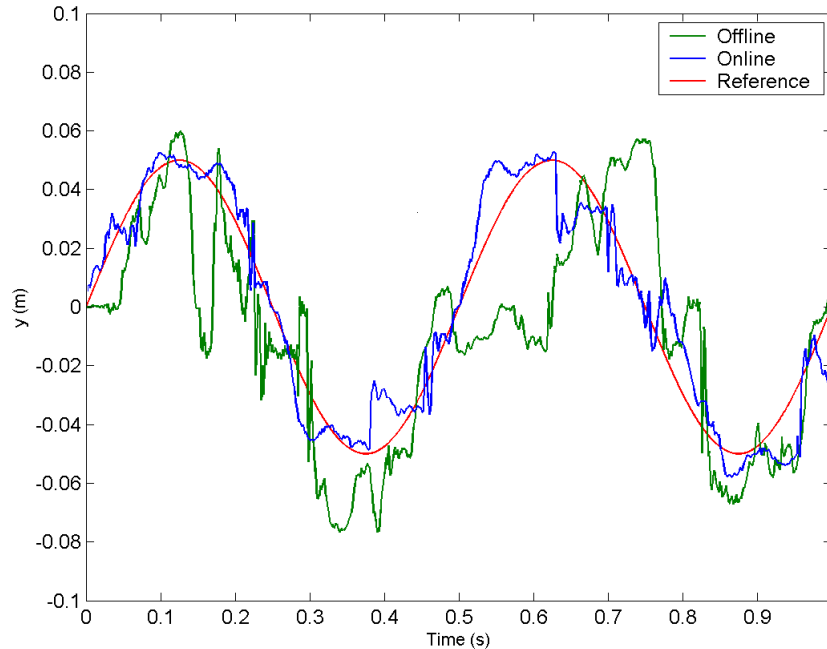
Parameter	Value
Oscillation Cycles	30
Oscillating Frequency, $f$ (Hz)	2.0
Oscillating Frequency, $\omega$ (rad/s)	12.566
CoM Lateral Shift Amplitude, $A$ (rad)	0.0100
Desired Peak ZMP Amplitude, $ p_{y(peak)} $ (m)	0.0502
Foot Clearance (m)	0.015
Time Period for Foot Lift Motion (s)	0.06
Time Period for Foot Landing Motion (s)	0.06
P Gain for Lateral Shift Amplitude Controller	0.2
I Gain for Lateral Shift Amplitude Controller	0.005
Stability Threshold for ZMP Compensator (m)	0.015
Stability Bound for Phase Generator (m)	0.01

#### 4.5.1 Online Generation of Walk-Oscillations

Using pre-computed offline gaits as the reference, the online gait generation approach is implemented on the humanoid to produce walk-oscillations on a typical flat carpeted surface. Fig. 4.16 shows the measured and recorded ZMP using the force sensors. The ZMP trajectory produced using the offline approach on the flat carpeted surface is presented for comparison. From the results, it can be seen that the magnitude of the ZMP fluctuations using the online approach are reduced in comparison to that generated using the offline approach. The ZMP trajectory of the online approach also follows the reference better with less deviations.

#### 4.5.2 Walking Environment Disturbances

Walk-oscillations are generated using the offline and online approaches on two different walking surfaces with inclinations of approximately  $2^\circ$  in the frontal plane. The two walking surfaces used are a hard solid surface



*Online gait generation approach is observed to have less deviations of the ZMP trajectory from the reference; ZMP of the online approach conforms better in compare to the offline approach.*

Figure 4.16: ZMP trajectories of online and offline walk-oscillations generated

and a thick pile foam surface (Fig. 4.17).

From the experimental results, walk-oscillations are produced by the online gait generation on both walking surfaces. The offline approach is successful in generating sustainable walk-oscillations on the solid surface but not on the foam surface; the humanoid fell over on the foam surface. The thick pile of foam allows additional uncontrolled depression at the outer edges of the foot when the humanoid sways during walk-oscillations. The uncontrolled depression resulted in undesired dynamic forces that eventually destabilized the humanoid. Fig. 4.19 shows the normalized amount of lateral shift applied on the different walk surfaces using online

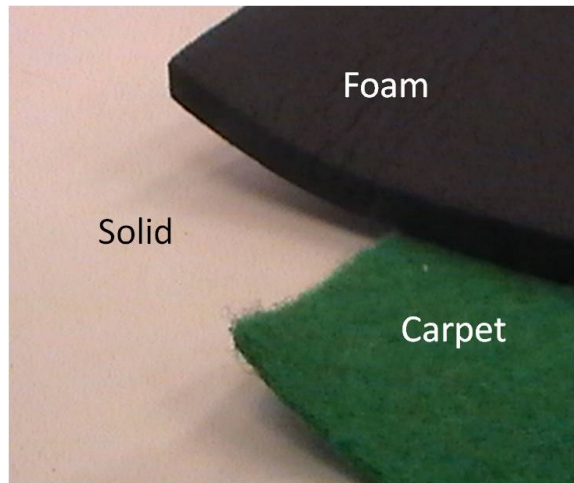


Figure 4.17: Different walking surfaces

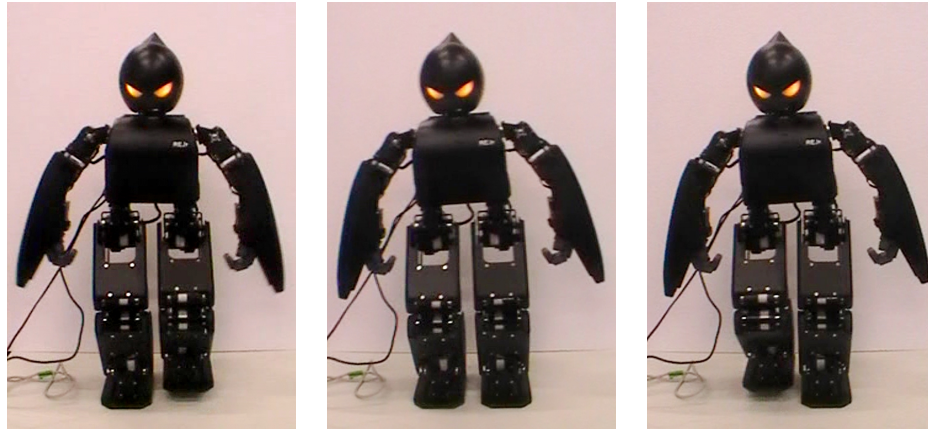
Table 4.4: Average time instances on different walking surface

Surface	Carpet	Solid	Foam
Left Foot Lift	0.023s	0.025s	0.020s
Left Foot Land	0.262s	0.245s	0.220s
Right Foot Lift	0.300s	0.306s	0.280s
Right Foot Land	0.512s	0.501s	0.460s
Single Support Period	0.2255s	0.2075s	0.1900s

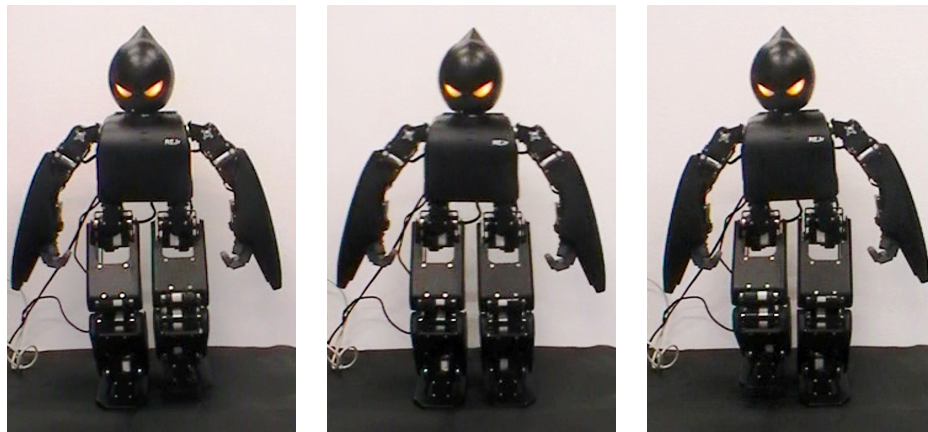
gait generation whereas Table .4.4 shows the average time instances of the foot lifting and landing, and, the single support time period measured using the force sensors. The experiment shows that the online approach can effectively reject disturbances attributed by the flat terrain walking environment.

### 4.5.3 Impulsive Disturbances

Impulsive disturbances are generated using similar set-up to that of the simulation. A free swinging pendulum, constructed using a string and soccer ball, is used to generate an impulsive disturbance on the humanoid during lateral walk-oscillations in the frontal plane. As the measurement



(a) Solid surface



(b) Foam surface

Figure 4.18: Walk-oscillations on different walking surfaces

of the force of impulsive disturbance is difficult to determine in the experiment, the potential energy is used as the indicator for the relative amount of force exerted. The ball is placed and released at different heights and 10 trials are conducted in each case. For every case in which the humanoid sustains oscillations for the 10 trials, the height is increment by 0.1 m. The humanoid is allowed to stabilized after each trial before the next successive trial commences. The experiment is carried out for both offline and online approaches. The potential energy is simply calculated using:

$$U = mgh, \quad (4.11)$$



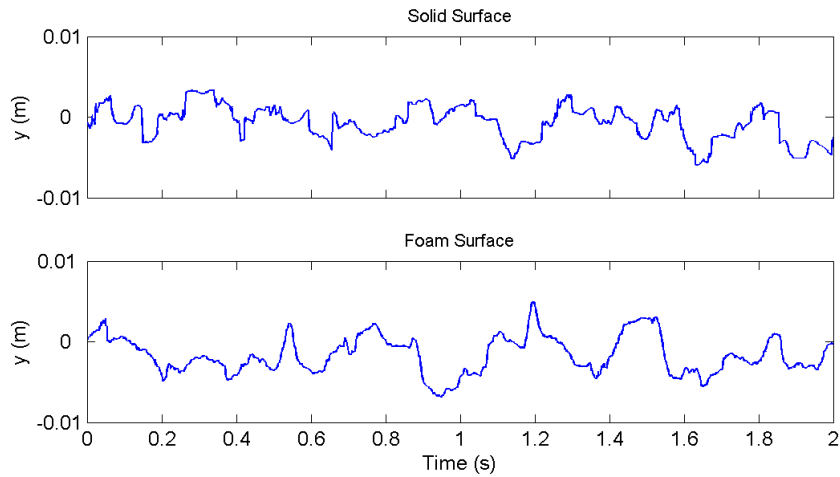


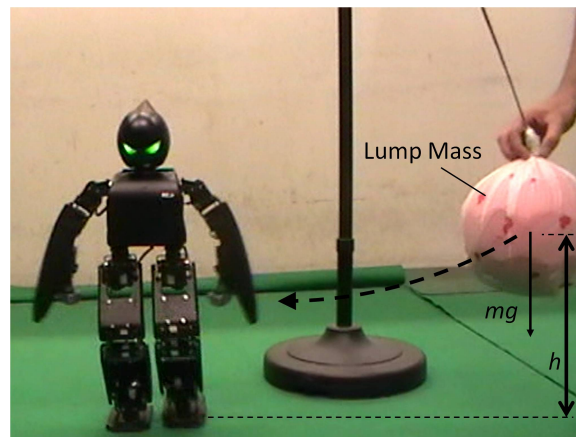
Figure 4.19: Normalized amount of lateral Shift compensation

where  $m$  is the mass of the soccer ball used as the lump mass,  $h$  is the height in which the pendulum is released and  $g$  is acceleration due to gravity.

The experimental results show that the offline approach is able to sustain oscillations up to 1.727 J (0.4 m) whereas the online approach is able to sustain up to 3.021 J (0.7m). The results indicates that with the online approach, there is improvement in the lateral walk-oscillations.

## 4.6 Conclusion

The generation of sustainable walk-oscillations is presented and discussed in this chapter. An online gait generation approach is realized by implementing a two stage compensation system, comprising of a lateral shift amplitude controller and a ZMP compensator, with a phase generator. Deviations in the ZMP peak amplitudes are minimize by the lateral shift amplitude controller after every oscillation cycle whereas deviations of



*$m$  is mass of the lump mass,  $h$  is the height in which the lump mass is released and  $g$  is the acceleration due to gravity.*

Figure 4.20: Impulse disturbance generation experiment

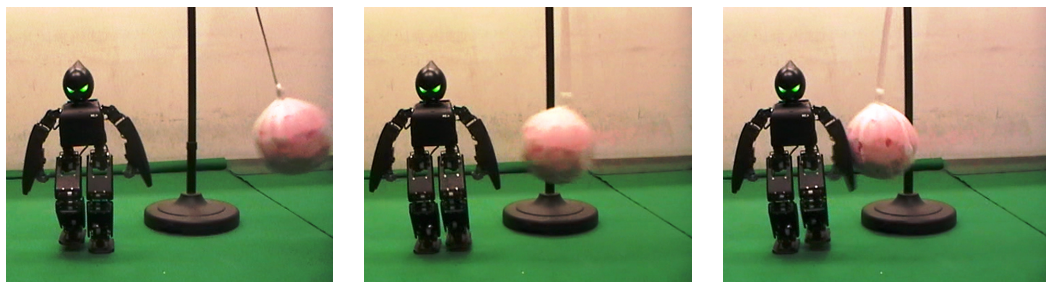


Figure 4.21: Experiment of impulse disturbance

the ZMP trajectory from the reference are minimized by the ZMP compensator. The phase generator ensures that the stability is asserted for phase transitions. Simulations and experimental results shows that the online gait generation approach enhances the robustness of the walk-oscillations on flat terrains. Future works can extend the gait generation approach to handle uneven and unknown terrain.

## Chapter 5

# OmniDirectional Walking

The concept of omnidirectional drives begins as early as 2000 when Cornell University, team Big Red [123], first introduced omnidirectional mobile wheeled robots for the RoboCup SmallSize league competition. Since then, research on omnidirectional drives manifested and have moved beyond the scope of wheeled robots. Omnidirectional walking for bipedal robots is one of the key research topics in humanoid robotics. The ability to move forward, sideways and turn at the same instance has proven to be advantageous in confined spaces and dynamic environments. Many researches have proposed gaits that fully parametrized the bipedal omnidirectional walking [90–93].

The use of sensory feedback for direction control for bipedal locomotion have been proposed in several separated works [101–104, 124, 125]. In most of these works, visual information is used for correcting the directional deviation of walk. The emphasis in some of these research focuses on path or trajectory planning for navigation in dynamic environment with obstacles. [104] proposed a robust direction control system that

utilized rate-gyroscope sensor feedback under environment with disturbance. In [124, 125], the use of foot slip for pivoting to generate turning motion for biped robot are presented.

The biped dynamic walking motion in this dissertation is decoupled into two components, ① lateral walk-oscillations and ② omnidirectional walking. Lateral walk-oscillations generate the single and double support phases and form the walking basis in which the omnidirectional walk leverage on. During the single support phase, the supporting foot pivots the humanoid towards the desired walking direction in a stable manner. The output of the omnidirectional walk generator is superimposed with the output from the lateral walk-oscillations generator to produce robust dynamic walking.

In this chapter, the real-time gait generation for omnidirectional walk is described and presented (Fig. 5.1). The omnidirectional dynamic walk is decoupled into the frontal, sagittal and transverse movements. These movements are generated in real-time using sinusoidal trajectories based on the time instances dynamically generated by the lateral walk-oscillation generator. A walk-stepper controller is implemented to manage the acceleration profile of the walking through the regulation of the stepping size. The movements are combined using superposition theorem to generate stable omnidirectional biped walking. A motion steering controller using the rate-gyro for sensory feedback is used to improve the directional walking of the humanoid. The validity of the approach is verified through simulations and experimentation.

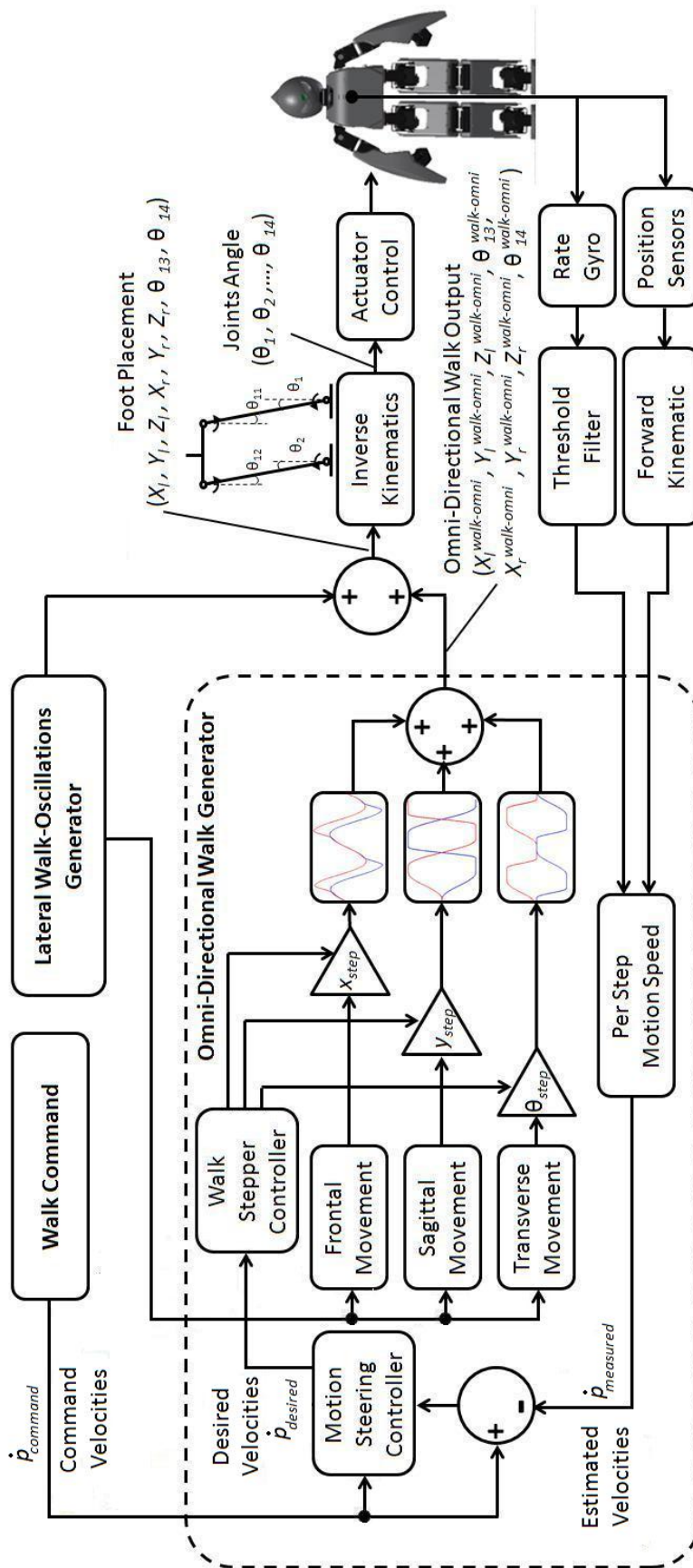


Figure 5.1: Omnidirectional gait generation

In section 5.1, the foot placements for the various directional walk are presented. Section 5.2 discussed the stability issues and algorithm for omnidirectional walk using the superposition theorem. Section 5.3 described the motion steering using the rate-gyro to enhance the performance of the walking gaits. The simulation and experimental results are presented in sections 5.4 and 5.5 respectively. Section 5.6 concludes for the chapter.

## 5.1 Real-Time Foot Placement Generation

The lateral walk-oscillations are classified into 6 stages of distinction motion execution (Fig. 5.3). Table 5.1 describes the motion executed in each stage where  $T^{lift}$  and  $T^{land}$  are the time instances in which the foot lifting and landing motion are executed.  $t_f$  is the time period of the foot lifting and landing motion, and,  $T$  is the time period of 1 lateral walk-oscillation cycle. The subscript notation denotes the foot. The time instances are generated dynamically by the phase generator within the lateral walk-oscillations generator.

The omnidirectional walk is divided into three planes movements, ① frontal, ② transverse and ③ sagittal. These movements are built upon the 6 stages of motion in the lateral walk-oscillations. The movements are realized by swinging / rotating the lifted foot towards the desired direction while the supporting foot pivots the body. Sinusoidal trajectories are applied for interpolation of the movements to provide smooth motions. The three plane movements are computed online and expressed in terms of the imposed foot placements for frontal ( $X^{frontal}$ ,  $Y^{frontal}$ ,  $Z^{frontal}$ ) and sagittal ( $X^{sagittal}$ ,  $Y^{sagittal}$ ,  $Z^{sagittal}$ ) movement, and, joint angles ( $\theta^{transverse}$ )

Table 5.1: Six stages of motion execution

Stage	Time Instance	Motion Description
0	N.A	Initial standing posture in double support phase.
1	$0 \leq t < (T_l^{lift} + t_f)$	Lateral shifting to the right with foot lifting for single to double support phase transition.
2	$(T_l^{lift} + t_f) \leq t < T_l^{land}$	Lateral shifting to the extreme right and returning with lifted foot in single support phase.
3	$T_l^{land} \leq t < T/2$	Lateral shifting back to standing posture with foot landing for double to single support phase transitions.
4	$T/2 \leq t < (T_r^{lift} + t_f)$	Lateral shifting to the left with foot lifting for single to double support phase transition.
5	$(T_r^{lift} + t_f) \leq t < T_r^{land}$	Lateral shifting to the extreme left and returning with lifted foot in single support phase.
6	$T_r^{land} \leq t \leq T$	Lateral shifting back to standing posture with foot landing for double to single support phase transition.

for transverse movement (Fig. 5.2). For the online computation of the sinusoidal trajectories, two frequency components are computed as:

$$\begin{aligned}
 T_{single} &= \frac{T_l^{land} - T_l^{lift} + T_r^{land} - T_r^{lift}}{2}, \\
 \omega_s &= \frac{\pi}{T_{single}}, \\
 \omega_f &= \frac{\pi}{T_{single} - 2t_f},
 \end{aligned} \tag{5.1}$$

where  $\omega_s$  and  $\omega_f$  are the computed frequencies of the single support phase and lifted foot time periods. The time instances  $T^{land}$  and  $T^{lift}$  in (5.1) are dynamically generated by the phase generator for the previous walk

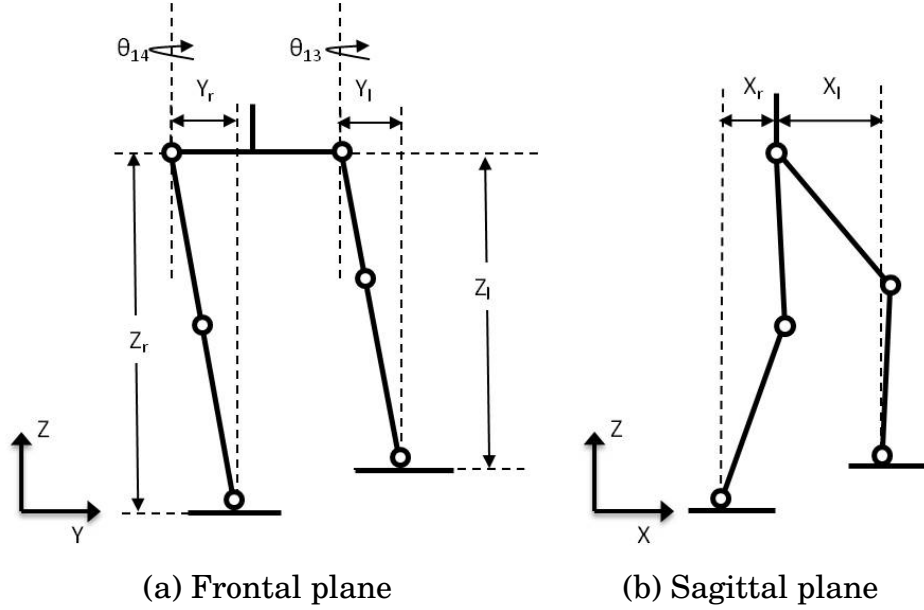


Figure 5.2: Foot placement trajectories and joint angles for omnidirectional walk movements

oscillation cycle.  $\omega_s$  and  $\omega_f$  are used for the sinusoid functions for the computations of the movement trajectories. The frontal, sagittal and transverse movements are superimposed with the lateral walk-oscillations to produce omnidirectional dynamic walking as:

$$\begin{aligned}
 X_r^{walk-omni}(t) &= X_r^{frontal}(t) + X_r^{sagittal}(t), \\
 Y_r^{walk-omni}(t) &= Y_r^{frontal}(t) + Y_r^{sagittal}(t), \\
 Z_r^{walk-omni}(t) &= Z_r^{frontal}(t) + Z_r^{sagittal}(t), \\
 X_l^{walk-omni}(t) &= X_l^{frontal}(t) + X_l^{sagittal}(t), \\
 Y_l^{walk-omni}(t) &= Y_l^{frontal}(t) + Y_l^{sagittal}(t), \\
 Z_l^{walk-omni}(t) &= Z_l^{frontal}(t) + Z_l^{sagittal}(t), \\
 \theta_{13}^{walk-omni}(t) &= \theta_{13}^{transverse}(t), \\
 \theta_{14}^{walk-omni}(t) &= \theta_{14}^{transverse}(t).
 \end{aligned}$$

(5.2)



### 5.1.1 Frontal Plane Movement

Frontal plane movement as the term implies relate to the movement in the  $y$ -axis direction of the anatomical position reference frame; also known as side stepping. The movement is realized by laterally shifting of the foot during single support phases (Fig. 5.4) where the total amount of lateral shift in the foot equates to the step size. The frontal foot placement trajectory for left side stepping for a single oscillation cycle is calculated as:

$$\begin{aligned}
 X_r^{frontal}(t) &= X_l^{frontal}(t) = 0, \\
 Z_r^{frontal}(t) &= Z_l^{frontal}(t) = 0, \\
 Y_r^{frontal}(t) &= \begin{cases} 0, & \text{for } 0 \leq t < \frac{T}{4} \\ & \text{and } T_r^{land} \leq t < T \\ \frac{y_{step}}{2}(\sin(\omega t) - 1), & \text{for } \frac{T}{4} \leq t < (T_r^{lift} + t_f) \\ \frac{y_{step}}{2}(\sin(\omega t) - 1) + \\ \frac{Y_{step}}{4}[1 - \cos(\omega_f(t - T_r^{lift} - t_f))], & \text{for } (T_r^{lift} + t_f) \leq t < \frac{3T}{4} \\ \frac{Y_{step}}{4}[1 - \cos(\omega_f(t - T_r^{lift} - t_f))], & \text{for } \frac{3T}{4} \leq t < T_r^{land} \end{cases} \\
 Y_l^{frontal}(t) &= \begin{cases} 0, & \text{for } 0 \leq t < (T_l^{lift} + t_f) \\ & \text{and } \frac{3T}{4} \leq t < T \\ \frac{y_{step}}{2}(\sin(\omega t) + 1), & \text{for } T_l^{land} \leq t < \frac{3T}{4} \\ \frac{y_{step}}{2}(\sin(\omega t) + 1) + \\ \frac{Y_{step}}{4}[1 - \cos(\omega_f(t - T_l^{lift} - t_f))], & \text{for } \frac{T}{4} \leq t < T_l^{land} \\ \frac{Y_{step}}{4}[1 - \cos(\omega_f(t - T_l^{lift} - t_f))], & \text{for } (T_l^{lift} + t_f) \leq t < \frac{T}{4} \end{cases}
 \end{aligned} \tag{5.3}$$

where  $y_{step}$  is the lateral step size in meters. The resultant ( $Y_l$ ,  $Y_r$ ) of the foot placement trajectories, lateral walk-oscillations imposed with frontal

plane movement, are shown in Fig. 5.7. For lateral stepping to the right, the computations of the left and right foot placement are interchanged.

### 5.1.2 Transverse Plane Movement

Transverse plane movement is the turning of the humanoid. The hip yaw joints are controlled directly to facilitate the rotation of the humanoid (Fig. 5.5). The joint trajectories (Fig. 5.8) for a right rotation are given as:

$$\theta_{13}^{transverse}(t) = \begin{cases} 0, & \text{for } 0 \leq t < (T_l^{lift} + t_f) \\ & \text{and } (T_r^{land} + t_f) \leq t < T \\ \frac{-\theta_{step}}{4}[1 - \cos(\omega_f(t - T_l^{lift} - t_f))], & \text{for } (T_l^{lift} + t_f) \leq t < T_l^{land} \\ \frac{-\theta_{step}}{2}, & \text{for } T_l^{land} \leq t < T_r^{lift} \\ \frac{-\theta_{step}}{4}[1 + \cos(\omega_s(t - T_r^{lift}))], & \text{for } T_r^{lift} \leq t < (T_r^{land} + t_f) \end{cases}$$

$$\theta_{14}^{transverse}(t) = \begin{cases} 0, & \text{for } 0 \leq t < T_l^{lift} \\ & \text{and } T_r^{land} \leq t < T \\ \frac{\theta_{step}}{4}[1 - \cos(\omega_s(t - T_l^{lift}))], & \text{for } T_l^{lift} \leq t < (T_l^{land} + t_f) \\ \frac{\theta_{step}}{2}, & \text{for } \\ & (T_l^{land} + t_f) \leq t < \\ & (T_r^{lift} + t_f) \\ \frac{\theta_{step}}{4}[1 + \cos(\omega_f(t - T_r^{lift} - t_f))], & \text{for } (T_r^{lift} + t_f) \leq t < T_r^{land} \end{cases}$$

(5.4)

where  $\theta_{step}$  is the amount of rotation in radians,  $\theta_{13}^{transverse}$  and  $\theta_{14}^{transverse}$  are the left and right hip yaw joints respectively.

### 5.1.3 Sagittal Plane Movement

Sagittal plane movement refers to the forward and backward walk movements in the  $x$ -axis direction of the anatomical position reference frame. The trajectory output is divided into a full step (5.5) for continuous walking (Fig. 5.6) and a half step (5.6) for moving off and stopping.

$$Y_r^{sagittal}(t)Y_l^{sagittal}(t) = 0,$$

$$Z_r^{sagittal}(t)Z_l^{sagittal}(t) = 0,$$

$$X_r^{sagittal}(t) = \begin{cases} -\frac{x_{step}}{2}, & \text{for } 0 \leq t < (T_r^{lift} + t_f) \\ & \text{and } (T_l^{land} + t_f) \leq t < T \\ -\frac{x_{step}}{2} \cos(\omega_f(t - T_r^{lift} - t_f)), & \text{for } (T_r^{lift} + t_f) \leq t < T_r^{land} \\ \frac{x_{step}}{2} & \text{for } T_r^{land} \leq t < T_l^{lift} \\ \frac{x_{step}}{2} \cos(\omega_s(t - T_l^{lift})), & \text{for } T_l^{lift} \leq t < (T_l^{land} + t_f) \end{cases}$$

$$X_l^{sagittal}(t) = \begin{cases} \frac{x_{step}}{2}, & \text{for } 0 \leq t < T_r^{lift} \\ & \text{and } T_l^{land} \leq t < T \\ \frac{x_{step}}{2} \cos(\omega_s(t - T_r^{lift})), & \text{for } T_r^{lift} \leq t < (T_r^{land} + t_f) \\ -\frac{x_{step}}{2}, & \text{for} \\ & (T_r^{land} + t_f) \leq t < (T_l^{lift} + t_f) \\ -\frac{x_{step}}{2} \cos(\omega_f(t - T_l^{lift} - t_f)), & \text{for } (T_l^{lift} + t_f) \leq t < T_l^{land} \end{cases}$$

(5.5)

where  $x_{step}$  is the step size in meters and the time ( $t$ ) is with respect to the full step time period.

$$Y_r^{sagittal}(t)Y_l^{sagittal}(t) = 0,$$

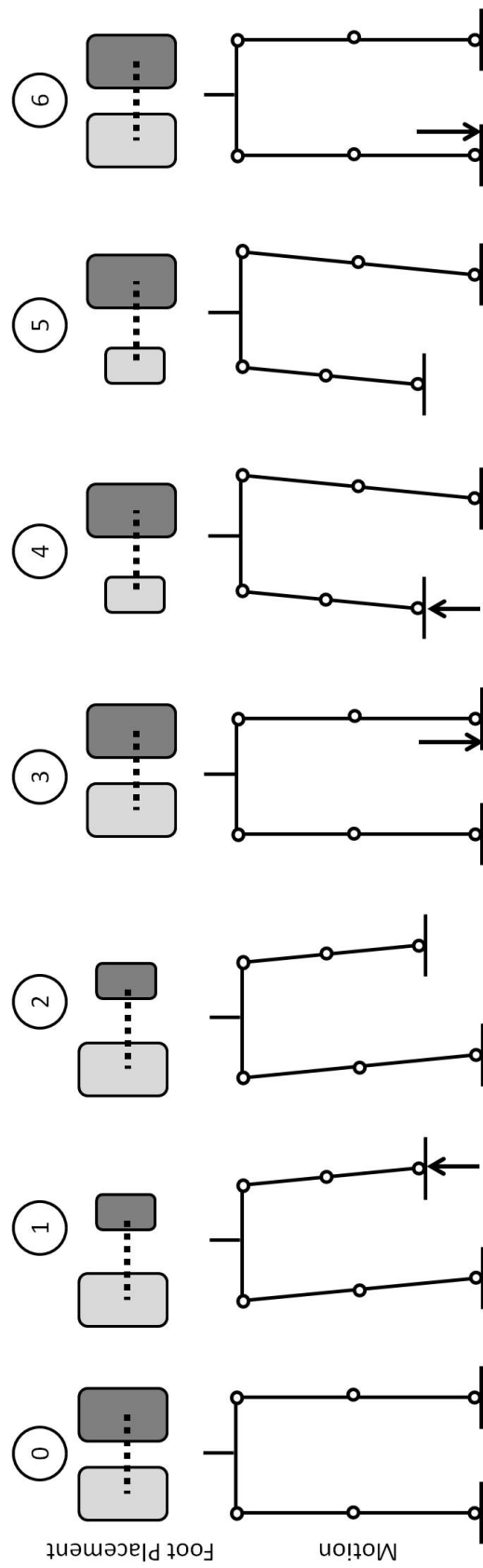
$$Z_r^{sagittal}(t)Z_l^{sagittal}(t) = 0,$$

$$X_r^{sagittal}(t) = \begin{cases} 0, & \text{for } 0 \leq t < T_l^{lift} \\ -\frac{x_{step}}{2} \sin(\omega_s(t - T_l^{lift})), & \text{for } T_l^{lift} \leq t < (T_l^{land} + t_f) \\ -\frac{x_{step}}{2} & \text{for } (T_l^{land} + t_f) \leq t < \frac{T}{2} \end{cases}$$

$$X_l^{sagittal}(t) = \begin{cases} 0, & \text{for } 0 \leq t < (T_l^{lift} + t_f) \\ \frac{x_{step}}{4} [1 - \cos(\omega_f(t - T_l^{lift} - t_f))], & \text{for } (T_l^{lift} + t_f) \leq t < T_l^{land} \\ \frac{x_{step}}{2} & \text{for } T_l^{land} \leq t < \frac{T}{2} \end{cases}$$

(5.6)

For stopping the same trajectories are used with a  $180^\circ$  phase shift in the sinusoids. The  $(X_l, X_r)$  of the foot placement trajectories with the sagittal plane movement are shown in Fig. 5.9 where the half step walk starts at time  $T$  and continuous walk begins at  $1.5T$ . Positive values of  $x_{step}$  relate to forward walking whereas negative values relate to backward walking. Arm swing movements are incorporated to make the walk look more realistic. Trajectories of the arm swing are in the opposite direction of the respective foot trajectories.



The 6 stages of classification of the walk-oscillation. Foot placement figures: The dotted line denote the physical link between the left foot (Darker grey) and the right foot (Lighter grey). A lifted foot is denoted by the smaller foot size.

Figure 5.3: Walk-oscillation - Dynamic walking

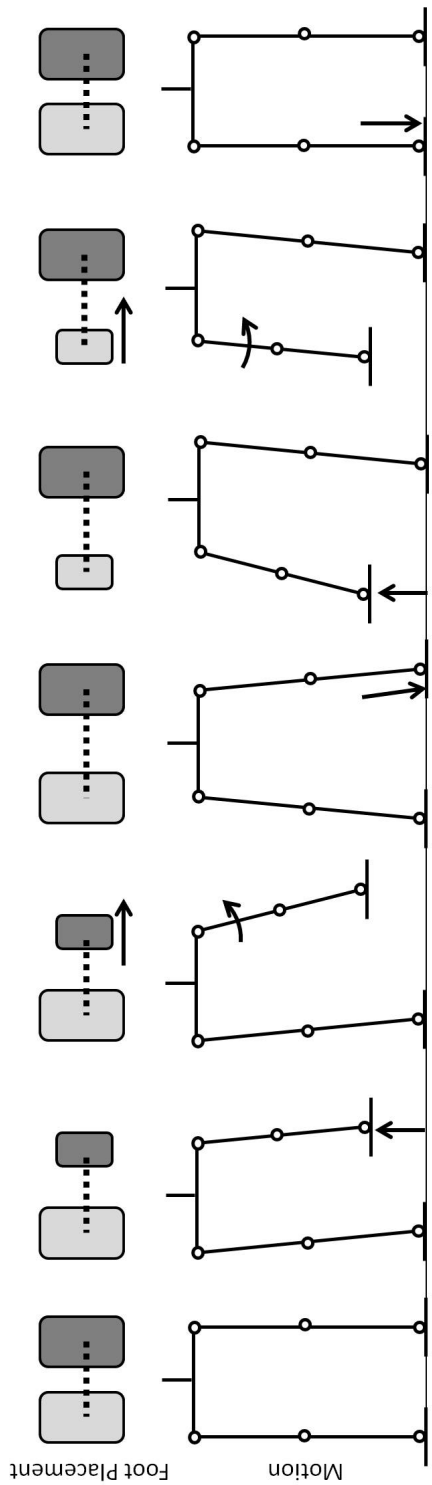


Figure 5.4: Frontal plane movement

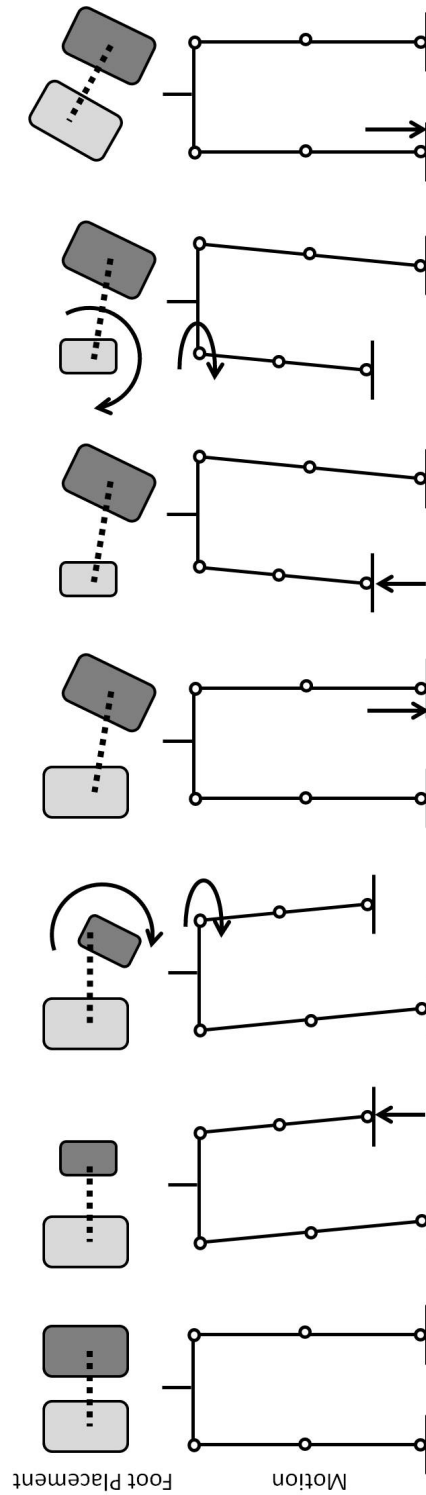


Figure 5.5: Transverse plane movement

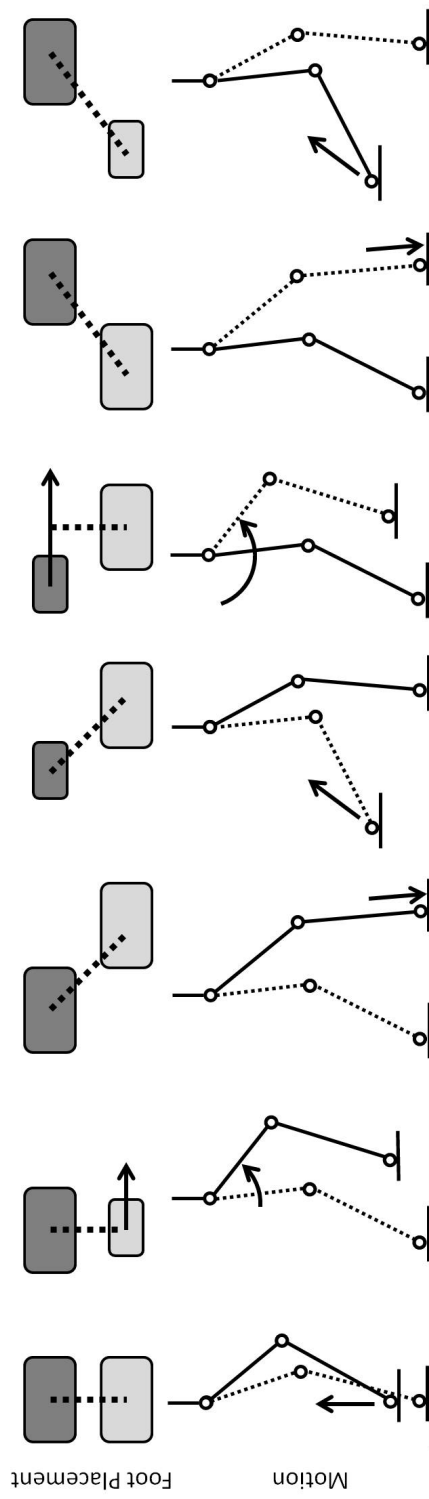


Figure 5.6: Sagittal plane movement

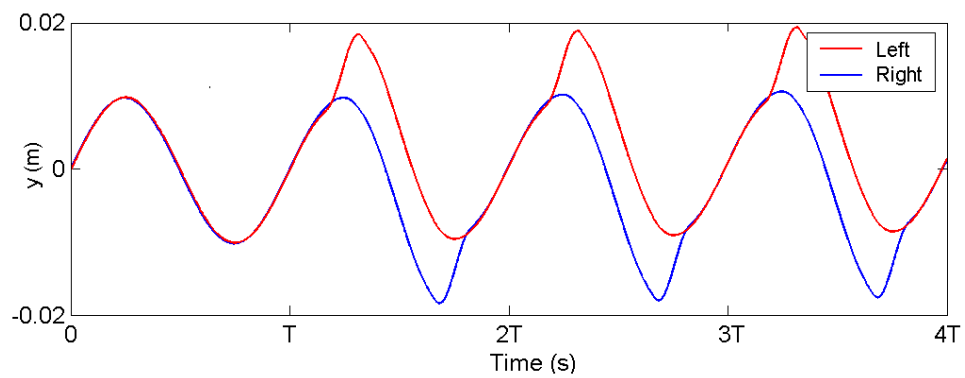


Figure 5.7: Foot placement trajectories for frontal plane movement

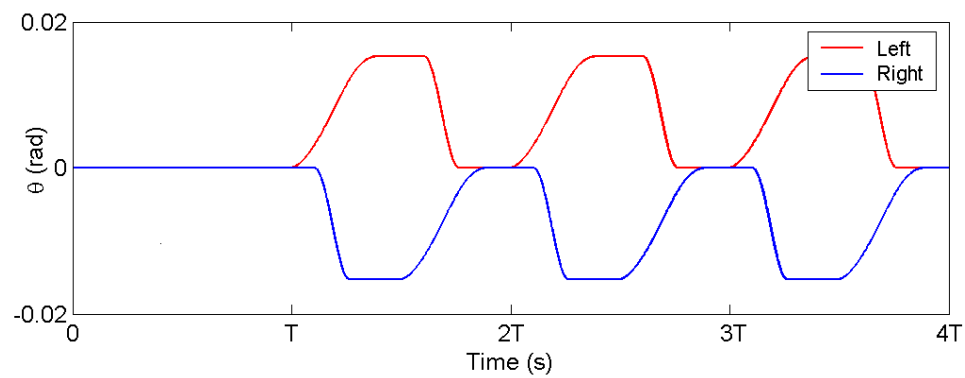


Figure 5.8: Joint trajectories for transverse plane movement

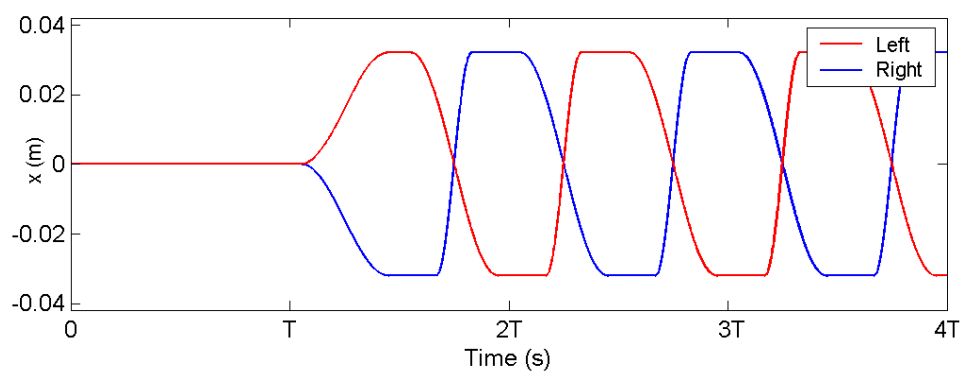


Figure 5.9: Foot placement trajectories for sagittal plane movement



## 5.2 Walk-Stepper Controller

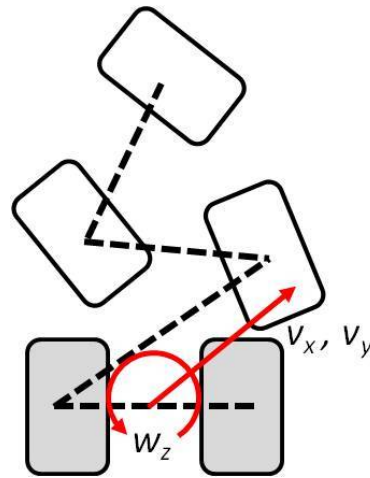
The omnidirectional walking is parametrized as  $p \in \{ p = (x_{step}, y_{step}, \theta_{step}) \mid p_{min} \leq p \leq p_{max} \}$  where  $(x_{step}, y_{step}, \theta_{step})$  are continuous values. As the frequency of the lateral walk-oscillations is pre-determined and fixed, the velocities of the walking can be defined as  $\dot{p} = (v_x, v_y, w_z)$  (Fig. 5.10). A walk-stepper controller is implemented to control the walking by regulating the step size for stability. The walk-stepper controller also determines the appropriate instances for step size to change in accordance to the input velocity commands  $(v_x, v_y, w_z)$ .

$$\begin{aligned} v_x &= f x_{step}, \\ v_y &= f y_{step}, \\ w_z &= f \theta_{step}, \end{aligned} \tag{5.7}$$

where  $f$  is the oscillating frequency.

### 5.2.1 Step Acceleration Control

The walk-stepper controller performs acceleration control by regulating the rate of change of the step size applied. Step acceleration control is adopted to minimize foot slip and sudden perturbations to maintain stability during fast dynamic walking. The step acceleration control regulates by determining the next step size in accordance to the velocity commands based on the current step size. A trapezoidal profile (Fig. 5.11) is applied for the acceleration / deceleration control where the maximum acceleration / deceleration for each movement is determined and tuned



*Arbitrary placement of the foot based on the input commanded velocities in the frontal, sagittal and transverse plane. The dotted line denote the physical link between the foot.*

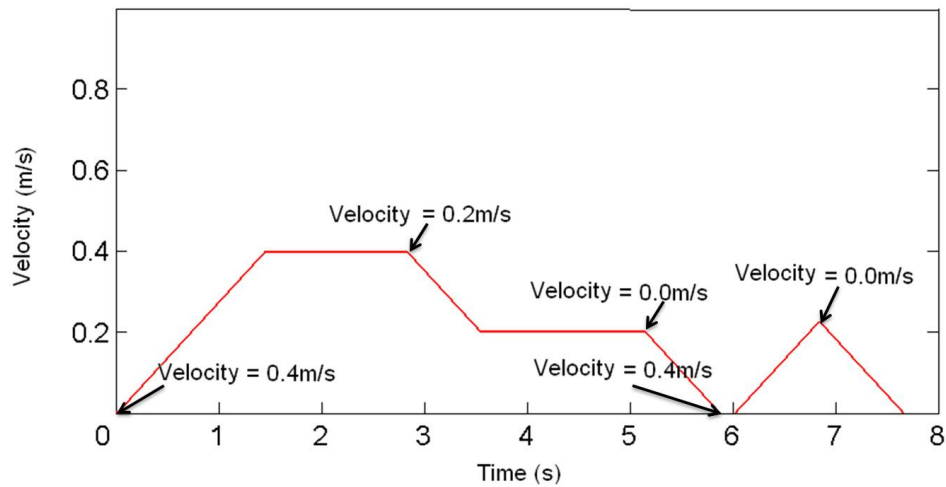
Figure 5.10: Omnidirectional walking

experimentally.

### 5.2.2 Concept of 'Master' Foot

The concept of a 'master' foot is used to determine the sequence and conditions that facilitate the combination of the movements to be executed. The 'master' foot is defined as the foot which is lifted and placed in the direction of the desired walk (Fig. 5.13). The 'master' foot is determined by the input velocity commands ( $v_x, v_y, w_z$ ) in the following order:

1. If  $v_y$  is non-zero, the 'master' foot is the foot of the direction of lateral stepping. Consider the humanoid is commanded to side step to the left ( $v_y > 0$ ), then the left foot is the 'master' foot. The rotation of the humanoid is solely facilitated by the 'master' foot using foot inner and outer turns (Fig.5.12).



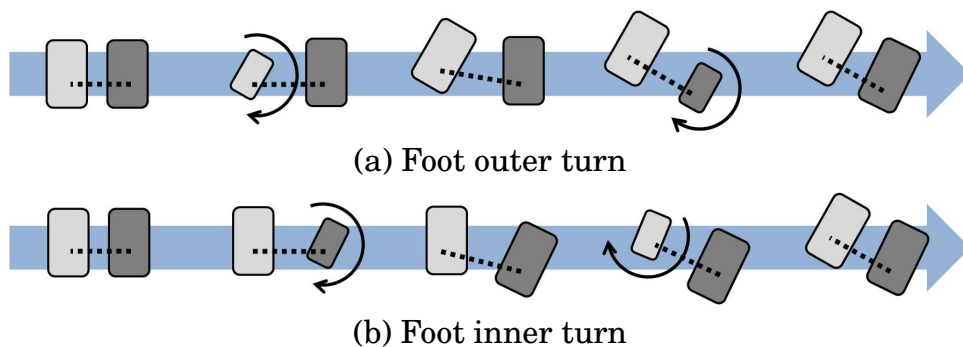
*Maximum walking velocity and acceleration / deceleration is  $0.4\text{m/s}$  and  $0.3\text{m/s}^2$  respectively. The arrow indicates the instance at which the walking velocity command is sent to the walk-stepper controller. Based on the acceleration profile, the walking velocity is determined and translated into the step size. Change of walking velocity is regulated to ensure that there is no abrupt change of velocity resulting in undesired dynamic forces being generated.*

Figure 5.11: Trapezoidal profile used for step acceleration control

2. If  $v_y$  is zero and  $w_z$  is non-zero, the 'master' foot is the lifted foot that facilitates a foot inner turn. A foot inner turn provides better stability in comparison to the outer turn.
3. In all other situations, the 'master' foot can be arbitrary selected to facilitate a faster response.

### 5.3 Motion Steering Controller

Foot slip occurs when the foot sole loses traction with the walking surface. When foot slips occurs, the motion control of the humanoid is severely degraded and it can lead to undesired motion behaviours such as instability.



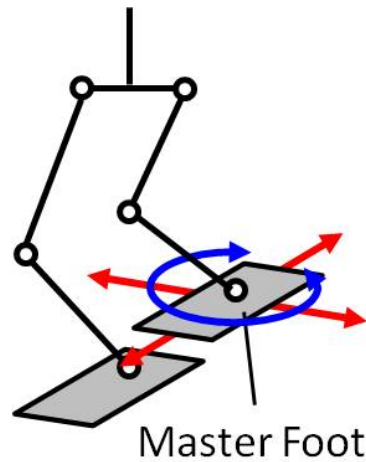
*The support polygon formed in the frontal plane by an inner turn is larger than an outer turn during double support phase (ankles are located nearer the heel than the toes) which allows larger deviations of ZMP from optimal and therefore, an inner turn provides better stability.*

Figure 5.12: Foot placement of transverse plane movement

Foot slip is not detectable through forward kinematics. In biped locomotion, foot slip occurs in the form of foot rotation (Fig. 5.14). In particular, foot rotation occurs during the single support phases where the supporting foot rotates and therefore changing the course of the walk direction. Solutions to reduce foot slip include the use of better traction material and limiting the acceleration and decelerations. In this work, a motion steering approach using rate gyroscope for feedback compensation is presented.

### 5.3.1 Motion Steering

The notion of motion steering is to compensate for foot slips to improve the directional control of the walk. Motion steering is realized through the use of sensory feedback. In this study, a rate gyroscope is used to determine the amount of angular deviation for feedback compensation. Motion steering attempts to correct not only angular deviations but also



*The placement of the 'master' foot determines the directional control of the walk.*

Figure 5.13: Concept of 'master' foot

displacement errors that are attributed due to error in angular velocity (Fig. 5.15). The estimations of the displacement errors is computed based on the angular error measured.

### 5.3.2 Step Displacement Estimation

The angular deviations of the humanoid is measured using a rate gyroscope mounted in the body. As instantaneous angular compensation for humanoid is difficult due to the complex dynamics involved for stability, a per step measurement method is used. Consider the scenario (Fig. 5.16) where the walk starts at the double support phase 'A' and is moving to double support phase 'B' based on the commanded velocities. At double support phase 'B', the amount of angular change ( $\theta_{measured}$ ) is measurable using the rate-gyroscope. The estimated displacement ( $\vec{x}_{y_{estimated}}$ ) based

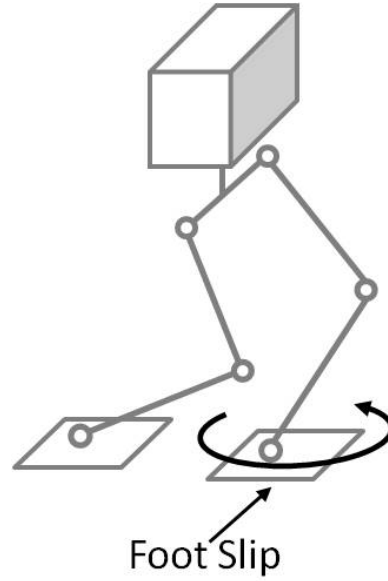
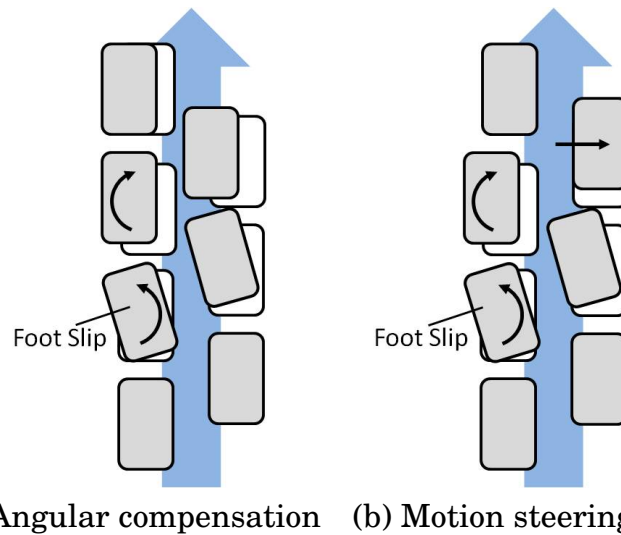


Figure 5.14: Foot slip problem

on the angular change is given as:

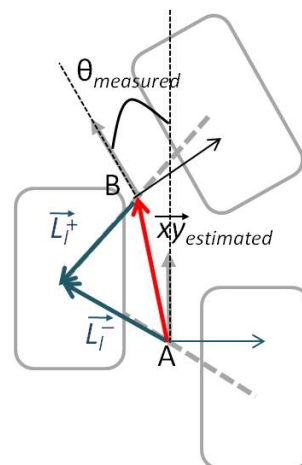
$$\vec{x}_{y_{estimated}} = \vec{L}_l^- - R(\theta_{measured}) \vec{L}_l^+, \quad (5.8)$$

where  $\theta_{measured}$  is the measured angular change per step using the rate-gyroscope.  $\vec{L}_l^-$  and  $\vec{L}_l^+$  are the positions of the support foot with respect to the CoM expressed in vectors.  $\vec{L}_l^-$  and  $\vec{L}_l^+$  are obtained using the forward kinematics of the joints.  $R$  is the rotational matrix that rotates the  $\vec{L}_l^-$  with respect to the CoM in double support phase 'A'. Based on the step displacement, the measured velocities of the step is given by  $\dot{p}_{measured} = (fxy_{estimated}, f\theta_{measured})$ , where  $f$  is the oscillating frequency.



*Angular compensation does not correct the displacement errors in the walk direction for the frontal and sagittal plane movements.*

Figure 5.15: Compensation techniques for foot slip



$\theta_{measured}$  is the amount of angular change measured using the rate-gyroscope and  $\vec{xy}_{estimated}$  is the displacement based on measure angular change.  $\vec{L}_l^-$  and  $\vec{L}_l^+$  are the kinematic vectors with respect to the CoM.

Figure 5.16: Step displacement estimation

### 5.3.3 Velocity Compensation

The motion steering controller tracks the displacement error and translate the error into additional velocity commands for compensation. Consider that  $p_{measured}^k$  and  $p_{desired}^k$  is the measured and desired displacement and angular position at step  $k$  respectively. The error,if any foot slip, is given by:

$$p_{error}^k = p_{measured}^k - p_{desired}^k. \quad (5.9)$$

The desired displacement and angular position at step  $k + 1$  is computed as:

$$\begin{aligned} p_{command}^{k+1} &= \frac{\dot{p}_{command}^{k+1}}{f}, \\ p_{desired}^{k+1} &= p_{desired}^k + p_{command}^{k+1} - p_{error}^k, \\ \dot{p}_{desired}^{k+1} &= f p_{desired}^{k+1}, \end{aligned} \quad (5.10)$$

where  $\dot{p}_{command}^{k+1}$  is the velocity command for step  $k + 1$ ,  $f$  is the oscillating frequency and  $\dot{p}_{desired}^{k+1}$  is the desired velocity for the following step.  $\dot{p}_{desired}^{k+1}$  is the compensated velocity output to the walk-stepper controller.  $p_{desired}^{k+1}$  is registered by the motion steering controller as the desired displacement and angular position for the next step and used for computation. This allows the motion controller to keep track of the error even when the following step fails to compensate due to constraints enforced by the walk-stepper controller.



## 5.4 Simulations

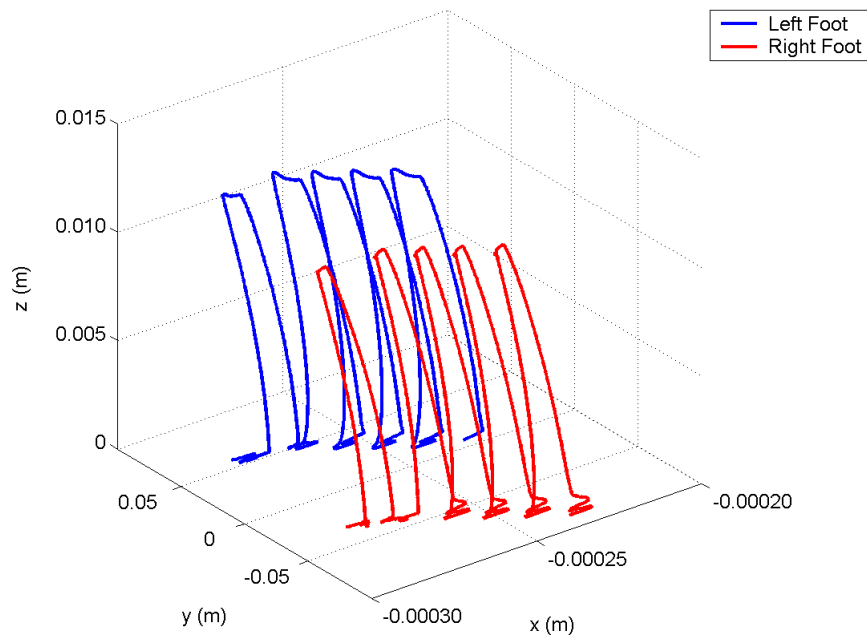
The omnidirectional walk generator is simulated in the MATLAB / Simulink and Autodesk Inventor Dynamic Simulation environment. Table 5.2 shows the parameters used in the simulation. Dynamic walk is initiated after the first oscillation cycle of lateral motion.

Table 5.2: Parameters for omnidirectional walk simulation

Parameter	Value
Oscillating Frequency, $f$ (Hz)	2.0
Oscillating Frequency, $\omega$ (rad/s)	12.566
CoM Lateral Shift Amplitude, $A$ (rad)	0.0100
Desired Peak ZMP Amplitude, $ p_{y(peak)} $ (m)	0.0502
Foot Clearance (m)	0.025
Time Period for Foot Lift Motion (s)	0.06
Time Period for Foot Landing Motion (s)	0.06
Ground Contact Stiffness (N/mm)	$2 \times 10^3$
Ground Contact Damping (N s/mm)	$2 \times 10^2$
Commanded Frontal Speed (m/s)	0.02
Commanded Sagittal Speed (m/s)	0.08
Commanded Transverse Speed (rad/s)	0.13

### 5.4.1 Frontal, Sagittal and Transverse Plane Movements

The movements in the various planes are independently simulated by applying the respective step / rotation commands. Movements are generated in real-time based on the time instances from the phase generator of the lateral walk-oscillations generator.



*Variation in the foot trajectories for single and double support phases is due to the phase generator to assert stability.*

Figure 5.17: Foot trajectories for frontal plane movement

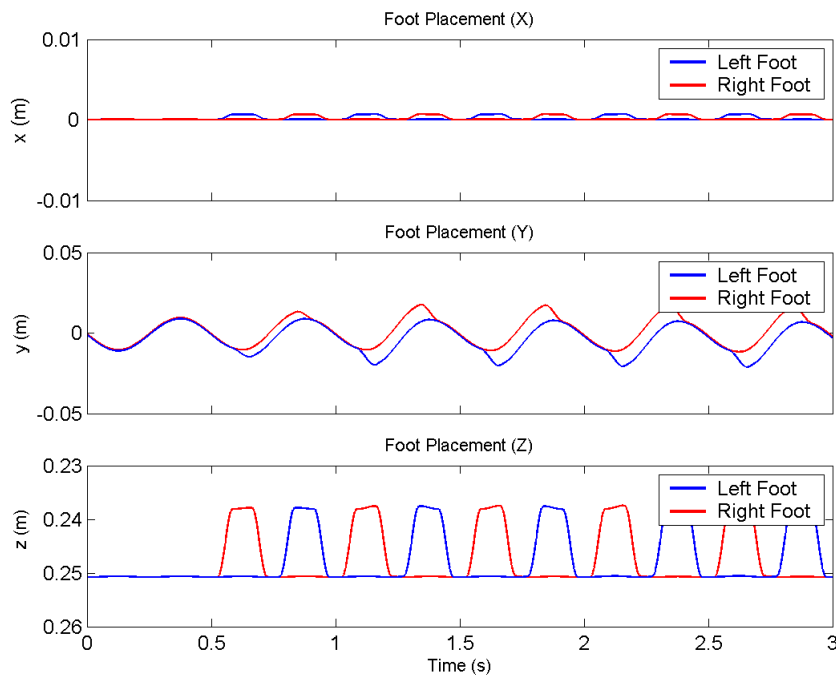


Figure 5.18: Real-time foot placement trajectories generated for frontal plane movement

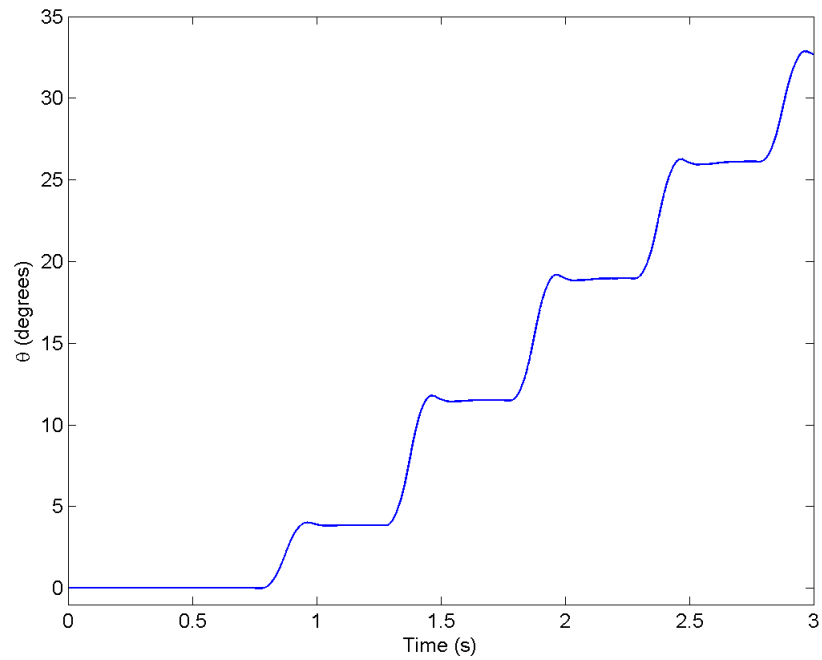


Figure 5.19: Angular change during transverse plane movement

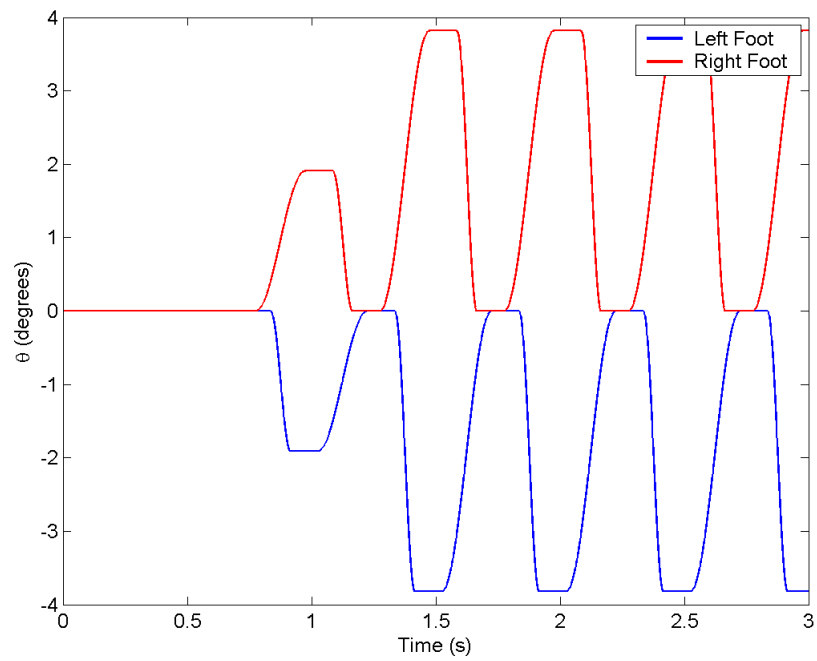
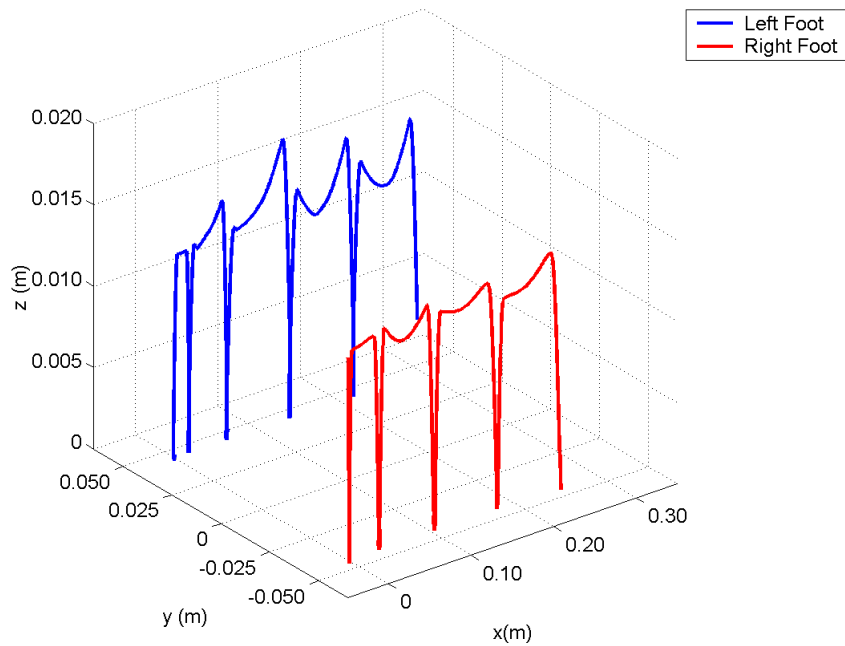


Figure 5.20: Real-time hip yaw joints trajectories generated for transverse plane movement



*Smaller step size during the initial phase of walking due to step acceleration control by Walk-Stepper controller.*

Figure 5.21: Foot trajectories for sagittal plane movement

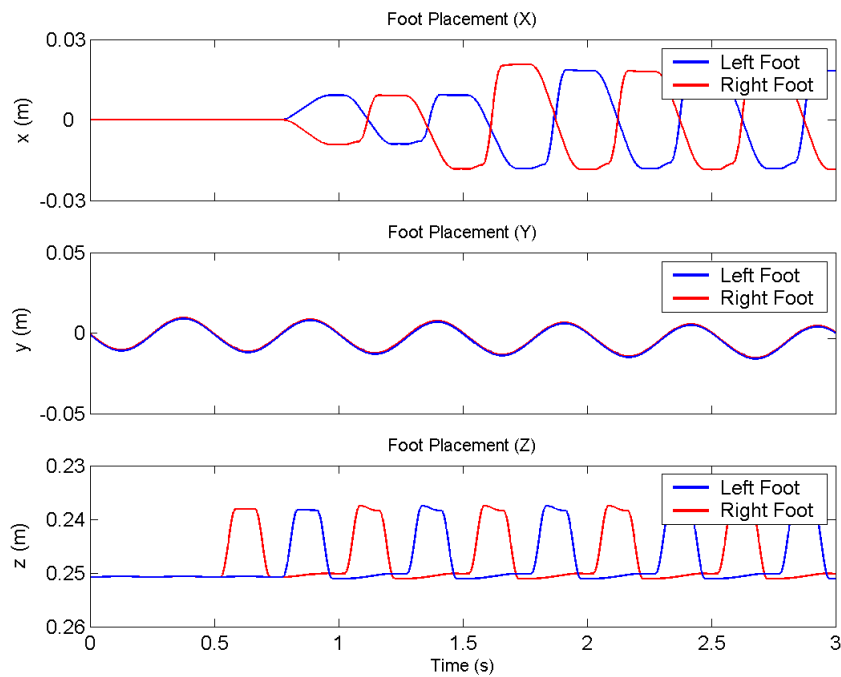


Figure 5.22: Real-time foot placement trajectories generated for sagittal plane movement

Fig. 5.17 to Fig. 5.22 show the result outputs of the individual plane movements generated in real-time for walking. It is seen that the foot placement trajectories generated produce sustained walking gaits in the various movements. The variations in the walking as observed in the foot placement trajectories in the 3D plot is due to the dynamic time instances generated by the phase generator within the lateral walk-oscillation generator.

### 5.4.2 OmniDirectional Walk

The generation of the omnidirectional walk is simulated by applying the velocity commands in various plane at the same instance. The velocity command  $\dot{p} = (0.08, 0.02, 0.13)$  is send to produce the omnidirectional walk.

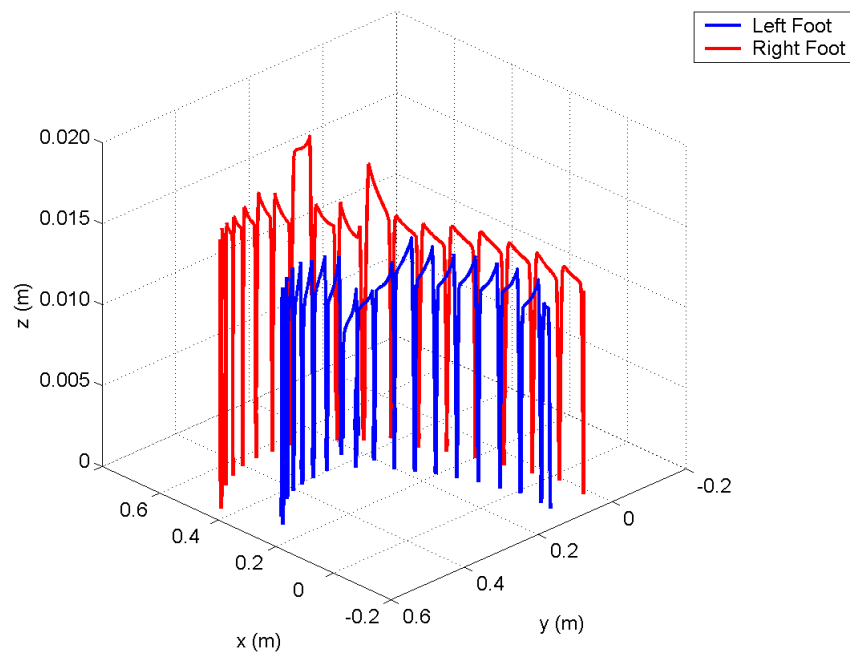


Figure 5.23: Foot trajectories for omnidirectional walk

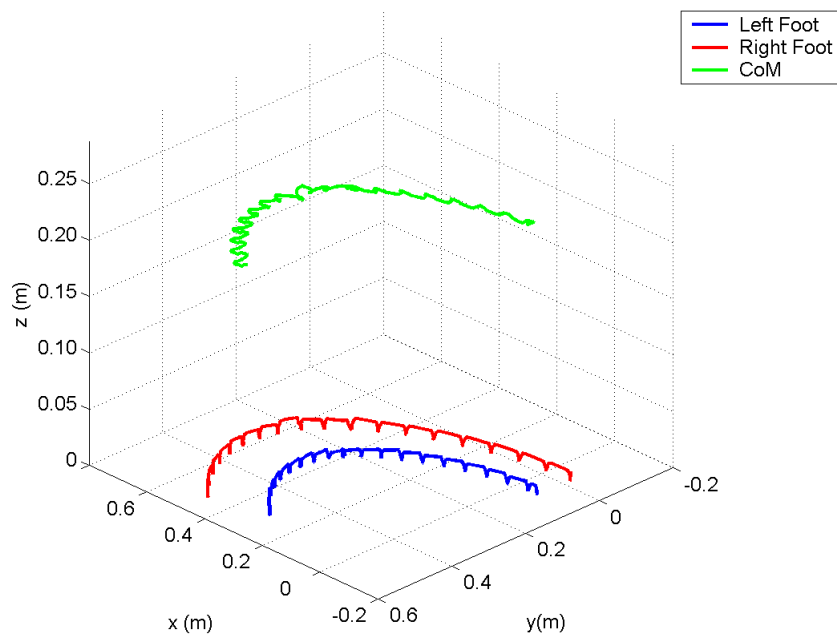


Figure 5.24: CoM and foot trajectories for omnidirectional walk

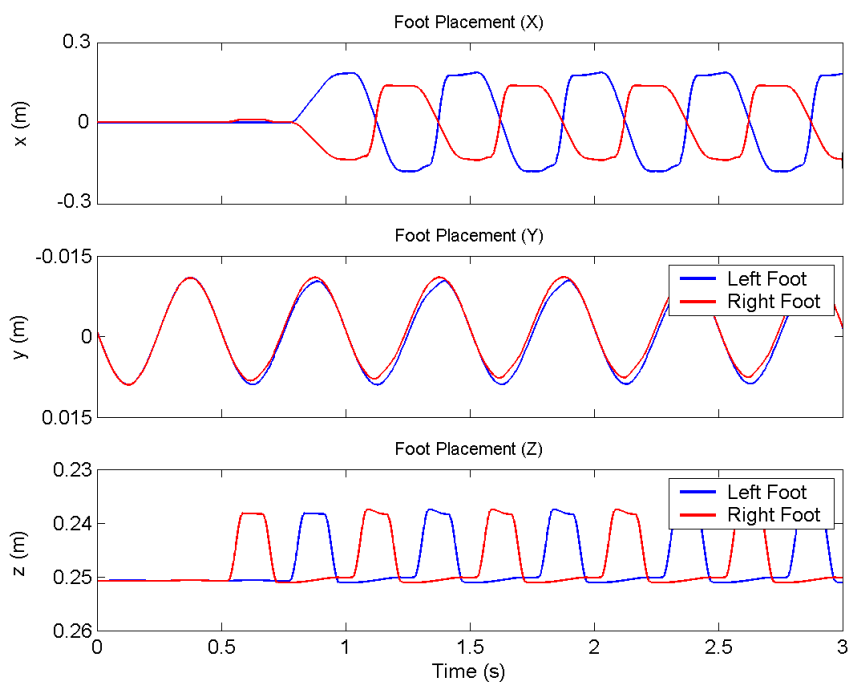


Figure 5.25: Real-time foot placement trajectories generated for omnidirectional walk

Fig. 5.23 and Fig. 5.24 show the trajectories of the CoM and foot in the 3D space. The results show that sustainable omnidirectional walking gaits are produced by using the superposition theorem to combine the various plane movements. The velocity command sent is constant which should result in a perfect circular path as the humanoid is walking forward, turning and side stepping at the same time. The distortion of the perfect circular path is due to the initial acceleration required based on the walk-stepper controller. The fairly repetitive foot placement trajectories (Fig. 5.25) generated in real-time highlight that the gaits produced is consistent and sustainable.

## 5.5 Experiments

The real-time gait generation of omnidirectional walking is applied to the REJr humanoid robot. The walk-stepper and motion steering controller are implemented in the low level micro processor of the robot which operates at 80MHz. Rate-gyroscope sensors mounted in the humanoid foot are used to measure the ZMP at a sampling of 200Hz. A threshold filter and Runge-Kutta filter is applied to the gyroscope readings. The joint actuators are commanded at a frequency of 50Hz. Position feedback of the joints are obtained at the same frequency. The commanded walking velocities are send wirelessly via a game controller. The parameters applied for the experiment are shown in Table 5.3.

Table 5.3: Parameters for omnidirectional walk experiment

Parameter	Value
Oscillating Frequency, $f$ (Hz)	2.0
Foot Clearance (m)	0.025
Time Period for Foot Lift Motion (s)	0.06
Time Period for Foot Landing Motion (s)	0.06

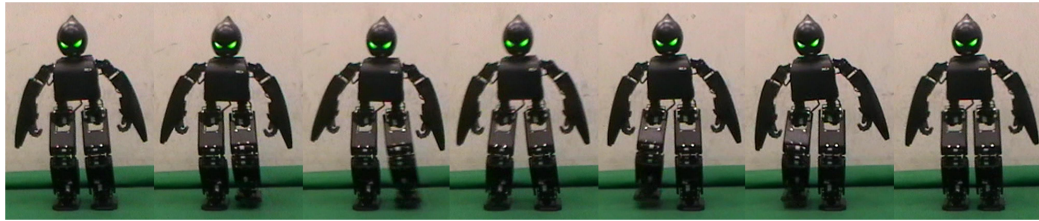
Table 5.4: Velocities and accelerations for omnidirectional walk

Parameter	Value
Maximum Sagittal Velocity (m/s)	0.35
Maximum Frontal Velocity (m/s)	0.15
Maximum Transverse Velocity (rad/s)	0.54
Maximum Frontal Acceleration ( $\text{m/s}^2$ )	0.20
Maximum Sagittal Acceleration ( $\text{m/s}^2$ )	0.10
Maximum Transverse Acceleration ( $\text{rad/s}^2$ )	0.18

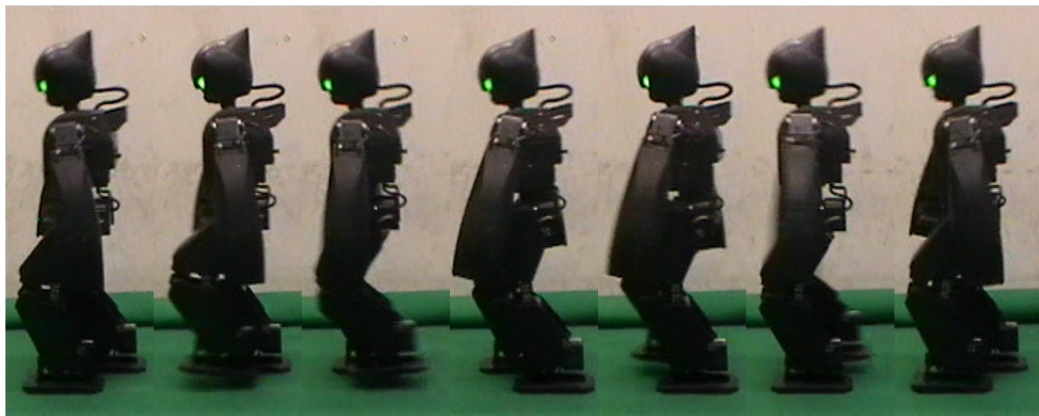
### 5.5.1 Plane Movements

The humanoid is commanded to generate frontal, sagittal and transverse movements separately on a carpeted surface (Fig. 5.26). The walk-stepper controller is manually tuned to ensure that the walk produced is sustainable. Fig. 5.26 shows the frontal, sagittal and transverse plane movement generated by the humanoid. The ability to produce sustainable walking motion highlights that the real-time gait generation approach is effective. The walking motions in the various planes are tuned experimentally by modifying of the walk-stepper acceleration profile. Table 5.4 shows the maximum walking speed and acceleration for the various plane movements.

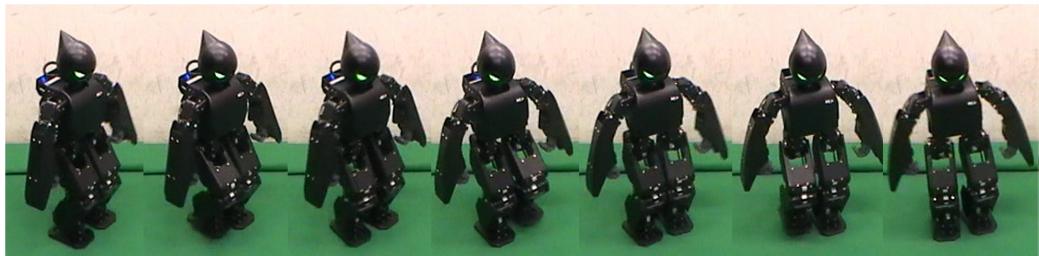




(a) Frontal plane movement



(b) Sagittal plane movement

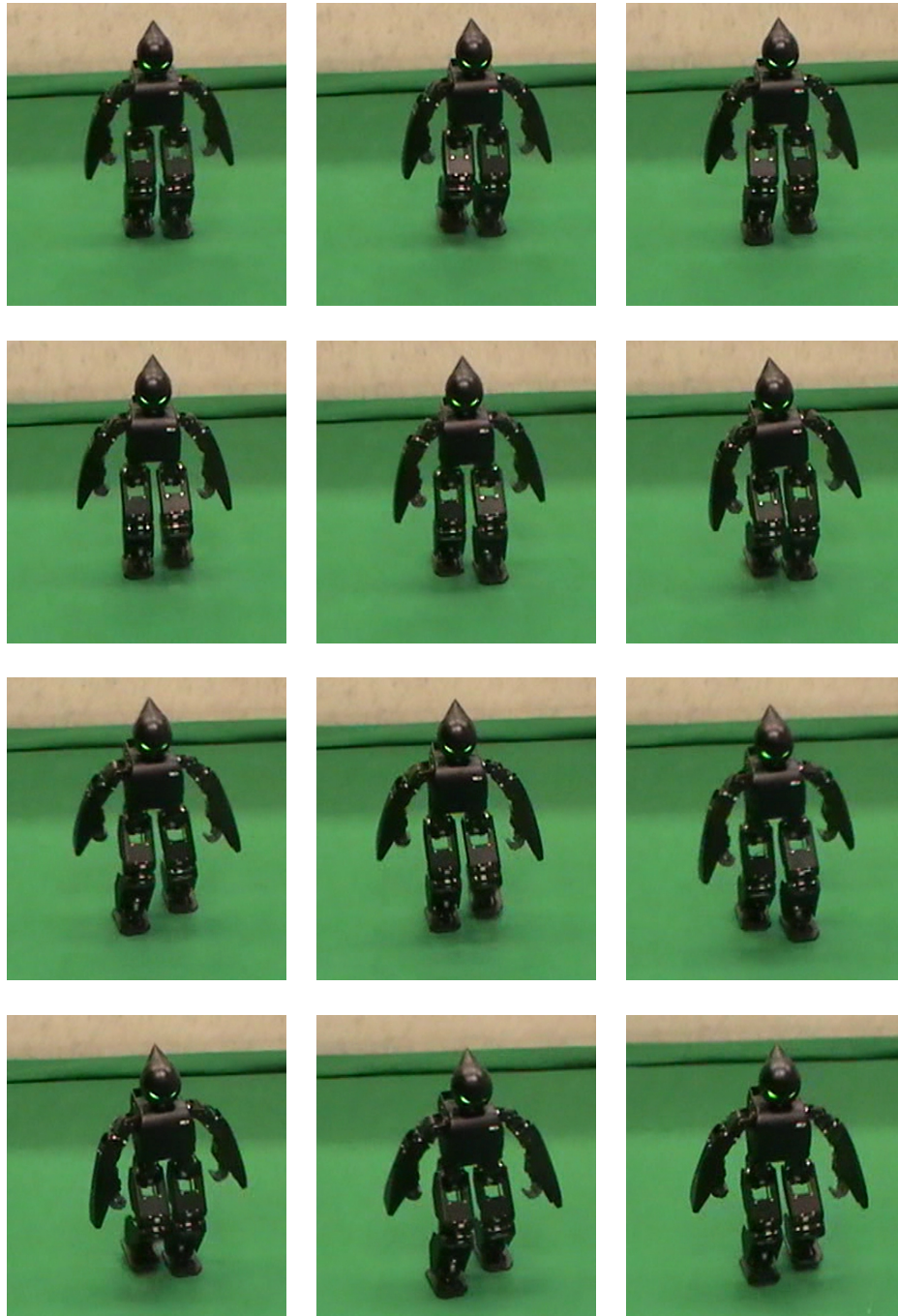


(c) Transverse plane movement

Figure 5.26: Walking movements

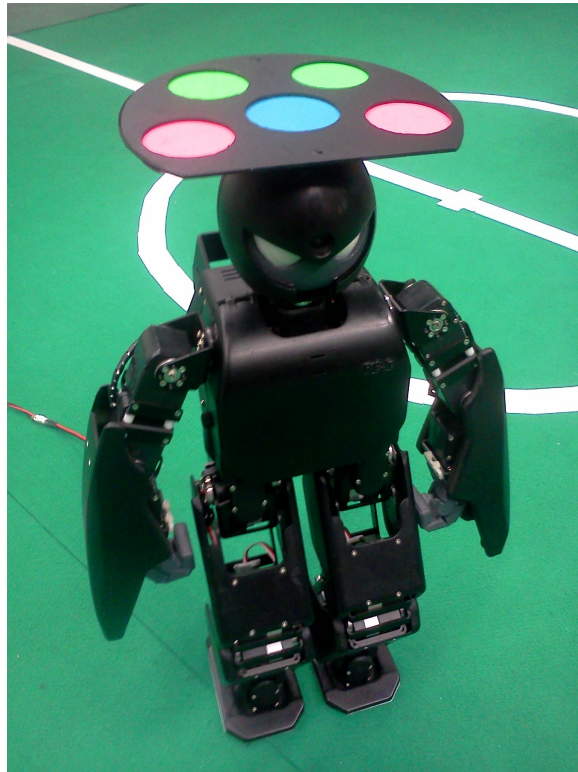
### 5.5.2 OmniDirectional Walk

The omnidirectional walk is implemented by combining the motions in various planes. Fig. 5.27 shows the snapshots of the implemented walk on the humanoid. The humanoid is moving forward, side stepping to the right and turning to the left.



*Humanoid robot performing the frontal, sagittal and traverse plane movement at the same time to achieve omnidirectional walking.*

Figure 5.27: Omnidirectional walking



*The overhead camera above the walking field tracks the position and orientation of the humanoid using the color markers mounted on the robot head.*

Figure 5.28: Color markers mounted on the humanoid head

The experimental results shows that the omnidirectional walk implemented is successful. Parametrization of the walking is also achieved with the walk-stepper controller.

### **5.5.3 Motion Steering**

The motion steering controller is implemented on the humanoid. To measure the walk, a camera tracking system based on the RoboCup SmallSize vision system [126] is used. A overhead camera tracks the movement of the humanoid by the color marker mounted on the head of the humanoid

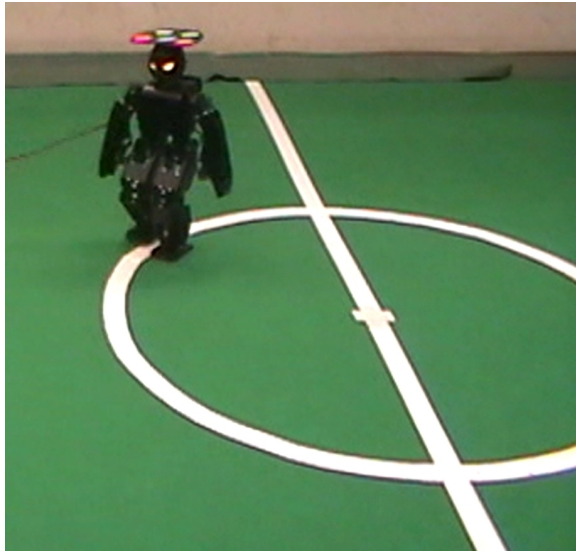


Figure 5.29: Humanoid set on a circular path

(Fig.5.28). Two experiments are conducted on the humanoid. The first is a straight line walk experiment where the humanoid accelerates from rest to the commanded velocity in a straight line for 2 m. The second experiment sets the humanoid on the circular path based on a fixed velocity command (Fig. 5.29).

From the experimental results, it is observed that the humanoid with motion steering is able to conform to the desired path better. In the straight line experiment, the humanoid direction changed without motion steering whereas with motion steering, the humanoid is fairly able to walk a straight path. In the circular path experiment, the humanoid with motion steering attempts to conform to the desired path whereas without motion steering the humanoid deviates away from the desired path (Fig.5.30). Due to foot slip and possibly asymmetric hardware, the humanoid in its nature can not conform well to the desired path. The problem of asymmetric hardware can be overcome by experimental calibration whereas the degrading control effect of foot slip is erratic. Although the

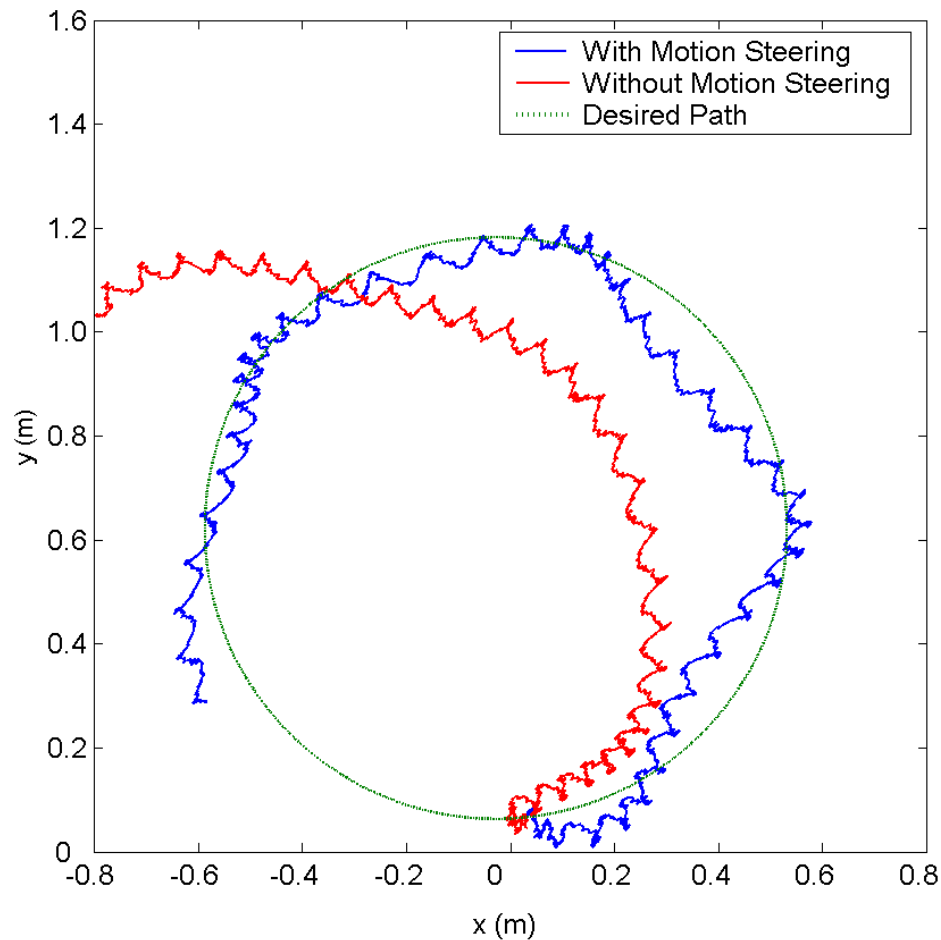


Figure 5.30: Captured movement of humanoid set on a circular path

humanoid without motion steering provides a much smoother and circular shape path, it deviates significantly from the desired path. This is particularly undesirable in the case of memory-mapping of the walking in humanoids for localization purposes. With motion steering, the conformation of the humanoid to the desired path improved. The inability to fully conform to the desired path with motion steering is due to the limitation enforced by the walk-stepper controller. The walk-stepper controller limits the rate of change of foot step to ensure stability and, therefore, instances where foot slip resulted in significant deviations which cannot

Table 5.5: Velocities and accelerations for omnidirectional walk with motion steering

Parameter	Without Motion Steering	With Motion Steering
Max. Sagittal Velocity (m/s)	0.35	0.40
Max. Frontal Velocity (m/s)	0.15	0.20
Max. Transverse Velocity (rad/s)	0.54	0.54
Max. Frontal Acceleration (m/s <sup>2</sup> )	0.20	0.30
Max. Sagittal Acceleration (m/s <sup>2</sup> )	0.10	0.12
Max. Transverse Acceleration (rad/s <sup>2</sup> )	0.18	0.18

be immediately compensated. Table shows the improved maximum velocities and accelerations for the plane movement with motion steering. The experiments show that motion steering helps to improve the directional control of the humanoid.

## 5.6 Conclusion

Real-time gait generation for omnidirectional walking is realized using simple sine and cosine functions that generate the foot placement trajectories in real-time. Based on the time instances dynamically generated by the lateral walk-oscillations, omnidirectional walking gaits are produced. A walk-stepper and motion steering controller is implemented. The walk-stepper controller regulates and superimposes the foot placement trajectories of various plane movements using a concept of a 'master' foot. Motion steering based on rate-gyroscope feedback is used to enhanced the directional control of the walk. The approach show successful results in both simulations and experiments in generating omnidirectional walking gaits.

# Chapter 6

## Compliant Control

The use of compliant control to improve biped locomotion has been studied extensively in recent years [78, 81, 83–85, 87, 88]. Compliant control is adopted to mimic the human muscles and tendons which can exercise controlled flexibility within a certain range. This flexibility makes the human walk versatile, dexterous and adaptable which is why researchers wish to adopt compliant control to enhance biped locomotion ability.

Compliant control is realizable using compliant mechanism and motion compliance. Compliant mechanism utilizes properties of material to achieve compliance. [79] proposed the use of compliant ankle joints using spring mechanism to provide good contact between the sole and the ground, and for foot landing impact reduction. The effective use of toe springs to facilitate running and hopping for biped robot is presented in [78]. A simple and low-cost leg-foot compliant system is achieved by combining visco-elastic material with metal [127]. Compliant mechanism is also realized by coupling compliant material with actuators. [128] employs ideas from both the active-actuated biped robot legs and the passive

dynamic walkers in the design of humanoid biped walking robot legs towards natural walking. However it is noted that the use of compliant material can induce undesired oscillations and disturb stability [129].

Motion compliant is realized by applying the control paradigm that produces motion exhibiting compliant characteristics such as a virtual spring-damper system. In [116] and [88], compliance is utilized to improve the quality of walk through the reduction of landing impact. The handling of dynamic walking environment is the key focus in many of the works on compliant motion in biped robots [82–85]. Robust walking control algorithm based on compliant control to handle uneven terrain has been reported in [86–88].

In this chapter, compliance is applied to the knees of a humanoid by configuring the parameters of the actuators. The compliant knees reduce the foot landing impact. The ground reaction force is estimated from the knee depression. For reduction of foot landing impact, a stiffness controller based on sensory feedback using the torso angular tilt of the humanoid is proposed. Estimation of the ground reaction forces is presented by utilizing the depression in the compliant knee joints and the readings of the accelerometers mounted on the humanoid body. The compliant joints in the ankle leads to saving in energy by under-actuating of the ankle roll joint during lateral walk-oscillations. The under-actuation of the knee joints leads to variable foot-step period which in turn leads to variation in walking frequency.

In section 6.1, the realization of compliant joints in the knee is presented. Section 6.2 describes the stiffness control used for reducing foot



landing impact. Section 6.3 discusses the estimation of the ground reaction forces with the help of the compliant joints and accelerometers. The energy-saving scheme is presented in Section 6.4. Section 6.5 concludes the chapter.

## 6.1 Compliant Knee Joints

In this work, the concept of compliant control is applied to the knee joints of the humanoid. Rather than using compliant mechanism which has the possibility of introducing uncontrollability [130], motion control based compliance is utilized.

### 6.1.1 Compliant Motion using Torque Control

Motion control based compliance is realized by manipulating the control of the knee joints. Considering the torque applied for the position control by the actuators in the knee is modelled as a proportional - derivative (PD) controller given by:

$$\tau = -k_p(\theta - \theta_{ref}) - k_v(\dot{\theta} - \dot{\theta}_{ref}) + \tau_{dist}, \quad (6.1)$$

where  $\theta$ ,  $\theta_{ref}$ ,  $\dot{\theta}$  and  $\dot{\theta}_{ref}$  are the current and reference positions and velocities.  $k_p$  and  $k_v$  are the gains of the PD controller and  $\tau_{dist}$  is the torque disturbance that is un-modelled or unknown. Assuming that  $\tau_{dist}$  is small, the torque applied is expressed as a torsional spring and damper system where the gains,  $k_p$  and  $k_v$ , are the spring constant and damping coefficient respectively. The knee actuators are realized as compliant joints (torsional spring and damper system) where the stiffness and damping of

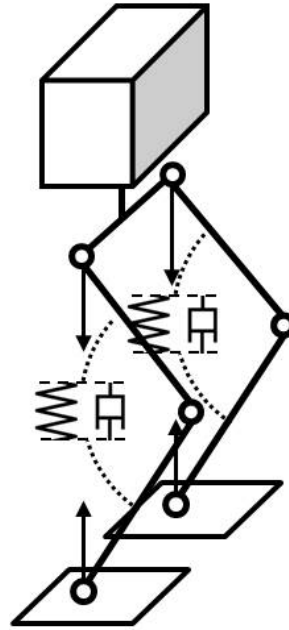


Figure 6.1: Spring-damper compliant knee joint

the joint is determined by the PD control gains (Fig. 6.1).

### 6.1.2 Stiffness and Damping Coefficients

The compliant joint is a position control system for actuation. To prevent the introduction of unwanted oscillations and vibrations, the critically damping of the compliant joint is desirable (damping ratio = 1). A critically damped spring-damper system returns to equilibrium as quickly as possible without oscillations. The stiffness and damping of the complaint joint is determined by:

$$\begin{aligned}\zeta &= 1, \\ &= \frac{k_v}{2\sqrt{mk_p}}, \\ k_v &= 2\sqrt{mk_p},\end{aligned}$$

(6.2)

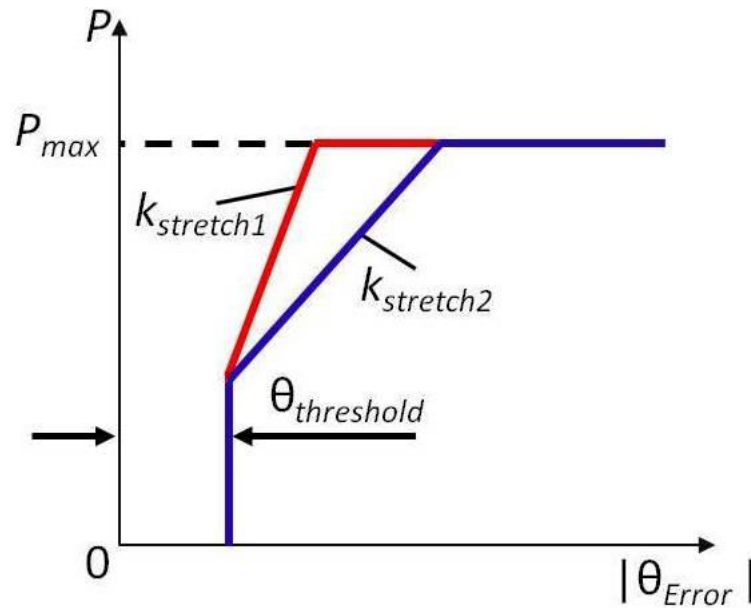


Figure 6.2: Servo control parameter  $k_{stretch1} > k_{stretch2}$  [4]

where  $m$  is the mass of the load and  $\zeta$  is the damping ratio. The gains of the PD controller are selected to ensure that the system is critically damped. With critically damped compliant joint, the controller parameter to decide is  $k_v$  or  $k_p$  (6.2). This parameter is to be translated to the actuator control parameter.

### 6.1.3 Translating to Actuator Control Parameter

The actuators utilized are digital servos with position control. The control gains of the servo are configured to model the PD torque controller for compliant control. Particularly of interest is the control gain parameter that determines the amount of the power applied. The control parameter

in relation to the power (Fig. 6.2) is given as:

$$P = \begin{cases} 0, & \text{for } \theta_{error} < \theta_{threshold} \\ k_{stretch}(\theta_{error}), & \text{for } \theta_{error} \geq \theta_{threshold} \\ & \text{and } P < P_{max}, \\ P_{max}, & \text{otherwise} \end{cases} \quad (6.3)$$

where  $k_{stretch}$  is the adjustable control parameter of interest in the servo.  $P_{max}$  is the maximum power rating of the servo and  $\theta_{threshold}$  is the minimum error threshold above which the power is delivered. As power relates to torque and velocity ( $P = \tau\dot{\theta}$ ), the parameter  $k_{stretch}$  relates to the gain by which the torque is supplied for actuation and is assumed to be equivalent to  $k_p$ . Experimental testing shows that the assumption is reasonable as the servo is able to exhibit stiffness characteristic of a compliant joint by adjusting  $k_{stretch}$ . Based on the maximum holding torque of the servo and from experiments, it is determined that the maximum and minimum stiffness are approximately 1103 Nm/rad and 8.689 Nm/rad respectively. It is noted that the servo does not allow a configuration where it can produce underdamped or undamped characteristic.  $k_{stretch}$  is an integer value ranging from 1 to 127 where 1 and 127 produce the minimum and maximum stiffness respectively. As such,  $k_p$  and  $k_v$  are step values of  $k_{stretch}$ . Compliance of the knee is determined by the parameter,  $k_{stretch}$ . The servo actuators in the knees of the humanoid are realized as compliant joints (Fig. 6.3).

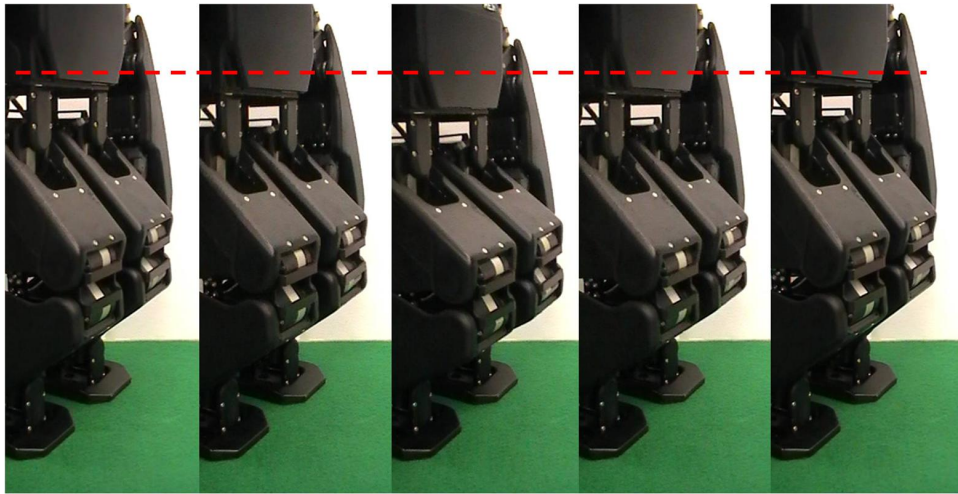


Figure 6.3: Compliant knee reacting to a force from the top

## 6.2 Foot Landing Impact Reduction

Impulsive forces are generated during foot landing which can cause instability to the humanoid during walking. Significant contact reaction forces are generated when the foot lands early and the foot strongly pushes down on the floor with large impact. This large impact creates a 'bounce' effect and introduces vibrations to the humanoid affecting stability. In this work, compliant knees are used for reducing the foot landing impact to enhance biped walking.

### 6.2.1 Foot and Ground Contact Model

The contacts between the humanoid foot and the ground are modelled as spring-damper interaction [87] (Fig. 6.4). The vertical ground reaction

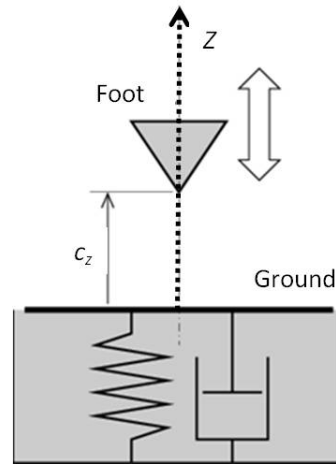


Figure 6.4: Spring-damper contact model

force is computed as:

$$F_{gz} = \max(0, -Kc_z - C\dot{c}_z f(-c_z)),$$

$$f(z) = \begin{cases} 1, & \text{for } 0.01 < z \\ 100z, & \text{for } 0 \leq z \leq 0.01 \\ 0, & \text{for } z < 0 \end{cases}$$

(6.4)

where  $F_{gz}$  is the vertical ground reaction force,  $c_z$  and  $\dot{c}_z$  are the position and velocity,  $K$  is the stiffness constant and  $C$  is the damping constant. No force is exerted when  $c_z$  is greater than zero. Contact forces are generated in two ways; when the foot 'penetrates' the ground giving  $z < 0$  or when the velocity upon impact is non-zero. In high stiffness material, penetration is minimum but the slightest penetration will result in large reaction forces being generated whereas in low stiffness material, the penetration will be larger but as the coefficient is small, smaller reaction force is generated. Hence, deformative material exhibiting low stiffness properties, such as foam and cushion, are often used for mechanical shock absorption in reducing landing impact.

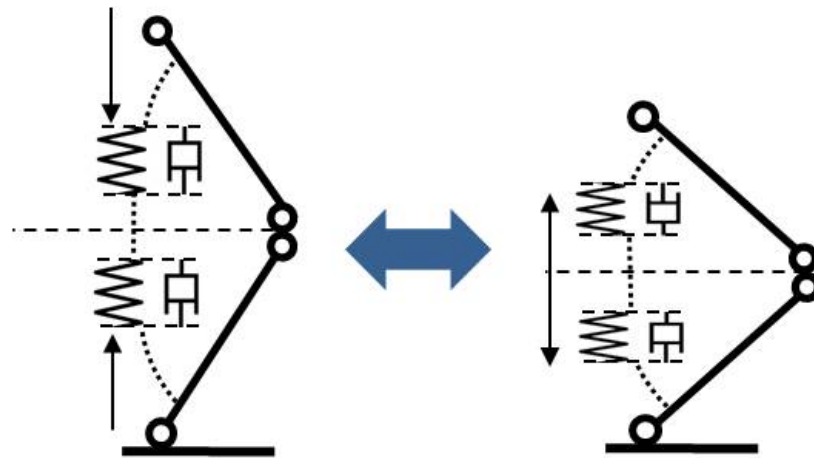


Figure 6.5: Virtual spring-damper system

### 6.2.2 Virtual Spring-Damper System

The compliant knee joints presented in Section 6.1 can be described as a virtual spring-damper system installed between the hips and the ankle. Using the parallel crank mechanism installed in the knee, the virtual spring-damper system with controllable stiffness is used to reduce the landing impact.

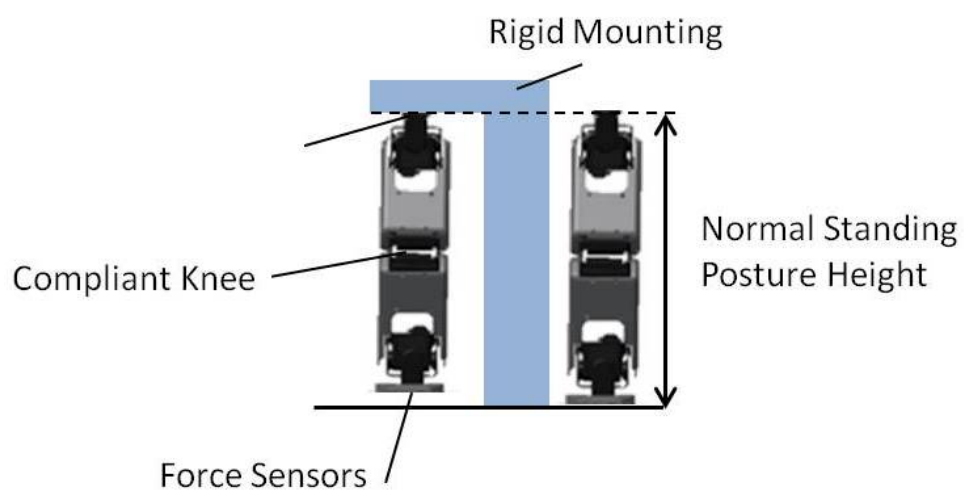


Figure 6.6: Foot landing impact experiment

Based on the foot and ground contact model, reaction forces are generated when the foot touches the ground with non-zero velocity and this describes the situation when the foot lands early. The problem is overcome by rapid modification of the hip vertical height to absorb the landing impact. This is achieved by applying an appropriate stiffness to the virtual spring-damper system. Using the force sensors mounted in the humanoid foot, an experiment is conducted to measure the ground reaction forces generated with various settings of stiffness executing the foot landing motion on a carpeted surface. The height of the hip is mounted at the standing posture (Fig. 6.6). Fig. 6.7 shows the results of the measured ground reaction forces with various stiffness coefficients. The result shows that with lower stiffness the impulse ground reaction force is reduced. However, if the stiffness is too low, oscillations are induced. Stiffness ( $k_p$ ) values of less than 260.55 Nm/rad are too low and cannot facilitate the foot lift and landing motion. Experiments (Fig. 6.7) shows that by applying a lower stiffness to the virtual spring-damper system (compliant knee joints) can reduce the landing impact. The stiffness coefficient of 434.3 Nm/rad is applied to the compliant knee joints to generate lateral walk-oscillations. The motion of the humanoid is observed to be smoother but with an increased tilting of the body in the frontal plane. Impact reduction is realized using the compliant knee joints without the need of force sensing devices.

### **6.2.3 Stiffness Control using Angular Tilt Measurement**

Using the inertia measurement unit and Kalman filter, the angular tilt of the body in the frontal plane is measured with and without the compliant



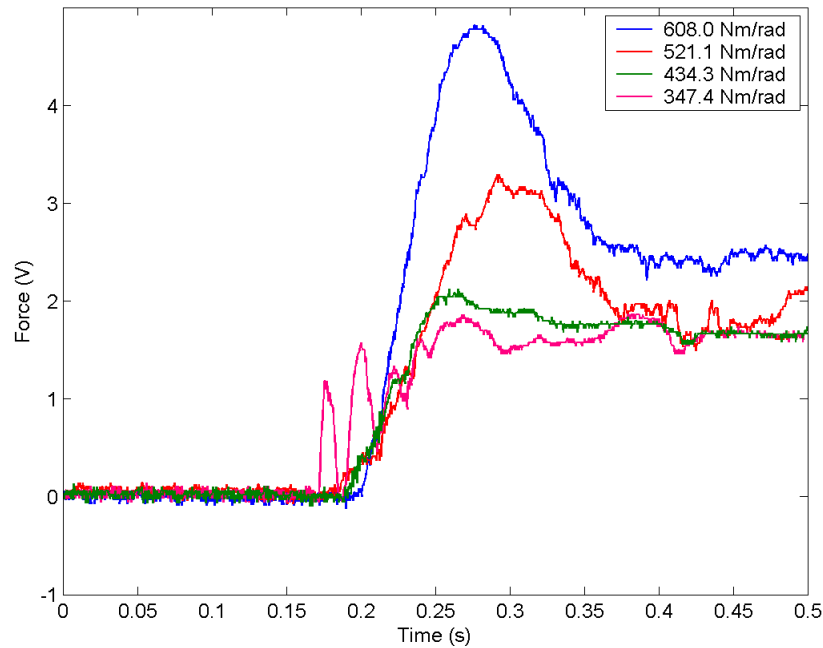


Figure 6.7: Stiffness versus ground reaction force

joints to validate the observation made in section 6.2.2. Fig. 6.8 shows the angular tilt of the humanoid in the frontal plane measured during lateral walk-oscillations with and without the compliant joints. The result show that the angular tilt of the body becomes smoother with the compliant knee joints which likely explains the smoother motion observed. However, there is an increase in the amount of body tilting (Fig. 6.9).

The forces acting on the two knees changes when the CoM shifts laterally towards the supporting foot during double support phase, this results in unequal depression of the compliant joints. The phenomena becomes more apparent when lower stiffness is applied as lower stiffness creates a greater amount of depression for the same force exerted. This leads to tilted hip and in turn leads to undesired tilting of the humanoid in the frontal plane (Fig. 6.10). A simple solution is to apply the lower stiffness

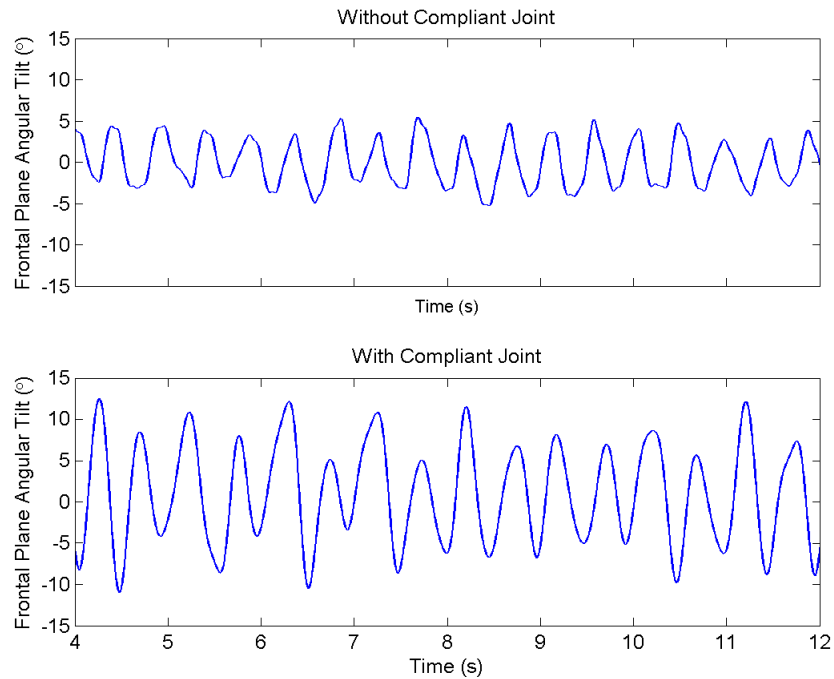


Figure 6.8: Angular tilt in the frontal plane with and without compliant knee joints

only during foot landing. However, instantaneous transitions from low stiffness to high stiffness can lead to sudden jerks in the motion and to determine the time instance for such transition is difficult. To address the issue, a stiffness controller is proposed to vary the compliance of the knee joints dynamically.

The notion of the stiffness controller is to allow the use of low stiffness while eliminating unequal knee depression and transition issues. The stiffness controller divides the control into the single and double support phases. It is assumed that the humanoid starts in the single support phase. A high stiffness coefficient  $k_{support}$ , equivalent to having no or little compliance, is first applied to the knee of the supporting foot whereas a low stiffness  $k_{impact}$  sufficient to facilitate foot lift and landing motion, and, for impact reduction is applied to the lifted foot. Upon foot landing,



Figure 6.9: Snapshot of unequal hip height phenomena

rather than immediately applying  $k_{support}$  to the landed foot's knee, the proportional-derivative (PD) controller takes ownership and governs the stiffness  $k_{control}$  applied. The PD controller performs a balancing act where it attempts to match the vertical height of the landed foot's side of the hip to that of the supporting foot hip side. To determine whether the hips are levelled, the angular tilt of the humanoid in the frontal plane is used as the reference input of the PD controller. The PD controller is implemented as follows:

$$k_{control} = k_p \theta_y + k_d \dot{\theta}_y, \quad (6.5)$$

where  $k_p$  and  $k - d$  are the controller gains.  $\theta_y$  and  $\dot{\theta}_y$  are the angular tilt and velocity of the body in frontal plane. The angular tilt and velocity is measured using the inertia measurement unit sensors mounted in

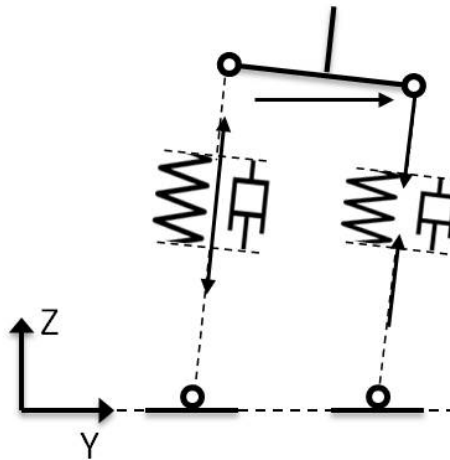
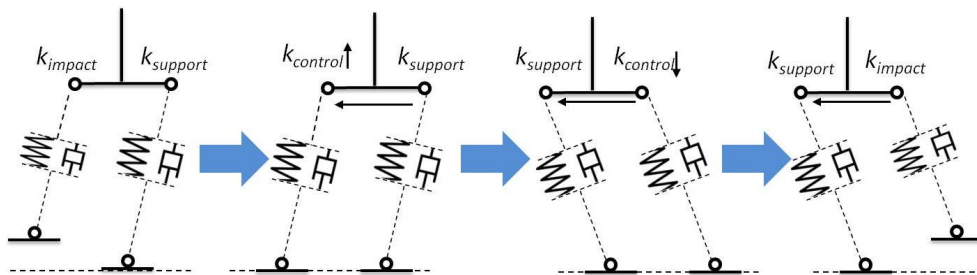


Figure 6.10: Resultant tilt due to unequal depression in compliant knees the body described in Chapter 2. The controller gains are tuned experimentally where the gains are adjusted to minimize the frontal angular tilting as much as possible without inducing undesired oscillations. As lateral shifting continue in which the CoM returns to the center,  $k_{control}$  is increased to  $k_{support}$ . The controller takes control over the stiffness of the supporting foot, which is intended to be lifted, whereas the other foot is applied with  $k_{support}$  stiffness. The controller releases the control upon foot lifting and  $k_{impact}$  is applied to the lifted foot. Fig. 6.12 shows the frontal plane angular tilt applying compliant knee joints with stiffness control. Fig. 6.13 shows the stiffness control system.

### 6.3 Estimation of Center of Pressure using Accelerometers and Compliant Joints

The humanoid has a total of 8 force sensors in the foot sole for ground reaction forces sensing to determine the CoP. These force sensors requires



*The stiffness of the knee is dynamically adjusted to minimize the amount of undesired angular tilt during double support phase.*

Figure 6.11: Stiffness control

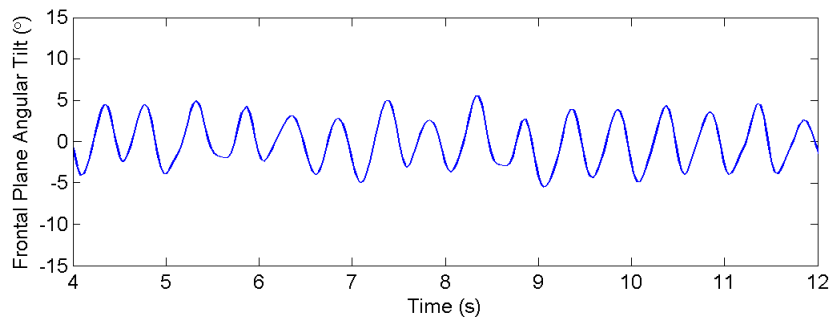


Figure 6.12: Angular tilt in the frontal plane with compliant knee joints and stiffness control

additional hardware such as power source, connections cable and customized foot mechanism installation. The approach is to eliminate the use of force sensors to minimize hardware dependency while maintaining the ability to infer the CoP. In this work, the accelerometers and compliant knee joints are used to infer the CMP.

### 6.3.1 Vertical Ground Reaction Force Estimation using Compliant Joints

Consider that the compliant knee joint is driving a load connected by a massless link in a particular plane with a force exerted on the load (Fig.

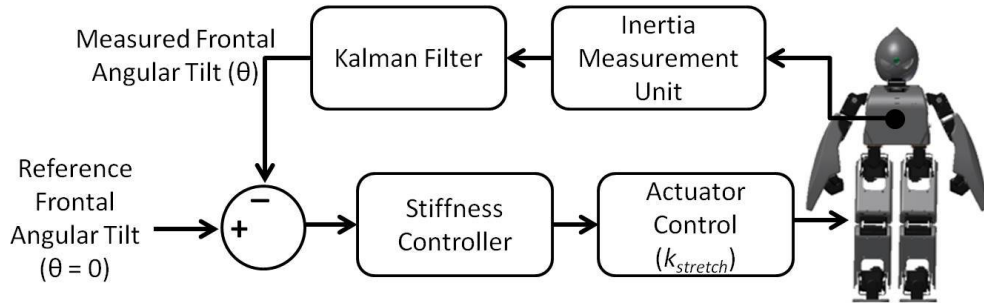


Figure 6.13: Stiffness control system

6.14). Motion equations of the system is given by:

$$k_p(\theta - \theta_{ref}) + k_v(\dot{\theta} - \dot{\theta}_{ref}) + ml^2\ddot{\theta} + lF_m \sin(\theta) = 0, \quad (6.6)$$

where  $F_m$  is the force acting on the system,  $\theta_{ref}$  is the reference position of the control system,  $k_p$  and  $k_v$  are the stiffness and damping coefficients, and,  $m$  is the mass of the load.  $\theta$ ,  $\dot{\theta}$  and  $\ddot{\theta}$  are the angular position, velocity and acceleration. Rearranging (6.6), the force acting on the system is given by:

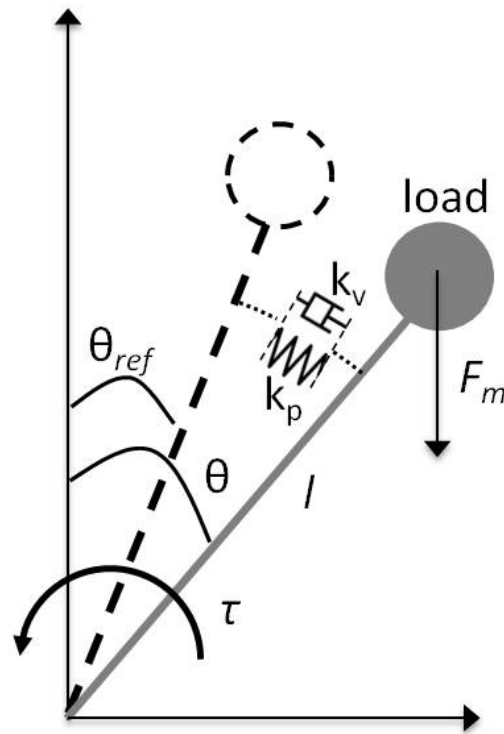
$$F_m = -\frac{k_p(\theta - \theta_{ref}) + k_v(\dot{\theta} - \dot{\theta}_{ref}) + ml^2\ddot{\theta}}{l \sin(\theta)}. \quad (6.7)$$

As  $\theta$ ,  $\dot{\theta}$  and  $\ddot{\theta}$  are measurable from the position feedback of the actuator, the force  $F$  exerted on the system is also measurable. The compliant knee joint therefore acts like a force measurement sensor.

The exerted force on the compliant knees is a force projection between the hip and the ankle (Fig. 6.15). Considering that the mass above the knees is much larger in comparison to that of below the knees, the force projected can be assumed as a vector estimation of the total vertical ground reaction forces acting on the system given by:

$$F_{gz} = -F_m \cos(\theta_{ankle-roll}) \cos(\theta_{ankle-pitch}), \quad (6.8)$$

where  $F$  is the measured force from the compliant joint,  $F_{gz}$  is the vertical ground reaction force, and,  $\theta_{ankle-roll}$  and  $\theta_{ankle-pitch}$  is the roll and pitch



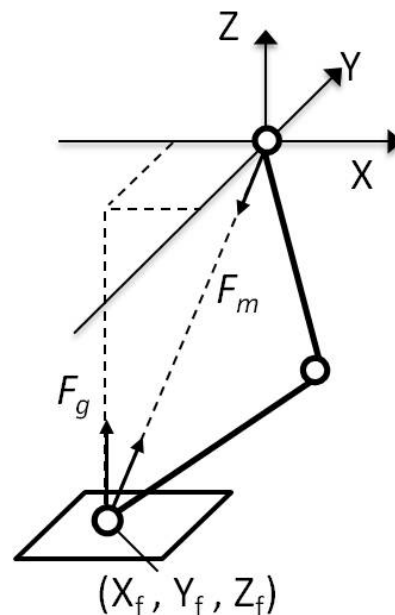
$\theta_{ref}$  is the reference position,  $\theta$  is the angular position,  $l$  is the length of the link,  $\tau$  is the torque acting on the system,  $F_m$  is the force acting downwards on the load, and,  $k_p$  and  $k_v$  are the stiffness and damping coefficients of the compliant joint.

Figure 6.14: Compliant knee joint with load

joint angles of the ankle respectively. Equating (6.7) into (6.8), the vertical ground reaction force is given by:

$$F_{gz} = \frac{k_p(\theta - \theta_{ref}) + k_v(\dot{\theta} - \dot{\theta}_{ref}) + ml^2\ddot{\theta}}{l \sin(\theta)} \cos(\theta_{ankle-roll}) \cos(\theta_{ankle-pitch}). \quad (6.9)$$

Fig. 6.16 shows the ground reaction force measured using force sensors and the compliant knee joints. The discrete readings of the force sensed by the compliant knee joints is due to the sampling rate of the actuators (50 Hertz). The estimated vertical ground reaction force is used to infer the CoP.



$F_g$  is the vertical ground reaction force,  $F_m$  is the projected and measured ground reaction force with respect to  $F_g$  between the hip and the ankle.  $X_f, Y_f, Z_f$  are the forces acting at the ankle.

Figure 6.15: Force projection and ground reaction force vector

### 6.3.2 Computation of Center of Pressure (CoP) using Accelerometers

The humanoid has accelerometers mounted in the body to measure the linear displacement acceleration in the frontal and sagittal directions. In Chapter 2, a Kalman filter with acceleration bias correction is presented that eliminates false acceleration readings due to angular tilting. The center of pressure (CoP) is the point on the ground where the resultant of the ground reaction force acts. When no horizontal moment acting about the body's CoM, the CoP coincides with the Centroidal Moment Pivot (CMP) [37] (Fig. 6.17). The ground reaction force is the cross product of the horizontal and vertical forces acting on the CoM. Assuming



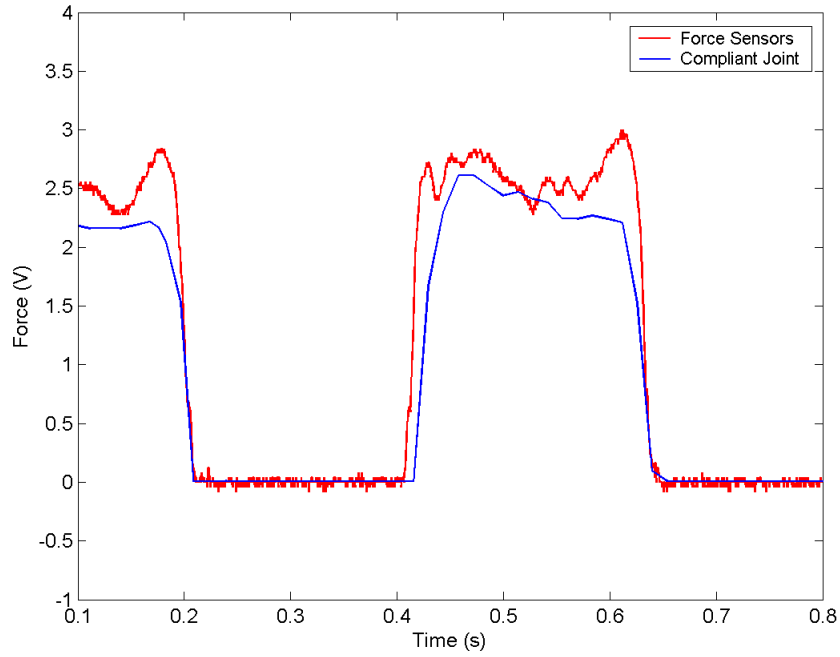


Figure 6.16: Force measured by force sensor and compliant knee joint

that the force exerted on the humanoid body is equivalent to that exerted on the CoM, the horizontal ground reaction forces are given by:

$$\begin{aligned} F_{gx} &= m\hat{X}_{Robot}, \\ F_{gy} &= m\hat{Y}_{Robot}, \end{aligned} \tag{6.10}$$

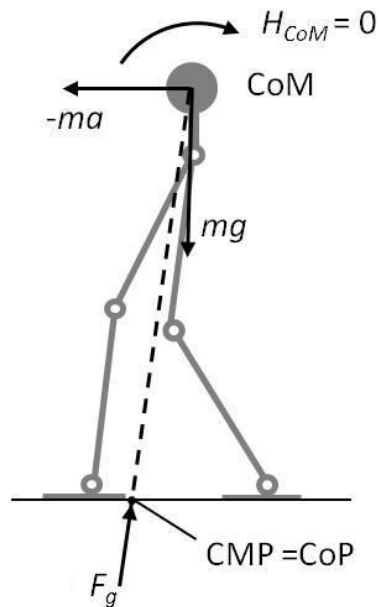
where  $\hat{X}_{Robot}$  and  $\hat{Y}_{Robot}$  are the sagittal and frontal accelerations of the CoM, and,  $m$  is the mass. The CMP location in terms of the CoM position [35] is given as:

$$\begin{aligned} x_{CMP} &= x_{CoM} - \frac{F_{gx}}{F_{gz}} z_{CoM}, \\ y_{CMP} &= y_{CoM} - \frac{F_{gy}}{F_{gz}} z_{CoM}, \end{aligned} \tag{6.11}$$

where  $(x_{CoM}, y_{CoM}, z_{CoM})$  is the position of the CoM in the Cartesian coordinate.  $F_{gx}$ ,  $F_{gy}$  and  $F_{gz}$  are the ground reaction forces.  $F_{gx}$  and  $F_{gy}$  are measurable from the accelerometers and  $F_{gz}$  is obtained by the compliant joints. The CMP is used to infer the CoP. However, in practice, accelerometer readings are noisy. Inferring of information from the accelerometer readings is non-trivial where the use of observer and filters can introduce time lag [93, 131]. Experimentations are used to strike a balance between the time lag and the noisy sensors reading. Fig. 6.18 shows the estimation of the CoP using the accelerometer readings and compliant joints obtained experimentally. The quantized trajectory is due to the low sampling rate (50 Hertz) of the compliant joint force measurement due to the commanding of the actuators. Further improvement work are required to make the estimation of the CoP suitable for better utilization. Concluding work on the estimation of the CoP did not totally materialize as the noisy reading from the accelerometer is difficult to utilize [93, 131]. Further research in the field of signal processing or sensor fusion is required to address the same. Nevertheless, the work on the estimation of the CoP serves as a demonstration on how the novel approach, using compliant joints for ground reaction force sensing, can be applied and highlighted future research work that can be done in compliant control.

## 6.4 Energy Saving using Under-Actuation

In this section, a method of under-actuation of the roll ankle joint during the single support phase is presented to conserve energy during lateral walk-oscillation. The method adopts the concept of passive-dynamics where momentum and inertia are used. The humanoid utilizes its own



$F_g$  is the ground reaction force,  $a$  is the horizontal acceleration of the CoM,  $g$  is acceleration due to gravity,  $m$  is the mass of the CoM.  $H_{CoM}$  is the body angular momentum.

Figure 6.17: Centroidal Moment Pivot (CMP)

momentum to return from the single support phase (Fig. 6.19).

### 6.4.1 Under-Actuation of Ankle Roll Joint

The under-actuation of the joint is realized by 'freeing' the actuator in the roll joint of the ankle in the supporting foot. It is noted that the 'freeing' of the actuator is different from having the lowest stiffness in the actuator. Due to the friction in the gearing, the freed actuator does not swing freely like a passive joint. The freed actuator exhibit characteristic of a damped oscillator. For ease of implementation, the model of the freed actuator is determined experimentally. Table 6.1 shows the characteristic of the freed actuator determined experimentally . However, if the humanoid body is

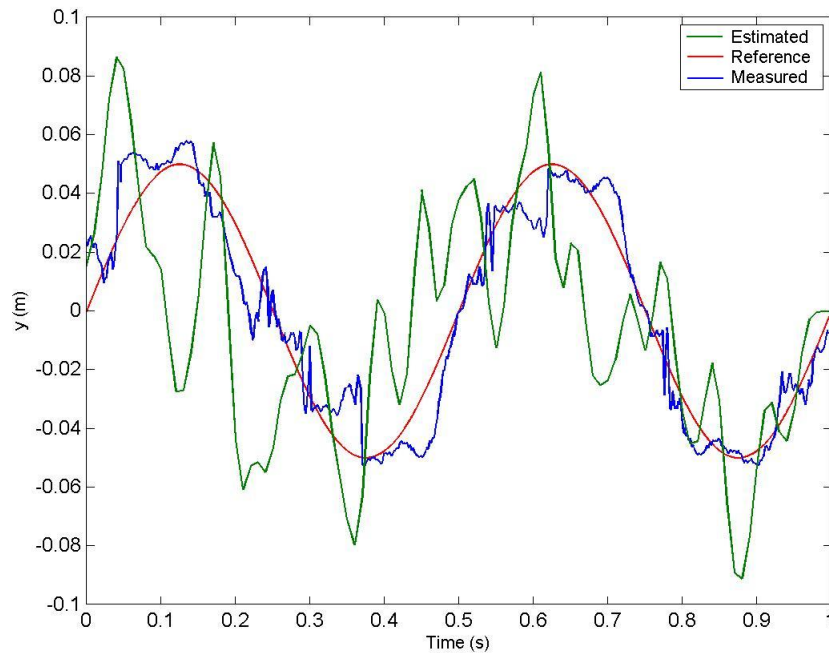


Figure 6.18: Center of Pressure (CoP) computed using accelerometer and compliant joint

allowed to fall freely, the hip of the lifted foot falls in the direction of the return (Fig. 6.20). To overcome this issue, during the period of under-actuation, the ankle roll joint (Fig. 6.21) of the supporting foot and the hip roll joints are commanded with under-actuated joint trajectories as follows:

$$\theta_{12} = \theta_{11} = \theta_2 = \theta_1, \text{ when } \theta_1 \text{ is under-actuated}$$

$$\theta_{12} = \theta_{11} = \theta_1 = \theta_2, \text{ when } \theta_2 \text{ is under-actuated}$$

(6.12)

Angular joints computed using inverse kinematic from the lateral walk-oscillation generator are over-written by the joints trajectories with under-actuation. Modifications are made to the phase generator within the lateral walk-oscillation generator.



Figure 6.19: Under-actuation for energy saving

Table 6.1: Characteristic of the freed actuator surface

Parameter	Values
Un-damped Natural Frequency, $w_d$ (rad/s)	5.342
Damping Ratio, $\zeta$	0.5222

## 6.4.2 Phase Tracking and Modified Oscillation Cycle

In Chapter 3, the generation of the offline gaits is based on predetermined oscillation frequency. With the introduction of under-actuation, the timing of the single support to double support phase possesses a certain degree of uncertainty. The phase generator tracks the single and double support phases. Based on the functions of the phase generator, the under-actuated phase is introduced as a special case of the single support phase. The phase occurs when the CoM is swinging laterally to the extreme and ending when the lifted foot lands (Fig. 6.22). During this phase, the applying of the joint trajectories given by (6.12) is the only change that occurs in principle. However, the time period of the under-actuation can vary in which the time for foot landing can be increased or decreased based on the

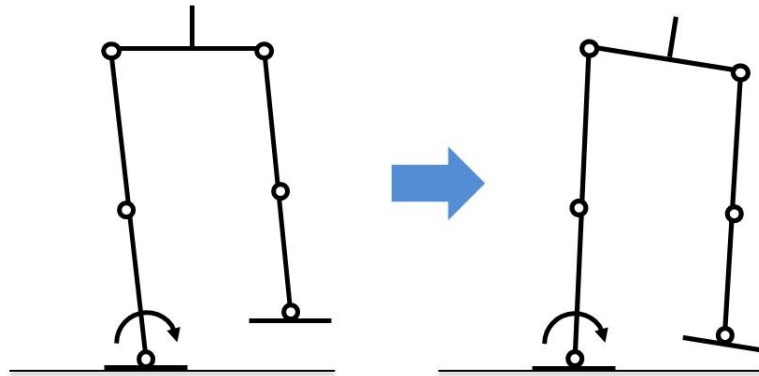


Figure 6.20: Falling of the lifted foot's hip

desired CoP. As such, there is a conflicting issue as depending on the difference between the walk oscillating frequency and the under-actuation damped frequency, the desired CoP might be drastically different. To overcome this issue, the phase generator is modified not to track the CoP for the bound (Chapter 4) given by:

$$y_{land} = A\left(1 + \frac{\omega^2}{\omega_n^2}\right) \sin(\omega(0.5T - T_{land})). \quad (6.13)$$

Instead, the bound is translated into the roll ankle joint in which the phase generator tracks the angular joint of the under-actuated ankle for determining the foot landing time instance. With the modified phase generator, the walk oscillates at a dynamic frequency.

### 6.4.3 Energy-Saving Measurement

The energy-saving scheme is implemented on the humanoid and an experiment is conducted to evaluate the effectiveness. The humanoid executes lateral walk-oscillation at two different frequencies, the desired walking frequency at 2 Hertz and the damped natural frequency of the freed actuator at 0.85 Hertz. In each oscillating frequency, a total of 20 trials

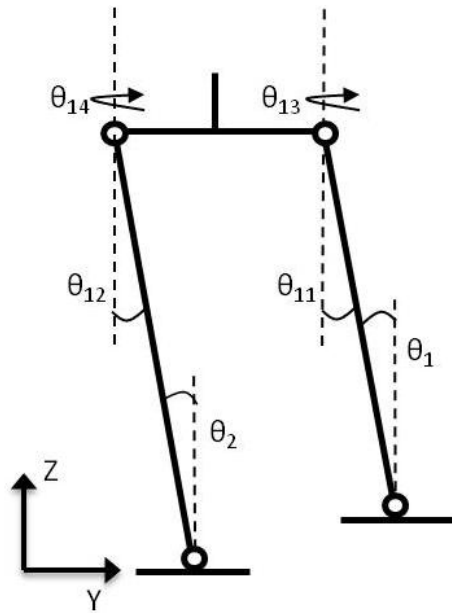
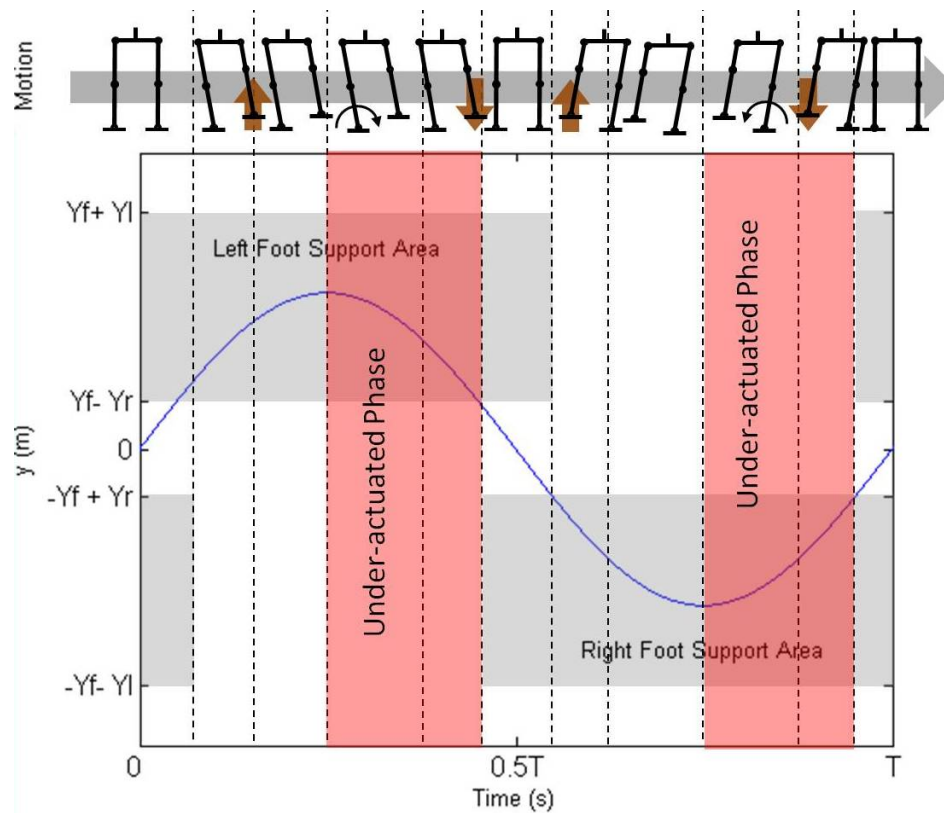


Figure 6.21: Roll joints of the ankle and hip

Table 6.2: Average voltage drop measured for 20 trials

Parameter	At 2Hz w/o scheme	At 0.85 Hz w/o scheme	At 2Hz w/ scheme	At 0.85 Hz w/ scheme
Avg. Volt. Drop.	0.647 v	0.455 v	0.619 v	0.378 v

are conducted. The humanoid runs on lithium polymer batteries which can provide up to 25 minutes of operation. At the beginning of each trial, the voltage is recorded and then the humanoid is set to oscillate for 10 minutes. Upon 10 minutes, the voltage of the battery is recorded again and the trial ends. The trial measures the amount of power consumed for providing 10 minutes of lateral walk-oscillations (Table 6.2). The result shows that the scheme is more effective if the humanoid is oscillating at the damped natural frequency of 0.85 Hertz.



*The under-actuated phase occurs when the body is swaying back from the single support phase at the extremes to the double support phase.*

Figure 6.22: Under-actuated phase

## 6.5 Conclusion

In this chapter, the use of compliant control implemented on the humanoid REJr is presented and discussed. Compliant control is applied to the knee joints of the humanoid and translated to the actuator parameter. The compliant knee joints are used for foot landing impact reduction and the estimation of the vertical ground reaction forces. The compliant knee joints act like a virtual spring-damper system installed between the ankle and the hip for shock absorption by applying low stiffness coefficient. A stiffness controller is proposed and implemented to eliminate the unequal



knee depression, and for a smooth transition from high to low stiffness to better facilitate the foot landing impact motion. A method of measuring the center of pressure (CoP) without explicit sensing is proposed. Utilizing force reading capability in the compliant joint and noisy accelerometer readings, the CoP is inferred from CMP. The use of under-actuation for energy-saving is realized through phase tracking. Experimental results show that the energy consumption is lower if the humanoid oscillates at the natural damped frequency of the under-actuated joints for smoother motion.

# Chapter 7

## Conclusion

### 7.1 Implemented Work

The research carried out on dynamic walking in this thesis is implemented on the humanoid robot 'REJr'. REJr actively participates in the KidSize Humanoid Soccer League competition at the annual robotics event, RoboCup. The work is successfully demonstrated during the competition where REJr has proved to be one of the faster walking robots in the competition (2011). Part of the work in the thesis, lateral walk-oscillations and omnidirectional walking, is generalized and have been applied to a larger size humanoid, 'Robo-Erectus Senior' (RESr) which participate in the AdultSize category of the soccer league competition. Success of the implemented work is highlighted when the RESr won the 1st runner-up for the AdultSize soccer league competition consecutively for 2 years, 2010 and 2011.

## 7.2 Summing Up

In this thesis, the work done on biped locomotion for a small size humanoid robot is presented. The aims for the research is to formulate an approach that provides a simple and effective dynamic walking gait generation for humanoid robot. Using a practical approach, the work presented addresses physical real system problem through theoretical studies, simulations and experimentations.

The first part of the thesis introduces the work done in the development of a small size humanoid robot, Robo-Erectus Junior (REJr). REJr is a 22 degree-of-freedom (DOFs) humanoid robot. The humanoid adopts the double parallel crank mechanism for actuation in the legs which provided redundancy in the DOFs for simplification of the inverse kinematic through the decoupling of motion. A closed-loop control architecture is implemented in the humanoid with various feedback sensors utilized for the gait generation of dynamic walking. Appropriate filters are applied with the necessary computations to make full use of the sensors equipped on-board.

In this research work, the dynamic walking motion is decoupled into ① lateral walk-oscillations and ② omn-directional walking. An offline gait generation of lateral walk-oscillations is presented and discussed. Using sinusoidal reference foot trajectories, stable lateral motion are generated using the linear inverted pendulum model (LIPM) based on the Zero Moment Point (ZMP) criterion. The lateral walk-oscillations are generated

from the ZMP trajectory in lateral motion. The influence of walking environment disturbance and limitation of the offline gait generation approach are studied through simulations. The proposed approach is successfully implemented on the humanoid REJr. Experimentation suggests that the use of the LIPM for reduced complexity and computation in designing the reference gait for lateral walk-oscillations is suitable. Implementation work on the humanoid shows that the offline gait generation of lateral walk-oscillations is viable.

The work on offline gait generation of lateral walk-oscillations is further extended. An online gait generation approach to produce sustaining lateral walk-oscillation online is presented. An offline gait reference with online feedback compensation approach is used for gait generation. ZMP based tracking and compensation control technique are applied and realized using a two-stage compensation system. The two-stage compensation system comprises of a lateral shift amplitude controller that corrects the shift amplitude after every oscillation and a real-time ZMP compensator that eliminates ZMP deviations within the oscillation cycle. A phase generator is incorporated to dynamically generate the time instances for the single and double support phases. The phase generator asserts stability for single to double support or vice versa transitions. The online gait generation approach is verified using simulation and through experimentation. Results show that the approach is able to produce sustainable lateral walk-oscillation even when subjected to walking environment disturbances.

The omnidirectional gait for dynamic walking is generated in real-time. The omnidirectional walking is decoupled into movement in the frontal,

sagittal and transverse plane. In each plane movement, sine and cosine functions are used to interpolate the motion for the desired direction of walk based on the dynamic time instances generated by the phase generator within the lateral walk-oscillation generator. Foot placement trajectories generated for the various plane movements are superimposed with the lateral walk-oscillations to produce omnidirectional walking. A walk-stepper controller is implemented to regulate the step size to generate sustainable dynamic walk. The concept of the 'master' foot is proposed to overcome the issues related to the superimposing of the plane movements. Improved directional control of the dynamic walk is achieved with the use of a motion steering controller. The controller determines the displacement and angular error due to foot slip during walking. The success of the approach is highlighted and demonstrated in simulation and implementation to produce sustainable dynamic walking.

Motion based compliance is introduced to improve the quality of the walking motion. Compliant control is applied to the knee joints of the humanoid and translated to actuator control parameter. Like a virtual spring-damper system installed between the hips and ankle, the compliant joint is utilized to reduce the landing impact of the foot. Experimentation shows that low stiffness can reduce landing impact but ill effects such as undesired tilting of the humanoid body during double support phase and jerky motion due to sudden change of stiffness are induced. A stiffness control based on the angular tilting of the body is implemented to vary the stiffness accordingly. Vertical ground reaction force sensing is realized by the measurement of the depression of the compliant knee joints. Coupled with accelerometer data, a method to infer the Center

of Pressure (CoP) without explicit sensing is proposed. A energy-saving scheme is devised to capitalise on the natural dynamics of the system using under-actuation of the ankle roll joints. Experimentation show that the scheme has its merit and drawback.

In summing up, the thesis's contributions to the field of robotics in biped gait generation are as follows:

1. A simplified bipedal model (LIPM) and simple sinusoidal functions are used to generate stable walk-oscillations in simulation and experiment.
2. ZMP compensation is realized solely by manipulating a single parameter in the lateral motion using a designed two stage ZMP compensation system.
3. The need for ZMP prediction is eliminated by asserting stability during support phase transitions.
4. The complexity involved in biped gait generation is addressed by using simple and computational inexpensive solutions by decoupling dynamic walking into independent motions.
5. Compliant joints are realized without the need of additional hardware and mechanism, or extensive control algorithms using commercial servos.
6. Compliant joints are applied for ground reaction forces measurement without explicit sensing devices.

### 7.3 Future Direction

Several refinements and extensions of the presented work are conceivable. The two-stage compensation in Chapter 4 can be extended to handle other terrains such as inclination surfaces. This can be achieved by incorporating the stiffness control in Chapter 6 where the system actually performs a balancing act of matching the height of the hips. Better control can be used to reinforce the stability of the omnidirectional walk. The possibility of introducing an upright postural controller [30] could improve and increase the amount of sagittal movement speed.

In conclusion, this thesis is drawn upon a practical approach where much of the focus is on feasible and simple implementable solutions. Problems are formulated and simplified based on certain assumptions.

# Chapter 8

## Author's Publications

1. Vadakkepat, Prahlad, Ng Buck Sin, Dip Goswami, Rui Xiang Zhang, and Li Yu Tan. "Soccer playing humanoid robots: Processing architecture, gait generation and vision system." *Robotics and Autonomous Systems* 57, no. 8 (2009): 776-785.
2. Ng, Buck Sin, Carlos A. Acosta Calderon, and Changjiu Zhou. "Robo-Erectus Jr-2010 KidSize Team Description Paper." In *Workshop Robocup Singapore*. 2010.
3. Pranggonoh, Yusuf, Buck Sin Ng, Tianwu Yang, Ai Ling Kwong, Pik Kong Yue, and Changjiu Zhou. "Field Rangers Team Description Paper." In *Robocup Singapore*. 2010.
4. Ng, Buck Sin, Carlos A. Acosta Calderon, and Changjiu Zhou. "Robo-Erectus Jr-2011 KidSize Team Description Paper." In *Robocup Istanbul*. 2011.



# Bibliography

- [1] S. H. Collins, A. Ruina, R. Tedrake, and M. Wisse, “Efficient bipedal robots based on passive dynamic walkers,” *Science*, vol. 307, pp. 1082–1085, Feb. 2005.
- [2] K. Hirai, M. Hirose, Y. Haikawa, and T. Takenaka, “The development of honda humanoid robot,” in *Robotics and Automation, 1998. Proceedings. 1998 IEEE International Conference on*, vol. 2, pp. 1321–1326, IEEE, 1998.
- [3] G. Welch and G. Bishop, “An introduction to the kalman filter,” 1995.
- [4] <http://www.kondo-robot.com>.
- [5] O. Ayhan and K. Erbatur, “Biped robot walk control via gravity compensation techniques,” in *Industrial Electronics Society, 2004. IECON 2004. 30th Annual Conference of IEEE*, vol. 1, pp. 621–626, IEEE, 2004.
- [6] Y. Fujimoto, S. Obata, and A. Kawamura, “Robust biped walking with active interaction control between foot and ground,” in *Robotics and Automation, 1998. Proceedings. 1998 IEEE International Conference on*, vol. 3, pp. 2030–2035, IEEE, 1998.
- [7] J. Yamaguchi, E. Soga, S. Inoue, and A. Takanishi, “Development of a bipedal humanoid robot-control method of whole body cooperative

- dynamic biped walking,” in *Robotics and Automation, 1999. Proceedings. 1999 IEEE International Conference on*, vol. 1, pp. 368–374, IEEE, 1999.
- [8] K. Fu, R. Gonzalez, and C. Lee, *Robotics: control, sensing, vision, and intelligence*. McGraw-Hill, Inc., 1987.
- [9] Y. Fujimoto and A. Kawamura, “Simulation of an autonomous biped walking robot including environmental force interaction,” *Robotics & Automation Magazine, IEEE*, vol. 5, no. 2, pp. 33–42, 1998.
- [10] J. Craig, “Introduction to robotics: mechanics and control,” 2004.
- [11] S. Kajita, F. Kanehiro, K. Kaneko, K. Yokoi, and H. Hirukawa, “The 3d linear inverted pendulum mode: A simple modeling for a biped walking pattern generation,” in *Intelligent Robots and Systems, 2001. Proceedings. 2001 IEEE/RSJ International Conference on*, vol. 1, pp. 239–246, IEEE, 2001.
- [12] S. Kajita, F. Kanehiro, K. Kaneko, K. Fujiwara, K. Yokoi, and H. Hirukawa, “A realtime pattern generator for biped walking,” in *Robotics and Automation, 2002. Proceedings. ICRA’02. IEEE International Conference on*, vol. 1, pp. 31–37, IEEE, 2002.
- [13] M. Bugeja, “Non-linear swing-up and stabilizing control of an inverted pendulum system,” in *EUROCON 2003. Computer as a Tool. The IEEE Region 8*, vol. 2, pp. 437–441, IEEE, 2003.
- [14] T. Komura, A. Nagano, H. Leung, and Y. Shinagawa, “Simulating pathological gait using the enhanced linear inverted pendulum model,” *Biomedical Engineering, IEEE Transactions on*, vol. 52, no. 9, pp. 1502–1513, 2005.
- [15] B. Lee, D. Stonier, Y. Kim, J. Yoo, and J. Kim, “Modifiable walking pattern generation using real-time zmp manipulation for humanoid robots,” in *Intelligent Robots and Systems, 2007. IROS*

2007. *IEEE/RSJ International Conference on*, pp. 4221–4226, IEEE, 2007.

- [16] N. Motoi, T. Suzuki, and K. Ohnishi, “A bipedal locomotion planning based on virtual linear inverted pendulum mode,” *Industrial Electronics, IEEE Transactions on*, vol. 56, no. 1, pp. 54–61, 2009.
- [17] K. Erbatur and O. Kurt, “Natural zmp trajectories for biped robot reference generation,” *Industrial Electronics, IEEE Transactions on*, vol. 56, no. 3, pp. 835–845, 2009.
- [18] A. Goswami, “Postural stability of biped robots and the foot-rotation indicator (fri) point,” *The International Journal of Robotics Research*, vol. 18, no. 6, pp. 523–533, 1999.
- [19] P. Sardain and G. Bessonnet, “Forces acting on a biped robot. center of pressure-zero moment point,” *Systems, Man and Cybernetics, Part A: Systems and Humans, IEEE Transactions on*, vol. 34, no. 5, pp. 630–637, 2004.
- [20] M. Vukobratovic, B. Borovac, D. Surla, and D. Stokic, *Biped Locomotion: Dynamics Stability, Control, and Application*. New York: Springer-Verlag, 1990.
- [21] K. Erbatur, A. Okazaki, K. Obiya, T. Takahashi, and A. Kawamura, “A study on the zero moment point measurement for biped walking robots,” in *Advanced Motion Control, 2002. 7th International Workshop on*, pp. 431–436, IEEE, 2002.
- [22] M. Vukobratovic and B. Borovac, “Zero moment point-thirty five years of its life,” *Int. Journal of Humanoid Robotics*, vol. 1, no. 1, pp. 157–173, 2004.
- [23] S. Kajita, M. Morisawa, K. Harada, K. Kaneko, F. Kanehiro, K. Fujiwara, and H. Hirukawa, “Biped walking pattern generator allowing auxiliary zmp control,” in *Intelligent Robots and Systems, 2006*

*IEEE/RSJ International Conference on*, pp. 2993–2999, IEEE, 2006.

- [24] K. Nagasaka, H. Inoue, and M. Inaba, “Dynamic walking pattern generation for a humanoid robot based on optimal gradient method,” in *Systems, Man, and Cybernetics, 1999. IEEE SMC’99 Conference Proceedings. 1999 IEEE International Conference on*, vol. 6, pp. 908–913, IEEE, 1999.
- [25] Q. Huang and Y. Nakamura, “Sensory reflex control for humanoid walking,” *Robotics, IEEE Transactions on*, vol. 21, no. 5, pp. 977–984, 2005.
- [26] B. Lee, D. Stonier, Y. Kim, J. Yoo, and J. Kim, “Modifiable walking pattern of a humanoid robot by using allowable zmp variation,” *Robotics, IEEE Transactions on*, vol. 24, no. 4, pp. 917–925, 2008.
- [27] T. Sugihara, Y. Nakamura, and H. Inoue, “Real-time humanoid motion generation through zmp manipulation based on inverted pendulum control,” in *Robotics and Automation, 2002. Proceedings. ICRA’02. IEEE International Conference on*, vol. 2, pp. 1404–1409, IEEE, 2002.
- [28] S. Kagami, T. Kitagawa, K. Nishiwaki, T. Sugihara, M. Inaba, and H. Inoue, “A fast dynamically equilibrated walking trajectory generation method of humanoid robot,” *Autonomous Robots*, vol. 12, no. 1, pp. 71–82, 2002.
- [29] J. Kim, I. Park, and J. Oh, “Experimental realization of dynamic walking of the biped humanoid robot khr-2 using zero moment point feedback and inertial measurement,” *Advanced Robotics*, vol. 20, no. 6, pp. 707–736, 2006.

- [30] I. Park, J. Kim, and J. Oh, "Online walking pattern generation and its application to a biped humanoid robotkhr-3 (hubo)," *Advanced robotics*, vol. 22, no. 2-3, pp. 159–190, 2008.
- [31] F. Xue, X. Chen, J. Liu, and D. Nardi, "Real time biped walking gait pattern generator for a real robot," *RoboCup 2011: Robot Soccer World Cup XV*, pp. 210–221, 2012.
- [32] C. Chevallereau, D. Djoudi, and J. Grizzle, "Stable bipedal walking with foot rotation through direct regulation of the zero moment point," *Robotics, IEEE Transactions on*, vol. 24, no. 2, pp. 390–401, 2008.
- [33] J. Ferreira, M. Crisóstomo, and A. Coimbra, "Human-like zmp trajectory reference in sagittal plane for a biped robot," in *Advanced Robotics, 2009. ICAR 2009. International Conference on*, pp. 1–6, IEEE, 2009.
- [34] M. Popovic, A. Hofmann, and H. Herr, "Angular momentum regulation during human walking: biomechanics and control," in *Robotics and Automation, 2004. Proceedings. ICRA'04. 2004 IEEE International Conference on*, vol. 3, pp. 2405–2411, IEEE, 2004.
- [35] M. Popovic, A. Goswami, and H. Herr, "Ground reference points in legged locomotion: Definitions, biological trajectories and control implications," *The International Journal of Robotics Research*, vol. 24, no. 12, pp. 1013–1032, 2005.
- [36] H. Herr and M. Popovic, "Angular momentum in human walking," *Journal of Experimental Biology*, vol. 211, no. 4, pp. 467–481, 2008.
- [37] A. Hofmann, M. Popovic, and H. Herr, "Exploiting angular momentum to enhance bipedal center-of-mass control," in *Robotics and Automation, 2009. ICRA'09. IEEE International Conference on*, pp. 4423–4429, IEEE, 2009.

- [38] S. Lee and A. Goswami, "Ground reaction force control at each foot: A momentum-based humanoid balance controller for non-level and non-stationary ground," in *Intelligent Robots and Systems (IROS), 2010 IEEE/RSJ International Conference on*, pp. 3157–3162, IEEE, 2010.
- [39] M. Morisawa, T. Yakoh, T. Murakami, and K. Ohnishi, "A comparison study between parallel and serial linked structures in biped robot system," in *Industrial Electronics Society, 2000. IECON 2000. 26th Annual Conference of the IEEE*, vol. 4, pp. 2614–2619, IEEE, 2000.
- [40] H. Sakamoto, H. Katayose, K. Miyazaki, and R. Nakatsu, "Extended-knee walk for humanoid robot with parallel link legs," *International Journal of Humanoid Robotics*, vol. 6, no. 04, pp. 565–584, 2009.
- [41] T. McGeer, "Passive dynamic walking," *The International Journal of Robotics Research*, vol. 9, no. 2, pp. 62–82, 1990.
- [42] G. Pratt and M. Williamson, "Series elastic actuators," in *Intelligent Robots and Systems 95. Human Robot Interaction and Cooperative Robots, Proceedings. 1995 IEEE/RSJ International Conference on*, vol. 1, pp. 399–406, IEEE, 1995.
- [43] J. Pratt and G. Pratt, "Exploiting natural dynamics in the control of a 3d bipedal walking simulation," in *In Proc. of Int. Conf. on Climbing and Walking Robots (CLAWAR99)*, 1999.
- [44] R. Tedrake, T. W. Zhang, M. fai Fong, and H. S. Seung, "Actuating a simple 3D passive dynamic walker," in *Proc. of IEEE Int. Conf. on Robotics and Automation*, vol. 5, (New Orleans, USA), pp. 4656–4661, Apr. 2004.

- [45] F. Asano, Z. Luo, and M. Yamakita, “Biped gait generation and control based on a unified property of passive dynamic walking,” *Robotics, IEEE Transactions on*, vol. 21, no. 4, pp. 754–762, 2005.
- [46] A. Dasgupta and Y. Nakamura, “Making feasible walking motion of humanoid robots from human motion capture data,” in *Proc. of IEEE Int. Conf. on Robotics and Automation*, 1999.
- [47] A. Safonova, N. Pollard, and J. Hodgins, “Optimizing human motion for the control of a humanoid robot,” *Proc. Applied Mathematics and Applications of Mathematics*, vol. 78, 2003.
- [48] K. Miura, M. Morisawa, S. Nakaoka, F. Kanehiro, K. Harada, K. Kaneko, and S. Kajita, “Robot motion remix based on motion capture data towards human-like locomotion of humanoid robots,” in *Humanoid Robots, 2009. Humanoids 2009. 9th IEEE-RAS International Conference on*, pp. 596–603, IEEE, 2009.
- [49] K. Yamane, S. Anderson, and J. Hodgins, “Controlling humanoid robots with human motion data: Experimental validation,” in *Humanoid Robots (Humanoids), 2010 10th IEEE-RAS International Conference on*, pp. 504–510, IEEE, 2010.
- [50] P. Vadakkepat, N. Sin, D. Goswami, R. Zhang, and L. Tan, “Soccer playing humanoid robots: Processing architecture, gait generation and vision system,” *Robotics and Autonomous Systems*, vol. 57, no. 8, pp. 776–785, 2009.
- [51] T. Arakawa and T. Fukuda, “Natural motion trajectory generation of biped locomotion robot using genetic algorithm through energy optimization,” in *Systems, Man, and Cybernetics, 1996., IEEE International Conference on*, vol. 2, pp. 1495–1500, IEEE, 1996.
- [52] T. Arakawa and T. Fukuda, “Natural motion generation of biped locomotion robot using hierarchical trajectory generation method

- consisting of ga, ep layers,” in *Robotics and Automation, 1997. Proceedings., 1997 IEEE International Conference on*, vol. 1, pp. 211–216, IEEE, 1997.
- [53] Y. Hasegawa, T. Arakawa, and T. Fukuda, “Trajectory generation for biped locomotion robot,” *Mechatronics*, vol. 10, no. 1, pp. 67–89, 2000.
- [54] Y. Fujimoto, “Trajectory generation of biped running robot with minimum energy consumption,” in *Robotics and Automation, 2004. Proceedings. ICRA'04. 2004 IEEE International Conference on*, vol. 4, pp. 3803–3808, IEEE, 2004.
- [55] E. Taskiran, M. Yilmaz, O. Koca, U. Seven, and K. Erbatur, “Trajectory generation with natural zmp references for the biped walking robot suralp,” in *Robotics and Automation (ICRA), 2010 IEEE International Conference on*, pp. 4237–4242, IEEE, 2010.
- [56] K. Matsuoka, “Sustained oscillations generated by mutually inhibiting neurons with adaptation,” *Biological Cybernetics*, vol. 52, pp. 367–376, 1985.
- [57] Y. Itoh, K. Taki, S. Kato, and H. Itoh, “A stochastic optimization method of cpg-based motion control for humanoid locomotion,” in *Robotics, Automation and Mechatronics, 2004 IEEE Conference on*, vol. 1, pp. 347–351, IEEE, 2004.
- [58] C. Acosta Calderon, R. Mohan, and C. Zhou, “Rhythmic locomotion control of humanoid robot,” *MICAI 2008: Advances in Artificial Intelligence*, pp. 626–635, 2008.
- [59] G. Endo, J. Morimoto, T. Matsubara, J. Nakanishi, and G. Cheng, “Learning cpg-based biped locomotion with a policy gradient method: Application to a humanoid robot,” *The International Journal of Robotics Research*, vol. 27, no. 2, pp. 213–228, 2008.



- [60] J. Or, “A hybrid cpg–zmp control system for stable walking of a simulated flexible spine humanoid robot,” *Neural Networks*, vol. 23, no. 3, p. 452, 2010.
- [61] C. Park, Y. Hong, and J. Kim, “Full-body joint trajectory generation using an evolutionary central pattern generator for stable bipedal walking,” *Proc. IEEE/RSJ Int. Conf. Intell. Robots Syst*, pp. 160–165, 2010.
- [62] C. Liu and Q. Chen, “Walking control strategy for biped robots based on central pattern generator,” in *Robotics and Automation (ICRA), 2012 IEEE International Conference on*, pp. 57–62, IEEE, 2012.
- [63] G. Capi, Y. Nasu, L. Barolli, and K. Mitobe, “Real time gait generation for autonomous humanoid robots: A case study for walking,” *Robotics and Autonomous Systems*, vol. 42, no. 2, pp. 107–116, 2003.
- [64] H. Wongsuwarn and D. Laowattana, “Neuro-fuzzy algorithm for a biped robotic system,” *Proceedings of the World Academy of Science, Engineering, and Technology*, vol. 15, 2006.
- [65] H. Picado, M. Gestal, N. Lau, L. Reis, and A. Tomé, “Automatic generation of biped walk behavior using genetic algorithms,” *Bio-Inspired Systems: Computational and Ambient Intelligence*, pp. 805–812, 2009.
- [66] J. Denk and G. Schmidt, “Synthesis of a walking primitive database for a humanoid robot using optimal control techniques,” in *Proceedings of IEEE-RAS International Conference on Humanoid Robots*, pp. 319–326, 2001.
- [67] T. Buschmann, S. Lohmeier, H. Ulbrich, and F. Pfeiffer, “Optimization based gait pattern generation for a biped robot,” in *Humanoid*

*Robots, 2005 5th IEEE-RAS International Conference on*, pp. 98–103, IEEE, 2005.

- [68] L. Yang, C. Chew, T. Zielinska, and A. Poo, “A uniform biped gait generator with offline optimization and online adjustable parameters,” *Robotica*, vol. 25, no. 5, pp. 549–566, 2007.
- [69] L. Roussel, C. Canudas-de Wit, and A. Goswami, “Generation of energy optimal complete gait cycles for biped robots,” in *Robotics and Automation, 1998. Proceedings. 1998 IEEE International Conference on*, vol. 3, pp. 2036–2041, IEEE, 1998.
- [70] W. Schiehlen, “Energy-optimal design of walking machines,” *Multi-body System Dynamics*, vol. 13, no. 1, pp. 129–141, 2005.
- [71] J. Park and H. Cho, “An online trajectory modifier for the base link of biped robots to enhance locomotion stability,” in *Robotics and Automation, 2000. Proceedings. ICRA’00. IEEE International Conference on*, vol. 4, pp. 3353–3358, IEEE, 2000.
- [72] P. Wieber and C. Chevallereau, “Online adaptation of reference trajectories for the control of walking systems,” *Robotics and Autonomous Systems*, vol. 54, no. 7, pp. 559–566, 2006.
- [73] V. Prahlaad, G. Dip, and C. Meng-Hwee, “Disturbance rejection by online zmp compensation,” *Robotica*, vol. 26, no. 1, p. 9, 2008.
- [74] S. Kajita, F. Kanehiro, K. Kaneko, K. Fujiwara, K. Harada, K. Yokoi, and H. Hirukawa, “Biped walking pattern generation by using preview control of zero-moment point,” in *Robotics and Automation, 2003. Proceedings. ICRA’03. IEEE International Conference on*, vol. 2, pp. 1620–1626, IEEE, 2003.
- [75] H. Lim, Y. Kaneshima, and A. Takanishi, “Online walking pattern generation for biped humanoid robot with trunk,” in *Robotics and*

*Automation, 2002. Proceedings. ICRA'02. IEEE International Conference on*, vol. 3, pp. 3111–3116, IEEE, 2002.

- [76] H. Diedam, D. Dimitrov, P. Wieber, K. Mombaur, and M. Diehl, “On-line walking gait generation with adaptive foot positioning through linear model predictive control,” in *Intelligent Robots and Systems, 2008. IROS 2008. IEEE/RSJ International Conference on*, pp. 1121–1126, IEEE, 2008.
- [77] I. Ha, Y. Tamura, and H. Asama, “Gait pattern generation and stabilization for humanoid robot based on coupled oscillators,” in *Intelligent Robots and Systems (IROS), 2011 IEEE/RSJ International Conference on*, pp. 3207–3212, IEEE, 2011.
- [78] S. Kajita, K. Kaneko, M. Morisawa, S. Nakaoka, and H. Hirukawa, “Zmp-based biped running enhanced by toe springs,” in *Robotics and Automation, 2007 IEEE International Conference on*, pp. 3963–3969, IEEE, 2007.
- [79] K. Yi, “Locomotion of a biped robot with compliant ankle joints,” in *Robotics and Automation, 1997. Proceedings., 1997 IEEE International Conference on*, vol. 1, pp. 199–204, IEEE, 1997.
- [80] D. Robinson, J. Pratt, D. Paluska, and G. Pratt, “Series elastic actuator development for a biomimetic walking robot,” in *Advanced Intelligent Mechatronics, 1999. Proceedings. 1999 IEEE/ASME International Conference on*, pp. 561–568, IEEE, 1999.
- [81] H. Kaminaga, J. Ono, Y. Nakashima, and Y. Nakamura, “Development of backdrivable hydraulic joint mechanism for knee joint of humanoid robots,” in *Robotics and Automation, 2009. ICRA'09. IEEE International Conference on*, pp. 1577–1582, IEEE, 2009.

- [82] S. Kawaji, K. Ogasawara, J. Iimori, and S. Yamada, "Compliance control for biped locomotion robot," in *Systems, Man, and Cybernetics, 1997. Computational Cybernetics and Simulation., 1997 IEEE International Conference on*, vol. 4, pp. 3801–3806, IEEE, 1997.
- [83] K. Hashimoto, Y. Sugahara, H. Sunazuka, C. Tanaka, A. Ohta, M. Kawase, H. Lim, and A. Takanishi, "Biped landing pattern modification method with nonlinear compliance control," in *Robotics and Automation, 2006. ICRA 2006. Proceedings 2006 IEEE International Conference on*, pp. 1213–1218, IEEE, 2006.
- [84] S. Hyon, "A motor control strategy with virtual musculoskeletal systems for compliant anthropomorphic robots," *Mechatronics, IEEE/ASME Transactions on*, vol. 14, no. 6, pp. 677–688, 2009.
- [85] K. Van Heerden and A. Kawamura, "An investigation on robust biped walking using compliant force control and a online walking pattern generator," in *IECON 2010-36th Annual Conference on IEEE Industrial Electronics Society*, pp. 1453–1458, IEEE, 2010.
- [86] Y. Sugahara, T. Hosobata, Y. Mikuriya, H. Lim, and A. Takanishi, "Realization of stable dynamic walking by a parallel bipedal locomotor on uneven terrain using a virtual compliance control," in *Intelligent Robots and Systems, 2003.(IROS 2003). Proceedings. 2003 IEEE/RSJ International Conference on*, vol. 1, pp. 595–600, IEEE, 2003.
- [87] M. Ogino, H. Toyama, and M. Asada, "Stabilizing biped walking on rough terrain based on the compliance control," in *Intelligent Robots and Systems, 2007. IROS 2007. IEEE/RSJ International Conference on*, pp. 4047–4052, IEEE, 2007.
- [88] W. Xu, R. Xiong, and J. Wu, "Force/torque-based compliance control for humanoid robot to compensate the landing impact force," in

*Networking and Distributed Computing (ICNDC), 2010 First International Conference on*, pp. 336–340, IEEE, 2010.

- [89] Y. Sakagami, R. Watanabe, C. Aoyama, S. Matsunaga, N. Higaki, and K. Fujimura, “The intelligent asimo: System overview and integration,” in *Intelligent Robots and Systems, 2002. IEEE/RSJ International Conference on*, vol. 3, pp. 2478–2483, IEEE, 2002.
- [90] S. Behnke, “Online trajectory generation for omnidirectional biped walking,” in *Robotics and Automation, 2006. ICRA 2006. Proceedings 2006 IEEE International Conference on*, pp. 1597–1603, IEEE, 2006.
- [91] X. Yuan and T. Yingzi, “Layered omnidirectional walking controller for the humanoid soccer robot,” in *Robotics and Biomimetics, 2007. ROBIO 2007. IEEE International Conference on*, pp. 757–762, IEEE, 2007.
- [92] G. Shi, H. Wan, and B. Fang, “Online omnidirectional walking patterns for biped robot,” *International Conf. on Electronic Measurement and Instruments*, vol. 3, pp. 856–861, 2009.
- [93] J. Strom, G. Slavov, and E. Chown, “Omnidirectional walking using zmp and preview control for the nao humanoid robot,” *RoboCup 2009: robot soccer world cup XIII*, pp. 378–389, 2010.
- [94] S. Hong, Y. Oh, Y. Chang, and B. You, “An omni-directional walking pattern generation method for humanoid robots with quartic polynomials,” in *Intelligent Robots and Systems, 2007. IROS 2007. IEEE/RSJ International Conference on*, pp. 4207–4213, IEEE, 2007.
- [95] Z. Yanjun, “Fuzzy omnidirectional walking controller for the humanoid soccer robot,” in *IEEE-RAS International Conference on Humanoid Robots*, 2009.

- [96] J. Park and O. Kwon, "Reflex control of biped robot locomotion on a slippery surface," in *Robotics and Automation, 2001. Proceedings 2001 ICRA. IEEE International Conference on*, vol. 4, pp. 4134–4139, IEEE, 2001.
- [97] K. Kaneko, F. Kanehiro, S. Kajita, M. Morisawa, K. Fujiwara, K. Harada, and H. Hirukawa, "Slip observer for walking on a low friction floor," in *Intelligent Robots and Systems, 2005.(IROS 2005). 2005 IEEE/RSJ International Conference on*, pp. 634–640, IEEE, 2005.
- [98] T. Hirabayashi, B. Ugurlu, A. Kawamura, and C. Zhu, "Yaw moment compensation of biped fast walking using 3d inverted pendulum," in *Advanced Motion Control, 2008. AMC'08. 10th IEEE International Workshop on*, pp. 296–300, IEEE, 2008.
- [99] A. Kawamura and K. Van Heerden, "Maintaining floor-foot contact of a biped robot by force constraint position control," in *Mechatronics (ICM), 2011 IEEE International Conference on*, pp. 857–862, IEEE, 2011.
- [100] T. Wang, C. Chevallereau, and C. Rengifo, "Walking and steering control for a 3d biped robot considering ground contact and stability," *Robotics and Autonomous Systems*, 2012.
- [101] O. Lorch, A. Albert, J. Denk, M. Gerecke, R. Cupec, J. Seara, W. Gerth, and G. Schmidt, "Experiments in vision-guided biped walking," in *Intelligent Robots and Systems, 2002. IEEE/RSJ International Conference on*, vol. 3, pp. 2484–2490, IEEE, 2002.
- [102] R. Cupec, O. Lorch, and G. Schmidt, "Vision-guided humanoid walking—concepts and experiments," *Autonome Mobile Systeme 2003: 18. Fachgespräch Karlsruhe, 4./5. Dezember 2003*, vol. 18, p. 1, 2003.

- [103] P. Michel, J. Chestnutt, J. Kuffner, and T. Kanade, "Vision-guided humanoid footstep planning for dynamic environments," in *Humanoid Robots, 2005 5th IEEE-RAS International Conference on*, pp. 13–18, IEEE, 2005.
- [104] K. Matsumoto and A. Kawamura, "The direction control of a biped robot using gyro sensor feedback," in *Advanced Motion Control, 2010 11th IEEE International Workshop on*, pp. 137–142, IEEE, 2010.
- [105] L. Geppert, "Qrio, the robot that could," *IEEE Spectrum*, vol. 41, no. 5, pp. 34–37, 2004.
- [106] <http://www.fira.net/>.
- [107] H. Kitano, M. Asada, Y. Kuniyoshi, I. Noda, and E. Osawa, "Robocup: The robot world cup initiative," in *Proceedings of the first international conference on Autonomous agents*, pp. 340–347, ACM, 1997.
- [108] B. Ng, C. Calderon, and C. Zhou, "Robo-erectus jr-2010 kidsize team description paper," in *Workshop Robocup Singapore*, 2010.
- [109] B. Ng, C. Calderon, and C. Zhou, "Robo-erectus jr-2011 kidsize team description paper," in *Robocup Istanbul*, 2011.
- [110] R. Yates and R. Lyons, "Dc blocker algorithms [dsp tips & tricks]," *Signal Processing Magazine, IEEE*, vol. 25, no. 2, pp. 132–134, 2008.
- [111] R. Brown and P. HWANG, "Introduction to random signals and applied kalman filtering(book)," *New York, John Wiley & Sons, Inc., 1992. 512*, 1992.
- [112] J. Dormand and P. Prince, "A family of embedded runge-kutta formulae," *Journal of computational and applied mathematics*, vol. 6, no. 1, pp. 19–26, 1980.

- [113] J. Denavit, "A kinematic notation for lower-pair mechanisms based on matrices.," *Trans. of the ASME. Journal of Applied Mechanics*, vol. 22, pp. 215–221, 1955.
- [114] T. Ishida, "Development of a small biped entertainment robot qrio," in *Micro-Nanomechatronics and Human Science, 2004 and The Fourth Symposium Micro-Nanomechatronics for Information-Based Society, 2004. Proceedings of the 2004 International Symposium on*, pp. 23–28, IEEE, 2004.
- [115] J. Morimoto, G. Endo, J. Nakanishi, S. Hyon, G. Cheng, D. Bentevegna, and C. Atkeson, "Modulation of simple sinusoidal patterns by a coupled oscillator model for biped walking," in *Robotics and Automation, 2006. ICRA 2006. Proceedings 2006 IEEE International Conference on*, pp. 1579–1584, IEEE, 2006.
- [116] I. Park, J. Kim, and J. Oh, "Online biped walking pattern generation for humanoid robot khr-3 (kaist humanoid robot-3: Hubo)," in *Humanoid Robots, 2006 6th IEEE-RAS International Conference on*, pp. 398–403, IEEE, 2006.
- [117] Y. Choi, B. You, and S. Oh, "On the stability of indirect zmp controller for biped robot systems," in *Intelligent Robots and Systems, 2004.(IROS 2004). Proceedings. 2004 IEEE/RSJ International Conference on*, vol. 2, pp. 1966–1971, IEEE, 2004.
- [118] P. Vadakkepat, N. B. Sin, D. Goswami, R. X. Zhang, and L. Y. Tan, "Soccer playing humanoid robots: Processing architecture, gait generation and vision system," *Robotics and Autonomous Systems*, vol. 57, no. 8, pp. 776–785, 2009.
- [119] G. Dip, V. Prahlad, and P. Kien, "Genetic algorithm-based optimal bipedal walking gait synthesis considering tradeoff between stability margin and speed," *Robotica*, vol. 27, no. 03, pp. 355–365, 2009.



- [120] C. Bauby and A. Kuo, "Active control of lateral balance in human walking," *Journal of biomechanics*, vol. 33, no. 11, pp. 1433–1440, 2000.
- [121] J. Kim, D. Kim, Y. Kim, K. Park, J. Park, C. Moon, K. Seow, and K. Koh, "Humanoid robot hansaram: Recent progress and developments," *J. of Advanced Computational Intelligence & Intelligent Informatics*, vol. 8, no. 1, pp. 45–55, 2004.
- [122] S. McGrath, J. Anderson, and J. Baltes, "Model-free active balancing for humanoid robots," in *RoboCup 2008: Robot Soccer World Cup XII*, pp. 544–555, Springer, 2009.
- [123] R. DAndrea, "The cornell robocup robot soccer team: 1999–2003," *Handbook of Networked and Embedded Control Systems*, pp. 793–804, 2005.
- [124] M. Koeda, T. Yoshikawa, and T. Ito, "Stability improvement by slip-based turning motion of humanoid robot," in *Proceedings of the 25th Annual Conference of the Robotics Society of Japan, 3H15*, 2007.
- [125] K. Miura, S. Nakaoka, M. Morisawa, F. Kanehiro, K. Harada, and S. Kajita, "Analysis on a friction based twirl for biped robots," in *Robotics and Automation (ICRA), 2010 IEEE International Conference on*, pp. 4249–4255, IEEE, 2010.
- [126] Y. Pranggonoh, B. Ng, T. Yang, A. Kwong, P. Yue, and C. Zhou, "Field rangers team description paper,"
- [127] F. Meyer, A. Sprowitz, M. Lungarella, and L. Berthouze, "Simple and low-cost compliant leg-foot system," in *Intelligent Robots and Systems, 2004.(IROS 2004). Proceedings. 2004 IEEE/RSJ International Conference on*, vol. 1, pp. 515–520, IEEE, 2004.

- [128] R. Luo, Y. Pu, C. Chen, J. Chang, and C. Li, “Design and implementation of humanoid biped walking robot mechanism towards natural walking,” in *Robotics and Biomimetics (ROBIO), 2011 IEEE International Conference on*, pp. 1165–1170, IEEE, 2011.
- [129] A. David, J. Chardonnet, A. Kheddar, K. Kaneko, and K. Yokoi, “Study of an external passive shock-absorbing mechanism for walking robots,” in *Humanoid Robots, 2008. Humanoids 2008. 8th IEEE-RAS International Conference on*, pp. 435–440, IEEE, 2008.
- [130] Q. Wang, J. Zhu, Y. Huang, K. Yuan, and L. Wang, “Segmented foot with compliant actuators and its applications to lower-limb prostheses and exoskeletons,” 2012.
- [131] S. Czarnetzki, S. Kerner, and O. Urbann, “Observer-based dynamic walking control for biped robots,” *Robotics and Autonomous Systems*, vol. 57, no. 8, pp. 839–845, 2009.